Investigating cell-ECM interactions with high resolution microscopy techniques

Zur Erlangung des akademischen Grades eines

DOKTORS DER NATURWISSENSCHAFTEN

(Dr. rer. nat.)

Fakultät für Chemie und Biowissenschaften

Karlsruher Institut für Technologie (KIT) - Universitätsbereich

genehmigte

DISSERTATION

von

Dipl.-Biol. Univ. Tatjana Grabovskij

aus

Charkiw, Ukraine

Dekan: Prof. Dr. Peter Roesky

Referent: PD Dr. Clemens Franz

Korreferent: Prof. Dr. Doris Wedlich

Tag der mündlichen Prüfung: 17.04.2014

Der experimentelle Teil der vorliegenden Arbeit wurde im Center for Functional Nanostructures und am Institut für Zell- und Neurobiologie (Zoologie I) des Karlsruher Instituts für Technologie (KIT) in der Zeit von August 2010 bis März 2014 durchgeführt.

Ich versichere, dass ich diese Arbeit selbstständig angefertigt und keine anderen als die angegebenen Quellen und Hilfsmittel benutzt sowie die wörtlich oder inhaltlich übernommenen Stellen als solche kenntlich gemacht und die Satzung der Karlsruher Instituts für Technologie (KIT) zur Sicherung guter wissenschaftlicher Praxis in der jeweils gültiger Fassung beachtet habe.

Tatjana Grabovskij Karlsruhe, den 03.03.2014

Contents

List of Figures

List of Tables

Abbrevations, symbols and units

Abbreviations

3D	three dimensional
AFM	atomic force microscopy
APS	ammonium persulfate
APTES	(3-Aminopropyl)-triethoxysilane
BSA	bovine serum albumin
CLSM	confocal laser scanning microscopy
Col I	collagen type I
DAPI	4,6-diamino-2-phenylindole
ddH_2O	double-destilled water
DMEM	Dulbecco's modified Eagle medium
DMSO	dimethyl sulfoxide
DOC	deoxycholate
ECM	extracellular matrix
EDTA	ethylenediaminetetraacetic acid
EG3O-Me	ethylenglycol-3-O-mercaptan
EM	electron microscopy
FA	focal adhesion
FAK	focal adhesion kinase
FCS	fetal calf serum
F-D curve	force-distance curve
Fig.	figure
FITC	fluorescein isothiocyanate
FN	fibronectin
FN-AF488	fibronectin conjugated with Alexa Fluor 488® dye
FN-AF568	fibronectin conjugated with Alexa Fluor 568® dye
FN-AF633	fibronectin conjugated with Alexa Fluor 633® dye
FX	focal complex
HFF	Human foreskin fibroblast
H_2O_2	hydrogen peroxide
mAB	monoclonal antibody
MDCK	Madin Darby canine kidney cell line
MEF	mouse embryonic fibroblasts
MEM	minimal essential medium
MeOH	methanol
pAB	polyclonal antibody
PAA	polyacrylamide
PBS	phosphate buffered saline

PDMS	polydimethylsiloxane
PFA	paraformaldehyde
RAW264.7	mouse leukaemic monocyte macrophage cell line
REF52	rat embrionic fibroblasts
RGD	arginine-glycine-aspartate
SDS-PAGE	sodium dodecyl sulfate polyacrylamide gel electrophoresis
SEM	scanning electron microscopy
SMFS	single-molecule force spectroscopy
TEM	transmission electron microscopy
TEMED	N,N,N',N'-Tetramethylethylendiamin
TIRF	total internal reflection fluorescence
Tris	tris(hydroxymethyl)aminomethane
TRITC	tetramethylrhodamin isothiocyanat
v/v	volume per volume
w/v	weight per volume

Symbols and units

Å	Angstrom (10^{-10} m)
°C	degree Celsius
∅	diameter
h	hour
L	liter
M	molar
m	meter
min	minute
mM	millimolar
µg	microgramm (10^{-6} g)
µl	microliter (10^{-6} L)
µm	micrometer (10^{-6} m)
µM	micromolar (10^{-6} M)
N	Newton (kg·m/s^2)
nm	nanometer (10^{-9} m)
nN	nanonewton (10^{-9} N)
Pa	Pascal (N/m^2)
pN	piconewton (10^{-12} N)
rcf	relative centrifugal force (m/s^2)
sec	second

Zusammenfassung

Zellen in Geweben sind von der extrazellulären Matrix (EZM) umgeben, einem komplexen Gemisch aus Makro- und Signalmolekülen. Zellen interagieren mit dieser Umgebung über verschiedene Rezeptoren, mit deren Hilfe sie auf die mechanischen Eigenschaften und die chemische Zusammensetzung der EZM reagieren und entsprechende Signale in die Zelle weiterleiten können. Durch diese Signale werden wiederum vielfältige zelluläre Prozesse reguliert, wie Zellteilung, Differenzierung oder Migration. Über Integrin-Rezeptoren, welche über intrazelluläre Adapterproteine mit dem Zytoskelett verbunden sind, kann die Zelle auch Kräfte auf die EZM ausüben und diese so umstrukturieren. Des Weiteren können Zellen durch Sekretion von Matrixproteinen und Enzymen die Komposition und die mechanischen Eigenschaften der EZM beeinflussen. In dieser Dissertation werden verschiedene Aspekte der Zell-EZM-Wechselwirkung behandelt, wobei hochauflösende Mikroskopietechniken wie die Rasterkraft- (*atomic force microscopy*, AFM), Rasterelektronen- (*scanning electron microscopy*, SEM) und Fluoreszenzmikroskopie eingesetzt wurden. Ein besonder Schwerpunkt lag dabei in der Kombination dieser Techniken, um so neue Möglichkeiten für die Analyse zellulärer und matrix-gebundener Strukturen zu eröffnen. So erlaubt die spezifsche Markierung ausgewählter Proteine mit Fluorophoren deren spätere Lokalisierung in komplementären, hochaufgelösten rastermikroskopischen Bildern. Allerdings finden in adhärenten Zellen viele Zell-EZM–Wechselwirkungen unterhalb des Zellkörpers statt, so dass deren direkte Beobachtung durch oberflächen-sensitive Methoden wie AFM oder SEM unmöglich ist. Deshalb wurde im Rahmen dieser Doktorarbeit eine Technik entwickelt, die es ermöglicht, die Zellunterseite samt assoziierter Matrix-Bestandteile unbeschadet freizulegen (Kapitel 3). Mit Hilfe eines UV-aushärtbaren Haftmittels werden dabei adhärente Zellen von ihrem Substrate gelöst und invertiert, so dass die zellulären Matrixadhesionspunkte an der basalen Membran und die daran gebundenen EZM Proteine exponiert werden. Bemerkenswert an dieser Methode sind die vollständige Bewahrung der zellulären Integrität während des Invertierungsschrittes und die hohe Reproduzierbarkeit. Um die Nützlichkeit des neuen Verfahrens zu demonstrieren, wurde zum ersten Mal die Struktur der basalen Seite von Podosomen, spezieller Zell-Matrix-Kontakte, bis in den Nanometerbereich aufgelöst (Kapitel 4). Podosomen sind hoch dynamische Zell-EZM-Adhäsionspunkte welche unter anderem bei der Matrixdegradation und dem Knochenabbau eine entscheidende Rolle spielen. Podosomen bestehen aus einem F-Aktin-Kern und

einem zentralen Membrankanal, welcher für die Sekretion von Enzymen verantwortlich sein könnte. Durch die Kombination von Fluoreszenzmikroskopie, AFM und SEM konnte hier erstmals eine apikale und basale Einstülpung der Podosomenstruktur nachgewiesen werden, welches für die Existenz eines zentralen Kanals spricht. Ein weiterer Aspekt der Dissertation betrifft die Interaktion zwischen Fibroblasten und dem EZM-Protein Fibronektin (FN, Kapitel 5). FN ist ein globuläres Protein, welches von Zellen über Integrine gebunden und mit Hilfe von zellulären Kräften in eine entfaltete Konformation überführt werden kann. Dadurch werden verborgene FN-FN Bindestellen freigelegt, so dass FN-Moleküle miteinander wechselwirken und sich in einem als Fibrillogenese bezeichneten Prozess zu dickeren Fibrillen anlagern. Bisher wurde die Fibrillogenese vorwiegend an fixierten Präparaten untersucht, welche die Fibrillen-Entstehung lediglich zu unterschiedlichen Zeitpunkten aufzeigen. AFM- oder Fluoreszenzmikroskopie-basierte Zeitrafferaufnahmen gab es dagen bislang nicht. Im Rahmen dieser Dissertation ist es gelungen, die Fibrillenbildung durch lebende Zellen mit Hilfe von AFM erstmals direkt zu visualisieren. Aus den hochaufgelösten AFM-Bildern kann die Dynamik des Fibrillen-Wachstum und die Fibrillen-Struktur bestimmt werden. Versuche, die FN-Fribrillogenese auch mit Hilfe der Fluoreszenzmikroskopie abzubilden waren dagegen zunächst nicht erfolgreich, führten jedoch zu der Erkenntnis, dass die FN-Fibrillogenese ein stark lichtsensitiver Prozess ist (Kapitel 6). So verhindert selbst kurzzeitige Belichtung mit UV- oder sichtbarem Licht unterhalb einer Wellenlänge von 560 nm effektiv die Zell-abhängige Fibrillenbildung des FNs. Nach Optimierung verschiedener Belichtungsparameter und der eingesetzten Wellenlänge konnte jedoch schließlich die Fibrillogenese auch fluoreszenzmikroskopisch beobachtet werden. Zusammenfassend lässt sich festhalten, dass Zell-EZM-Interaktionen trotz intensiver Erforschung noch immer viele offene Fragen bieten, deren Klärung neue experimentelle Vorgehensweisen erfordert. So kann durch die neue Invertierungs-Methode die Zellunterseite für hochauflösendede Abbildungsverfahren wie AFM und SEM zugänglich gemacht werden. Des Weiteren muss beachtet werden, dass die eingesetzten Mikroskopietechniken selbst die beobachteten biologischen Prozesse stark beeinflussen können. So kann durch die notwendige Belichtung der Probe während der Fluoreszenzmikroskopie die Fibrillenbildung des FN vollständig verhindert werden, was wiederum zur Beeinflussung zellulärer Wechselwirkungen mit der EZM führen kann.

Summary

Cells in tissues are surrounded by the extracellular matrix (ECM), a complex mixture of different macro- and signaling molecules. Cells interact with the ECM using a variety of receptors, which enables them to respond to the mechanical properties and chemical composition of the ECM and to transmit signals into the cell. These intracellular signaling pathways then regulate a wide variety of cellular processes, such as cell division, differentiation and migration. Via cytoskeleton-attached integrin receptors, cells can also exert external forces on the ECM, leading to matrix processing and remodeling. Furthermore, cells may secrete additional matrix components and enzymes to modify the composition and mechanical properties of the ECM. This thesis addresses different aspects of cell-ECM interactions by using high-resolution microscopy techniques, including atomic force microscopy (AFM), scanning electron microscopy (SEM), and fluorescence microscopy, with a special focus on combining these techniques to obtain complimentary information. For instance, fluorescent labeling of specific proteins allows for relocating them in corresponding high-resolution AFM or SEM images. However, in adherent cells the majority of cell-matrix interactions occur at the basal cell side, making them inaccessible to surface-sensitive scanning techniques. In this thesis, a new method was developed for non-destructively inverting adherent cells, exposing the basal cell side including associated matrix components (Chapter 3). In this method, adherent cells are embedded in a UV-curable adhesive, removed from their substrate and finally inverted for further analysis. A special advantage of this technique is the complete preservation of the structural integrity of the cells during inversion and the high degree of reproducibility. To demonstrate the feasibility of this method, the basal surface of podosomes, specialized cell-matrix adhesion sites, were imaged with nanometer resolution for the first time (Chapter 4). Podosomes are highly dynamic cell-ECM adhesion sites which play a crucial role in matrix degradation and bone resorption. Podosomes contain an F-actin-rich core and possible a central membrane channel proposed to participate in enzyme secretion into the extracellular space. Using a combination of fluorescence microscopy, AFM and SEM and the cell inversion technique, it could be shown here for the first time that podosomes contain a central depression at both their apical and basal side, strongly supporting the idea of a central channel. A further topic of this thesis concerns interactions between fibroblasts and the ECM protein fibronectin (FN, Chapter 5). FN is a globular protein,

which can be bound by cells via integrins and stretched into an elongated conformation as a result of cellular contraction forces. FN extension exposes cryptic FN-FN binding sites, which enables FN molecules to laterally interact with each other and to form large fibrillar structures in a process termed fibrillogenesis. So far FN fibrillogenesis has been mainly studied using chemically fixed samples, displaying intermediate steps of fibrillogenesis at different time points only, while AFM- or fluorescence-based time-lapse imaging experiments had been missing. Within the framework of this thesis, the rearrangement of FN fibrils by living cells could be visualized for the first time using time-lapse AFM imaging. In contrast, complimentary fluorescence-based time-lapse experiments initially proved unsuccessful, but revealed that FN fibrillogenesis is a strongly light-sensitive process (Chapter 6). Even short exposure to UV or visible light below a wavelength of 560 nm effectively inhibits cell-induced fibril formation of FN. However, after optimizing different exposure conditions, including exposure time and intensity, and illumination with light of longer wavelength, cell-induced FN remodeling could be visualized in real time by fluorescence microscopy as well. In summary, cell-ECM interactions still pose numerous questions despite extensive research in this field. Important novel insight can be gained by developing new sample preparation and imaging techniques, such as the cell inversion method which makes the basal cell side accessible to high resolution raster scanning by AFM and SEM. However, it must be noted that different microscopy techniques themselves may strongly affect the investigated biological processes. In particular, sample illumination during fluorescence microscopy can completely inhibit fibril formation of FN, which in turn may influence cellular interactions with ECM.

1 Introduction

1.1 The extracellular matrix (ECM)

The different tissues of the vertebrate body consist of two main components: a cellular part and a surrounding extracellular matrix (ECM). The ECM is mainly composed of water, proteoglycans, glycoproteins, such as collagens, laminins and fibronectin (FN), and signaling proteins, such as growth factors (Berrier and Yamada, 2007). ECM macromolecules are secreted by cells and then assembled into a complex, three dimensional (3D) network. Each tissue has an ECM with a unique composition (Table 1.1) and structure generated during tissue development (Frantz et al., 2010). For instance, the bulk of bone, cartilage and dermal tissue is formed by the ECM. In contrast, in epithelia and muscle most of the tissue is cellular and the matrix is confined to a basal lamina surrounding the cellular component (Goodman, 2007).

Besides providing a scaffold for cell embedding, the ECM also promotes and restricts cell adhesion and movement and acts as a reservoir for growth factors, limiting their diffusion and facilitating the transmission of environmental signals to cells (Goodman, 2007; Rozario and DeSimone, 2010).

1.2 Collagen

Collagens are the most abundant structural ECM proteins of animal tissue (Frantz et al., 2010). In vertebrates, there are 28 different collagens, numbered in order of their discovery with Roman numerals I-XXVIII (Myllyharju and Kivirikko, 2004) (Table 1.2). Structurally, all collagens are built-up of tropocollagen, a right-handed bundle of three parallel, left-handed proline-rich α-helices. The most common motif in the amino acid sequence of the α-helix is the repeating sequence (glycine-X-Y)n, where X and Y represent any amino acid other than glycine. However, proline is often found at the X position, and 4-hydroxyproline at the Y position (Brodsky and Persikov, 2005; Myllyharju and Kivirikko, 2004; Shoulders and Raines, 2009). In some collagens all three α-helices are identical, whereas in others the triple helix contains two or even three different α-helices (Myllyharju and Kivirikko, 2004). Different collagen classes can be defined depending on the tropocollagen

ECM macromolecule	Components	Localization
collagens	collagen type I	skin, tendon, bone
glycoproteins	fibronectin	blood, connective tissue
	laminin	basal lamina
	vitronectin	blood
	entactin	basal lamina
	tenacscin	embryonic connective tissue
	osteopontin	bone, kidney
proteoglycans	decorin	connective tissue
	aggrecan	cartilage
	perlecan	epithelium, muscle
	fibromodulin	cartilage, skin, tendon
glycosaminoglycans	keratan	

Table 1.1: Composition of the ECM matrix (adapted from (Gartner and Hiatt, 2010)).

organization, including fibrillar and network-forming collagens, fibril-associated collagens with interrupted triple helices (FACIT), membrane associated collagens with interrupted triple helices (MACITs) and multiple triple-helix domains and interruptions (Kadler et al., 2008; Rest and Garrone, 1991) (Table 1.2). Generally, collagen assembly is a complex and hierarchical process, ultimately resulting in the creation of macroscopic fibers and networks (Shoulders and Raines, 2009) (Fig. 1.1).

Fibrillar collagen is synthesized in the endoplasmatic reticulum as soluble procollagen with large propeptides at both ends of the α-helix (Myllyharju and Kivirikko, 2004). Outside the cell, the propeptides are cleaved by special metalloproteinases leaving short telopeptides (Colige et al., 2005; Maki et al., 2005). The collagen α-helix with cleaved ends is called tropocollagen. Three tropocollagen α-helices then assemble into a triple helix in an entropically driven process. Since tropocollagen molecules are less soluble than procollagen, the loss of solubility results in the creation of a triple helix with minimized area to volume ratio (Kadler et al., 1987). Several tropocollagen triple helices are organized into collagen fibrils, where lysine residues in the telopeptide and triple-helical hydroxylysines are covalently cross-linked. This stabilization of collagen fibrils results in a high tensile strength (Canty and Kadler, 2005). For example, collagen type I fibrils consists of tropocollagen subunits being 280 nm long and having a diameter of 1.5 nm (Fig. 1.1B). These subunits form fibrils in a self-assembly process (Kadler et al., 1996) by aligning with each other with a regular stagger. This leads to a periodical structure of gaps and overlaps every 67 nm forming so called D-bands (Kadler et al., 2008). Since the 1960s it has been possible to visualize the collagen structure with nm resolution by transmission electron microscopy (TEM), revealing showing the D-band periodicity directly (Fig. 1.1C).

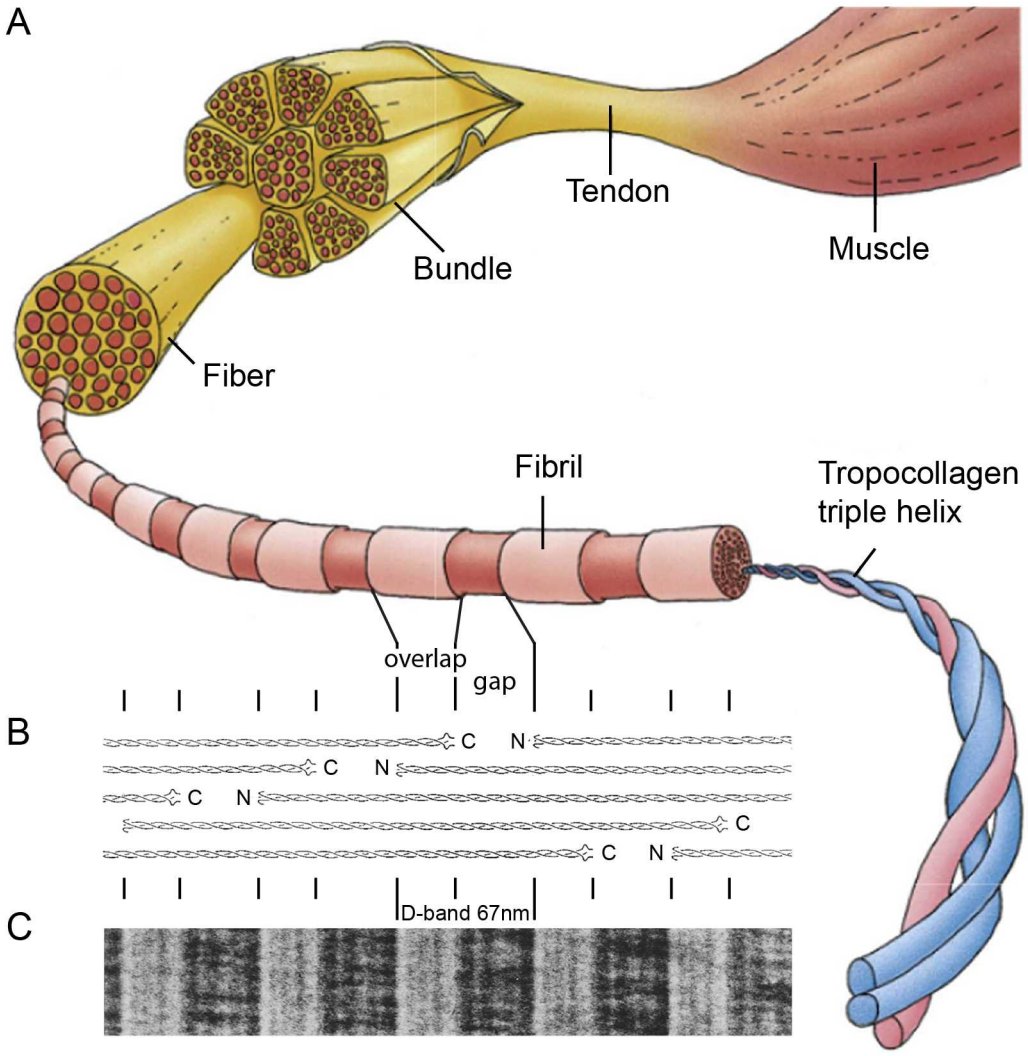

Figure 1.1: Molecular organization of collagen type I. (A) The hierarchical organization of collagen in the tendon. The triple helix of tropocollagens associate with other helices into fibrils. Then, several fibrils form larger fibers, which are composed into bundles resulting in the tendon (adapted from (Gartner and Hiatt, 2010)). (B) During the self-assembly of tropocollagen triple helices into fibrils overlap and gap regions are created, resulting in a staggered structure with a period of 67 nm, the so called D-band. (C) A TEM image of a collagen type I fibril contains brighter and darker regions, corresponding to overlap and gap regions, respectively (adapted from (Kadler et al., 1996)).

Class	Collagen type	Representative tissues
fibrillar	I, II, III, V, XI, XXIV, XXVII	dermis, bone, tendon, ligament, cornea placenta, cartilage.
fibril associated collagens with interrupted triple helices on the fibril surface (FACIT)	IX, XII, XIV, XVI, XIX, XX, XXI, XXII, XXVI	cartilage, cornea, vitreous, dermis, tendon, bone, kidney, basement membrane, tissue junctions, ovary, testis
hexagonal networks	IV, VI, VIII, X	basement membranes, dermis, brain, bone, cornea, heart, kidney, cartilage
anchoring fibrils	VII	dermis, bladder
membrane-associated collagen with interrupted triple helices (MACIT)	XIII, XVII, XXIII, XXV	endothelial cells, dermis, eye, heart, hemidesmosomes in epithelia, brain, testis
multiple triple-helix domains and interruptions	XV, XVIII	capillaries, testis, kidney, heart, basement membrane, liver

Table 1.2: Overview of vertebrates collagens (adapted from (Shoulders and Raines, 2009)).

1.3 Fibronectin (FN)

Fibronectin (FN) is an ubiquitous ECM protein. It plays a crucial role not only in tissue organization as a scaffold protein, but also in regulating cellular processes, such as cell differentiation, growth, adhesion and migration (Hynes, 1990). FN is also important for vertebrate development. For example, the inactivation of the FN gene in mice embryos results in early embryonic lethality (George et al., 1993).

1.3.1 FN structure

FN is a dimeric glucoprotein containing two nearly identical monomers with a molecular weight of approximately 250 kDa each. The monomers are covalently linked near their C-terminal ends via disulfide bond pairs (Johnson et al., 1999) (Fig. 1.2). Each FN monomer contains three types of repeating units, called FN type I (FNI), II (FNII) or III (FNIII) (Pankov and Yamada, 2002; Singh et al., 2010; Wierzbicka-Patynowski and Schwarzbauer, 2003). The FN gen encodes twelve different FNI, two FNII, and 15 constitutively expressed and two alternatively spliced (EIIIA and EIIIB) FNIII repeats, and a non-homologous variable (V) region (To and Midwood, 2011). The molecular diversity of FN is therefore generated by alternative splicing (Hynes, 1990).

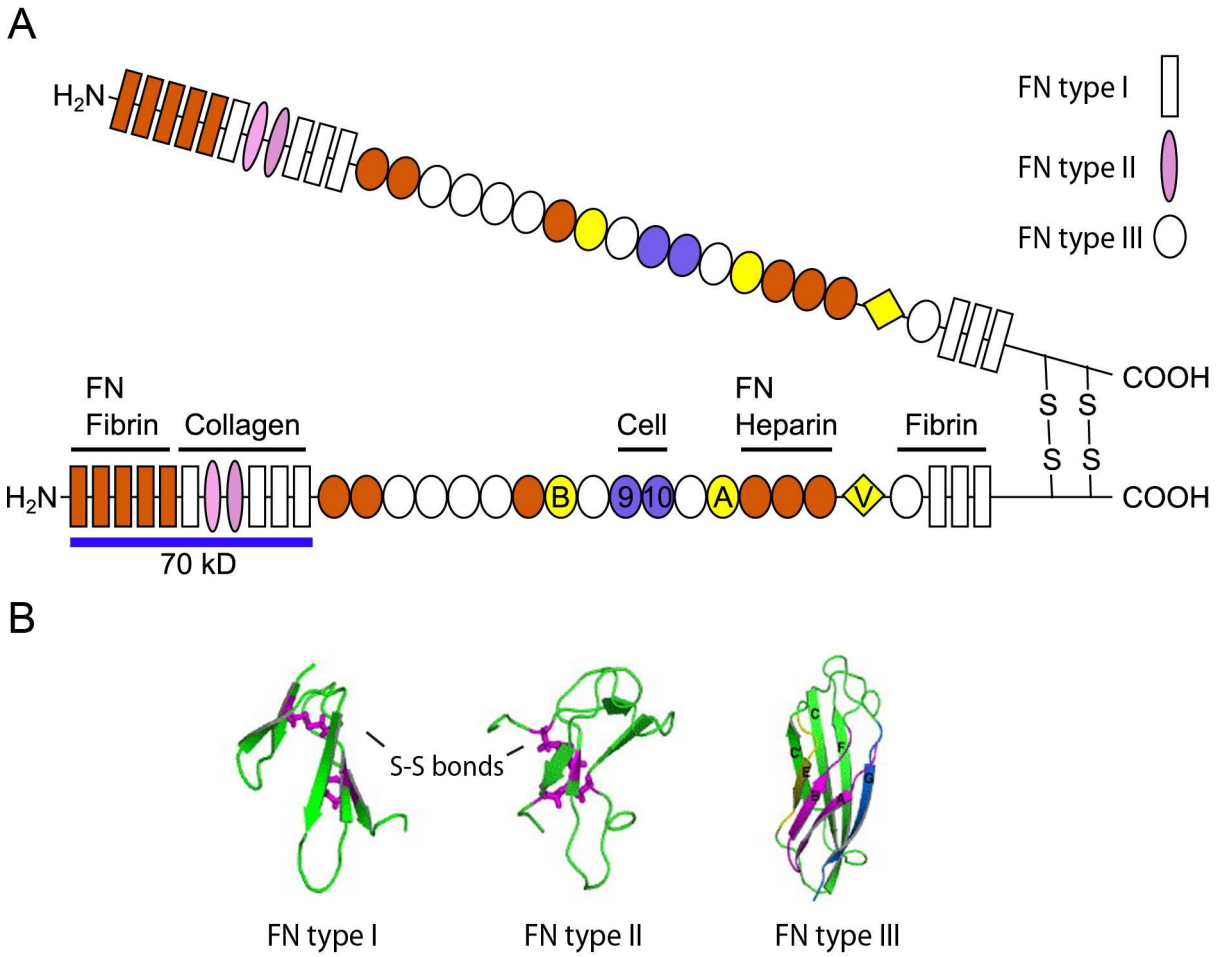

Figure 1.2: Schematic picture illustrating the structure of the dimeric FN molecule. (A) Each FN monomer contains type I (rectangular), type II (oval) and type III (circle) repeating units. The alternatively spliced FNIIIA and FNIIIB units and the V-region are colored in yellow. Blue circles represent the cell binding domains containing the RGD ($FNIII_{10}$) and the synergy site ($FNIII_9$). Domains containing FN binding sites are colored in orange, binding sites for other ECM molecules are marked with black lines and the 70 kDa N-terminal fragment is underlined (blue). The FN monomers are covalently linked near their C-terminal ends via disulfide bonds pairs. (B) Ribbon structures of the FNI_1, $FNII_1$ and $FNIII_{10}$ repeating units. The FNI and FNII units contain intramolecular disulfide bonds (in magenta) (modified from (Mao and Schwarzbauer, 2005a)).

Within the FN monomers, the repeats are organized into binding domains for extracellular molecules (collagen, heparin, fibrin and FN) and cell-surface receptors (Hynes, 1990; Pickford and Campbell, 2004) (Fig. 1.2A). One of the major FN cell-binding domains is present within the $FNIII_{10}$ repeat and contains an RGD (Arg-Gly-Asp) sequence. The RGD motif promotes cell adhesion mainly via $\alpha_5\beta_1$-integrin (Hynes, 1990; Singh et al., 2010; Takagi, 2004). The amino acid sequence PHSRN (Pro-His-Ser-Arg-Asn) in $FNIII_9$, which is located next to the RGD site, was identified as a synergistically site enhancing the cell-adhesive function of the RGD site (Aota et al., 1994; Grant et al., 1997).

1.3.2 FN types

FNs are classified into plasma (pFN) and cellular FN (cFN). Both FN types possess a distinct molecular composition, solubility and rate of assembly into the 3D matrix (To and Midwood, 2011). Hepatocytes secrete pFN into blood plasma, where it circulates at a concentration of 300 - 400 µg/ml (Zardi et al., 1979) in a compact, globular conformation. The pFN dimer contains only one V region, but EIIIA and EIIIB units are absent (Magnusson and Mosher, 1998; Tressel et al., 1991; Wilson and Schwarzbauer, 1992).

Compared to pFN cFN is expressed by a larger variety of cell types, including fibroblasts, endothelial cells, myocytes, chondrocytes and synovial cells (To and Midwood, 2011). cFN is a mixture of up to 20 different isoforms generated by alternative splicing of EIIIA, EIIIB and V regions (ffrench-Constant, 1995). The expression of different cFN isoforms is tissue and cell specific and temporally regulated (Hershberger and Culp, 1990; To and Midwood, 2011; Tressel et al., 1991; Van Vliet et al., 2001).

Both, pFN and cFN can be incorporated into a 3D matrix. The order of the insertion depends on the tissue. For example, during wound healing, pFN is responsible for early wound healing events, whereas cFN is expressed and incorporated later. Directly after wound creation, soluble, circulating pFN associates into fibrin clots which regulate platelet adhesion (Corbett et al., 1997), spreading (Cho et al., 2005) and aggregation (Cho and Mosher, 2006; Ni et al., 2003). In late wound healing after clot formation has been achieved, endothelial cells and fibroblasts migrate into the wound, and secrete and assembly cFN into a high-molecular weight multimeric matrix (To and Midwood, 2011). This dense network helps these cells to spread, polarize, proliferate and migrate (Knox et al., 1986; Manabe et al., 1997; Sechler and Schwarzbauer, 1998; Wang et al., 2005a). In the further course of wound healing, incorporation of cFN also regulates the deposition of other ECM molecules (Sottile and Hocking, 2002; To and Midwood, 2011), such as collagens (Chiang et al., 2009; Dzamba and Peters, 1991; Dzamba et al., 1993), fibrinogen (Pereira et al., 2002), laminins (Sottile and Hocking, 2002), tenascin (Chung et al., 1995) and fibulin (Godyna et al., 1995) into the matrix.

1.3.3 FN fibrillogenesis

Both pFN and cFN are secreted in a compact, globular and inactive form stabilized by intramolecular interactions between the FNI_{1-5}, $FNIII_{2-3}$ and $FNIII_{12-14}$ domains (Johnson et al., 1999; Rocco et al., 1983; To and Midwood, 2011). Low concentrations of chemical denaturants destabilize these ionic interactions, leading to a separation of the crossed-over arms (extended structure). Higher denaturant concentrations result in complete FN molecule unfolding (Smith et al., 2007). FN type I and II repeats are stabilized by intramolecular disulfide bonds inside the FN molecule (Fig. 1.2B), whereas type III repeats do not have these bonds in their seven-stranded β-barrel structure (Leahy et al., 1996; Potts and Campbell, 1994) (Fig. 1.2B). Therefore, only FNIII repeats can be unfolded by external force applied on the FN molecule (Mao and Schwarzbauer, 2005a; Smith et al., 2007).

In solution, secreted FN does not polymerize (Mosher and Johnson, 1983) and does not form a 3D matrix in absence of cells (Mao and Schwarzbauer, 2005b). However, the assembly of FN into fibrils, the so called FN fibrillogenesis, plays a key role in many physiological processes during embryonal development and also later in the adult organism. For example, during embryogenesis fibrillar FN is a major guidance component for gastrulation (Boucaut et al., 1990) and neural crest cell migration (Duband et al., 1986; Dufour et al., 1986). Fibrillar FN is also required for branching morphogenesis during kidney, lung, salivary gland and gonad formation (Jiang et al., 2000; Larsen et al., 2006; Paranko et al., 1983; Sakai et al., 2003).

Mechanisms of FN fibrillogenesis have been extensively studied *in vitro*. For instance, cellular rearrangement of surface-bound FN into fibrils has been visualized by immunolabeling in fixed cells (Pankov and Momchilova, 2009). The initial step of FN fibrillogenesis takes place at the cell surface through integrin receptor binding to FN (McKeown-Longo and Mosher, 1983) (Fig. 1.3A). The major FN receptor is $\alpha_5\beta_1$, which binds to the RGD sequence of FN (Wennerberg et al., 1996; Wu et al., 1993). However, other integrins can also interact with FN and are involved in fibrillogenesis (Table 1.4). It has been suggested that initiating FN-matrix assembly may not dependent on just a single type of integrin or single region within the FN molecule, but that this process involves additional cellular proteins (Singh et al., 2010; To and Midwood, 2011). Integrin binding induces FN unfolding by tensin-dependent integrin translocation (Baneyx et al., 2002; Pankov et al., 2000) and exposure of cryptic FN-FN binding sites (Ingham et al., 1997; Zhong et al., 1998). These sites are located inside of $FNIII_1$ (Hocking et al., 1994), $FNIII_{1-2}$ (Zhong et al., 1998), $FNIII_{10}$ (Hocking et al., 1996), $FNIII_7$ and $FNIII_{15}$ repeats (Ingham et al., 1997; To and Midwood, 2011), which are not stabilized by intramolecular disulfide bonds and therefore can be unfolded by applying external force (Baneyx et

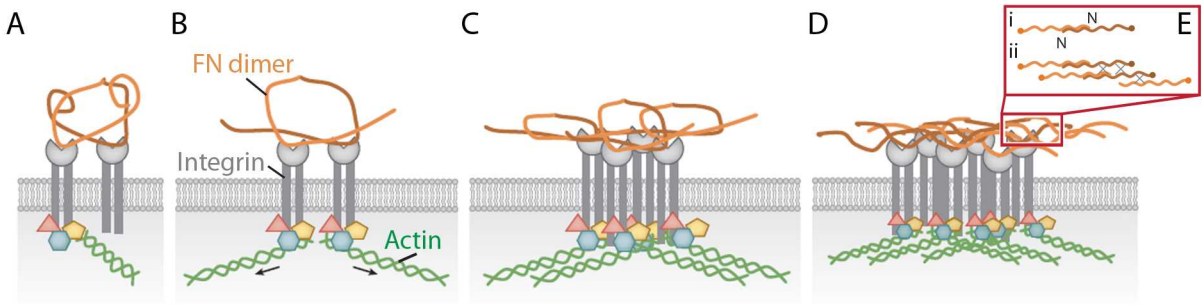

Figure 1.3: Major steps of FN fibrillogenesis. (A) Integrins (grey) bind globular FN dimers (the FN monomers are colored in two shades of orange). (B) Intracellular proteins (red, yellow, blue) are recruited to integrins and connected to the actin cytoskeleton (green). Increased cell contractility (black arrows) results in conformational changes of the FN molecules. (C) Integrin clustering leads to further FN extension. (D) FN unfolding results in the exposure of FN-FN binding sites, leading to mutual interaction and to fibril formation. (E) Possible interactions between FN dimers inside the fibril are shown, where N indicates the N-terminus of FN molecule. Two possible association mechanisms inside the fibril:end-to-end FN dimer association (i) and lateral fibril association (ii) (modified from (Singh et al., 2010)).

al., 2002; Pankov et al., 2000). Unfolding of FNIII results in the exposure of cryptic FN-FN binding sites promoting fibril creation. FNIII repeats pass through several intermediate states during its stretching from a compact, over partially unfolded to an unfolded conformation (Craig et al., 2001; Gao et al., 2003; Gao et al., 2002; Li et al., 2005). For example, experimental unfolding of FNIII_{1-2} domains exposes a cryptic FN binding site, resulting in increased FN binding activity after stretching (Aguirre et al., 1994; Hocking et al., 1994; Zhong et al., 1998). Investigating the mechanical stability of individual FNIII domains is therefore important for better understanding how FN-FN interactions are regulated. Recombinant FNIII domains have been unfolded using single-molecule AFM (Oberhauser et al., 2002). Domain unfolding has also been simulated using SMD (steered molecular dynamics) (Craig et al., 2004). The SMD predictions agree well with the AFM results, demonstrating a decreasing mechanical stability in the order of $\mathrm{FNIII}_7 > \mathrm{FNIII}_1 \geqslant \mathrm{FNIII}_2 > \mathrm{FNIII}_{12} \geqslant \mathrm{FNIII}_{13} \approx \mathrm{FNIII}_{\mathrm{EDB}} > \mathrm{FNIII}_{14} > \mathrm{FNIII}_{10}$ (Craig et al., 2004; Craig et al., 2001; Oberhauser et al., 2002). Thus, the FNIII_{10} module is mechanically least stable and therefore most prone to cell binding and unfolding (Oberhauser et al., 2002).

The exposed FN binding sites then induce interactions between other FN molecules to create fibrils (Ingham et al., 1997; Singh et al., 2010) (Fig. 1.3D). In turn, FN-integrin interactions promote integrin clustering in focal adhesions (Friedland et al., 2009; Pankov et al., 2000) and further unfolding of FN molecules. Once assembled, FN fibrils are continu-

ously polymerized and remodeled within the fibrillar matrix on the cell surface (Sottile and Hocking, 2002; To and Midwood, 2011). FN remodeling is a dynamic process involving frequent fibril extension, stretching, retraction and bending (Dallas et al., 2006; Davidson et al., 2008; Ohashi et al., 2002; Sivakumar et al., 2006). Moreover, initial thin fibrils grow in length and thickness creating a 3D FN matrix with covalent and non-covalent FN-FN interactions inside (Singh et al., 2010). Such an FN matrix is deoxycholate (DOC) insoluble, providing stability and rigidity within the tissue (McKeown-Longo and Mosher, 1983). The incorporation of new FN fibrils into the 3D matrix occurs along pre-existing fibrils, so that the initial matrix acts as a scaffold for further fibril deposition (Klotzsch et al., 2009; Mao and Schwarzbauer, 2005b). Moreover, FN fibrillogenesis is required for the incorporation of other ECM molecules, such as collagen (Kadler et al., 2008), fibrillin (Sabatier et al., 2009) and fibrinogen (Pereira et al., 2002), into a 3D matrix.

1.4 Cell-matrix adhesions

Cell-matrix interactions are essential in many physiological processes, such as cell adhesion, migration, growth, proliferation, survival and differentiation (Boudreau and Bissell, 1998; Giancotti and Ruoslahti, 1999; Howe et al., 1998; Ruoslahti, 1999), and are particularly crucial during embryonic development of multicellular organisms (Hogan, 1999). Cell adhesion to the ECM is generated through interactions between matrix molecules and membrane receptors. The major membrane receptors involved in this interaction are integrins. Integrins form a mechanical link between ECM and the cytoskeleton through multiple adaptor proteins, like talin, vinculin, paxillin, creating adhesions sites. Cell matrix adhesions contain 180 cytoplasmatic proteins (Zaidel-Bar and Geiger, 2010). Three basic categories of proteins are recruited to cell-matrix adhesions: (1) integrin-binding proteins, for example talin, (2) adaptors and/or scaffolding proteins that lack intrinsic enzymatic activity, for example vinculin, paxillin or α-actinin, and (3) enzymes, such as nonreceptor tyrosine kinases FAK and Src (Berrier and Yamada, 2007).

Adhesion sites can be classified into focal adhesions (FAs), focal complexes (FXs), fibrillar adhesions, invadopodia and podosomes, depending on their organization and composition (Geiger and Bershadsky, 2002; Petit and Thiery, 2000; Webb et al., 2002) (Fig. 1.4). The morphological characteristics of FAs, podosomes and invadopodia are summarized in Table 1.3. FAs, FXs and fibrillar adhesions are involved in cell-matrix adhesion, cell polarization, migration, signaling and ECM remodeling, for example, FN matrix creation. In contrast, invadopodia and podosomes are more dynamic but are also involved in migration, as well as matrix invasion and degradation, for example, bone resorption (Linder, 2007).

	FAs	Podosomes	Invadopodia
Location	leading edge	ventral cell surface, often clustered behind the leading edge	ventral cell surface, often situated under the nucleus
Actin arrangement	parallel actin filament bundles, with branched actin at the end of the filament	branched and unbranched actin filaments perpendicular to the surface	branched actin filaments at cell surface and unbranched actin filaments through the tip of the protrusion.
Pericellular proteolysis	minimal	yes	yes
Lifetime	hours, depending on cell migration rate	minutes	hours

Table 1.3: Morphological characteristics of cell-matrix adhesions (adapted from (Murphy and Courtneidge, 2011)).

1.4.1 Integrins

Integrins are heterodimeric glycoproteins composed of non-covalently linked α- and β-subunits. Mammals contain 18 α-subunits and 8 β-subunits, generating 24 αβ integrin combinations in total (Hynes, 2002a) (Fig. 1.5). The integrin expression profile varies depending on tissue type or developmental stage (Humphries et al., 2006). Additional diversity of integrins is generated by alternative splicing. Most integrin heterodimers are widely expressed in many tissues. However, some integrins are more restricted in their expression. For example, integrin $\alpha_{IIb}\beta_3$ is only found on platelets and integrins $\alpha_E\beta_7$, $\alpha_4\beta_7$, $\alpha_4\beta_1$, and the β_2 integrin families are restricted to leukocytes (Takada et al., 2007).

Most integrins can recognize several different ECM proteins (ligands). At the same time, a particuclar ligand, e.g. FN, laminins, collagens, or vitronectin, can be recognized by several different integrin types, indicating that integrins have overlapping functions (De Arcangelis and Georges-Labouesse, 2000). Knock-out experiments of most integrin chains demonstrated their essential role in many developmental processes (De Arcangelis and Georges-Labouesse, 2000; Fassler et al., 1996; Harburger and Calderwood, 2009; Hynes et al., 2002b). For example, inactivation of the β_1 integrin chain affects the assembly of more than 10 different integrin types (Fig. 1.5), resulting in early embryonic lethality (Fassler et al., 1996; Fassler and Meyer, 1995; Stephens et al., 1995). Knock-out of the α_4, α_5 or α_v subunit is also lethal for the embryo (Arroyo et al., 1996; Bader et al., 1998; Goh et al., 1997). However, knock-out of other α subunits usually only results in different aberrations during development (De Arcangelis and Georges-Labouesse, 2000).

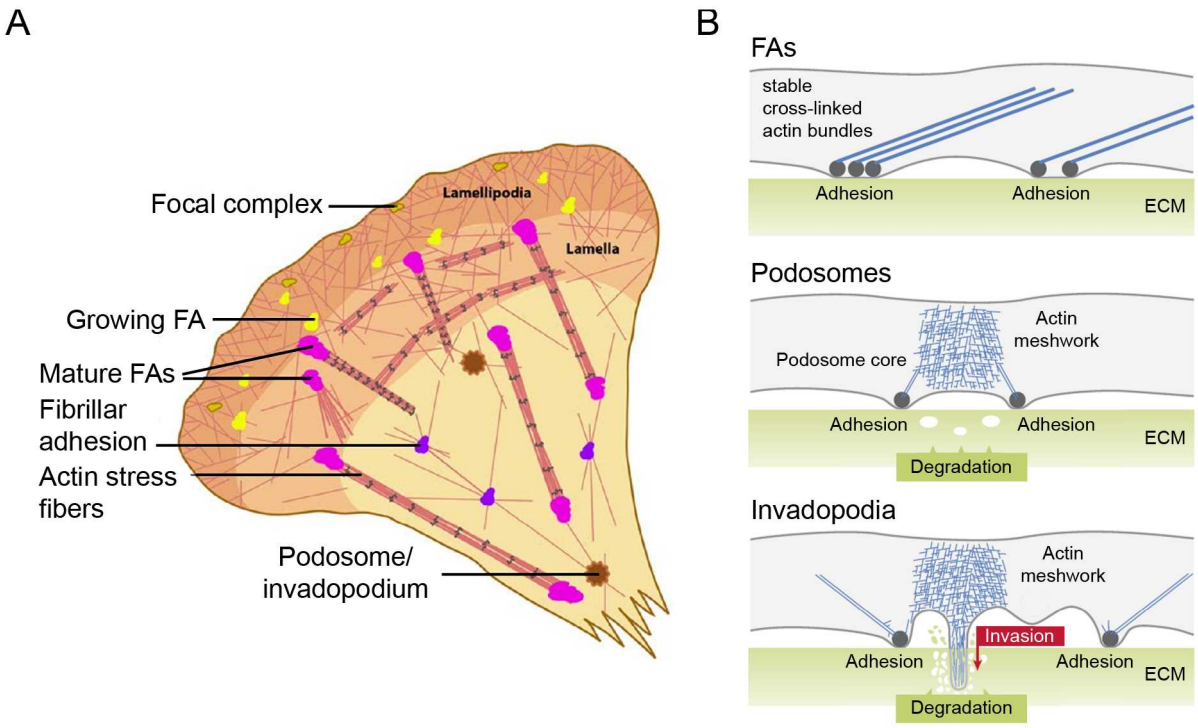

Figure 1.4: Cell-matrix adhesion structures. (A) Schematic depiction of the location of different cell-matrix adhesions in the cell. Focal complexes are located at the edge of the lamellipodium. During maturation, FAs translocate to the lamella region and fibrillar adhesions form closer to the cell center. Podosomes and invadopodia are distributed throughout the cell body (adapted from www.mechanobio.info). (B) Cell-matrix adhesions shown as a cross sections perpendicular to the substrate. At sites of cell-ECM contact, FAs anchor bundled actin filaments oriented parallel to the surface. In contrast, podosomes and invadopodia have disorganized actin cores surrounded by a ring of adhesion structures. Moreover, podosomes and invadopodia are involved into matrix degradation (white circles). Invadopodia are used by cells for matrix invasion (adapted from (Gimona et al., 2005)).

1.4.1.1 Integrin structure

The crystal structure of integrins ($\alpha_x\beta_2$, $\alpha_v\beta_3$) shows that the α- and β-subunits are composed of several domains with flexible linkers between them (Campbell and Humphries, 2011). Integrins contain a large N-terminal ectodomain, a single transmembrane domain and a short C-terminal cytoplasmic tail domain (Fig. 1.6A) (Shattil et al., 2010). The ectodomains of α- and β-integrin subunits are assembled by non-covalent interactions forming a "head", which is responsible for ligand bindings in the extracellular environment (ECM proteins, metal ions). The cytoplasmatic tail domain forms a link to the cytoskeleton via cytoplasmatic adaptor proteins (Hynes, 2002a). Electron microscopy studies have demonstrated three integrin conformations (Takagi et al., 2002; Takagi et

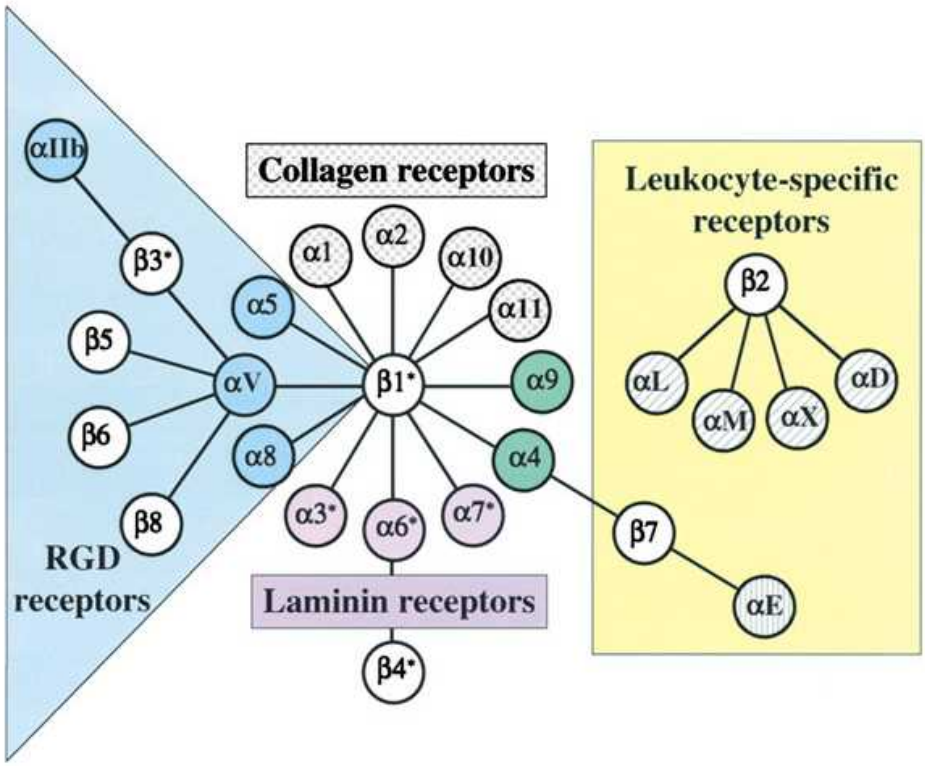

Figure 1.5: Schematical view of integrin heterodimers. The 18 α- and 8 β-integrin mammalian subunits can form 24 distinct integrins. Integrins can be divided into several subfamilies based on evolutionary relationships (coloring of α subunits), ligand specificity and, in the case of β_2 and β_7 integrins, restricted expression on white blood cells (yellow box). The α_1, α_2, α_{10}, and α_{11} subunits (gray hatching) have an additional structural element (or "domain") inserted toward the N-terminal, the A-domain. α subunits with specificities for laminins (purple) or the RGD motif (blue) are found throughout metazoa. Asterisks denote alternatively spliced cytoplasmic domains (modified from (Hynes, 2002a)).

al., 2003): low-affinity or bent, intermediate or extended with a closed headpiece, and high affinity or extended with an open headpiece (Fig. 1.6B).

1.4.1.2 Integrin activation and signaling

Integrins are not constitutive active in cells. Structural and functional studies have demonstrated that depending on the presence or absence of divalent cations or ligands, integrins can exist in three different conformations which correspond to different activation states. Depending on activation, integrin function is either blocked, or partially or completely turned on. Activation, i.e. the change from a bent to an extended conformation (Takagi et al., 2002), can be triggered in two ways: by the binding of activator proteins to the

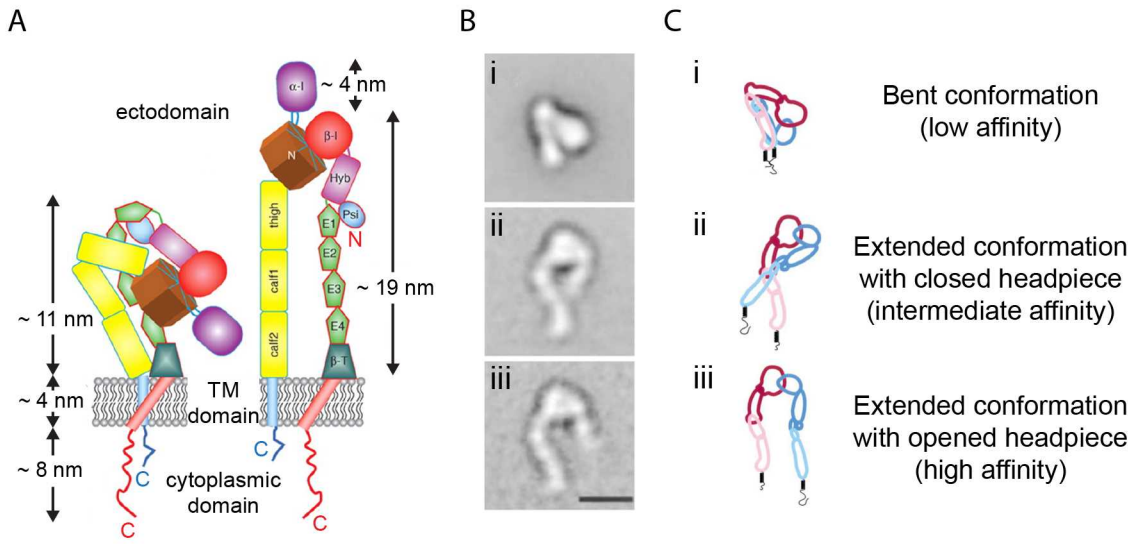

Figure 1.6: Integrin structure and conformations. (A) Domain arrangement of $\alpha_x\beta_2$ integrin showing approximate integrin dimensions (adapted from (Campbell and Humphries, 2011)). (B) Electron microscopy images of three $\alpha_v\beta_3$ integrin conformations: bent or low affinity (i), extended with closed headpiece or intermediate affinity (ii) and extended with opened headpiece or high affinity (iii). (C) Schematic representation of integrin conformations (α integrin - red, β integrin - blue) (modified from (Takagi et al., 2002)).

cytoplasmic tail of β-integrins, or by binding of ligands or divalent cations to the integrin ectodomain (Takagi et al., 2002).

Divalent cations such as Mn^{2+}, Mg^{2+} and Ca^{2+} have distinct effects on integrin function *in vitro*. Mn^{2+} converts integrins into a high affinity conformation stimulating ligand binding, whereas Ca^{2+} inhibits ligand binding. Mg^{2+} also stimulates the high affinity state, but the integrin conformation is less extended compared to Mn^{2+}. Studies on the $\alpha_5\beta_1$ integrin demonstrated the presence of three distinct cation binding sites for Mn^{2+}, Mg^{2+} and Ca^{2+} in the β subunit (Mould et al., 1995a; Tiwari et al., 2011). The high affinity Ca^{2+} binding site, a so called "effector site" stabilizes the inactive integrin conformation. At a second site both Ca^{2+} and Mg^{2+} can bind in a competitive manner (Mould et al., 1995a; Smith et al., 1994).

Beside divalent cation activation, integrins can be also activated through binding to both extracellular and intracellular ligands. In this way, integrins provide a transmembrane link for bidirectional signal transmission. Integrin activation by binding of an intracellular activator protein, such as talin or kindlin, to the β-integrin cytoplasmic tail is called inside-out signaling (Fig. 1.7). Integrin activation results in an increased affinity to extracellular ligands, allowing cells to regulate adhesion strength to the ECM and to transmit forces required for cell migration and ECM remodeling and assembly (Calderwood, 2004; Shattil et al., 2010). Integrin activation via multivalent ligand binding to the

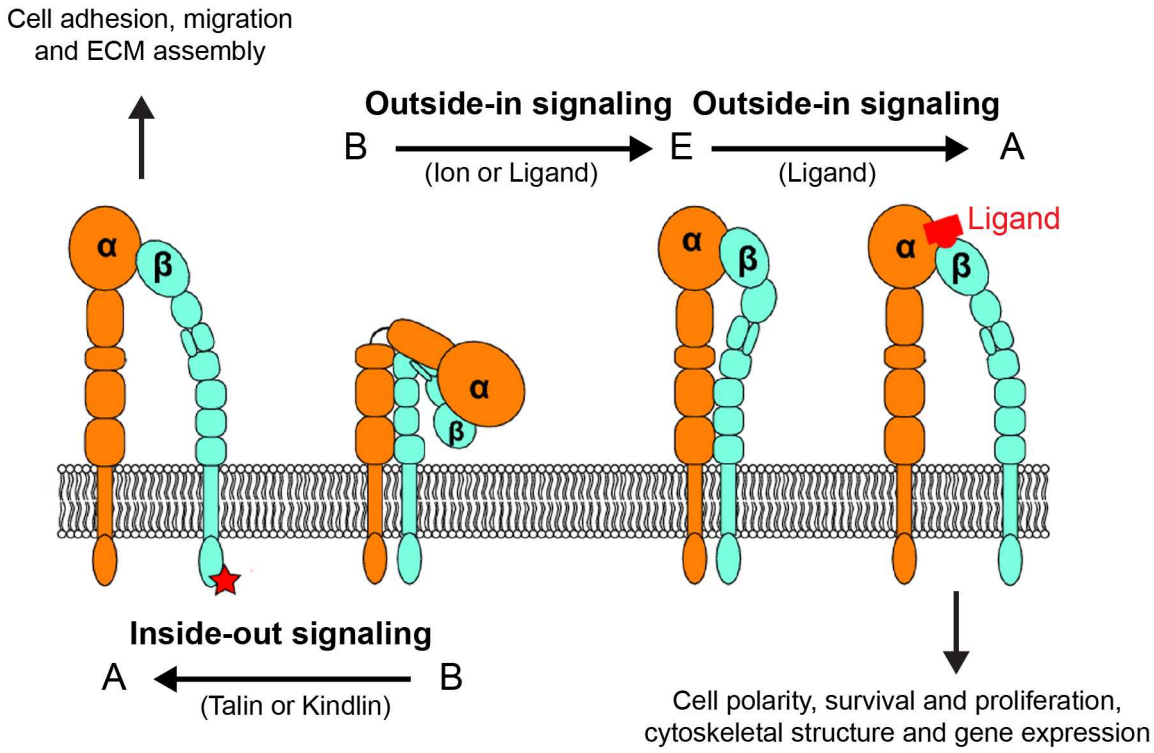

Figure 1.7: Model of bidirectional integrin signaling. Integrins in an inactive bent conformation with low affinity to the ligand (B) can be activated either by ligand binding (outside-in signaling) or by binding events at the cytoplasmic domains (inside-out signaling). Integrin activation leads to straightening of the ectodomain into an extended conformation (E, extended closed conformation) and separation of the transmembrane and cytoplasmic α and β domains integrins (A, extended open conformation) (modified from www.ks.uiuc.edu).

extracellular head ectodomain is called outside-in signaling (Fig. 1.7). During outside-in signaling, integrins transmit signals into the cell, generating intracellular signals controlling cell polarity, cytoskeleton structure, gene expression, cell survival and proliferation. Inside-out and outside-in signaling are often closely linked. For example, integrin activation can increase ligand binding, resulting in outside-in signaling, while ligand binding can generate signals that cause inside-out signaling (Shattil et al., 2010).

1.4.1.3 Integrin receptors for FN

$\alpha_5\beta_1$ integrin is the first identified FN receptor (Pytela et al., 1985). It is expressed in many cell types and it is the major receptor for FN recognition (Ruoslahti, 1991; Wu et al., 1993). However, other integrins can also bind FN via specific binding motives (Table 1.4) (Fogerty and Mosher, 1990). After binding, FN molecules are remodeled by the cell, resulting in FN fibrillogenesis. However, not all FN binding integrins support fibril creation. For example, integrin $\alpha_8\beta_1$ is mainly expressed in epithelial cells, smooth

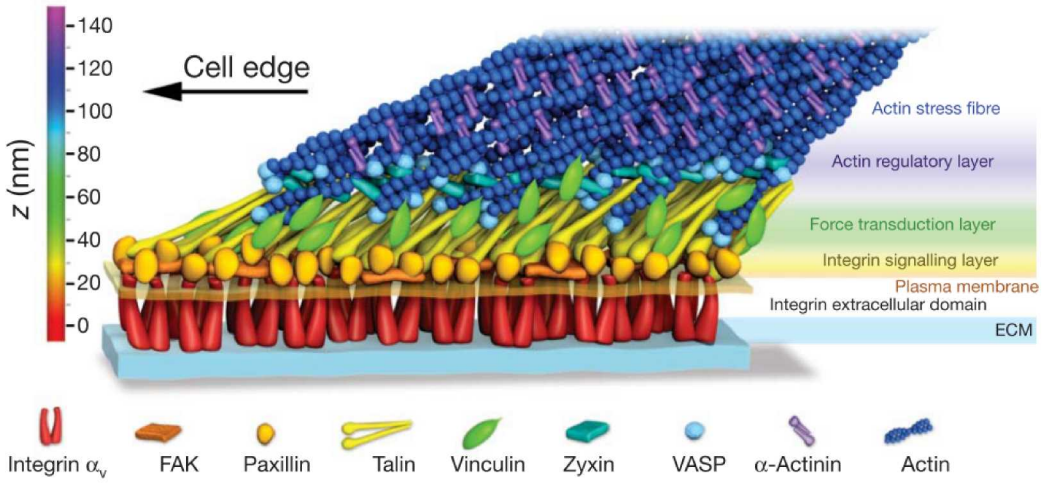

Figure 1.8: Model of the FA molecular architecture showing experimentally determined protein positions (adapted from (Kanchanawong et al., 2010)).

muscle cells, myofibroblasts, and embryonic neural cells (Bossy et al., 1991; Schnapp et al., 1995a) where it functions as a major FN receptor , but is not involved in FN fibrillogenesis (Johansson et al., 1997).

1.4.2 Focal adhesions, focal complexes, fibrillar adhesions

FAs, FXs and fibrillar adhesions are found in many cell types. These adhesion plaques connect cells to surrounding ECM molecules. Cell-matrix adhesion formation is a highly dynamic process (Webb et al., 2002). After cell attachment, small dot-like nascent adhesion structures (FXs), form at the cell periphery. Early FXs contain paxillin, vinculin, and thyrosine-phosphorylated proteins. Furthermore, FXs are enriched with activated (high-affinity) $\alpha_v\beta_3$ integrins (Kiosses et al., 2001). FXs can maturate into FAs (Geiger et al., 2001; Zamir et al., 2000), recruiting further cytoplasmic adaptor proteins (Fig. 1.8). Development of FAs is stimulated by the small GTPase Rho-A, and is driven by acto-myosin contractility (Geiger et al., 2001). In contrast to FXs, FAs are linked to actin stress fibers by talin (Kiosses et al., 2001). As force is applied to FAs, $\alpha_5\beta_1$-integrin and tensin translocate to the cell center at a rate of $6.5 \pm 0.7\,\mu m/h$ (Pankov et al., 2000) resulting in the formation of fibrillar adhesions (Geiger et al., 2001; Webb et al., 2002; Zamir et al., 2000). Characteristic features of FA, FX and fibrillar adhesions are summarized in Table 1.5.

Integrin	Ligand	Binding motive	Supports fibrillogenesis	Referenz
$\alpha_3\beta_1$	FN, laminin	70-kDa	+	(Johansson et al., 1997; To and Midwood, 2011)
$\alpha_4\beta_1$	FN, VCAM-1	LDV/IDS, (RGD)	+	(Johansson et al., 1997; To and Midwood, 2011; Wu et al., 1995)
$\alpha_5\beta_1$*	FN	RGD, (PHSRN)	+	(Johansson et al., 1997; Takagi et al., 2003; To and Midwood, 2011; Wennerberg et al., 1996; Wu et al., 1993)
$\alpha_8\beta_1$*	FN, vitronectin, tenascin	RGD	-	(Johansson et al., 1997; Schnapp et al., 1995b; To and Midwood, 2011)
$\alpha_9\beta_1$	FN,	EIIIA	-	(Liao et al., 2002; To and Midwood, 2011)
$\alpha_v\beta_1$*	FN, vitronectin, fibrinogen, collagens, laminin, osteopontin	RGD	-	(Johansson et al., 1997; Schnapp et al., 1995b; To and Midwood, 2011)
$\alpha_{IIb}\beta_3$*	FN, vitronectin, fibrinogen, thrombospondin, von Willebrand factor	RGD, KQAGDV	+	(Johansson et al., 1997; Kauf et al., 2001; To and Midwood, 2011)
$\alpha_v\beta_3$*	FN, vitronectin, fibrinogen, osteopontin, collagens, tenascin, von Willebrand factor	RGD, RLD/KRLDGS	+	(Johansson et al., 1997; To and Midwood, 2011; Wennerberg et al., 1996)
$\alpha\beta_6$*	FN, vitronectin, tenascin	RGD	+	(Johansson et al., 1997; To and Midwood, 2011)

Table 1.4: FN binding integrins. Integrins for which FN is the main ligand are denoted by an asterisk (modified from (Johansson et al., 1997; To and Midwood, 2011)).

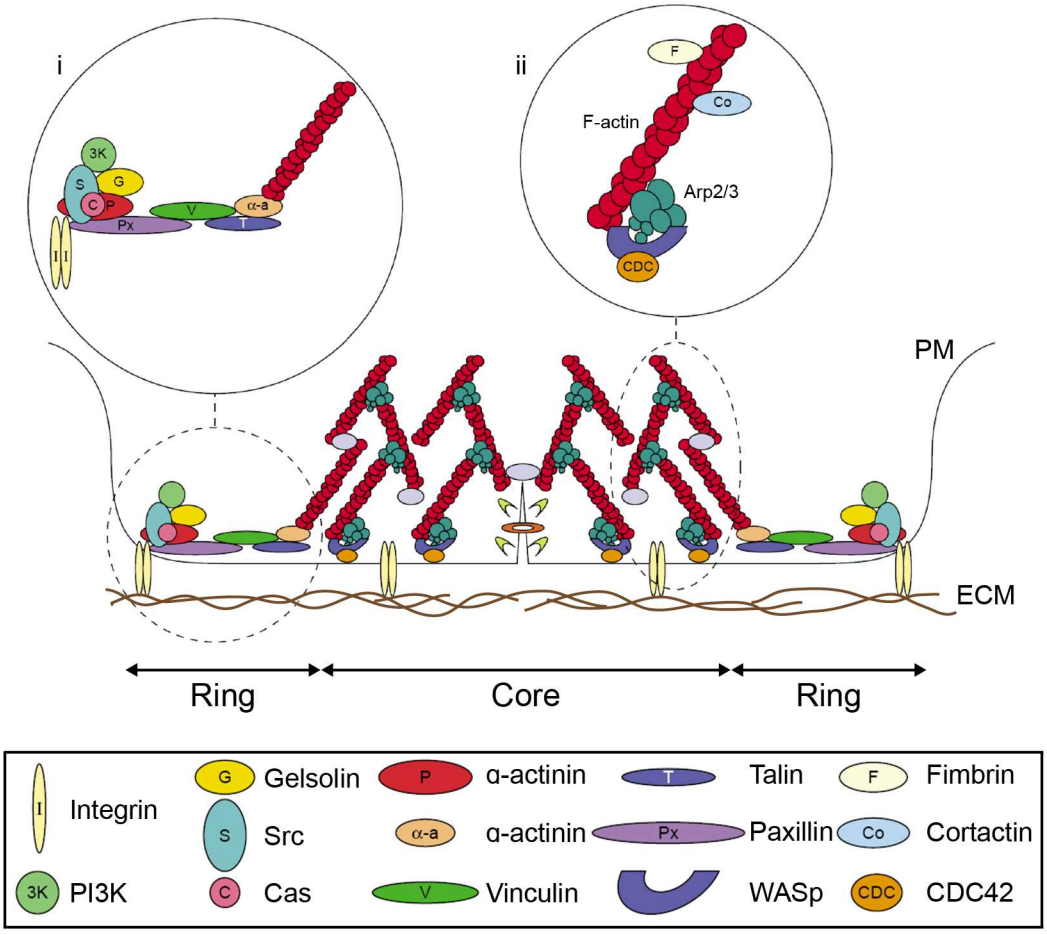

Figure 1.9: Schematic podosome cross section perpendicular to the substrate. Podosomes consist of an actin-rich core which is surrounded by a ring of adhesion proteins (e.g. talin, vinculin, paxillin). Matrix receptors such as integrins are anchored within the plasma membrane and mediate the linkage between the actin cytoskeleton and the ECM. (i) Molecular composition of podosomal ring. Paxillin acts as a scaffold for an intracellular complex consisting of Src, Pyk2/FAK, gelsolin, phosphoinositide 3-kinase (PI3K) and p130cas. This complex is linked via vinculin, talin and α-actinin to the F-actin core. (ii) Detailed view of the podosomal core structure. Actin filaments are nucleated at the membrane via CDC42-activated WASp/N-WASp and the Arp2/3 complex, and are linked to each other via cortactin and fimbrin. The orange circle in the middle of the actin core represents the proposed dynamin localization. Lower panel: description of symbols used (modified from (Linder and Aepfelbacher, 2003)).

Structure	Focal complex (FX)	Focal adhesion (FA)	Fibrillar adhesion
Location	edge of lamellipodium	cell periphery	central region of cells
Morphology	dot-like	elongated, oval	fibrillar or beaded
Size (long axis)	1 µm	2 - 5 µm	1 - 10 µm
Typical constituents	$\alpha_v\beta_3$ integrin, paxillin, vinculin, tyrosine-phosphorylated proteins	$\alpha_v\beta_3$ integrin and $\alpha_5\beta_1$, paxillin, vinculin, α-actinin, talin, FAK, tyrosine-phosphorylated proteins	$\alpha_5\beta_1$ integrin, tensin

Table 1.5: Characteristic features of FA, FX and fibrillar adhesions. (adapted from (Geiger et al., 2001)).

1.4.3 Podosomes and invadopodia

Migratory and invasive cells build-up so called podosome-type adhesions (Linder, 2007). These can be classified into podosomes and invadopodia, depending on their structure and function (Block et al., 2008). Podosomes were first found in cells of the monocytic lineage (macrophages (Lehto et al., 1982), osteoclasts (Marchisio et al., 1984) and dendritic cells (Burns et al., 2001)), whereas invadopodia were identified in carcinoma cells (Linder and Aepfelbacher, 2003). Podosome formation can also be induced in other cell types, including smooth muscle cells and endothelial cells (Linder and Kopp, 2005). In contrast to FAs, podosomes have not only adhesive function, but are also involved in matrix degradation. Each podosome consists of an F-actin rich core surrounded by a ring structure composed of integrins and integrin-associated proteins, such as talin, paxillin and vinculin (Bowden et al., 1999; Gaidano et al., 1990; Pfaff and Jurdic, 2001) (Fig. 1.9). The F-actin filaments are oriented perpendicular to the substratum. Moreover, they are associated with regulatory proteins such as cortactin (Hiura et al., 1995), Wiskott-Aldrich Syndrome protein (WASP) (Calle et al., 2004), actin-related protein complex 2/3 (Arp2/3) (Hurst et al., 2004), gelsolin (Chellaiah et al., 2000) and dynamin (Ochoa et al., 2000). However, in contrast to FAs, zyxin and tensin are not recruited to the podosome ring structure (Block et al., 2008). Different integrins are present in podosomes depending on the cell type. Podosomes of endothelial cells contain $\alpha_6\beta_4$, while osteoclasts recruit $\alpha_v\beta_1$, $\alpha_2\beta_1$, $\alpha_v\beta_3$ (( )Buccione2004). In osteoclasts cultured on rigid surfaces, such as glass, podosomes change their organization, from individual structures, distributed throughout the ventral cell membrane, via clusters or rosettes into ring structures (Fig. 1.10A-C). The podosome ring formation can be subdivided into several steps. Firstly, podosomes are assembled

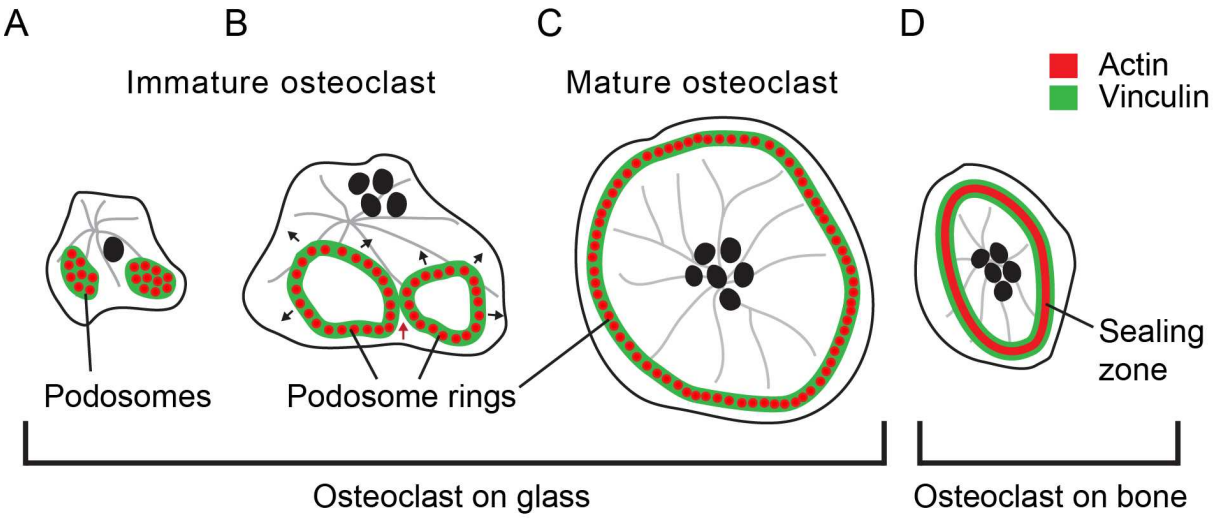

Figure 1.10: Model of podosome dynamics during osteoclast maturation. (A). Osteoclast precursor cells plated on glass surface form individual podosomes separated from each other. Podosomes are composed of a dense actin core (red circles) surrounded by integrin associated proteins (green), e.g. vinculin. During precursor cell differentiation into mature osteoclasts, single podosomes form a podosome ring (B). The podosome rings expand (black arrows) and fuse (red arrow), while inhibiting new podosome formation inside the ring. (C). A mature osteoclast on glass surfaces often have a single podosome ring near the cell periphery. (D). Osteoclasts seeded on bone create a dense podosome ring, called sealing zone. In the sealing zone, single podosomes cannot be distinguished anymore, instead a dense actin ring (red) is surrounded by outer and inner rings of integrin-associated proteins (green) (modified from (Destaing et al., 2003)).

de novo at the leading edge of a cell and are stabilized by microtubules. Neighboring podosomes fuse together (Cox et al., 2012) forming clusters which are shaped to small rings. Then, these structures expand and fuse to a larger ring. During this process, new podosomes are assembled at the outer ring edges, while podosome formation is inhibited inside the rings. The ring fusion is a self-organization process regulated by local mechanisms (Destaing et al., 2003; Gerhart and Kirschner, 1997). For example, a podosome itself might stimulate but also inhibit the formation of other podosomes in its immediate surroundings (Gerhart and Kirschner, 1997; Destaing et al., 2003). However, osteoclasts seeded on bone substrates usually create a stable peripheral belt, the so called sealing zone (Fig. 1.10D), a condensed actin structure ($\sim 4\,\mu$m-wide), flanked by integrins and focal adhesion proteins at the outer and inner areas (Destaing et al., 2003; Lakkakorpi et al., 1993). The sealing zone is essential for matrix degradation and stable for minutes to hours. Degradation enzymes are secreted into the sealed space between cell membrane and matrix surface (Chiusaroli et al., 2004; Salo et al., 1997) by an unknown mechanisms.

Invadopodia are invasive cell structures. Similar to podosomes, they consist of an actin structure positioned perpendicular to the cell membrane. However, the architecture of invadopodia appears less well-defined and integrin-associated proteins are also found in the actin core of these structures (Linder, 2007). Invadopodia have a diameter of $\sim 8\,\mu m$ and penetrate into the matrix by up to $5\,\mu m$. In contrast, podosomes are comparatively small structures with a diameter of $\sim 1\,\mu m$ entering the matrix by 0.2 to $0.4\,\mu m$ (Buccione et al., 2004). Typically, cells contain 20 to 500 single podosomes which have a relatively short life-span of 2 to 12 min, except for the sealing zone (Destaing et al., 2003). In contrast, cells contain only up to 10 individual invadopodia and these structures have a persistence time of hours (Yamaguchi et al., 2006).

1.5 Microscopy techniques for investigating cell-ECM interactions

Microscopy is one of the primary tools not only for studying cell surfaces and cell compartments, but also cell-cell and cell-ECM interactions. There are different kinds of microscopy techniques most commonly used for biological applications: light, electron and atomic force microscopy. Each microscopy technique has advantages and disadvantages, which are summarized in Table 1.6. Light microscopy is one of the earliest and most frequently-used methods to observe structures too small for the human eye. Since the 1960s , fluorescence microscopy has become particularly important in biological research (Diaspro, 2010). This light microscopy technique allows for the visualization even of low numbers of fluorescently-labeled molecules. A great advantage of light microscopy in general is that it is possible to observe the sample in real time and under physiological conditions. Except for labeling structures or molecules with fluorophores, there is no need for sample preparation. However, the conventional type of light microscopy yields a rather low resolution compared to other microscopy techniques.

The electron microscope was developed in 1930s (Hayat, 2000) and allows for the observation of structures with nm or even subnanometer resolution. However, samples for EM usually require a special preparation protocol including chemical fixation and staining. Furthermore, only the surface or very thin slices of the sample can be investigated. Thus, particular features of the cell can be studied in detail, while it is impossible to investigate dynamic biological processes. In the 1980s, the atomic force microscope (AFM) was developed (Binnig et al., 1986). It provides high resolution imaging in air or liquids. Since no special sample preparation and even fixation is required, one is able to observe time-dependent processes with sub-nanometer resolution (Baro and Reifenberger, 2012). However, similar to scanning electron microscope, AFM only allows for imaging

the surface of the sample. In the past, different microscopy techniques were used mostly independent from each other, making it necessary to prepare different probes for different microscopy techniques. Nowadays, devices are used which combine several microscopy techniques and which thus bring together the advantages of the different methods.

1.5.1 Fluorescence microscopy

The main advantage of a fluorescence microscope is that a particular molecule type of interest can be imaged after labeling it with a specific fluorophore. Depending on the used fluorophore, the sample is illuminated with light of a specific wavelength ranging from UV to infrared. This excitation light is absorbed by the fluorophores and reemitted as light with a longer wavelength. Furthermore, it is also possible to mark several types of molecules in one sample and image them during one run by using fluorophores of different wavelengths and corresponding filters. Thus, the locations of different molecules can be overlaid allowing the investigation of cellular processes on a molecular level in real time (Diaspro, 2010).

1.5.1.1 Confocal scanning microscopy

Fluorescence imaging of dense tissues in a conventional way is difficult and results in a poor contrast. In the late 1950s, Marvin Minsky developed a new type of microscope that has become known as the confocal microscope (Kubitscheck, 2013). A confocal microscope scans the sample in 3D point by point, instead of illuminating the whole sample at once, providing not only better contrast but also an image stack in z-direction. The excitation light passes through the illumination pinhole (Fig. 1.11), is deflected by a dichromatic mirror and focused by an objective into a small spot. This spot might be positioned at any position of interest in the 3D space. When using a laser as the light source, the pinhole is not required, so that the mirror and the objective just control the laser beam path. In any case, the imaged point in the xy-plane is controlled by the dichromatic mirror. Excited fluorophores emit light, which passes through the objective and the dichromatic mirror. Depending on the z-plane from where the light is coming, the light is focused at different positions. Thus, only light coming from a particular z-plane is detected by varying the position of the confocal pinhole in front of the detector (Fig. 1.11). The resolution of confocal images in the xy-plane is about 180 nm and thus hardly improved in comparison to a standard fluorescence microscope. The main advantage of a confocal microscope is the increased z-resolution of about 400 nm and the improved image contrast by blocking background fluorescence, both of which are controlled by size of the pinhole.

	CLSM	TIRF	SIM	PALM	SEM	TEM	AFM
Sample preparation	fluorescent labeling	fluorescent labeling	fluorescent labeling	fluorescent labeling	dehydration, OsO_4 staining, metallic coating	sample staining, cross sectioning	not neccessary
Operating environment	physiological environment	physiological environment	physiological environment	physiological environment	vacuum	vacuum	physiological environment
Working distance	mm - µm	mm - µm	mm - µm	mm - µm	mm	mm	nm
Lateral resolution (XY)	∼ 180 nm	∼ 180 nm	∼ 100 nm	∼ 20 nm	nm	Å	Å
Z-resolution	∼ 400 nm	∼ 250 nm *	µm	∼ 50 nm	-	-	Å - nm **
Maximum scanning size	mm^2	mm^2	mm^2	mm^2	mm^2	mm^2	$100 \times 100\ \mu m^2$
3D imaging	yes	no	yes	yes	no	no	
3D image from single scan	no	no	no	no	no	no	yes
Inner structure visible	depends on fluorescent labeling	no	depends on fluorescent labeling	depends on fluorescent labeling	no	yes	no
Sample damage after imaging	photobleaching	photobleaching	photobleaching	photobleaching	mass loss due to electron beam irradiation	mass loss due to electron beam irradiation	no
Live imaging	yes	yes	yes	yes	no	no	yes

Table 1.6: Comparison of microscopy techniques for biological applications. CLSM - confocal laser scanning microscopy; TIRF - total internal reflection microscopy (* max. imaging depth from the bottom of the sample); SIM - structured illumination microscopy; PALM - photo activated localization microscopy; SEM - scanning electron microscopy; TEM - transmission electron microscopy; AFM - atomic force microscopy (** by changing the scanning force, stiffer inner cell structures can be visualized).

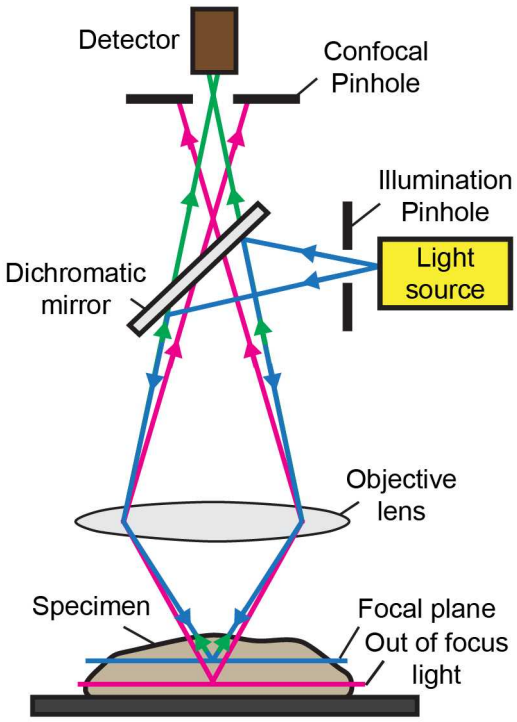

Figure 1.11: Principle of laser scanning confocal microscope (CLSM). The excitation light passes a pinhole, and is deflected by a dichromatic mirror and focused by the objective onto to the sample. Emitted light from the sample passes through back through the objective, the dichromatic mirror and the pinhole aperture before reaching the detector. The pinhole acts as a spatial filter for the z-dimension, creating optical sections (adapted from www.jic.ac.uk).

1.5.1.2 Total internal reflection fluorescence microscopy

The refraction of light is an optical phenomenon occurring at interfaces between media of different optical densities. As shown in Fig. 1.12B, when light passes from an optically denser (higher refractive index) to an optically less dense media (lower refractive index), the exitangle θ' is larger than the incident angle θ (measured from the surface normal, dashed line in Fig. 1.12B). Therefore, there is a critical angle, θ_c, at which the exitangle equals 90°, i.e. the light travels parallel to the interface. If θ is larger than θ_c, the incident light is totally reflected at the interface (Fig. 1.12C). However, due to the wave-nature of light, the electromagnetic wave penetrates into the adjacent medium. There, it decays exponentially and is therefore called the evanescent wave (Kubitscheck, 2013).

For studying biological samples, usually glass is used as the substrate. Therefore, glass is the optically denser medium, while the optically less dense medium is liquid. The penetration depth of the evanescent wave is about 250 nm (Axelrod, 2001), so that it is able to excite the fluorophores located in direct proximity of the glass surface (Fig. 1.12D). Fluorescence excitation of this thin zone results in images with improved signal-to-noise ratio, compared to epi-illumination. Moreover, at the glass-water interface the illumination intensity is increased up to five fold compared to epi-fluorescence using the same laser beam, allowing for detecting low intensity fluorescence signals with the total internal reflection microscope TIRFM (Axelrod et al., 1984; Kubitscheck, 2013).

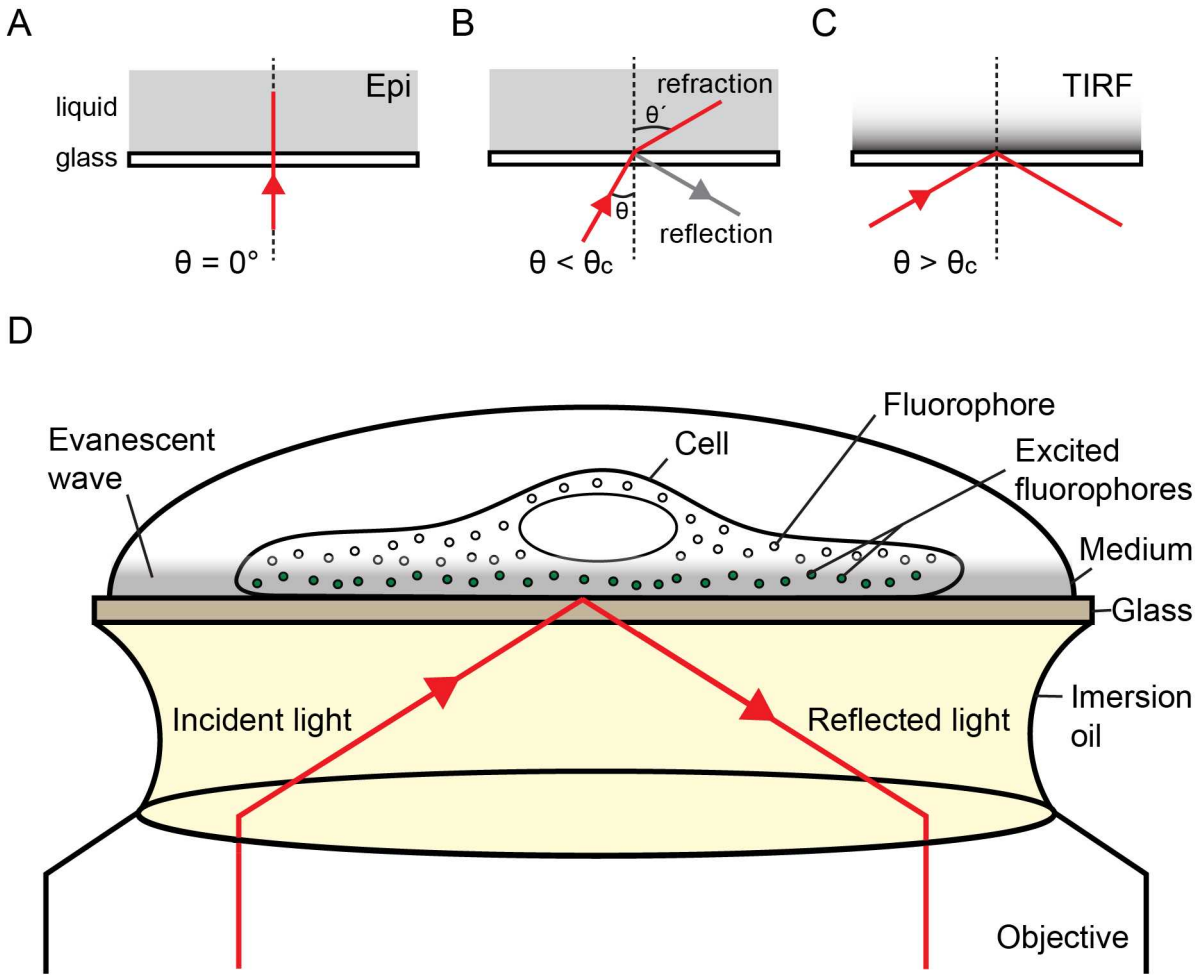

Figure 1.12: Principle of TIRF microscopy. (A) In Epi-fluorescence, the angle of incident light θ is zero and light (red line) passes glass and medium nearly unobstructed. (B) When the laser beam is tilted from the surface normal (dashed line), a small portion is reflected (gray line), while the major part of the light beam is refracted with an exitangle θ′ larger than θ. As in (A), the fluorophores in the whole medium are excited (gray background). (C) Increasing θ yields to an increase of θ. For θ > θc (critical angle, see text) the incident beam is totally reflected creating an exponentially decaying evanescent wave in the liquid (black to white gradient). (D) In TIRFM a laser beam (red) is focused through an objective onto the optical density interface to create an evanescent wave within the liquid. Only fluorophores near the glass surface are excited (green circles) and detected (via the same objective).

These unique features of TIRFM are broadly used by numerous applications in biochemistry and cell biology. (1) TIRFM is used for the selective visualization and quantification of cell-substrate contact regions (Gingell et al., 1987; Todd et al., 1988; Weis et al., 1982). (2) Time-lapse imaging of single molecules located near a surface using TIRF allows quantitative analysis of molecular motion (Dickson et al., 1998; Khan et al., 2000; Vale et al., 1996). (3) Motion of molecules in the vertical direction can be calculated with nm accuracy by measuring the changes of the fluorescence intensity and using the exponential dependence of the evanescent wave amplitude. For example, the secretory processes of granules were studied in this way (Lang et al., 1997; Steyer and Almers, 1999; Steyer and Almers, 2001; Toomre et al., 2000). (4) TIRFM in combination with fluorescence recovery after photobleaching (FRAP) was used to measure the kinetic rates of protein binding to cell surface receptors or artificial membranes (Burghardt and Axelrod, 1981; Hellen and Axelrod, 1991; Kalb et al., 1990; Thompson and Axelrod, 1983; Thompson et al., 1981). (5) Combination of TIRFM with AFM allows for examining the force transmission from the apical to the basal cell membrane in living cells (Mathur et al., 2000).

1.5.2 Electron microscopy techniques

First EM was built in 1931 by Max Knoll and Ernst Ruska (Freundlich, 1963; Ruska and Knoll, 1931) and is thus one of the oldest high-resolution microscopy techniques. Already in 1934, the tobacco mosaic virus was one of the first biological samples imaged by EM (Kausche et al., 1939). The first EM picture of a cell was published in 1945 by Porter *et. al* (Porter et al., 1945).

EM techniques can be classified in transmission electron microscopy (TEM) and scanning electron microscopy (SEM), which are briefly discussed in the following. Both EM types use an electron beam for sample imaging. After generation, electrons are accelerated towards the sample. The accelerating voltage of the beam is quoted in kilovolts (kV) and determines the microscope resolution. Electrons are deflected via electromagnetic lenses, which are in principle magnetic coils. This results in a path of electrons similar to the optical path in a light microscope (Fig. 1.13). The main difference between TEM and SEM are the irradiation conditions and electron detection.

1.5.2.1 Transmission electron microscopy

TEM (Fig. 1.13) is the original form of EM. TEM operates at an acceleration voltage of the electron beam between 50 and 150 kV. In principle, the resolution of TEM increases with the acceleration voltage. However, the power of resolution is usually restrained by the quality of the lens system and, especially, by the sample preparation technique. Modern microscopes have powers of resolution ranging between 0.2 and 0.3 nm. The electron beam

in TEM is rather broad to illuminate the complete sample at once. Like in the optical microscope, the transmitted beam carries the whole image information. The electron beam is formed by several magnetic lenses building the objective before detection. The detector is a fluorescent screen or photographic material.

Images taken with TEMs are always in grayscale, representing the electron density leaving the sample and so the sample structure. Thus, on the one hand, the sample has to be thin (about 100 nm) to be sufficiently transparent for electrons. On the other hand, the chemical composition of specimen should vary strong enough to be able to resolve structural differences. In biological probes this is usually not the case, because they consist of basically four elements (H, C, O and N) which are homogenously distributed. However, the different cell compartments can be visualized by staining with special contrast enhancing chemicals, e.g. heavy metals (Hayat, 2000).

1.5.2.2 Scanning electron microscopy

The principle of SEM differs from that of the TEM (Fig. 1.13). The energy of electrons emitted by the electron gun lies in the range between 1 and 50 keV. The electron beam is formed by the condenser lenses (one or two) and is focused into a fine spot of about 1 to 3 nm in diameter on the probe (Fig. 1.13). These primary electrons interact with atoms of the sample surface and cause the emission of secondary electrons, backscattered electrons and X-rays. Secondary electrons are the most important product for imaging with SEM. The intensity of this type of electrons is dependent on the angle between the surface and the primary electron beam. The thickness of the specimen for SEM is not such a crucial factor as for TEM. Nevertheless, the probe has to be covered with a thin metallic film, e.g. platinum or gold, to increase the number of secondary electrons (Hayat, 2000). In contrast to TEM, the specimen is scanned point by point which results in a kind of 3D-image displaying the tilt of the surface. The spatial resolution for biological specimens is generally in the range between 1.5 and 2 nm. Moreover SEM allows not only for visualizing the sample structure, but also for analyzing its chemical composition by X-ray detection. In contrast to fluorescence microscopy and AFM, where biological samples can be observed without fixation, all samples for electron microscopy have to be fixed. Furthermore, best results are achieved with dehydrated probes treated with contrast enhancing agents such as heavy metal salts (Hayat, 2000).

1.5.3 Atomic force microscopy

AFM belongs to the family of scanning probe microscopes (SPM). This type of microscopes records the sample topography by using distance dependent interactions between a sharp probe (tip) and the sample. In fact, different SPMs use different tip-sample inter-

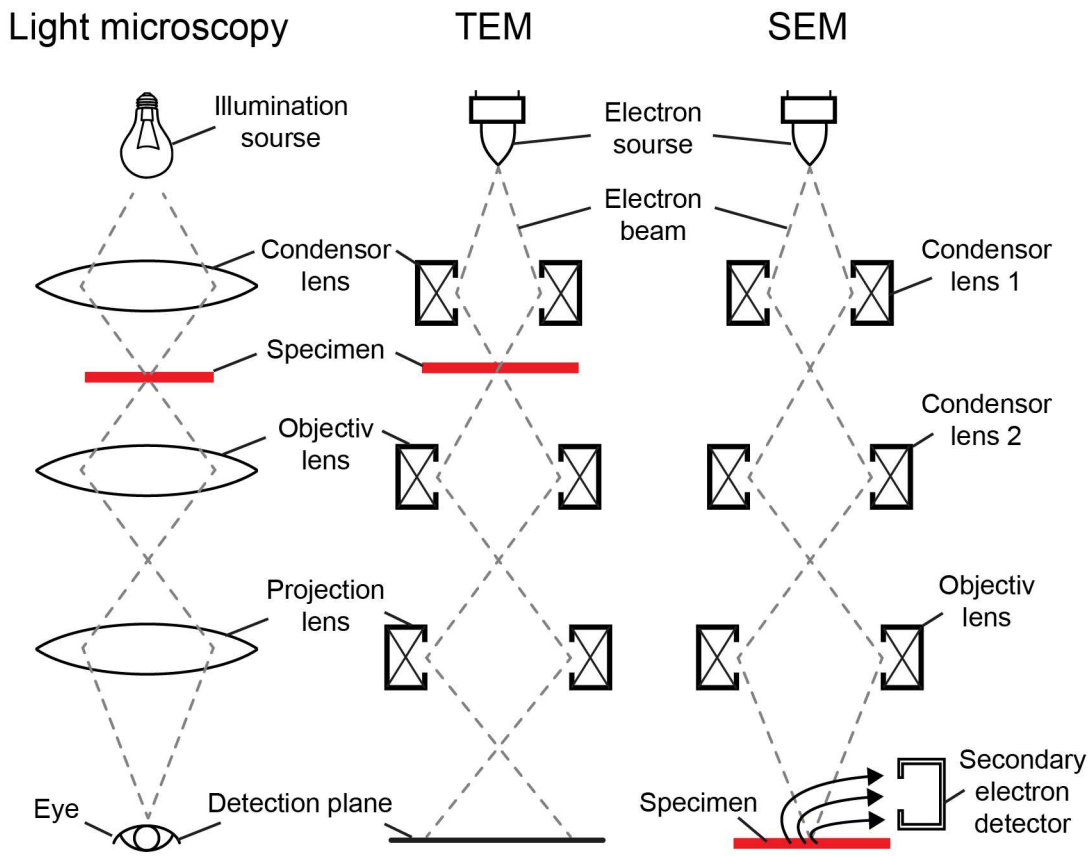

Figure 1.13: Principles of light microscopy, TEM and SEM. In contrast to the light microscope, the beam in TEM and SEM consists of electrons. TEM and SEM also use lenses to form the beam, which in this case are magnetic coils. While in TEM electrons pass through the sample and non-deflected electrons are detected, in SEM the electron beam is focused onto a point of the sample and secondary electrons are measured (adapted from cmrf.research.uiowa.edu).

action types. In case of AFM, it is the van-der-Waals, electrostatic and capillary forces interactions. By using piezoelectric actuators to control the tip position, one can achieve resolutions far beyond the optical limit down to atomic scale.

Since its development in 1986 (Binnig et al., 1986), AFM has become an important tool for studying a broad range of biological applications. AFM can operate in almost any environment including liquids. Since no special sample preparation is required, one can perform experiments under physiological conditions (Moreno-Herrero and Gomez-Herrero, 2012). For example, non-fixed cells or bacteria can be scanned at high resolution (Oberleithner et al., 1993) or one can study the self-assembly of proteins, e.g. collagen fibrils. Moreover, in the force mode it is possible to measure the interaction strength between the cell and the substrate or between two cells, or the unfolding force of proteins (Baro and Reifenberger, 2012).

1.5.3.1 Basic principles

AFM can be subdivided into three main components: the tip on a spring (cantilever), the piezoelectric component, and the detection with a feedback mechanism (Fig. 1.14). The AFM tip mounted on the end of the cantilever interacts with the sample surface. The tip and the cantilever are made of hard materials, e.g. silicon (Si) or silicon nitride (Si_3N_4), to withstand large forces on a very small area. Commercially produced cantilevers are available with different tip geometries (pyramidal, spike, hyperbolic circular symmetric) and tip apex diameters ranging from several nm to about 20 nm. A subnanometer change of the tip position is achieved via piezoelectric actuators, irrespective whether the tip or the sample is shifted (Morris et al., 1999). A force acting on the tip results in a deflection of the cantilever, z, according to Hook's law

$$F = -k \cdot z, \tag{1.1}$$

where F (N) is the acting force and k (N/m) is the spring constant of the cantilever. The deflection is monitored by a laser beam focused onto the backside of the cantilever. Cantilevers can be coated with gold or aluminum to increase reflectivity. The reflected laser beam is projected onto a photodetector. A photodiode is a semiconductor component which converts light into an electrical signal. Frequently, the photodiode is composed of four segments (Fig. 1.14). This allows the detection of lateral and torsional motion of the cantilever in a very simple way (Morris et al., 1999). Lateral deflection is measured by monitoring the vertical change of the laser position, which equals $(A + B) - (C + D)$, while $(A + C) - (B + D)$ corresponds to friction due to torsion of the cantilever (Fig. 1.14), providing lateral force information (Leite and Herrmann, 2005). In this way, the orientation of the AFM tip can be measured and the information is provided to the

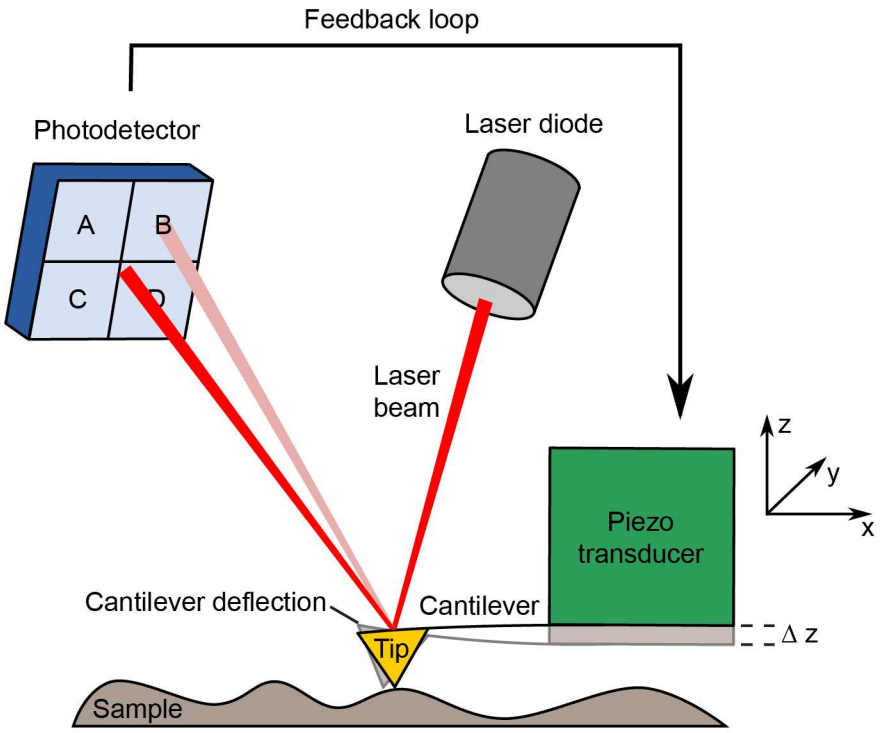

Figure 1.14: Principle of AFM. An AFM tip (yellow) interacts with the sample surface resulting in cantilever deflection (gray) towards or away from the surface. A laser light (red) is focused on the cantilever and reflected to a photodetector. Usually, the photodetector is divided into four areas so that the cantilever deflection (vertical shift of the laser beam) and torsion (horizontal shift of the laser beam) can be measured. The feedback loop adjusts the cantilever-sample distance (Δz) via a piezo transducer (green), e.g., to compensate the cantilever deflection.

feedback loop. Thus, e.g., the force acting on the tip can be kept constant by adjusting the z-position via piezoelements.

1.5.3.2 AFM imaging modes

There are three main forces between the tip and the sample: van der Waals, electrostatic and capillary forces (Binnig and Rohrer, 1999). Depending on the sample's nature and the tip morphology, one force type may dominate over the others. In the case of biological samples imaged in liquid, the cantilever is deflected mostly by van der Waals forces. The dependence of these forces on the tip-sample distance is modeled by the Lennard-Jones-Equation (Jones, 1924), which approximates the energy of interaction between two neutral atoms or molecules as a function of their distance of separation. Attractive van der Waals forces are too small to deflect the cantilever at larger tip-sample separation (Fig. 1.15, green) (Binnig and Rohrer, 1999) and it increases during movement of the cantilever towards the sample resulting in cantilever bending downwards (Fig. 1.15, red).

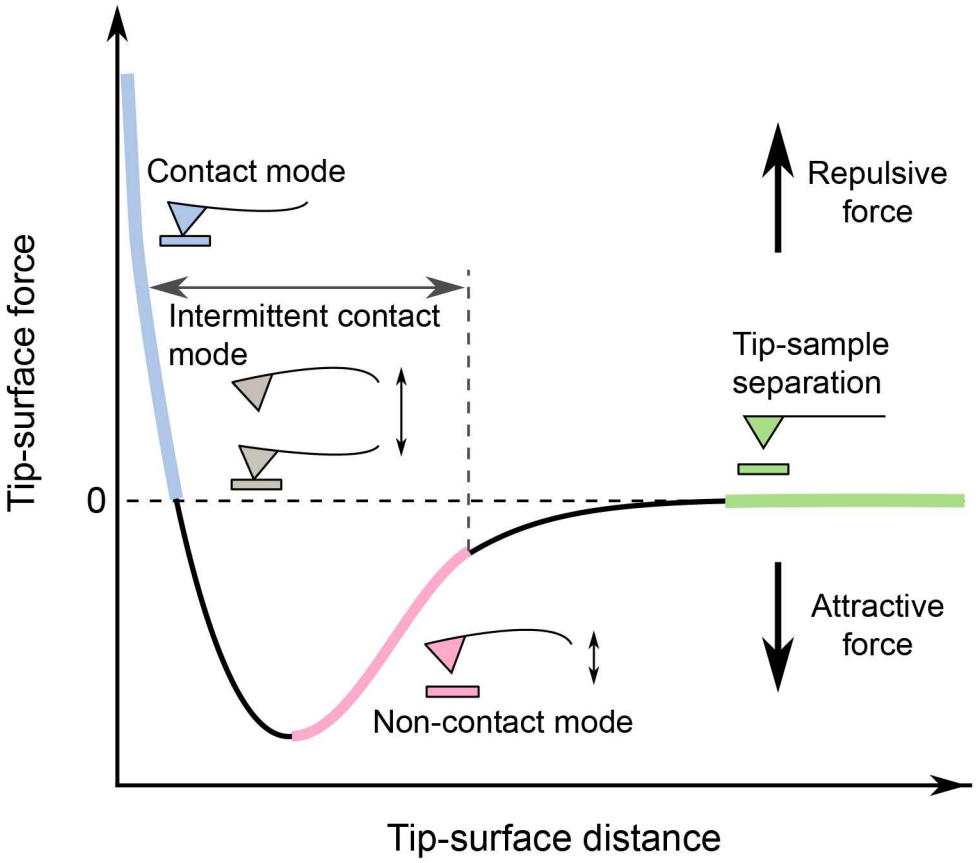

Figure 1.15: Idealized plot illustrating the forces between AFM tip and sample in relation to the tip height. The force between the tip and the sample changes from an attractive to a repulsive regime while bringing the tip closer to the surface. The three marked regions on the curve visualize the tip-surface distances during different imaging modes (adapted from (Braga and Ricci, 2004) and (Dao, 2012)).

Attractive van der Waals forces are largest in the range of 1 - 10 nm measured from the sample surface (Bèguin et al., 2013). A further approach of the cantilever towards the surface introduces repulsive forces due to the Pauli principle, resulting finally in a net repulsive interaction and therefore an upward bending of the cantilever (Fig. 1.15, blue).

The samples can be scanned in three different imaging modes, which are classified into static (contact mode) and dynamic modes (intermittent and non-contact mode) (Baro and Reifenberger, 2012). Due to the different imaging pirnciples, the three modes operate at different tip-sample distances (Fig. 1.15). The comparison of these modes is summarized in Table 1.7.

	Cantilever spring constant, $N \cdot m^{-1}$	**Resonance frequency, kHz (in air)**	**Scanning force**	**Advantages and Disadvantages**
Contact mode	0.01 - 1.0	7 - 50	µN - nN	+ high speed + high (atomic) resolution – lateral force causes sample damage – not negligible capillary forces occur while scanning in air
Intermittent contact mode	30 - 60	250 - 350	nN	+ high lateral resolution + nearly no lateral forces + minimizes capillary forces – slower than contact mode
Non-contact mode	0.5 - 5	50 - 120	pN	+ no force exerted on the sample – low lateral resolution – slowest scan speed – works only on extremely hydrophobic samples

Table 1.7: Comparison of different AFM imaging modes (adapted from (Dao, 2012)).

1.5.3.2.1 Contact mode

In contact mode the AFM tip is in direct contact with the sample and pressed against the probe with a particular force during scanning (Fig. 1.14). This interaction corresponds to a repulsive tip-surface force and an upward deflection of the cantilever. The position of the laser beam on the photodiode in this initial situation corresponds to "zero". While scanning, the cantilever becomes sometimes more, sometimes less bended, depending on topographical features. Since a different deflection corresponds to a different force, a feedback mechanism is required to keep the interaction force between the tip and the sample constant during the scan. Therefore, the vertical position of the cantilever is continuously adjusted via the piezo actuator to adjust the deflected laser beam back to the user-defined set point. For scanning biological samples soft cantilevers with spring constants ranging from 0.01 to $1\,Nm^{-1}$ are often used to avoid damaging the sample (Baro and Reifenberger, 2012; Braga and Ricci, 2004). The height data collected from AFM scans can be used to create a 3D reconstruction of the surface. The contact mode imaging in liquid has two common drawbacks. Firstly, due to temperature changes the cantilever drifts during imaging, e.g., leading to a deviation from the initial set point and drift of the scanning force. Therefore, cantilever deflection adjustment and scan force minimization plays a crucial role for each scan, in particular in liquids (Baro and Reifenberger, 2012). Secondly, lateral motion of the cantilever during the scan introduces lateral forces onto the sample, resulting in sample movement or damage. Thus, soft samples or weakly attached

structures to the surface, such as proteins or viruses, are often not suitable for contact mode imaging (Baro and Reifenberger, 2012).

1.5.3.2.2 Intermittent contact mode

The intermittent contact mode were developed to minimize shear forces applied on the sample during scaning (Baro and Reifenberger, 2012). In this mode the cantilever is stimulated by the piezo actuator to oscillate close to its resonance frequency with amplitudes between 100 and 200 nm, so that the tip only intermittently touches the sample. During each cantilever oscillation the tip changes between repulsive and adhesive interactions with the surface (Fig. 1.15). With changes in topography, the average distance between the tip and the sample varies resulting in a changed amplitude and oscillation frequency (Baro and Reifenberger, 2012). A piezoelectric actuator adjusts the distance between the tip and the surface in order to maintain a preset cantilever oscillation amplitude and frequency (Braga and Ricci, 2004). Often, the main quantity for the feedback loop and the measurement is the amplitude of oscillations, however, the frequency can be used as well. In comparison to the contact mode, the lateral force is reduced due to the short contact time between the tip and the sample, resulting in less sample damages and improved lateral resolution for soft samples (Baro and Reifenberger, 2012).

1.5.3.2.3 Non-contact mode

In non-contact mode, the oscillating tip is brought into proximity to the sample albeit without making any contact. The tip should not be farther away from the surface as 10 nm for a maximal effect. Therefore, the oscillation amplitude should be sufficiently small to stay in the attractive regime of the van der Waals forces (Fig. 1.15). The changing sample topography will then cause a varying strength of the tip-sample interaction and induce a shift of the resonance frequency and also a change of the amplitude. The imaging and feedback mechanism is based on measuring the oscillation frequency or amplitude, similar to the intermittent contact mode. Stiff cantilevers are typically used for non-contact mode imaging. The great advantage of this mode is that the tip never touches the sample and that the interaction forces are very low in the range of pN (Braga and Ricci, 2004).

1.5.3.3 Resolution limitation in AFM imaging

Although piezoelectric actuators can work close to atomic accuracy, the effective AFM scan resolution is often lower. The resolution of AFM scans strongly depends on the tip sharpness and geometry. In particular, the radius of the tip apex is an important parameter. Sharp edges in the sample appear often smoothed out due to the convolution phenomenon. As shown on Fig. 1.15A, during scanning the tip starts to move upwards

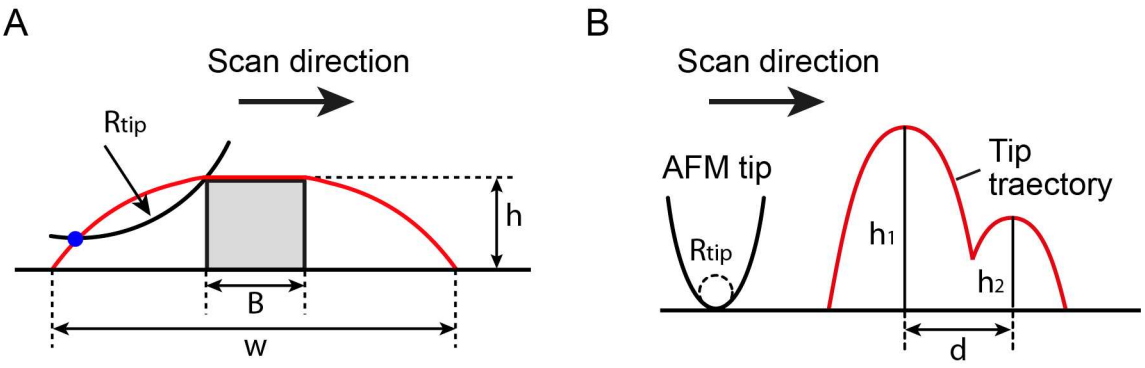

Figure 1.16: Resolution limitation of AFM. Spatial resolution of AFM scans depend on the tip size and geometry. (A) Scanning of objects with AFM tip having the radius R_{tip} results in broadening of the object due to convolution, so that the object with a width B appears to be widened to the width w. The height h remains unchanged. (B) Two objects must be separated from each other at least by the distance d to be resolved. d depends on the tip geometry and on the relative heights, h_1 and h_2, of the objects.(adapted from (Baro and Reifenberger, 2012))

when it hits the edge of the object. Due to the finite tip apex radius, this happens before the tip center reaches the edge. Correspondingly, the tip hits again the substrate at a particular distance from the second object edge. Altogether, the object appears on the AFM scan larger as it is in reality. Furthermore, also the depths of surface invaginations with a diameter smaller than the tip apex diameter can only be measured as far as the tip immerses (Fig. 1.15B) (Baro and Reifenberger, 2012). Fabry and Perot defined a criteria for the resolution limit for optical microscopy (Lauterborn and Kurz, 2003) which can be also applied on AFM. According to that, two peaks of equal intensity are resolved if they are separated from each other at least by full width at half maximum (FWHM). This yields for the minimal distance d between two neighboring features

$$d \geq \sqrt{2 \cdot R \cdot (h_1 - h_2)}, \tag{1.2}$$

where R is tip radius, and h_1 and h_2 are the heights of the objects. Therefore, imaging of smaller objects with AFM is only possible with a tip that is sufficiently sharp (Baro and Reifenberger, 2012). On the other hand, tips with a larger apex radius are more robust. Therefore, tips with different radii ranging from 1 to 20 nm are commercially available. In case of scanning non-fixed samples, one should also take the scanning time into account for choosing the appropriate resolution. Imaging a larger area with maximal resolution can easily take several hours (Baro and Reifenberger, 2012).

1.5.3.4 AFM imaging of biological samples

AFM is a universal tool for imaging a great variety of biological samples at scales ranging from subnanometer to tenth of µm. For example, cell motion, growth, division and organization into cell masses and tissues can be visualized by AFM time-lapse imaging (Kuznetsov et al., 1997). Also, the dynamics of cellular structures were studied with AFM in living cells. To mention only some further applications, the activation of platelets (Fritz et al., 1994), protrusion of lamellipodia (Rotsch et al., 1999; Schoenenberger and Hoh, 1994), cytoskeletal rearrangement (Henderson et al., 1992) and also membrane structures involved in exocytosis (Schneider et al., 1997) have been successfully imaged in AFM contact mode. The architecture of FAs and actin cytoskeleton organization were studied with AFM (Franz and Muller, 2005). On the protein level, collagen remodeling by cells (Friedrichs et al., 2007) as well as self-organization of collagen matrices (Stamov et al., 2013) could be resolved by AFM. The extracellular self-assembly of collagen type I was observed by time-lapse AFM with subnanometer resolution, showing characteristic 67 nm D-band fibril structure its substructure (Cisneros et al., 2006; Yadavalli et al., 2010). Furthermore, the structure and conformation of proteins was investigated with AFM, e.g. collagen, laminin, lumican, decorin and FN (Muller and Engel, 2002). Even the submolecular structure of the major intrinsic proteins from lens fiber cells and its structural changes at the surfaces of biomolecules was detected with a time resolution of a few milliseconds, sufficient to monitor conformational changes involved in biological processes (Fotiadis et al., 2000). In summary, AFM is a very convenient and successful tool for observing and studying many biological phenomena. Fortunately, commercially available AFMs achieve easily subnanometer resolutions in contact (Muller et al., 1999; Muller et al., 1995) as well as in tapping mode (Moller et al., 1999).

1.5.3.5 AFM force spectroscopy mode

AFM introduced not only a revolution in imaging, but also opened a way to obtain information about forces acting between tip and the sample, in the range between ~ 10 - 100 nN. Thus, in biological applications the interaction between cells, proteins and/or substrates can be studied. For example, one can attach a cell to the cantilever tip, let the cell interact with the substrate or another cell and then determine the adhesion force by detaching the cell from its partner (Benoit et al., 2000; Roure et al., 2006; Franz et al., 2007; Taubenberger et al., 2007).

In contrast to scanning, in force spectroscopy mode the XY-position of the AFM cantilever is fixed, while the cantilever is moved in Z-direction only. Because the actual spring constants of commercial cantilevers vary, a calibration procedure has to be performed for each cantilever before data collection. Usually, the spring constant is determined via the

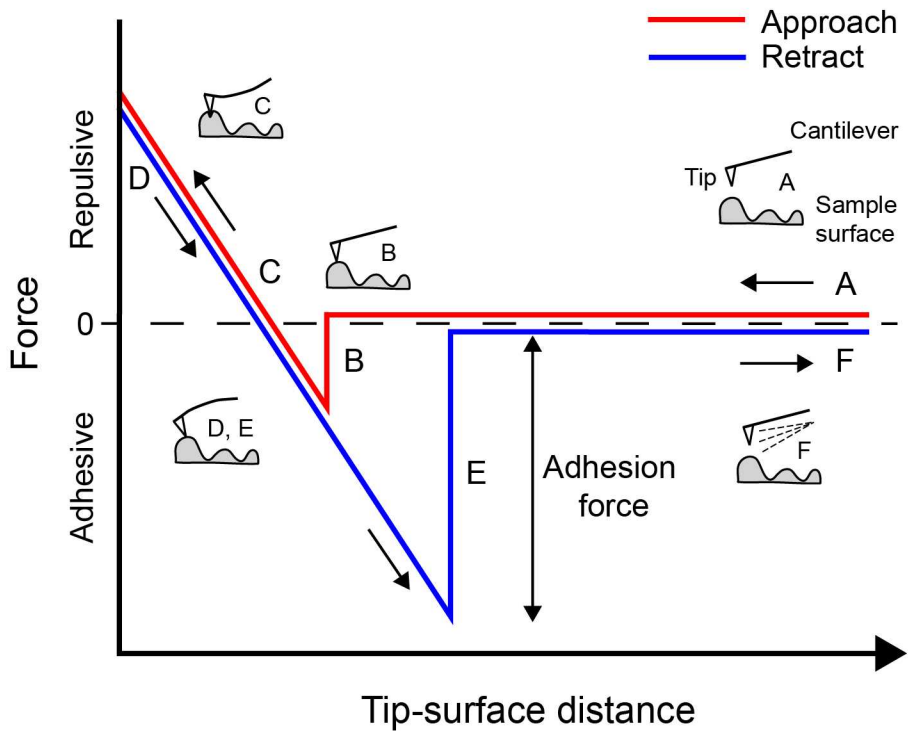

Figure 1.17: A typical force-distance curve of an approach-retract cycle between a tip and a substrate. The cantilever is approached to the sample until the required force is reached (A, B, C). After retraction and detachment of the tip from the surface (D, E, F), the loose of contact appears at another force-distance point than the establishment of contact (E compared to B). adapted from (Shahin et al., 2005)

thermal noise calibration. Other methods are, e.g., calibration over reference cantilever or over dimension calculations (Noy, 2007). A typical force-distance curve between a sample and the tip is schematically shown in Fig. 1.17. The force on the tip is zero while the tip is approaching the substrate (Fig. 1.17A). The tip is subject to adhesive forces very close to the substrate, bending the cantilever downwards (Fig. 1.17B). Further cantilever movement towards the sample first decreases the attractive force between the tip and the substrate and then turns the tip-sample interaction into a repulsive one, until the required force is reached (Fig. 1.17C). These three steps can also be observed in reversed order while moving the cantilever away from the substrate (Fig. 1.17D, E, F). However, the cantilever must move further away from the surface before the tip detaches from the substrate due to strong adhesive tip-sample forces. This is clearly visible on the force-distance curve. A high force resolution can be achieved by moving the cantilever slowly, while a more frequent vertical displacement can be useful to investigate other mechanical properties (Braga and Ricci, 2004). The detected forces range from pN to µN depending on the cantilever stiffness (Benoit and Gaub, 2002). This is in the range of forces

present in intramolecular interactions inside proteins, so that even the forces needed to unfold proteins (Best et al., 2003; Rief et al., 1997) as well as adhesive receptor-ligand interaction forces can be measured.

2 Matherials and methods

2.1 Materials

2.1.1 Reagents and Kits

Reagents and Kits	**Company**	**Applications**
3-Glycidyloxypropyl-trimethoxysilane	www.sigmaaldrich.com	silanization
Acetic acid	www.sigmaaldrich.com	contains in solutions
Acryl-bisacrylamide mix	www.carlroth.de	PAA-gel
Alexa Fluor® 488	www.invitrogen.com	FN labeling
Alexa Fluor® 568	www.invitrogen.com	FN labeling
Alexa Fluor® 633	www.invitrogen.com	FN labeling
APS	www.carlroth.de	PAA-gel
APTES	www.sigmaaldrich.com	PDMS functionalization
Borax anhydrous	www.sigmaaldrich.com	silver staining
Bovine collagen type I	www.advancedbiomatrix.com	surface coating
Bromophenol blue	www.sigmaaldrich.com	loading buffer
CO_2 independent medium	www.invitrogen.com	SCFS
DMEM	www.invitrogen.com	cell culture
Dymax OP-29	www.dymax.com	cell inversion
EDTA	www.sigmaaldrich.com	contains in buffer
Ethanol/EtOH (>99.8%)	www.carlroth.de	washing, solvent
Fibronectin	www.roche.de	surface coating
FITC conjugated collagen type I	www.sigmaaldrich.com	surface coating
Fluorescent mounting medium	www.dako.com	fluorescence microscopy

Formaldehyde	www.carlroth.de	contains in solutions
Gelatine	www.sigmaaldrich.com	degradation experiment
Geneticin/G-418 Sulfate	www.invitrogen.com	cell culture
Glutaraldehyde	www.sigmaaldrich.com	cell fixation
Glycine	www.carlroth.de	collagen buffer
Hepes	www.sigmaaldrich.com	buffer
Hydrochloric acid	www.carlroth.de	contains in solutions
L-glutaminie	www.invitrogen.com	cell culture medium supplement
Isopropanol/2-propanol	www.carlroth.de	washing
Methanol (MeOH)	www.carlroth.de	contains in solutions
$MnCl_2$	www.sigmaaldrich.com	integrin activation
Mowiol®	www.sigmaaldrich.com	mounting solution
Nanofectin Kit	www.paa.com	cell transfection
Osmiumtetroxide (4%)	www.sigmaaldrich.com	electron microscopy
OxyFluor™ Oxyrase	www.oxyrase.com	fluorescence imaging
Paraformaldehyd/PFA	www.sigmaaldrich.com	fixation
Penicillin-streptomycin	www.invitrogen.com	cell culture
Recombinant mouse M-CSF	www.rndsystems.com	RAW264.7 cell differentiation
Recombinant mouse RANK-L	www.rndsystems.com	RAW264.7 cell differentiation
Silver nitrate	www.sigmaaldrich.com	silver staining
Sodium borohydride	www.sigmaaldrich.com	FN treatment, GA inactivation
Sodium bicarbonate	www.sigmaaldrich.com	buffer

Sodium cacodylate trihydrate	www.sigmaaldrich.com	electron microscopy
Sodium carbonate	www.sigmaaldrich.com	buffer
Sodium-DL-Lactate	www.sigmaaldrich.com	substrate for oxyrase
Silicone elastomer kit Sylgard®184/PDMS	www.dowcorning.com	cell inversion
Potassium chloride	www.sigmaaldrich.com	collagen buffer
TEMED	www.carlroth.de	PAA-gel
Tris	www.sigmaaldrich.com	Buffer
Triton X-100	www.carlroth.de	cell permeabilizing
Trypsin/EDTA	www.invitrogen.com	cell detachment
Trypsin inhibitor	www.sigmaaldrich.com	inhibits trypsin after cell passaging

Table 2.1: Reagents and Kits

2.1.2 Buffers and solutions

0.1 M Cacodylate buffer	0.1 M Na($CH_3$2As0_2·3$H_2$0, 0.04 M HCl, pH 7.2
0.1 M Carbonate-bicarbonate buffer	80 mM $NaHCO_3$, 20 mM Na_2CO_3, pH 9.3
Electroporation buffer	120 mM KCl, 10 mM K_2PO_4/ KH_2PO_4 (pH 7.6), 2 mM $MgCl_2$, 25 mM Hepes (pH 7.6) and 0.5% Ficoll 400
5x Loading buffer	250 mM Tris-HCl (pH 6.8), 50% (v/v) glycerol, 0.2% (m/v), bromophenol blue
PBS	137 mM NaCl, 2.7 mM KCl, 10mM Na_2HPO_4·2H_2O, 2 mM KH_2PO_4, pH 7.4
Running buffer	25 mM Tris-HCl (pH 8.8), 192 mM glycine
Silver stain developer	6% (w/v) Na_2CO_3, 0.05% (v/v) formaldehyde, 0.004% (w/v) $Na_2S_2O_3$
Silver stain fixative	40% (v/v) MeOH, 10% (v/v) acetic acid, 0.05% (v/v) formaldehyde
Silver stain oxidizer	0.1 M borax anhydrous, 1% (v/v) glutaraldehyde
Silver reagent	0.2% (w/v) $AgNO_3$, 0.076% (v/v) formaldehyde
Silver stain stop solution	12% (v/v) acetic acid
TBS	120 mM Tris-HCl and 150 mM NaCl, pH 7.4

Table 2.2: Buffers and solutions

2.1.3 Antibodies and labeling reagents list

Primary antibodies	**Company**	**Reacts with**	**Appl.**	**Dilution**
mouse monoclonal anti-**paxillin**	www.bdbiosciences.com	M, R, H	IF	1:200
mouse monoclonal anti-**vinculin**, clone hVin-1	www.sigmaaldrich.com	M, R, H	IF	1:100
rabbit polyclonal anti-**fibronectin**	www.sigmaaldrich.com	M, R, H	IF	1:100

Table 2.3: Primary antibodies. M - mouse, R - rat, H - human, IF - immunofluorescence.

Secondary antibodies and labeling reagents	**Company**	**Dilution**
4, 6-Diamidino-2-phenylindol Dihydrochlorid, DAPI	www.carlroth.de	1:1000
Alexa Fluor® 568 phalloidin	www.lifetechnoligies.com	1:200
goat anti-mouse IgG (H+L)-FITC	www.dianova.com	1:200
goat anti-rabbit IgG (H+L)-Alexa Fluor® 488	www.dianova.com	1:200
goat anti-rabbit IgG (H+L)-Cy3	www.dianova.com	1:200

Table 2.4: Secondary antibodies and labeling reagents.

2.1.4 Aparatus

Apparatus	Company	Applications
2K Dialyse cassette	www.thermoscientific.com	FN dialysis
AxioObserver inverted optical microscope	www.zeiss.com	optical imaging
Biorad Genepulser	www.bio-rad.com	cell transfection
Bright light-UV table	www.vilber.de	adhesive polymerization
Carry 300 UV-Vis Spectrophotometer	www.agilent.com	absorbance measurement
EM CPD030	www.leica.com	critical point drying
Eppendorf microcentriguge 5415R	www.eppendorf.com	centrifugation
Fluorodish FD35-100	www.wpiinc.com	optical imaging
Harrick PDC-002 plasma cleaner	www.harrickplasma.com	PDMS treatment, cantilever cleaning
iMIC Digital Microscope	www.till-photonics.com	TIRF imaging
Laser scanning microscope, LSM 510	www.zeiss.com	optical imaging
NanoDrop2000c	www.thermoscientific.com	protein concentration determination
NanoWizard II AFM	www.jpk.com	AFM scanning
Petridish heater	www.jpk.com	control temperature during AFM scanning
Scanning electron microscope, LeoSupra55VP	www.zeiss.com	SEM imaging
Sephadex G-10 column	www.sigmaaldrich.com	gel filtration
Sigma 4-16K centrifuge	www.sigma-centrifuges.co.uk	centrifugation
V-shaped Si_3N_4 cantilever, MLCT	www.brukerafm-probes.com	AFM scanning
V-shaped Si_3N_4 cantilever, MSNL-10	www.brukerafm-probes.com	AFM scanning
Universal 320R centrifuge	www.hettichlab.com	centrifugation

Table 2.5: Apparatus.

2.1.5 Software

Adobe Illustrator CS5	www.adobe.com
Adobe Photoshop CS2	www.adobe.com
EndNote X4	endnote.com
Gwyddion	gwyddion.net
ImageJ 1.45r	http://imagej.nih.gov/ij
JPK Data Processing	www.jpk.com
LaTeX	www.latex-project.org
Matlab	www.mathworks.de
OriginPro 8.6G	www.originlab.de
TeXstudio	texstudio.sourceforge.net
Volocity	www.perkinelmer.com

Table 2.6: Software.

2.2 Methods

2.2.1 FN preparation

2.2.1.1 FN labeling

For FN labeling three different Alexa Fluor® carboxylic acid succinimidyl (NHS) ester dyes were used. The NHS ester group reacts with primary amines of FN to form a stable dye-protein conjugate. Before labeling human plasma FN (2 mg/ml) was dialyzed against PBS in a 2K Dialyse Casette overnight at 4°C to remove glycine, which significantly inhibits the labeling reaction, from the solution. Afterwards, FN was incubated with the Alexa Fluor® dye at room temperature in the dark for 1 h. The unbound dye was removed from the conjugate by gel filtration using a Sephadex G-10 column. Final elution was performed using 1.2 ml PBS.

Dye	Excitation wavelength, Ex (nm)	Emission wavelength (nm)	Moles dye per FN	Correction factor, cf	Extinction coefficient, ε_{AFdye} ($M^{-1}cm^{-1}$)
Alexa Fluor® 488	494	519	5 - 8	0.11	71 000
Alexa Fluor® 568	577	603	2 - 6	0.46	91 300
Alexa Fluor® 633	632	647	1 - 3	0.55	100 000

Table 2.7: Properties of Alexa Fluor® dyes

The amount of protein can be determined by measuring the absorbance at 280 nm (A_{280}). However, A_{280} of the labeled protein includes also the dye absorbance. Therefore, it is necessary to also measure the absorbance at the corresponding dye excitation wavelength A_{Ex}. Then, the protein concentration after elution equals

$$\text{protein concentration (M)} = \frac{[A_{280} - (A_{Ex} \cdot cf)] \cdot \text{dilution factor}}{\varepsilon_{FN}}, \tag{2.1}$$

where cf and ε_{FN} are a correction factor and the molar extinction coefficient of FN ($292\,250\,M^{-1}cm^{-1}$), respectively. Since the amount of dye bound to FN might influence the structural conformation of the protein (Hoffmann et al., 2008), the average molar ratio of dye bound to FN was estimated by spectrophotometry as

$$\text{moles dye per mole protein (M)} = \frac{A_{Ex} \cdot \text{dilution factor}}{\varepsilon_{AF,dye} \cdot \text{protein concentration}}, \tag{2.2}$$

where $\varepsilon_{AF,dye}$ is the molar extinction coefficient of the Alexa Fluor® dyes. The FN Alexa Fluor® conjugates were stored at a concentration of 1 mg/ml at -80 °C.

2.2.1.2 Surface coating with FN

Before coating, pure FN or fluorescently labeled FN conjugates were centrifuged at 15 700 rcf for 5 min to separate protein aggregates from the solution. Afterwards, glass bottom cell culture dishes (Fluorodish, FD35) or freshly cleaved mica were coated with FN or FN conjugates at a concentration of 50 µg/ml at room temperature for 1 h in the dark. Afterwards, the mica surface was rinsed with 10 ml PBS to remove unbound proteins.

2.2.1.3 FN exposure

For investigating FN properties as a function of exposure to visible light, three types of experiments were performed: exposure using different wavelength, exposure using different light intensities using a photo mask and exposure using different irradiation times.

2.2.1.3.1 FN exposure at different wavelengths

FN was exposed with different wavelengths (400, 440, 480, 520, 560, 600 and 640 nm) using a self-built setup (Fig. 2.1) containing a monochromator light source (Polychrome 5000 with a 150 W Xenon lamp). The light was focused on the FN coated surface through a 63x LD Plan-Neofluar objective with numerical aperture of 0.75. The position of the probe was adjusted with µm accuracy, so that on one substrate different areas could be exposed with different wavelengths. In physics, the wave-particle duality of light is well known. This means, that some experiments like interference can be easily explained with waves. However, atomic excitations occur due to absorption of photons, which are energy packets of light. Therefore, light induced changes of the protein structure at different wavelength should be compared via the photon number and not via the photon energy. This can be achieved by measuring the incident light power and adjusting the exposure time (Table 2.8). The energy of a photon E_λ equals

$$E_\lambda = \frac{h \cdot c}{\lambda}, \tag{2.3}$$

where h is the Planck's constant, c is the light velocity and λ is the wavelength. The power of the incident light on the sample was measured as a function of the wavelength, P_λ, with a power meter. The number of incident photons equals

$$N_\lambda = \frac{P_\lambda \cdot t_\lambda}{E_\lambda}, \tag{2.4}$$

Wavelength (nm)	Measured incident power ($\mu W/mm^2$)	Calculated exposure time (sec)
400	27	667
440	39	419
480	50	300
520	45	308
560	41	314
600	38	316
640	31	363

Table 2.8: Exposure time as a function of wave length and incident power.

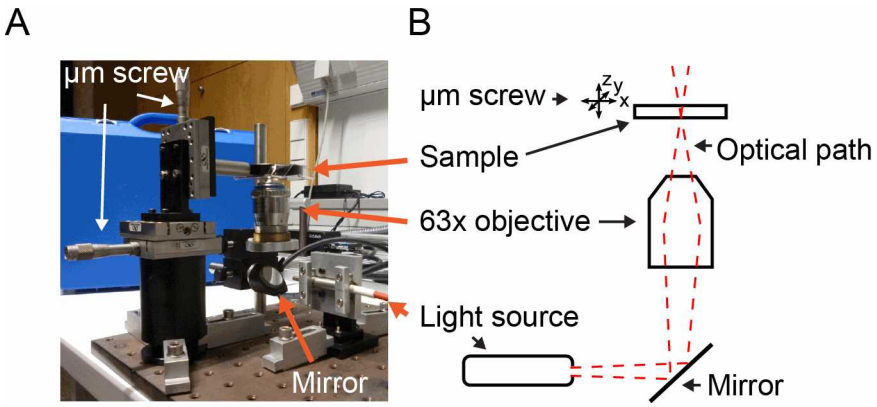

Figure 2.1: Self-built setup for FN exposure. The setup is shown in (A) and the corresponding schematic view in (B). An optical fiber was used to guide the light to the mirror. A 63x objective focuses the reflected light onto the sample. It was possible to precisely position the sample in x-, y- and z-direction through using a micrometer gauge.

with the exposure time t_λ. Different exposure times were normalized to the reference condition at 480 nm with $P_{480} = 50\,\mu W/mm^2$ and $t_{480} = 5$ min. Thus, the exposure time as a function of the wavelength is

$$t_\lambda = \frac{P_{480} \cdot 480\,\text{nm} \cdot t_{480}}{P_\lambda \cdot \lambda}. \tag{2.5}$$

2.2.1.3.2 FN exposure at different light intensities

An area of $\sim 1.5\,cm^2$ was exposed by a non-focused beam using an Axio Observer inverted optical microscope and an X-Cite 120Q Xenon lamp (120 W). To control the light intensity, a grey-scale pattern was printed on a transparent film. This photo mask was attached to the underside of an FD35 glass bottom dish coated with FN-AF488 from the top. Afterwards, the FD35 was placed directly onto the objective holder of the fluorescence microscope and exposed for 10 min at a power of $76\,\mu W/mm^2$. Alternatively, the FD35 carrying the photo mask was exposed with UV light (365 nm) on a Bright Light UV table

at a power of 0.1 mW/mm^2 for 5 min. Finally, the FN was washed once with PBS before further using.

2.2.1.3.3 FN exposure for different times

FN was exposed using irradiation times ranging from 1 to 300 sec (1, 3, 5, 7, 10, 30, 100 and 300 sec) using the Axio Observer inverted optical microscope and X-Cite 120Q. Via an optical band pass filter, the wavelength was restricted to a range between 480 and 490 nm, and the beam was focused on the sample with a 63x objective. Afterwards, the sample was prepared as described in Section 2.2.1.3.2.

2.2.1.4 Chemical fixation of FN

FN samples were incubated with 1% glutaraldehyde for 30 min and then washed with PBS. To remove free aldehyde groups, FN was incubated with 0.1% BH_4 for 5 min and finally washed again with PBS.

2.2.1.5 FN thermal denaturation

To examine denatured FN, a FN solution (50 µg/ml) was incubated for 30 min at 60°C. Afterwards, a FD35 glass bottom dish was coated with the thermally denaturated FN for 1 h at room temperature before cell seeding. Alternatively, the glass bottom of a FD35 dish or freshly cleaved mica was first coated with FN (50 µg/ml) and the sample was then incubated for 30 min at 60°C. Finally, in both cases the FN was washed with PBS before cell seeding.

2.2.2 PDMS substrates

A pre-polymer solution of polydimethylsiloxane (PDMS) was thoroughly mixed with the cross-linker at a ratio of 10:1. The mixture (1 ml) was placed into a Ø 35 mm plastic cell culture dish. The PDMS substrate was degassed in a vacuum chamber before curing in a drying chamber at 60°C for 4 h. Immediately before cell seeding, the cured PDMS substrates were treated with oxygen plasma in a Harrick PDC-002 plasma cleaner for 5 min to increase their hydrophilicity.

2.2.2.1 PDMS coating with FN

Before coating, the PDMS substrate was treated with oxygen plasma for 1 min to increase its hydrophilicity. Afterwards, the FN-AF488 was incubated on the plasma activated PDMS for 1 h at room temperature in the dark. Then, unbound FN was washed out with PBS. The coated substrate was kept in PBS till further usage.

2.2.2.2 PDMS coating with collagen type I fibrils

Bovine collagen type I monomers were diluted in ice-cold PBS to a final concentration of 50 µg/ml and mixed with 1 µg/ml FITC-conjugated monomeric bovine collagen I. Collagen fibrillogenesis was performed in a reaction tube at 37°C overnight in the dark. The formed fibrils were then attached to the PDMS using a covalent coating protocol (Wipff et al., 2009). Briefly, the activated, plasma-treated PDMS was incubated with a 10% solution of 3-aminopropyltriethoxysilane (APTES) in ethanol at 60°C for 30 min to introduce amino groups to the surface. Afterwards, the PDMS was rinsed with PBS and incubated with 3% glutaraldehyde for 20 min followed by washing with PBS. Finally, the suspended collagen I fibrils were incubated on the PDMS for 60 min, where they covalently bound to the surface, and washed with PBS.

2.2.3 Silanization of glass coverslips

Glass coverslips (Ø 24 mm) were cleaned in 100% ethanol in an ultrasonic bath for 30 min and dried with N_2 gas. Clean glass coverslips were incubated in 3-glycidoxypropyltrimethoxysilane (2%) in 95% ethanol for 5 min at room temperature in the dark, then dried with N_2 gas, washed in 100% ethanol and dried again with N_2 gas. Finally, glass coverslips were treated with plasma for 10 min in the plasma cleaner.

2.2.4 Surface coating with gelatine-FITC

Gelatine (20 mg/ml) was incubated with FITC (40 µg/ml) in 0.1 M carbonate-bicarbonate buffer (pH 9.3) at room temperature for 18 h. The unbound dye was removed by gel filtration through a Sephadex G-10 column in PBS. Gelatin-FITC aliquots were stored at -20°C. Gelatin-FITC was incubated on silanized glass coverslip at room temperature in the dark for 1 h.

2.2.5 Cell culturing, passaging and differentiation

2.2.5.1 Cell culture

Rat embryonic fibroblasts (REF52), mouse embryonic fibroblasts (MEF), human foreskin fibroblasts (HFF), Madin Darby canine kidney (MDCK) and a mouse macrophage cell line (RAW 264.7) were cultured in DMEM containing 10% fetal bovine serum, 100 IU/ml penicillin, and 100 µg/ml streptomycin at 37°C and 5% CO2. Cells were not cultured for more than 30 passages. All cells were passaged every 2 - 3 days or before reaching confluency. For passaging, cells were rinsed with PBS and incubated with 1 ml trypsin/EDTA at 37°C for 5 min to detach the cells from the cell culture flask bottom. To inactivate

trypsin, 9 ml of growth medium were added and the cells were diluted according to their growth at a ratio of 1:3 to 1:10.

2.2.5.2 Osteoclast differentiation

To induce osteoclast differentiation, RAW 264.7 cells were seeded at a density of 100 cells/mm^2 and cultured for 6-7 days in alpha MEM medium containing 10% fetal bovine serum, 100 IU/ml penicillin supplemented with soluble Receptor Activator of NFκB Ligand (RANK-L; 50 ng/ml) and Macrophage Colony Stimulating Factor (M-CSF; 50 ng/ml). The medium was changed every 3 days.

2.2.6 Cell transfection methods

2.2.6.1 Transfection via electroporation

Cells were grown in tissue culture plates (Ø 140 mm) to 95% confluence. Cells were washed with PBS and trypsinized with 1.5 ml trypsin/EDTA for 5 min. After detachment, cells were resuspended in 8.5 ml ice-cold electroporation buffer (pH 7.6), transferred to a 15 ml Falcon tube and centrifuged for 4 min at 170 rcf. Afterwards, the supernatant was removed and cells were resuspended in 200 µl ice-cold electroporation buffer and transferred to a 0.4 cm electroporation cuvette on ice containing 1 µg plasmid DNA. Electroporation was performed using a Biorad Genepulser at 250 V and 960 mF. Subsequently, cells were diluted into 10 ml growth medium and plated into tissue culture plates (Ø 60mm). For TIRF imaging, cells were further diluted in growth medium at 1:1000 and seeded into FD35 dishes and grown for 16 to 24 h.

2.2.6.2 Transfection via FuGENE

For osteoclasts transfection, RAW 264.7 cells seeded in an FD35 dish at a density of 50 cells/mm^2 were first differentiated into osteoclasts for 6 days in alpha MEM medium containing 10% fetal bovine serum, 100 IU/ml penicillin supplemented with 50 ng/ml RANK-L and 50 µg/ml M-CSF. Afterwards, cells were transfected with 5 µg plasmid DNA in serum free alpha MEM medium according to the supplier's manual.

2.2.7 Inverting cells

Cells were cultured on PDMS for 4 to 48 h and then fixed with 4% PFA/1% glutaraldehyde for 30 min. Fixed cells were washed in PBS, rinsed with 70% and then 100% ethanol for 30 sec, respectively. Samples were then quickly dried with N_2 gas to remove excess water. A drop of Dymax OP-29 optical adhesive was applied onto the PDMS substrate

and covered with a glass coverslip. The adhesive was then exposed with UV light (365 nm) on a Bright Light UV table at a power of 0.1 W/cm^2 for 5 min. Afterwards, the coverslip-attached adhesive was gently peeled-off the PDMS substrate, exposing the basal side of the embedded cells for further investigation. Alternatively, for AFM imaging a region of interest within the cell layer was cut out of the PDMS substrate with a scalpel. One drop of the optical adhesive was placed into a Fluorodish and the PDMS cutout was placed onto the adhesive with the cells pointing towards the adhesive. After curing, the PDMS cutout was carefully detached from the cured adhesive in the glass bottom dishes and 1 ml of PBS was added for subsequent AFM imaging in liquid.

2.2.8 Immunofluorescence staining

Cells were fixed for 30 min with 4% PFA, permeabilized with PBS containing 0.2% Triton X-100 for 5 min and incubated with primary antibodies at room temperature for 1 h. After two wash steps with PBS containing 0.2% Tween and one wash step with PBS, samples were incubated with the corresponding secondary antibodies for 1 h at room temperature. Actin filaments were labeled with Alexa488-coupled Phalloidin. Cell nuclei were stained with 4,6-diamidino-2-phenylindole (DAPI) and finally washed with PBS.

2.2.9 Protein separation via electrophoresis

Total protein concentrations in cell lysates were determined using the NanoDrop2000c spectrophotometer. Equal amounts of protein were mixed with 5x loading buffer and denatured at 95°C for 5 min. Samples were then loaded along with a molecular weight marker (Precision Plus Protein™ Kaleidoscope™ standards) into the wells of 7.5% PAA gel. Electrophoresis was performed at 100 V in an electrophoresis chamber containing the running buffer.

2.2.10 Detection of proteins in PAA gel using an silver staining technique

Separated proteins in PAA gel were fixed by using silver stain fixative for 20 min. Afterwards, a PAA gel was incubated three times in 30% ethanol for 10 min each and then rinse twice in water for 10 min each. Then, the PAA gel was transfered into the silver stain oxidizing solution for 1 min and rinsed three times in water (about 30 sec each). Then, the gel was incubated with the silver reagent for 20 min and rinsed three times in water (about 30 sec each). Proteins were visualized by incubating the PAA gel in the silver stain developer solution until bands became visible, then the gel was rinsed three times

in water (about 30 sec each) and incubated in silver stain stop solution to prevent fading of the bands. Finally, the gel was imaged for further analysis.

2.2.11 Microscopy techniques

2.2.11.1 Atomic force microscopy (AFM) techniques

2.2.11.1.1 AFM imaging

AFM imaging was performed using a JPK NanoWizard II AFM mounted on top of an AxioObserver inverted optical microscope. AFM scans of fixed cells were performed in PBS at room temperature in contact mode by using gold-coated silicon nitride V-shaped cantilevers (MLCT-C) with a nominal spring constant of 0.06 N/m. Cellular structures on the basal cell membrane were scanned at room temperature in contact mode by using gold-coated silicon nitride V-shaped cantilevers (MSNL-10-C) with a nominal spring constant of 0.01 N/m. Living cells were scanned in DMEM containing 10% FCS, 1% Penicillin/streptomycin and 20 mM HEPES pH 7.6 at 37°C in contact mode. Imaging was performed using MLCT-C cantilevers and a line scan rate between 0.3 and 2.5 Hz. AFM images were processed using the JPK image processing software (version 3.1.6).

2.2.11.1.2 Rearrangement FN with the AFM tip

For rearranging FN by AFM, four different samples were prepared: native, light-exposed, chemically fixed and thermally denatured FN. For all probes, freshly cleaved mica discs were coated with FN at a concentration of 50 µg/ml at room temperature for 1 h and washed with PBS. FN rearrangement experiments were performed in PBS at room temperature in contact mode using a JPK NanoWizard II AFM and gold coated silicon nitride V-shaped cantilevers (MLCT-C) with a nominal spring constant of 0.06 N/m. First, a $15 \times 15\,\mu m^2$ overview scan of FN with a resolution of 512 x 512 pixel was performed with a force of 0.1 nN applied to the cantilever tip to monitor the FN-coated area. The low force of 0.1 nN was used to prevent the creation of FN fibrils by lateral scanning forces exerted by the AFM tip. Afterwards, $3 \times 3\,\mu m^2$ sections within the overview area were scanned applying contact forces between 0.5 nN and 4 nN. After manipulation, an overview area of $15 \times 15\,\mu m^2$ was reimaged at 0.5 nN contact forces to illustrate FN rearrangements caused by the AFM tip. To ensure reproducibility in force application, the sensitivity and spring constant of cantilevers were calibrated before each experiment using the JPK software. For characterizing the roughness of the remodeled areas, the height amplitudes (height signal decreased by the mean value) were used to calculate R_a (average value of absolute height amplitudes), R_q (standard deviation of the height amplitudes) and R_p (peak-to-peak distance). These values were directly extracted using the JPK software.

Component	Final concentration
DL-Lactate	10 mM
$MnCl_2$	1 mM
Oxyrase	0.3 - 0.6 U/ml

Table 2.9: Medium supplements for time-lapse imaging.

2.2.11.2 Scanning electron microscopy (SEM)

For SEM imaging samples were fixed for 1 h in 2.5% glutaraldehyde dissolved in 0.1 M cacodylate buffer (pH 7.2) and washed afterwards with 0.1 M cacodylate buffer. For complementary fluorescence microscopy, the actin cytoskeleton was stained with phalloidin-TRITC and phase contrast and fluorescence images of cells were collected using an AxioObserver inverted optical microscope. Afterwards, cells were incubated in 1% osmiumtetroxide for 1.5 h on ice to increase the contrast between cells and surface during SEM imaging. Samples were then washed three times with ddH_2O for 30 min each. Afterwards, samples were dehydrated in an ethanol series (30%, 50%, 70%, 90%, 95% and two times with 100%, each for 10 min), transferred into acetone and critical point-dried in a Leica EM CPD030 dryer. Dried samples were immediately sputtered with 2 nm platinum and analyzed with a LeoSupra55VP scanning electron microscope using an aperture size of 20 µm and an accelerating voltage of 7.0 kV.

2.2.11.3 Imaging by optical microscopy

2.2.11.3.1 Imaging by total internal reflection microscopy (TIRF-M)

TIRF imaging was performed on an iMIC microscope with APON 60xOTIRF objective (Olympus) using a 491 nm (100 mW) or 561 nm (75 mW) diode-pumped solid state laser. The generated images were processed with the ImageJ software.

2.2.11.3.2 Fluorescence imaging of FN fibrillogenesis

Cells were seeded on FN-coated glass surfaces of FD35 dishes immediately before imaging. The composition of DMEM serum free medium is summarized in the Table 2.9. Imaging of FN-AF488 or FN-AF568 was performed on an iMIC microscope at 37°C using APON 60xOTIRF or UPLSAPO 40x2 objectives (Olympus). Fibrillogenesis of FN-AF633 was imaged on the Axio Imager2 microscope using the ZEISS Colibri LED illumination system and a 40x Zeiss Fluar oil immersion objective. All imaging was performed at 37°C. The collected images were processed in ImageJ.

2.2.11.3.3 Fluorescence imaging of fixed cells by confocal laser scanning microscopy

For spatial analysis of fluorescently-labeled samples (e.g. immunostained cells or fluorescently labeled FN), imaging was performed on a LSM 510 Meta confocal laser scanning microscope. For this, samples were embedded in Mowiol® before imaging, with the exception of inverted cells, which were imaged in PBS. The images were collected with the LSM 510 software. The 3D reconstruction of confocal image stacks was performed using the Volocity 3D imaging software.

2.2.12 Statistical analysis

2.2.12.1 Cell shape and area

To determine cell shape and cell area, cells were imaged by phase contrast using a 20x Plan-Apochromat objective. The cell border was outlined manually in the program ImageJ. Afterwards, the cell shape and area were analyzed by the software. The data were presented as Box-and-Whisker plots using the OriginPro 8.6G software. Statistically significant differences between conditions ($p < 0.05$, 0.01 and 0.001) were denoted as one, two or three asterisks.

2.2.12.2 Analysis of focal adhesion distribution

To visualize focal adhesions, the marker protein vinculin was stained with a monoclonal antibody. Fluorescence images of vinculin and phase contrast images of the cells were then collected using a 40x Plan-Apochromat objective. Focal adhesions on the fluorescence images were analyzed using ImageJ. First, a brightness threshold was defined for separating focal adhesions from the background. Then, unsing the Analyze Particle Plugin, the area, length and width (by fitting of an ellipse) and the roundness (width over length) of each focal adhesion was extracted. The cell outlines were then superimposed onto the phase contrast images and the fluorescence images of vinculin to calculate the distance of each focal adhesion to the cell border. The obtained values were plotted as histograms using OriginPro 8.6G.

2.2.12.3 Topographic analysis of single podosomes

The analysis of the podosome surface was performed via a self-written script in Matlab. In high-resolution AFM images (10 nm/pixel in x-,y-direction), podosome borders were marked manually and the lowest point of the resulting enclosed area was identified. If the deepest point lay inside the podosome area and not on its border, the podosome was considered to possess an invagination, the depth and width of which were extracted.

2.2.12.4 Background subtraction for FN fibril analysis

For better visualization, the background was subtracted from fluorescence images of FN fibrils using a rolling ball function with a radius of 50 pixels. Fibril area, length and roundness were extracted using the Analyze Particles plugin. The plugin threshold for the smallest detectable FN fibril area was set to $0.04\,\mu m^2$, assuming a resolution limit of the light microscopy images of ~ 200 nm. Statistical data analysis was performed using the OriginPro 8.6G software.

3 A novel cell inversion method for visualizing cell-ECM interactions at the basal side

The following chapter is based on the publication "Inverting adherent cells for visualizing ECM interactions at the basal cell side" (Gudzenko and Franz, 2013).

3.1 Abstract

Cell-ECM interactions provide a wide range of cellular functions, including survival, migration and invasion. However, in adherent cells, these interactions occur primarily on the basal cell side, making them inaccessible to high-resolution, surface-scanning imaging techniques such as atomic force microscopy (AFM) or scanning electron microscopy (SEM). To investigate basal cell-ECM interactions, a novel cell inversion method was developed. This technique exposes the basal cell membrane for direct analysis by AFM or SEM in combination with fluorescence microscopy. In addition to single cells, complete cell layers can also be inverted with this technique and cell-cell contacts stay intact during the procedure. Likewise, cellular matrix adhesion sites, such as focal adhesions (FAs), remain intact after cell inversion and the full array of basally-associated ECM proteins is inverted together with the cell and molecular features of the ECM proteins can be investigated. To further demonstrate the versatility of the method, basal interactions of fibroblasts with fibrillar collagen I and fibronectin (FN) matrices were compared. While fibroblasts remodel the FN layer exclusively from above, they actively invade even thin collagen layers by contacting individual collagen nanofibrils both basally and apically through a network of cellular extensions. Cell-matrix entanglement coincides with enhanced cell spreading and flattening, indicating that nanoscale ECM interactions govern macroscopic changes in cell morphology. The presented cell inversion technique can therefore provide novel insight into nanoscale cell-matrix interactions at the basal cell side.

3.2 Introduction

Many cellular processes, such as proliferation, differentiation, and migration are governed by interactions between the cell and the surrounding ECM (Berrier and Yamada, 2007; Gumbiner, 1996). The interplay between cells and the ECM is complex and involves chemical and mechanical aspects. Adherent cells interact with ECM via adhesion receptors, which transmit cellular contraction forces to the ECM (Frantz et al., 2010; Wolf and Friedl, 2009) contributing to cell-induced matrix remodeling. Matrix remodeling frequently occurs on the level of individual ECM proteins (Friedrichs et al., 2007; Schwarzbauer and Sechler, 1999), while in turn cells are able to recognize and to respond to nanoscale features in their environment (Andersson et al., 2003; Biela et al., 2009; Curtis and Wilkinson, 1998; Poole et al., 2005; Teixeira et al., 2003).

Better understanding the intricate structural and functional interplay between the ECM and matrix-embedded cells is an ongoing challenge in cell biological and medical research and would benefit substantially from high-resolution images of the underlying molecular interactions. SEM yields sub-nanometer resolution images and is frequently applied to image ECM components (Engel, 1994) and cell-ECM interactions (Chen et al., 2008; Nermut, 1989). Alternatively, basal cell-matrix interactions can be investigated by transmission electron microscopy (TEM) (Fleischmajer and Timpl, 1984) or *in situ* by light microscopy. However, since conventional optical resolution is limited to $\sim 200\,\mathrm{nm}$, individual ECM proteins usually cannot be resolved unless recently-developed super-resolution microscopy techniques are used (Huang, 2010; Huang et al., 2009; Schermelleh et al., 2010). However, super-resolution light microscopy still features a limited resolution in the z-range and usually provides little information on the molecular scale about the 3D organization of membrane-associated extracellular components. AFM (Binnig et al., 1986) is increasingly becoming popular for studying cell-matrix interactions, as they can be examined with nanometer resolution in 3D under physiological conditions and even in living cells (Friedrichs et al., 2010; Lal and John, 1994). Additional advantages of this technique are the simple sample preparation protocol and non-destructive conditions during scanning. Investigating the ultrastructure of adherent cells by AFM has so far focused on the apical cell side, as it is readily accessible to the AFM tip. In contrast, the basal cell side, where the majority of cell-matrix interactions occur, is hidden underneath the cell body and has consequently been less thoroughly studied by AFM. Suitable techniques for inverting cells and exposing the basal cell membrane would therefore greatly facilitate the investigation of these processes.

Previously several protocols have been developed to expose basal cell sides for SEM imaging. In one approach, the entire cell culture substrate was dissolved from underneath a confluent cell monolayer. Arnold and Boor (Arnold and Boor, 1986), as well as Revel

and Wolken (Revel and Wolken, 1973) used plastic petri dishes for cell culture and organic solvents for substrate dissolving and cell detachment, while Singer *et al.* (Singer et al., 1989) dissolved glass cover slips in 10% hydrofluoric acid. In another approach, cells were cultured on titanium-coated silicon wafers, fixed, embedded into LR White resin and finally removed from the substrate (Goto et al., 1999; Richards et al., 1993). Since the resin also penetrates the space underneath the cells, it needs to be removed by glow discharge etching after cell inversion to expose the basal cell membrane. All of these methods use comparatively aggressive chemicals, potentially leading to structural artifacts or even wide-scale damage of the cell surface. Furthermore, these techniques are experimentally challenging and often yield low success rates. Less invasive and more reliable methods for basal cell membrane preparation are therefore desirable.

In this study, a new protocol for cell inversion was developed by significantly improving a previously described reversed cell imprinting (RCI) method (Zhou et al., 2010). The cell inversion technique allows preparing basal cell membranes for high-resolution imaging by AFM and SEM. This technique involves polymerizing an adhesive on top of adherent cells and the subsequent removal of the adhesive together with the embedded cells from the cell culture substrate. By using a silicone cell culture substrate, the adhesive together with the embedded cells can be easily peeled-off from the substrate without the use of aggressive chemicals or introducing structural damages to the cells. AFM and fluorescence images of cells before and after inversion show excellent agreement, demonstrating the high fidelity and quality of the inversion technique. Moreover, cells are transferred together with the complete set of basally-associated ECM proteins. Using the cell inversion technique, it was shown that differences in the cell spreading behavior on collagen type I and FN coincide with different mechanisms of matrix remodeling on the basal cell side, thereby providing novel insight into basal matrix remodeling processes.

3.3 Results

3.3.1 Embedding and inverting adherent cells

To expose basal plasma membranes of adherent cells for high resolution imaging by scanning microscopy techniques (AFM and SEM) the substrate-attached cells were covered with an UV-sensitive adhesive, followed by curing of the adhesive and detaching it together with the embedded cells from the cell culture substrate (Fig. 3.1B).

To demonstrate the general feasibility of this approach, human foreskin fibroblast (HFF) cells were seeded on a PDMS substrate, cultured overnight, then fixed with 4% PFA and washed with PBS. Before starting the cell inversion procedure, the region of interest was scanned by AFM, showing the topography of two cells. Then, the cells were briefly rinsed in ethanol and quickly dried in a nitrogen flow. Afterwards, the cells were overlaid with a drop of Dymax OP-29 optical adhesive, covered with a glass coverslip and exposed to UV light. Afterwards, the cured adhesive could be easily detached from the PDMS substrate by gently lifting off the coverslip.

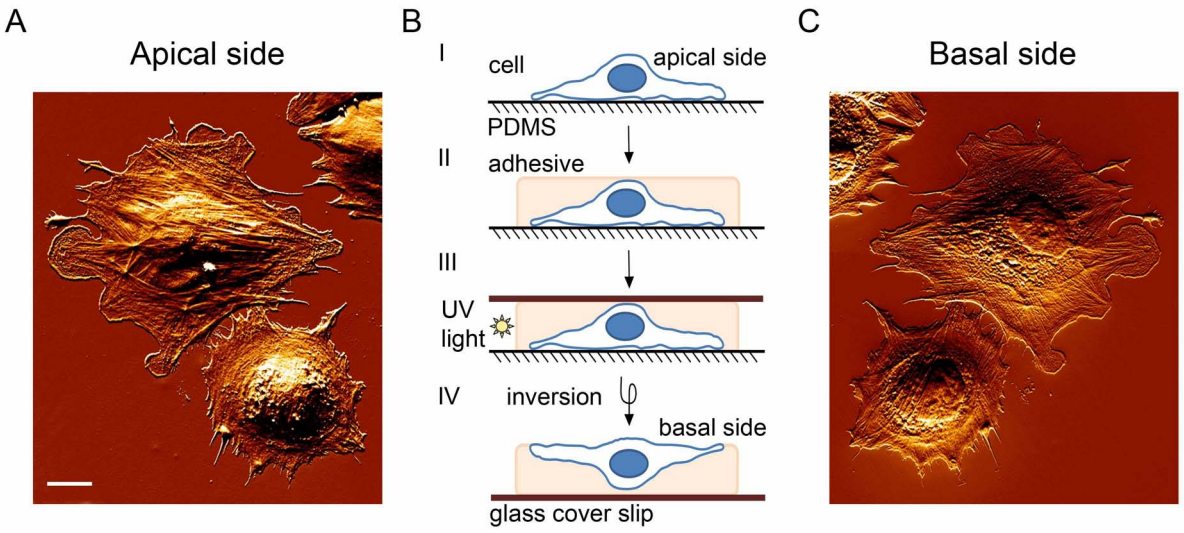

Figure 3.1: Procedure for inverting adherent cells. HFF Cells are cultured on PDMS for 16 h and fixed with 4% PFA. (A) AFM deflection image of the apical cell side before inverting. (B) For inverting, cells are briefly dried to remove excess water from the cell surface (I) and then covered with an UV adhesive (II). After applying a glass cover slip, the adhesive is cured under UV light (III). Afterwards, the glass coverslip together with the adhesive and the embedded cells is lifted off from the PDMS substrate and inverted (IV), exposing the basal cell side. (C) The same group of cells shown in (A) rescanned from the basal side. Scale bar 20 µm.

Inverted cell samples were transferred to PBS buffer and the cell morphology after inversion was examined again by AFM scanning. Comparison of AFM scans of the same sample

region before and after inversion shows excellent agreement of the same group of cells indicating complete cell transfer and maintenance of overall cell architecture (Fig. 3.1A and C). Moreover, the AFM images show that the adhesive did not fracture, deform or shrink after curing, and cells had an identical spread area before and after inversion. Inverted cells displayed an intricate network of fine cytoskeletal structures bulging against the basal cell membrane. Also, the position of the nucleus could be identified in the cells (Fig. 3.1C).

3.3.2 Validation of cell transfer after inversion

The excellent agreement of AFM contact mode scans of the same group of cells performed before and after inversion suggested complete cell transfer during inversion (Fig. 3.1A and C). Nevertheless, obtaining reliable, high-resolution structural information about the basal cell membrane requires that the entire cell remains intact during the inversion procedure, including potentially fragile membranous structures. The inversion protocol should also ensure that all cells on a cell culture substrate, not just the most weakly adhering cells, are inverted to provide a representative view on the full range of cell-matrix interactions within a particular cell culture sample. Furthermore, a complete and non-destructive inversion of the whole cell layer would facilitate re-locating individual cells after inversion so that the same cell can be imaged from both the apical before and the basal side after inversion.

To verify complete cell transfer from the PDMS surface into the adhesive, HFF cells were labeled with CellTracker Green, a fluorescent live-cell staining reagent seeded on PDMS and fixed. Phase contrast and fluorescence images of the cell sheet were taken before and after the inversion procedure. Before inversion, HFF cells were uniformly distributed on the substrate (Fig. 3.2A). Adding the adhesive and the subsequent UV-curing step did not affect cell arrangement. To determine the efficiency of the cell transfer into the adhesive, the border of the area covered by the adhesive was imaged, which appeared slightly darker in phase contrast images (Fig. 3.2B). The UV adhesive did not noticeably degrade the fluorescence image quality, demonstrating its excellent optical properties, in particular the absence of autofluorescence. After removing the glass coverslip together with the adhesive from the substrate, both, phase contrast and fluorescence images demonstrate complete cell denuding of the PDMS surface originally covered by the adhesive. Furthermore, the absence of CellTracker fluorescence signals in this area indicated that cells do not disintegrate during detachment and inversion. Likewise, AFM scanning of the cell-free substrate revealed flat, featureless surfaces, confirming complete cell removal from the substrate.

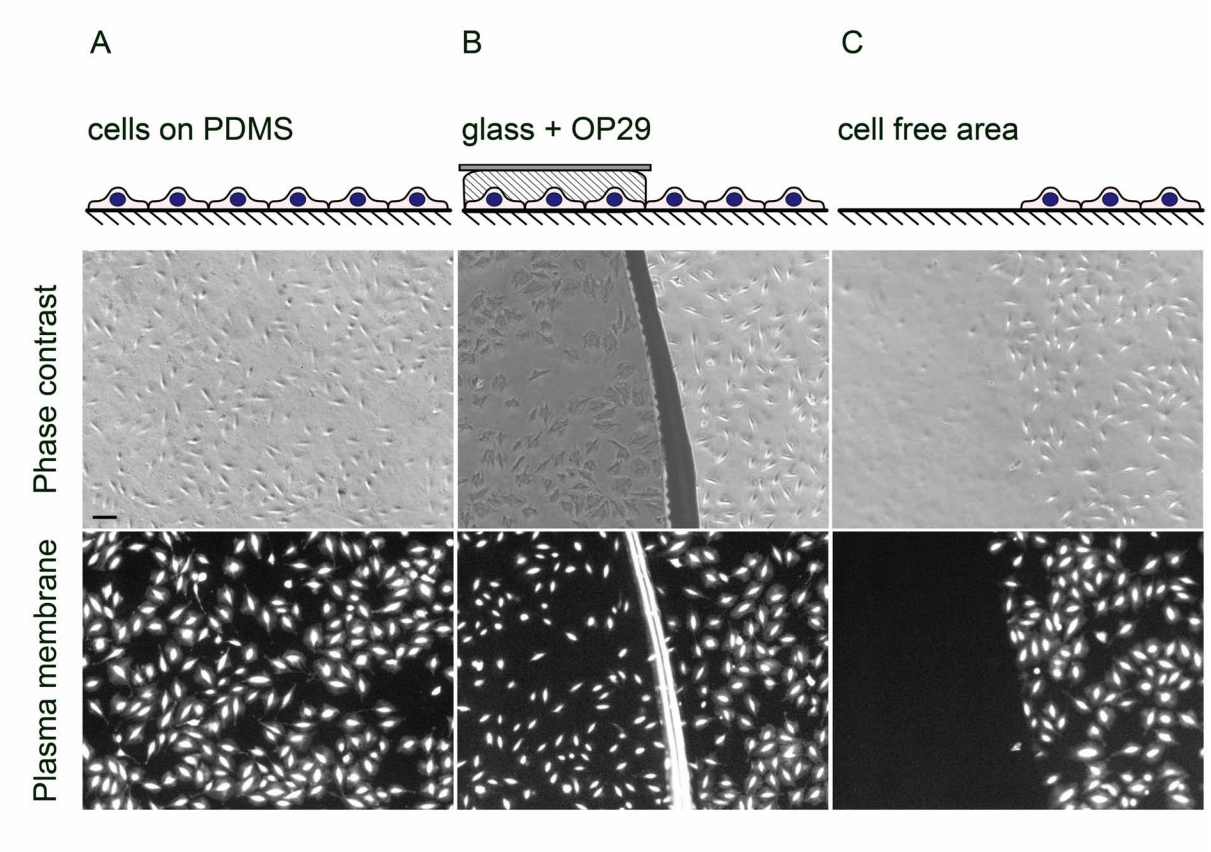

Figure 3.2: Verifying the efficiency of the inversion method. HFF cells were cultured on PDMS, stained with CellTracker Green and fixed. Representative phase contrast and fluorescence images of cells on the PDMS substrate taken before (A), during (B) and after inversion(C). In (B), the area covered by the UV adhesive corresponds to the darker region on the left side of the phase contrast image. Removing the cover slip from the PDMS surface produces a cell-free area on the left side of the images (C). The absence of fluorescence staining in this area confirms the complete transfer of intact cells and demonstrates the efficiency of the method. Scale bar 200 µm.

To demonstrate that cells are transferred together with their FAs, rat embryonic fibroblasts (REF52) stably expressing YFP-Paxillin as a FA marker (Turner et al., 1990) were inverted. FA arrangement and the relative fluorescence intensities of the contacts stayed unchanged (Fig. 3.3) after inversion. The resolution of FAs imaged with an inverted light microscope after inversion was superior due to better optical properties of the adhesive compared to the PDMS substrate.

For a more accurate verification of the integrity of the cell, AFM scans and fluorescence images of the same cell from the apical side before and from the basal after inversion were performed. The scans demonstrate that the inverted cells have undamaged membranes including the membrane-associated adhesion complexes, while the fluorescence images proof that the quantity and location of FAs stays the same (Fig. 3.4).

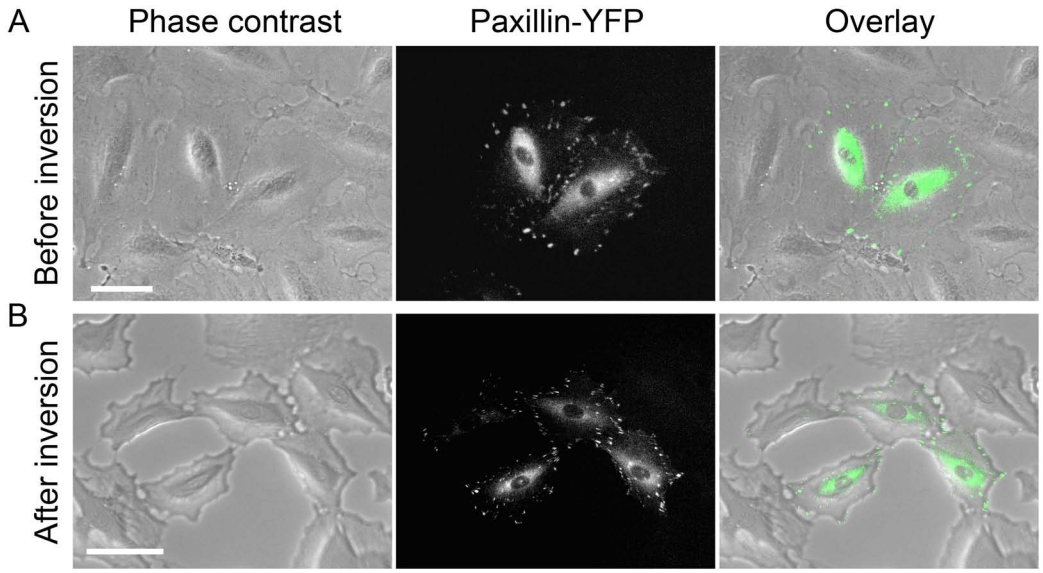

Figure 3.3: Demonstration of FA transfer after inversion. Phase contrast (left), fluorescence image (middle) and its overlay (right) of REF52 YFP-Paxillin expressing cells shows a transfer of whole cells including their FAs. Scale bar 20 µm.

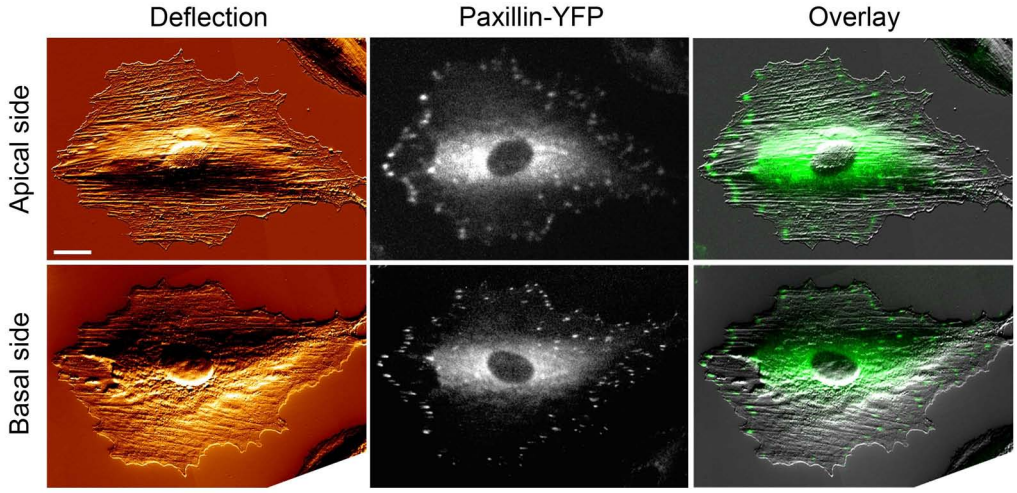

Figure 3.4: Comparison of FAs of one and the same cell before and after inversion. AFM deflection (left), fluorescence (middle panels) and AFM/fluorescence overlay (right) images show the apical (top panels) and the basal (bottom panels) side of a REF52-Paxillin-YFP cell. In the fluorescence images, paxillin localization visualizes FAs. FAs imaged with an inverted fluorescence microscope from the apical side are better resolved due to superior optical properties of the UV adhesive in comparison to PDMS. Scale bar 20 µm.

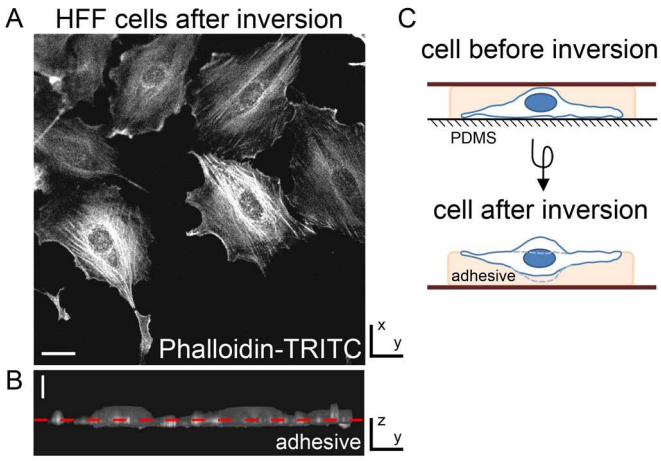

Figure 3.5: Verification of the cell shape after inversion. Fixed HFF cells were stained with phalloidin-TRITC, inverted and imaged with a confocal microscope. The x-y cross-section (A) and the y-z plane (B) are shown. The central cell region is bulging, while the cell periphery remains flat. Scale bars 20 µm (A), 5 µm (B). (C) Schematic of the cell inversion procedure. The cell is completely embedded into the adhesive before inversion. After exposing the adhesive with UV light and inverting the cells, the region at the cell center extends above the plane of the adhesive top surface, indicated by the dotted line.

Remarkably, AFM scans of inverted cells sometimes showed an upward bulging of the central cell region above the plane of the adhesive, while the cell edges remained rather flat (Fig. 3.4). The schematic draw of cell inversion (Fig. 3.1) shows that the cell body after inversion is embedded into cured adhesive. To verify the cell shape inside the adhesive after inversion, the HFF cells were cultured on PDMS until spreading and fixed with 4% PFA. The actin cytoskeleton was stained with phalloidin-TRITC. Afterwards, the cells were inverted and imaged with a confocal microscope. This type of microscope allows imaging the region of interest at several layers along the z-direction creating a z-stack and therefore providing an insight into the cell shape inside the adhesive (Fig. 3.5B). The z-y cross-section shows cells with a bulged central region and flat regions at the cell periphery like in AFM scans. Furthermore, the cell regions embedded into adhesive are rather flat and do not contain the whole cell body inside, indicating that it was pushed out during polymerization of the adhesive. Nevertheless, the shape of the structures at the cell periphery stays unchanged, and the method is therefore very suited for studying cell adhesion structures, e.g. FAs or podosomes.

3.3.3 Inverting cell-sheets

As shown in Section 3.3.2, single cells or groups of non-connected cells can be inverted with a high success rate. It was also tested whether larger groups of connected cells

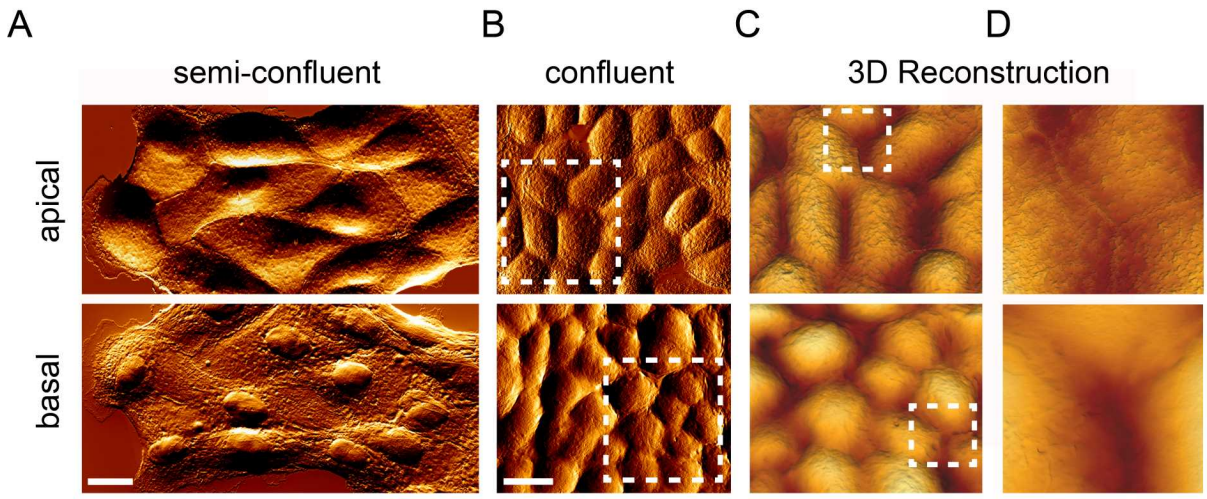

Figure 3.6: Inverting semi-confluent and confluent cell layer of MDCK cells. (A) A semi-confluent and (B) confluent cell layer was scanned by AFM from its apical and basal side. (C) 3D reconstructions were generated from the region marked with a white dotted box in (B). (D) A magnified 3D reconstruction image of the region marked by the white box white box in (C) showing cell-cell contacts before and after inversion. Scale bar 20 µm.

or even small cell colonies can also be inverted together. Madin-Darby canine kidney (MDCK) cells, an epithelial cell line known for forming extensive cell-cell junctions, were cultured on PDMS at different confluences (semi-confluent at 100 cells/mm^2 and confluent at 500 cells/mm^2) for 16 h. In contrast to fibroblasts, MDCK cells establish contiguous cell-cell contacts with neighboring cells, creating a dense cell sheet. Before inversion, both semi and fully confluent cell layers were scanned by AFM (Fig. 3.6A and B, upper row). As expected, the less dense cell layer contained well-spread, rather flat cells (max. height $\sim$1.5 - 2 µm, Fig. 3.6A, top row), while at higher seeding density cells have limited spreading space available and therefore extend further into the vertical direction (max. height $\sim$ 5 - 6 µm). The same regions scanned from the apical side were also scanned from the basal cell side (Fig. 3.6A and B, lower row), showing that the layer integrity is preserved after cell inversion. Likewise, scans of a region containing cell-cell contacts at even higher magnification indicate no structural damage (Fig. 3.6D).

3.3.4 Investigating cell-ECM interactions at the basal cell side

On planar tissue culture surfaces cells basally interact with the underlying ECM, leading to nanoscale rearrangements of individual ECM molecules. Investigating these cell-ECM interactions in inverted cells requires that the ECM macromolecules are transferred together with the inverted cells. To monitor the degree of matrix transfer, PDMS was coated with plasma FN fluorescently-labeled with AlexaFluor® 488 (FN-AF488) and incubated

HFF cells on this coating for 24 h. Before and after inversion, cells and FN were imaged by phase contrast and fluorescence microscopy and scanned with AFM. Merged phase contrast and fluorescence overview images of larger groups of cells (Fig. 3.7A) revealed extensive reorganization of FN into large, brightly-stained areas. The overall organization of these macroscopic patches was well preserved after inverting cells, demonstrating the complete transfer of the extracellular FN matrix together with the cells. Comparing the mirror-images of the FN patches also helped relocating individual cells on the inverted samples. Higher magnification fluorescence images of individual cells revealed a much finer level of FN fibril reorganization occurring below cells. Basal FN fibrils frequently assumed a zigzag pattern along the cell periphery. In contrast, in the cell vicinity, FN was often completely removed from the substrate, indicated by a complete absence of the fluorescence signal. Again, fluorescence imaging of FN structures before and after inversion yielded largely identical results (Fig. 3.7B). To prove basal localization of the FN fibrils, FN-rich region on the basal cell side by AFM was scanned and the obtained topography (Fig. 3.7C) was overlaid with the corresponding fluorescence image of FN (Fig. 3.7E). The high-resolution AFM image clearly resolved the FN fibrils at the cell basal side and revealed the same zigzag pattern consisting of thin FN fibrils (Fig. 3.7D). Height profiles generated along cross sections of several FN fibrils displayed a typical height of $\sim$20 - 80 nm (Fig. 3.7F).

3.3.5 Nanoscale differences in matrix remodeling affect cell spreading

To investigate whether cells remodel different ECM matrix proteins differently at the basal cell membrane, HFF cells were cultured on FN or collagen-coated glass for four hours and fixed. AFM scans of HFF cells on FN (Fig. 3.8A) suggested that cells grow exclusively on top of the FN coating, indicated by the absence of fibrillar structures crossing over the apical side of cells. In contrast, cells on collagen displayed numerous collagen fibrils apparently extending over the apical cell surface (Fig. 3.8B), indicating that cells had partly invaded the 2D matrix.

To test whether these differences in matrix interaction coincided with changes in cell morphology, the cell spreading area was analyzed by taking phase contrast light microscopy images after four hours of culture. The HFF mean spreading area was significantly larger on collagen ($5683 \pm 1922\,\mu m^2$) than on FN ($4859 \pm 1610\,\mu m^2$, Fig. 3.9B). Furthermore, analyzing AFM height images generated from the same samples revealed that increased spreading on collagen correlated with a decrease in cell height ($2.03 \pm 0.28\,\mu m$) compared to cells spreading on FN ($3.08 \pm 0.62\,\mu m$, Fig. 3.8D). Thus, collagen matrix intertwining coincided with increased cell spreading and flattening.

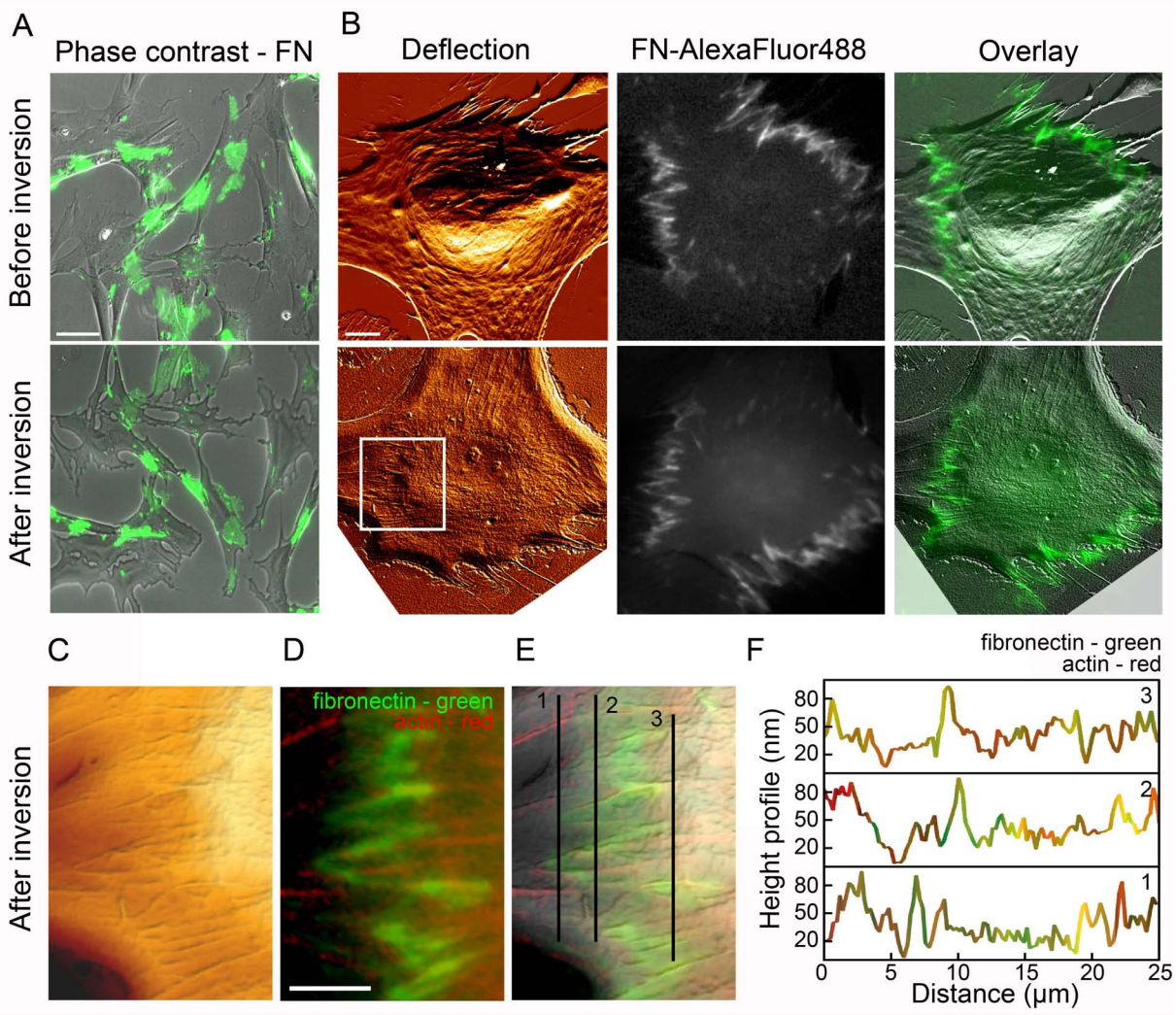

Figure 3.7: Imaging basal FN arrangement with high resolution. (A) HFF cells were incubated overnight on FN-AF488 (green). The FN arrangement after inversion mirrors the original arrangement, demonstrating complete ECM transfer. Scale bar 50 µm. (B) AFM deflection, fluorescence and overlay images of a single representative cell from its apical and basal side visualizes the FN fibril arrangement in detail. Scale bar 10 µm. (C) A 3D reconstruction of a high-resolution AFM height image (not shown) of the area marked by the white box in (B). (D) Overlay image of FN fibrils distributed at the basal cell side and the actin cytoskeleton labeled with phalloidin-TRITC. Scale bar 10 µm. (E) Overlay of the 3D reconstruction and the fluorescence image shows good overall correlation between topography, and FN fibrils and actin stress fiber location. (F) Height profiles along the cross sections indicated in (E) perpendicular to actin stress fibers and FN fibrils overlaid with the corresponding fluorescence intensities (green for FN and red for actin) for a better representation of the affiliation of profile peaks and fluorescence intensities.

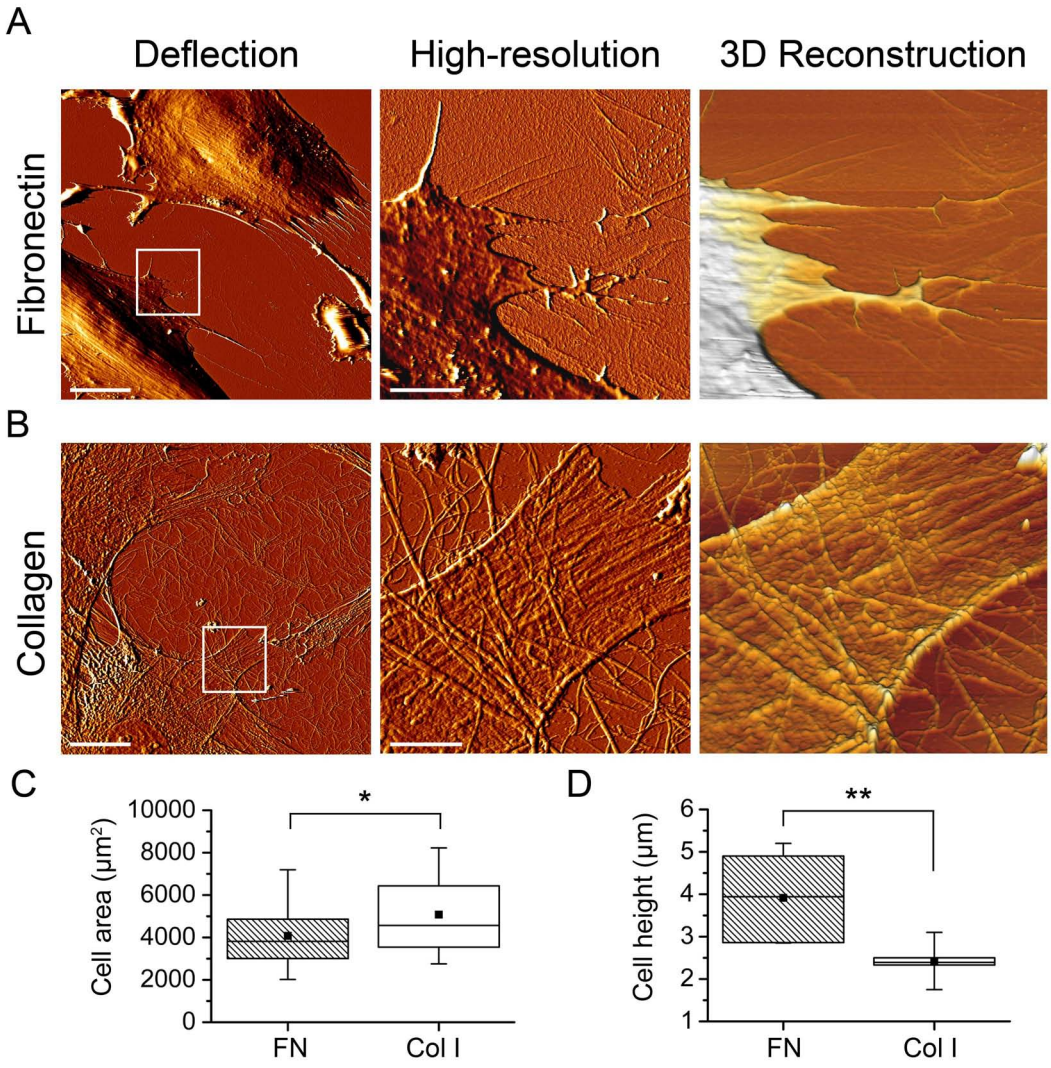

Figure 3.8: Comparing the nanoscale rearrangement of collagen and FN matrices by HFF cells. AFM deflection and 3D reconstruction images show the apical side of HFF cells cultured on glass coated with FN (A) or collagen type I fibrils (B). On the higher resolution scans (A and B, middle panels) of the regions indicated by the white boxes (left panels), collagen fibrils extending above cells are visible, while FN fibrils are completely restricted to the basal cell side. Scale bars 20 µm (left panel) or 5 µm (middle panel). Box-and-Whisker-plot of HFF cell area (B) and cell height (C) on collagen or FN. Statistically significant differences between different conditions ($p < 0.01$, 0.001) are denoted by one and two asterisks, respectively.

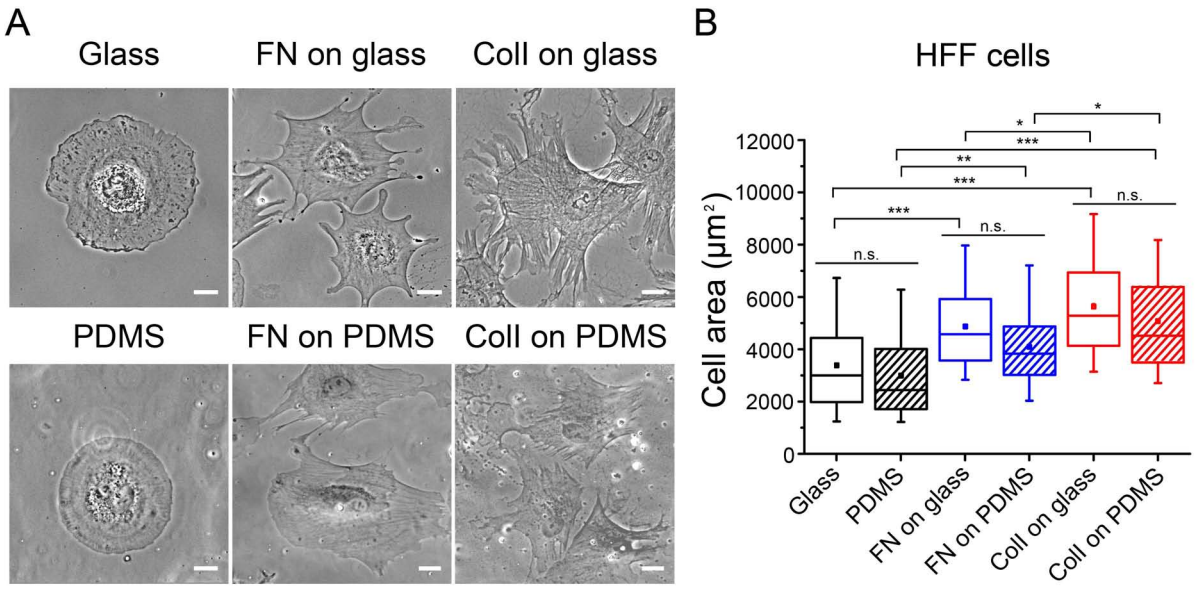

Figure 3.9: Spreading behavior of HFF cells cultured on uncoated glass and PDMS, or on glass and PDMS coated with FN or collagen type I fibrils. (B) Median spread areas of more than 100 cells per condition are displayed in Box-and-Whisker-plots. Statistically significant differences between different conditions ($p < 0.05$, 0.01, 0.001) are denoted by one, two and three asterisks, respectively. Scale bar 20 µm.

To investigate basal matrix remodeling and entanglement with collagen fibrils in more detail, HFF cells were grown on collagen-coated PDMS for four hours and individual cells were imaged with AFM before and after inversion (Fig. 3.10A and B). In these experiments collagen fibrils were covalently bound to the PDMS substrate to improve cell attachment and spreading in comparison to collagen coatings using hydrophobic or electrostatic interactions (Wipff et al., 2009). The good agreement of apical and basal images made it possible to relocate individual collagen fibrils and to track them across the apical and basal cell side (Fig. 3.10A and B). Many fibrils showed alternating basal and apical localization, indicating a high degree of cell-matrix intertwining. Thus, fibroblasts had remodeled the flat and thin collagen layer into a complex, semi-3D network. High-resolution AFM imaging of basally located collagen fibrils (Fig. 3.10C) also revealed the characteristic 67 nm periodic D-band resulting from the staggered array of collagen building blocks. This demonstrated that the molecular structure of collagen fibrils is preserved during the inverting process and that it can be analyzed with nanometer-range resolution in inverted cells.

Finally, the collagen matrix remodeling was analyzed after inversion by SEM. HFF cells were cultured on a collagen-FITC fibril matrix, fixed, stained with phalloidin-TRITC to visualize the actin cytoskeleton and inverted. After collecting phase contrast and fluo-

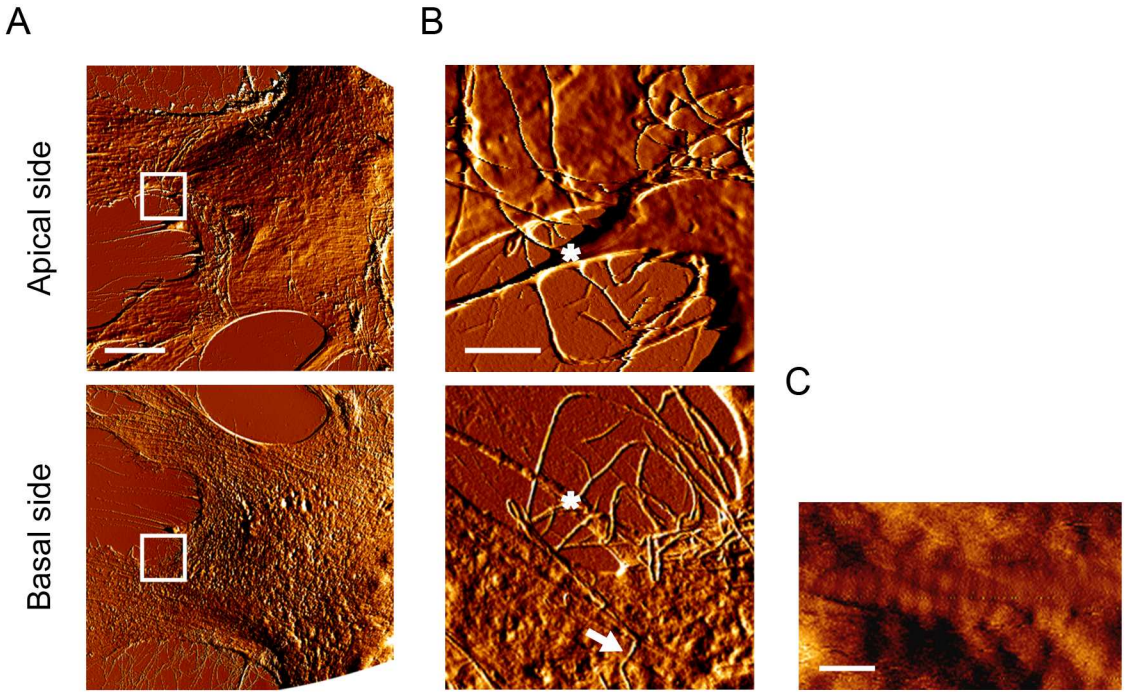

Figure 3.10: Comparing the nanoscale rearrangement of collagen type I fibrils at the apical and basal side of HFF cells. (A) Deflection images of the apical and basal side of the same HFF cell incubated on PDMS coated with collagen type I fibrils. (B) The region marked with white box in (A) was imaged at higher magnification, showing Individual collagen fibrils extending above as well as below the same cellular extension (white asterisks). (C) In a higher magnification image of an area indicated by the white arrow in (B), the characteristic 67 nm collagen D-banding is visible, demonstrating that the collagen ultrastructure is undamaged after inversion. Scale bars in 20 µm (A), 3 µm (B), 200 nm (E).

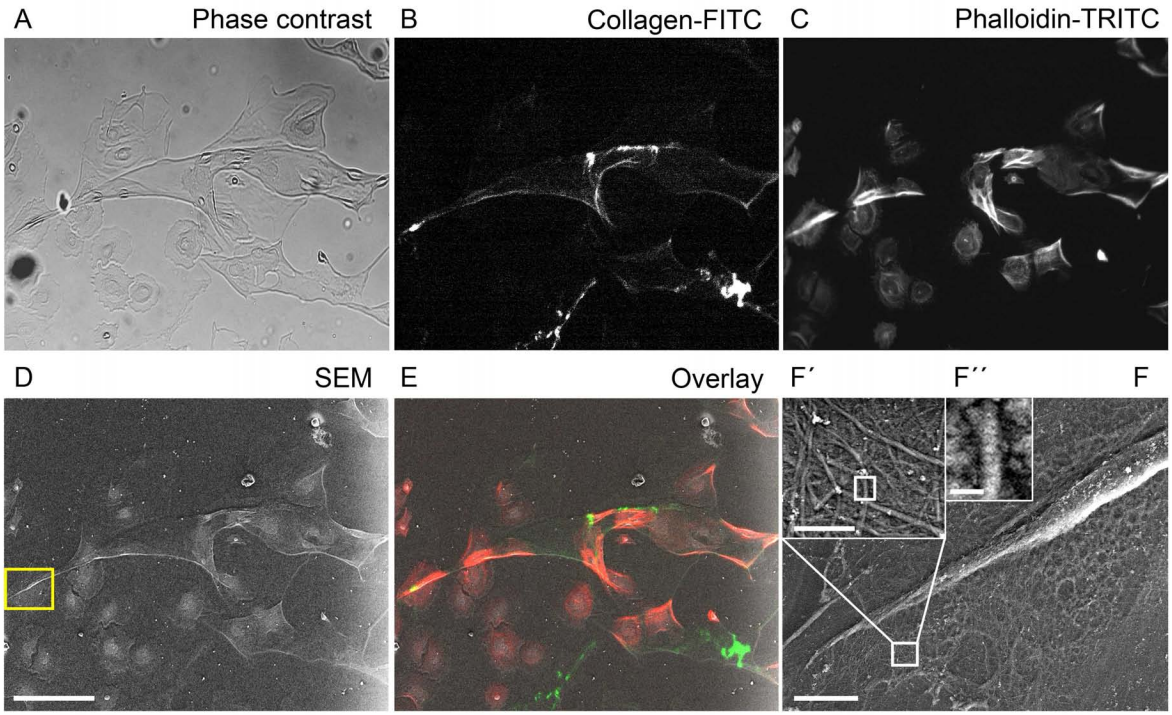

Figure 3.11: Localization of collagen type I fibrils on the basal cell side. Phase contrast (A) and fluorescence images of collagen fibrils (B) and the actin cytoskeleton of the HFF cells (C) taken before inversion. (D) The same region as in (A) imaged by SEM after inversion. (E) Overlay of fluorescence images of F-actin (red) and collagen (green) and the SEM image. (F) Higher magnification of the region marked by the yellow box in (D). To monitor collagen fibril structure on the basal cell side, higher magnification images were recorded (F′, F″) showing typical collagen 67 nm D-band. Scale bars 100 µm (D), 10 µm (F), 1 µm (F′), 200 nm (F″).

rescence images (Fig. 3.11A-C), the sample was dehydrated, critical point-dried, coated with platinum and imaged with SEM (Fig. 3.11D). The good correspondence between SEM and fluorescence images (Fig. 3.11E) indicated that cells and collagen matrix were not destroyed or deformed by the preparation procedure. Moreover, higher magnification of the collagen matrix associated with the basal cell side (Fig. 3.11F′ and F″) demonstrates preservation of the collagen fibril ultrastructure indicated by the presence of the 67 nm periodic D-band. The preservation of this nanoscale-feature again demonstrates the suitability of our cell inversion technique for high-resolution imaging of basal cell sides, including cell-associated matrix proteins.

3.4 Discussion

3.4.1 Cell inversion protocol

This chapter describes a new cell inversion protocol for investigating the basal cell surface with high resolution scanning microscopy techniques, such as AFM and SEM. The introduced method has several important advantages over previous protocols described in the literature (Arnold and Boor, 1986; Goto et al., 1999; Revel and Wolken, 1973; Richards et al., 1993; Singer et al., 1989). In contrast to other methods exposing the basal cell side for investigation (Arnold and Boor, 1986; Goto et al., 1999; Revel and Wolken, 1973; Richards et al., 1993; Singer et al., 1989), this method does not require any aggressive chemicals. Instead, an UV-adhesive is used to glue the cells to a glass cover slip. Advantages of the one-component adhesive are favorable optical properties, including an index of refraction similar to glass ($n = 1.5$), its high transparency and low autofluorescence. Furthermore, the adhesive polymerizes in seconds by exposing it with UV-light and displays low shrinkage ($< 1\%$) and low water adsorption during curing. Also after cell inversion no fracture or deformation of the adhesive could be observed. Using an elastic PDMS polymer as cell substrate is crucial as the adhesive cannot be removed from stiff glass or tissue culture plastic surfaces due to strong bonding to these surfaces. PDMS is biocompatible and a suitable substrate for culturing different mammalian cell types (Bélanger and Marois, 2001; Chen et al., 2008; Lee et al., 2004). However, freshly polymerized PDMS is hydrophobic, while efficient cell spreading and growth generally benefit from hydrophilic surfaces (Kottke-Marchant et al., 1996). After rendering the PDMS hydrophilic by oxygen plasma treatment (Lee et al., 2004), HFF cell spreading was comparable to that on glass surfaces (Fig. 3.9). Additional advantage of the adhesive is that after inversion the adhesive did not fracture, deform or shrink after curing, and cells had an identical spread area before and after inversion, that was shown by AFM imaging of the same cell (Fig. 3.1A and C).

In this protocol cells are initially fixed and shortly dried. Importantly, phase contrast and AFM images demonstrate that the drying step does not introduce obvious structural damage to the cells. However, AFM scans of inverted cells sometimes showed an upward bulging of the central cell region above the plane of the adhesive, while the cell edges remained rather flat. Both dry and re-hydrated samples displayed a similar degree of bulging, ruling out cell swelling after hydration as the responsible mechanism. Bulging of the basal cell membrane was also observed by Zhou *et al.* (Zhou et al., 2010), which the authors attributed to the comparatively low stiffness and the visco-elastic properties of fixed cells, so that cell is deformed while being pulled from the substrate. However, a 3D reconstruction of confocal image stacks of phalloidin-stained inverted HFF cells

(Fig. 3.5B) demonstrates that after removal from the PDMS substrate the cured adhesive assumes a nearly-planar surface even in the region of the embedded cells, possibly due to surface tension. As a result, the inverted cells are pushed outwards and partially extend above the surface of the adhesive, rather than being fully embedded. As the cell body is pushed upwards to the greatest extent in the cell center, the bulging effect should be taken into account when quantifying height differences in this area. In contrast, the bulging effect is small within the extremely flat cell periphery, which typically measured $\sim 200\,\text{nm}$ in height. Here, relative height differences between neighboring structures are not significantly affected, making the inversion method suitable for studying cell adhesion sites, for instance.

3.4.2 Investigating cell adhesion sites after inversion

Cells interact with extracellular substrates primarily via integrin-containing FAs (Burridge and Chrzanowska-Wodnicka, 1996; Wozniak et al., 2004). These specialized cell-substrate contact points constitute the strongest cell attachment areas and frequently remain behind after cell detachment using, for instance, hydrodynamic shear (Ziegler et al., 1998) or sonication (Franz and Muller, 2005). FA arrangement and the relative fluorescence intensities of the contacts were unchanged after inversion. Moreover, the resolution of FAs imaged with an inverted light microscope after inversion was superior due to better optical properties of the adhesive compared to the PDMS substrate.

3.4.3 Investigating ECM after cell inversion

The investigation of cell-ECM interactions at the basal cell side was performed on FN and collagen substrate. Cells bind dimeric plasma FN and reorganize them into long FN fibrils as a result of cellular pulling forces (Mao and Schwarzbauer, 2005a; Schwarzbauer and Sechler, 1999). The inversion protocol strictly requires using PDMS instead of glass or tissue culture plastic as the substrate. However, the initial conformation of the FN molecule depends on the substrate chemistry to which it is attached. For instance, on hydrophobic surfaces FN assumes a compact or semi-compact conformation (Bergkvist et al., 2003; Erickson and Carrell, 1983; Pitt et al., 1987), whereas FN assumes an elongated conformation on glass or hydrophilic PDMS (Bergkvist et al., 2003; Erickson and Carrell, 1983). The elongated conformation is more favorable for cell attachment, spreading and proliferation (Chen et al., 2008; García et al., 1999; Grinnell and Feld, 1981). Furthermore, the PDMS substrate may have an influence on the creation of fibrillar FN structure. The fluorescence images show that on PDMS rendered hydrophilic by plasma treatment before FN coating HFF cells are able to remodel FN into fibrils (Fig. 3.9B), similar to what has

been observed on glass surfaces (Mao and Schwarzbauer, 2005a). However, the fibril ultrastructure might still be dependent on the substrate.

Previously, FN fibrillogenesis has been mainly studied by fluorescence microscopy using labeled FN. However, the size of the smallest FN fibrils is well below the diffraction limit of optical microscopy of $\sim 200\,\text{nm}$. As a result, these small FN fibrils cannot be resolved by conventional fluorescence microscopy. Here, AFM proves to be an especially valuable tool for analyzing the arrangement of complete FN network including FN nanofibrils.

While investigating FN fibrils on the basal cell side after inversion, some structures in the same height range were observed that did not co-localize with stained FN (Fig. 3.9F) but with phalloidin-TRITC co-stained F-actin (Fig. 3.9D-F). Cell membranes are relatively pliable compared to stiff submembraneous actin structures, such as FAs or cortical actin stress fibers, which then push against the cell membrane form the cell interior. The actin-rich ridge structures therefore likely correspond to membrane impressions of intracellular actin filaments (Fig. 3.9D). Unequivocally attributing cell membrane features to subcellular ECM components may therefore require fluorescently-labeling both cytoskeletal and matrix components and overlaying AFM topographs with the fluorescence images to distinguish between ECM and cellular structures (Fig. 3.9E).

3.4.4 Investigating invasion into collagen type I fibrils by fibroblasts

In contrast to FN, culturing cells on planar collagen type I fibrils shows a matrix invasion effect, where the cells penetrate into the ECM layer. Given the extensive collagen nanofibril entanglement, even cells growing on 2D collagen coatings may receive structural and chemical signals from the environment similar to cells partially or fully embedded in 3D collagen matrices (Fraley et al., 2010). Such potential 3D aspects of adhesion may thus need to be considered when interpreting results obtained on nominally 2D coatings. The functional significance of strong cell-matrix entanglement seen on collagen matrices is not entirely clear. Fibroblast migration on 2D substrates usually involves repeated cycles of lamellipodial extension, attachment, translocation of the cell body and retraction of the cell rear (Ridley et al., 2003). However, cells migrating on collagen substrates have been observed to translocate individual collagen fibrils across the cell body by forming membrane protrusions along fibrils and retracting them in a so called “hand-over-hand” mechanism (Meshel et al., 2005). A similar process of cellular extension along collagen fibrils and subsequent cell retraction has been observed on cells adhering to thin collagen sheets (Friedrichs et al., 2007). The contribution of fibril translocation to cell migration on two-dimensional or in three-dimensional collagen networks is not fully understood. Nevertheless, alternating cycles of extension and retraction appear to help cells inserting these protrusions into the collagen network to maximize traction.

3.5 Conclusions

The novel cell inversion protocol described here opens the door for high-resolution imaging of basal cell surfaces, including nanoscale cell-matrix interactions. This technique has several important advantages: (1) The preparation protocol is fast and efficient. (2) The inversion procedure does not damage the cell or cell membrane and the adhesive does not penetrate the space underneath the cell. (3) The basal cell side can be imaged by surface sensitive imaging techniques, such as AFM or SEM. (4) Due to the optical properties of the embedding adhesive, it is possible to use fluorescence labeling to locate specific cellular structures, such as ECM or cytoskeletal proteins, in corresponding high-resolution AFM or SEM scans. (5) The inversion method is suitable for investigating different cellular structures, such as podosomes, providing new insight about their possible functions. (6) Single cells, as well as cell layers, can be inverted even together with the underlying matrix coat, providing a unique nanoscale look at basal cell-ECM interactions. Using the described cell inversion technique, basal interactions of fibroblasts with fibrillar collagen and FN matrices were compared. It was demonstrated that nanoscale differences in matrix remodeling may lead to macroscopic changes in cell morphology. In future, the presented inversion technique could easily be extended to investigate other cell membrane compartments, such as cellular adhesion sites or processes related to endo- and exocytosis, thereby providing additional insight into the ultrastructure of the basal membrane of adherent cells.

4 Investigating the basal side of podosomes

4.1 Abstract

Podosomes are dot-like adhesion structures primarily found in cells of monocytic lineage, where they play an active role in matrix degradation. They consist of an F-actin core ($\sim 1\,\mu m$ diameter) surrounded by additional adhesion proteins. It has been previously was proposed that podosomes may contain a channel in the center of the actin core to facilitate enzyme secretion, but the existence of a central channel has not been conclusively demonstrated. Here, podosome structure was investigated using a cell inversion technique, exposing the basal cell side to high-resolution imaging by SEM and AFM in combination with fluorescence microscopy. AFM height images show that about 50% of investigated podosomes possess a membrane depression at their basal side with a diameter and depth ranging between 80 and 320 nm and between 6 and 24 nm, respectively. The presence and the diameter of these depressions were also confirmed by SEM imaging. These results support the idea of a central membrane channel in podosomes.

4.2 Introduction

Cell-ECM interactions occur at the basal membrane side and they are therefore usually inaccessible to investigation by high resolution scanning microscopy techniques. However, the cell inversion method (Chapter 3) allows exposing the basal cell side with cell adhesion structures staying intact. In this chapter the cell inversion method was used to study the basal surface structure of podosomes. Podosomes are dot-like ($\sim 1\,\mu m$ diameter) adhesions first found in cells of monocytic lineage, including macrophages (Lehto et al., 1982), osteoclasts (Marchisio et al., 1984) and dendritic cells (Burns et al., 2001). Podosome formation can also be induced in other cell types, including smooth muscle and endothelial cells (Linder and Kopp, 2005). Podosomes are involved in cell adhesion, migration and they are also responsible for degrading the underlying ECM substrate. Substrate degradation occurs directly below podosomes, suggesting that podosomes may be points of protease secretion. However, the mechanisms behind this process are not well understood (Murphy and Courtneidge, 2011). Podosomes consist of an F-actin core with a column structure oriented perpendicularly to the substrate. The core is surrounded by a ring structure containing integrin receptors and focal adhesion proteins, such as vinculin or talin (Bowden et al., 1999; Gaidano et al., 1990; Pfaff and Jurdic, 2001) (Fig. 1.9). The podosomes are dynamic structures. During osteoclast differentiation, single podosomes cluster and fuse together forming small podosome rings. These rings continue to fuse and create a large podosome ring along the cell periphery. Podosomes in mature osteoclasts seeded on bone substrate create an even denser ring, called the sealing zone. Early TEM studies of chondrocytes transformed with the Rous sarcoma virus demonstrate a tubular channel and a membrane invagination within the F-actin core (Nitsch et al., 1989). This supports the hypothesis that podosomes may contain a pipeline for enzyme secretion. However, TEM images of podosomes in dendritic cells do not show similar membrane invaginations (Gawden-Bone et al., 2010). Furthermore, images of podosomes obtained by 3D structured illumination microscopy (SIM) have provided data about the spatial distribution of actin and vinculin. SIM images demonstrate that the actin core has a rather condense structure without internal channel structures (Gawden-Bone et al., 2010). On the other hand, SEM images have revealed occasional concavities at the cytoplasmic peak of podosomes (Luxenburg et al., 2007), which may indicate the terminus of a central channel. Thus, studies of podosome ultrastructure have provided partially contradictory results. Here, the cell inversion method was used in combination with AFM and SEM to investigate the possible existence of a central channel and membrane invaginations at the basal surface of the podosomes.

4.3 Results

4.3.1 Differentiated RAW264.7 cells form functional podosomes

Podosome structure was investigated in osteoclast cells. This cell type is responsible for bone degradation and is known to form multiple podosomes (Marchisio et al., 1984). To induce differentiation of osteoclasts precursors into mature osteoclasts and to promote podosome formation, RAW264.7 cells were incubated for 6 days in presence of the soluble cytokines Receptor Activator of NFκB Ligand (RANK-L; 50 ng/ml) and Macrophage Colony Stimulating Factor (M-CSF; 50 ng/ml). These cytokines bind to receptors of osteoclast precursor cells, leading to osteoclast maturation (Lacey et al., 1998). As a result, cells differentiate into large ($\varnothing \sim 100$ - 200 µm) multinuclear osteoclasts (Nijweide et al., 1986) containing a large number of podosomes.

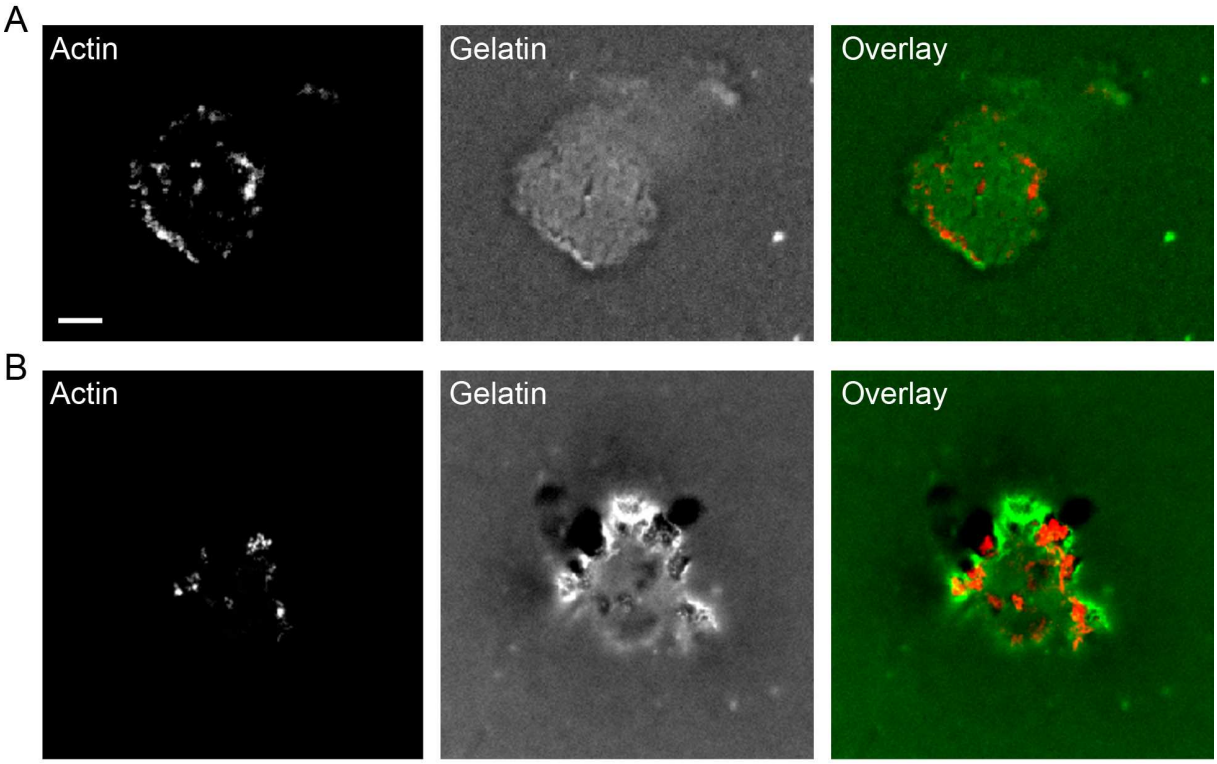

Figure 4.1: Degradation of gelatin-FITC by podosomes of osteoclasts cells. Cells were incubated on gelatin for 2 h (A) or 4 h (B), fixed and stained for F-actin with phalloidin-TRITC. Gelatin-FITC free regions are represented by black areas (middle column) and agree well with podosome location (overlay images). Scale bar: 30 µm.

Podosomes are formed at the basal cell surface (Linder, 2007) of different cell types (Burns et al., 2001; Lehto et al., 1982; Marchisio et al., 1984). In macrophages and smooth muscle cells it has been observed that the ECM is degraded only strictly below

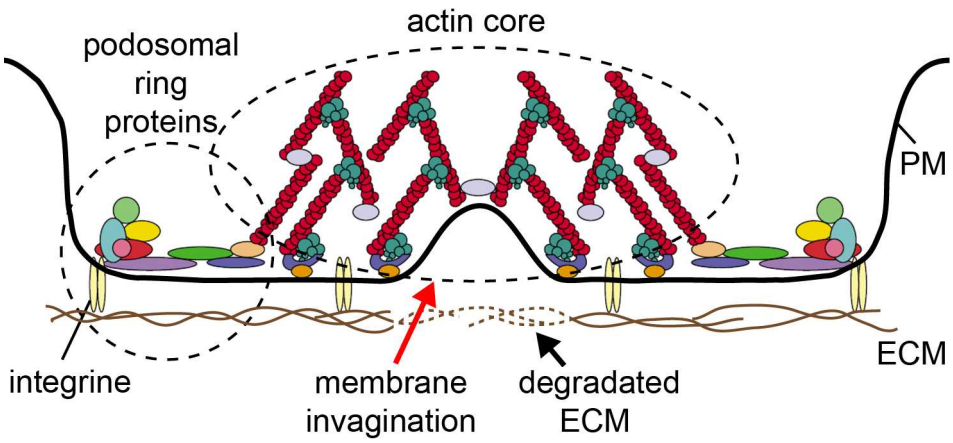

Figure 4.2: Schematic podosome cross section indicating a proposed membrane invagination. For a detailed explanation of podosome structure see also Fig. 1.9. The membrane at the basal side of podosomes may possess an invagination (red arrow). The black arrow indicates the area where ECM degradation occurs (adapted from (Linder and Aepfelbacher, 2003)).

the podosomes (Lener et al., 2006; Murphy and Courtneidge, 2011; Nitsch et al., 1989), indicating that podosomes play an important role in ECM degradation (Linder, 2007). To verify that ECM is degraded exclusively below podosomes, and therefore that the differentiated osteoclasts form functional podosomes, the cells were seeded on gelatin-FITC coated glass and incubated for 2 or 4 h. Afterwards, cells were fixed and the actin cytoskeleton was stained with phalloidin-TRITC. Podosomes consist of a characteristic condensed actin core (Fig. 1.9) and they can therefore be identified by actin staining (Murphy and Courtneidge, 2011). The fluorescence images of actin reveal several spot-like podosomes per cell (Fig. 4.1, left column). After 2 h of cell spreading, there is a punctate degradation of gelatin-FITC below the cell body (black areas) (Fig. 4.1A, middle). The areas of degraded gelatin-FITC expand with incubation time (Fig. 4.1B, middle). Overlay images of actin and gelatin-FITC validate the coincidence of podosomes and the degraded areas (Fig. 4.1, right column). Thus, gelatin-FITC degradation apparently starts underneath single podosomes and then extends over larger areas as podosomes mature and merge into clusters.

4.3.2 Imaging the basal podosome surface with AFM

The previous experiment demonstrated that ECM degradation by osteoclasts occurs in the vicinity of podosomes. As mentioned before, the actin core of podosomes may form a scaffold containing an internal tubular membrane structure involved in enzyme secretion for ECM degradation (Nitsch et al., 1989). In this case, one would expect to find a membrane invagination at the basal podosome side (Fig. 4.2).

To investigate this idea, cells were inverted according to the cell inversion technique described in Chapter 3 with the aim to image areas at the basal cell side corresponding to podosomes by AFM. For cell inversion, cells were cultured on PDMS substrates in presence of the differentiation factors RANK-L and M-CSF for 6 days and finally fixed and the actin cytoskeleton was stained with phalloidin-TRITC. Osteoclasts that had formed individual podosomes suitable for AFM imaging were identified by fluorescence microscopy and inverted (Section 2.2.7). Afterwards, the sample was scanned by AFM in contact mode in PBS with a MSNL-10 cantilever with a nominal tip radius of 2 nm. The AFM overview image of a single inverted osteoclast cell reveals a variety of different structures at the cell periphery (Fig. 4.3A). By overlaying the AFM with the fluorescence image (F-actin), the location of single podosomes can be identified in the AFM image (Fig. 4.3C). A region containing several individual podosomes was afterwards imaged with higher magnification (Fig. 4.3D). The height images are also presented as 3D reconstructions to demonstrate the podosome topography at the basal side in more clarity (Fig. 4.3E). Several podosomes are visible, three of which possess an apparent membrane invagination. In total, 350 podosomes of twelve different cells were scanned and analyzed with a self-written routine in Matlab. In presence of a depression, the Matlab function finds the deepest point around the podosome center and calculates the depression depth and diameter with respect to the highest point of the podosome. Approximately 50% of the analyzed podosomes possess a clear central depression with diameters ranging between 80 and 320 nm and depths ranging from 6 to 24 nm (Fig. 4.3F and G).

4.3.3 Visualizing basal podosome side by SEM and correlated fluorescence microscopy

To complement the AFM experiments, podosomes at the basal side of osteoclasts were also scanned by SEM. For this, RAW264.7 cells were seeded on PDMS as before, differentiated into osteoclasts for 6 days, fixed and stained with phalloidin-TRITC. Afterwards, both phase contrast images and fluorescence images of cells were taken before inverting and preparing the samples for SEM scanning (Section 2.2.11.2). Light microscopy images needed to be collected before processing the samples for SEM, since sample becomes unusable for other microscopy techniques due to the drying and coating with a 2 nm platinum layer.

An SEM overview image of an inverted osteoclast and the corresponding fluorescence image are shown in Fig. 4.4A, B and C. The fluorescence image demonstrates strong F-actin staining along the cell periphery corresponding to a dense belt of individual podosomes. A region containing single podosomes (Fig. 4.4C, white box) was rescanned

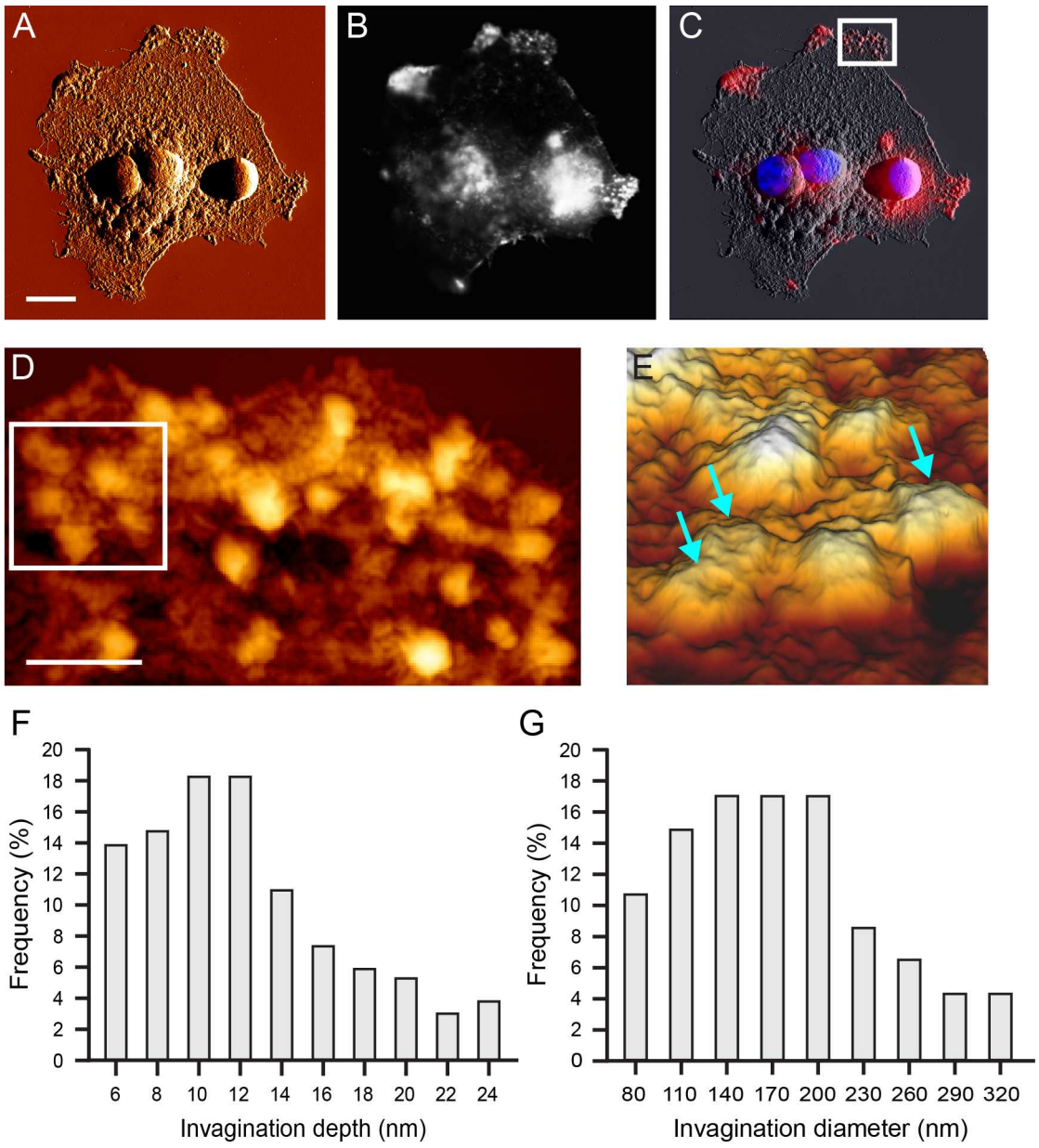

Figure 4.3: Imaging of podosomes after cell inversion by AFM in combination with fluorescence microscopy. (A) The AFM deflection image showing the basal cell side of a representative osteoclast cell scanned in contact mode. (B) F-Actin staining provides information about podosome localization. (C) An overlay image of (A) and (B) identifies cell regions containing several individual podosomes suitable for further scanning by AFM. Nuclei stained with DAPI (blue)). (D) The region marked with a white box in (C) rescanned at higher magnification. Several podosomes are visible as local elevations. The region in the white rectangle was reimaged and presented in a 3D reconstruction (E) to reveal the basal topography. Three individual podosomes containing a central depression are marked by cyan arrows. Scale bars: 10 µm (A) and 2.5 µm (D). Quantification of podosome depression (Section 2.2.12.3) depth (F) and diameter (G).

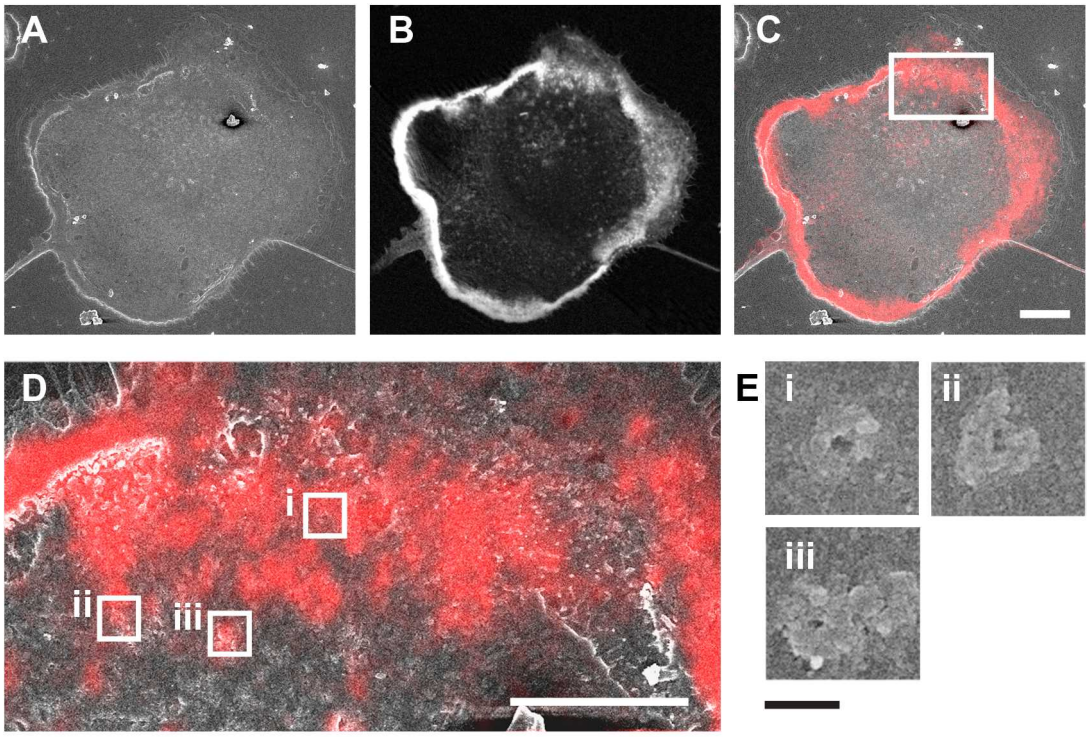

Figure 4.4: Visualization of podosomes in inverted cells by SEM in combination with fluorescence microscopy. (A) SEM image of a single inverted osteoclast. (B) Fluorescence image of the same cell. Actin-rich podosomes localize to bright regions at the cell periphery. (C) An overlay of the fluorescence image (taken before inversion) and the SEM image (taken after inversion) confirms that the cell shape is preserved during sample preparation. (D) A part of the cell marked by the white box in (C) imaged by SEM at higher magnification and overlaid with the corresponding part of the fluorescence image. Three single podosomes (white boxes i-iii) rescanned at higher magnification. The darker spots at the podosome center indicate the possible existence of membrane invaginations. Scale bars: 20 µm (C), 10 µm (D) 1 µm (i-iii).

at higher magnification (Fig. 4.4D). Most podosomes appear to contain a central cavity (Fig. 4.4D, i-iii), in agreement with results obtained by AFM scanning.

4.4 Discussion

The cell inversion method presented in the previous chapter allows inverting cells to expose their basal side without damaging the membrane or cell adhesion contact sites. Here this method was applied to study the structure of the basal podosome surface. Both, AFM topographs and SEM images indicate that podosomes frequently possess a central depression at their basal side. These depressions may result from membrane invagination and a central cavity within the F-actin core as previously proposed (Nitsch et al., 1989). This idea can be verified by staining the cell membrane and imaging the inverted cell with a confocal microscope.

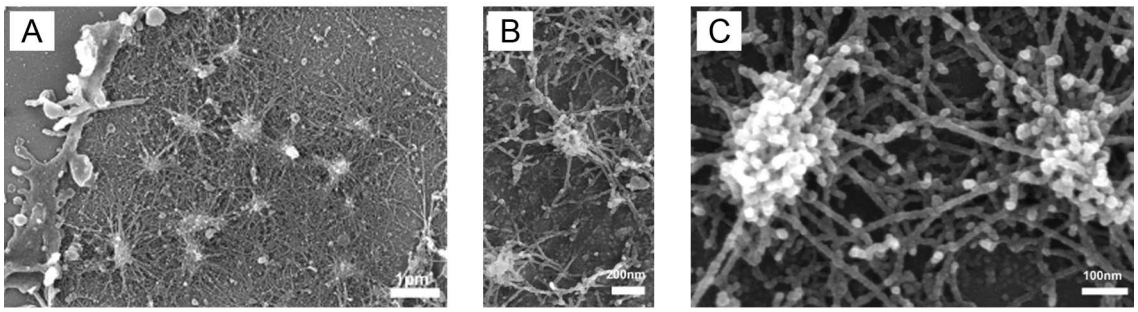

Figure 4.5: Cytoplasmic actin organization of podosomes in osteoclasts imaged by SEM. (A) Overview image of part of a osteoclast after deroofing show several podosomes. (B) Three podosomes imaged at higher magnification and image of the podosome actin core showing a concavity at the top of the podosome. Scale bars: 1 µm (A), 200 µm (B) and 100 µm (C) (adapted from (Luxenburg et al., 2007))

The molecular architecture of the podosome actin core has been previously studied from the cytoplasmic side by SEM (Luxenburg et al., 2007). In this study, the apical cell membrane and the cytoplasmic part of the cell were removed by cell "de-roofing" prior to high resolution SEM imaging of single podosomes (Fig. 4.5A). The obtained images show densely packed actin fibers at the actin core with a perpendicular orientation to the substrate and a concavity at the apex of the podosome actin structure (Fig. 4.5B and C) (Luxenburg et al., 2007). Using a similar osteoclast preparation procedure, concave features on the apical podosome side were also observed by AFM (Fig. 4.6, unpublished data from Dr. C. Franz). In that case, the depth of the invaginations ranges from 19 to 37 nm (Fig. 4.6F).

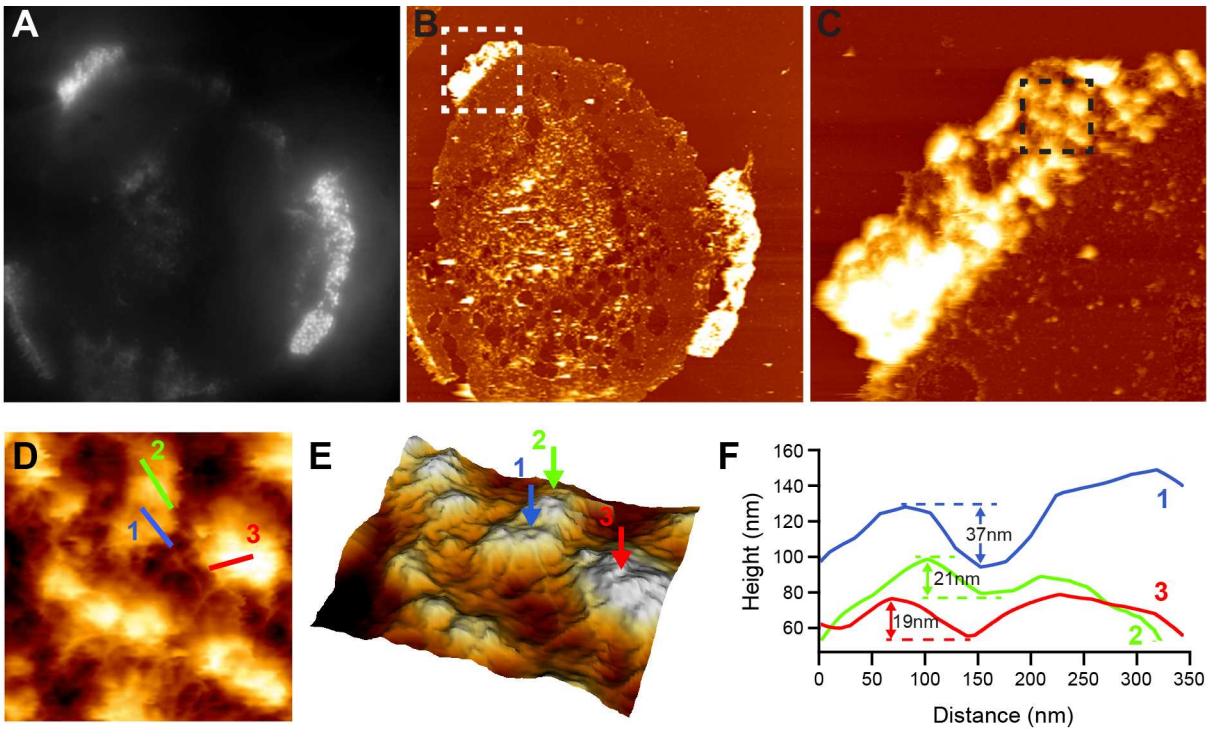

Figure 4.6: Investigating podosome structure from the cytoplasmic side. (A) Fluorescence image of the actin cytoskeleton and (B) an AFM height image of the ventral membrane of de-roofed osteoclasts. (C) An AFM scan of the region marked by the white dotted box in (B) shows part of the cell periphery containing single podosomes. The area marked by the black dotted box in (C) rescanned at higher magnification. Height profiles of three podosomes (blue, green and red) along the three corresponding lines marked in (D) are plotted in (F) visualizing a central cavity within the actin structure. (E) A 3D reconstruction of the AFM height image (D) reveals a better representation of the central depression (images provided by Dr. C. Franz)

The imaging of the podosome basal side with AFM provides 3D information about podosome topography. According to the data obtained from AFM height images, depressions on the podosome surface have a depth ranging between 6 and 24 nm and a diameter ranging from 80 to 320 nm. Thus, a true to scale schematic can be drafted (Fig. 4.7) visualizing the podosome topography. The podosome height (H) measured from the flat membrane of the cell periphery to the podosome peak ranges from 150 to 250 nm, while the height between neighboring podosomes (h) is smaller and ranges between 65 to 155 nm. The difference between H and h can be explained by the fact, that the actin core of each podosome is surrounded by FA proteins. In the case that podosomes are close enough to each other, the FA proteins of neighboring podosomes build a denser structure.

The pore-like structures at the cytoplasmic side and the depression at the basal cell side suggest that podosomes may contain a central channel. These findings support a previ-

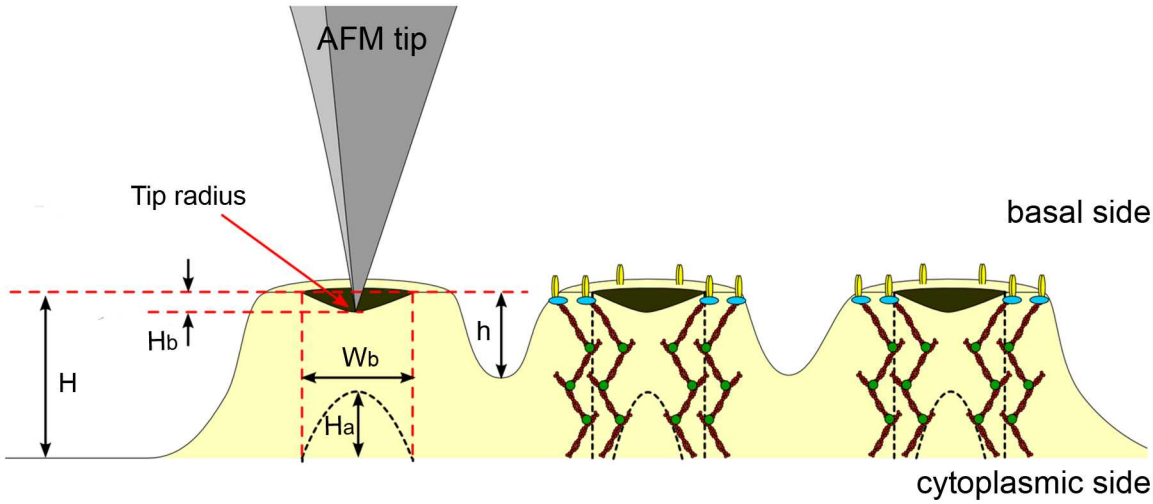

Figure 4.7: True to scale schematic of podosome basal side scanned by AFM. Three podosomes are schematically shown having a height *H* measured from the cell periphery and *h* measured from the gap between podosomes. The podosome core is indicated on the right two podosomes by F-actin in red and the Arp2/3 complex in green. Cyan and yellow ellipses represent the FA proteins and integrins, respectively. The basal side of podosomes possesses a depression (black) with a depth *Hb* and a width *Wb*. On the cytoplasmic side, the podosomes have a cavity (black dashed line) with height *Ha*. The AFM tip with a nominal radius of 2 nm is shown in grey.

ously proposed model about tubular membrane structures inside the podosome actin core (Nitsch et al., 1989). Interestingly, TEM micrographs of podosome sections cut perpendicularly to the substratum demonstrate dense tubular structures (Nitsch et al., 1989). Under favorable sectioning conditions, these dense areas appear to represent channels (Fig. 4.8C and D). The membrane of these channels is in continuity with the ventral plasma membrane and is surrounded by a cuff of dense filamentous matrix (Nitsch et al., 1989). The diameter of such channels is around 25 nm (Ochoa et al., 2000). Moreover, podosomes are associated with dynamin, a GTPase involved in vesicle formation at the plasma membrane and endocytosis (Hinshaw, 2000). TEM and fluorescence images demonstrate that dynamin surrounds the tubular invaginations of the plasma membrane of podosomes. These observations suggest that a membrane may flow through the podosome core and that vesicles may pinch off at its top on the cytoplasmic side (Ochoa et al., 2000). Similar to podosomes, invaginations of tubular plasma membrane surrounded by a dense F-actin network have been observed in yeast by TEM (Mulholland et al., 1994). However, these membrane invaginations are smaller (up to 7 nm in diameter) than those in podosomes (Fig. 4.3F). Furthermore, the actin cytoskeleton surrounding yeast membrane invaginations colocalizes with the vesicle generation protein Rvs167, a homologue of the amphiphysin protein which has similar functions as dynamin (Takei et al., 1999).

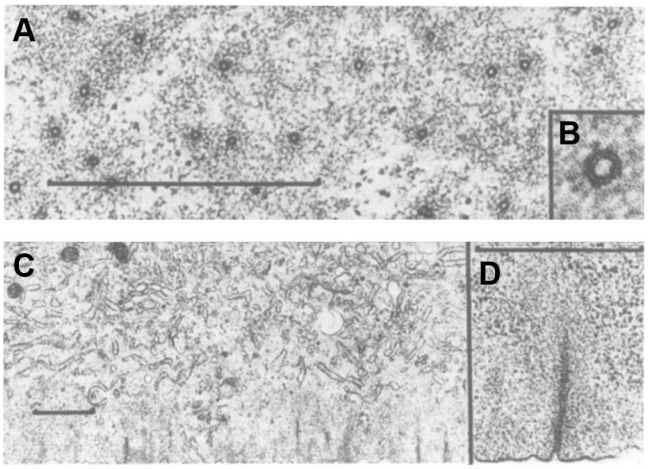

Figure 4.8: TEM images of podosomes. (A-D) TEM images of RSV-transformed chick embryo chondrocytes. (A) Section cut parallel and close to the bottom of the culture dish. Dark dots with a size of 30 nm in this area have been identified as podosomes. (B) A magnified view of a single podosome showing a dense ring of microfilaments. (C) A cross section perpendicularly to the dish shows several membrane invaginations. (D) Magnification view of a membrane invagination, which is 30 nm thick and up to 1 µm long. Magnification factors: 50 000x (A), 230 000x (B), 11 000 (C), 31 000x (D) (adapted from (Nitsch et al., 1989))

A recent model of endocytosis in yeast shows that the assembly of a dense branched actin network can promote the formation of plasma membrane invaginations. Once the extended membrane tubule forms, the vesicle scission apparatus (Rvs161/167 and Vps1) narrows the neck of the vesicle forming at the invagination tip to promote scission (Boettner et al., 2012). A similar mechanism may be involved in enzyme secretion though membrane invagination of podosomes.

Interestingly, according to the SEM and AFM images presented in this chapter only 50% of podosomes display a depression at the basal side. In case of SEM, one could argue that the metal coating partly disguises the cavities. However, the 2 nm coating is thin compared to the invagination depth (6 - 24 nm) observed by AFM (Fig. 4.3F, G), making it unlikely that the metal coating filled the depression. High podosome dynamics could provide an alternative explanation for the mixed morphologies. The fixative glutaraldehyde chemically crosslinks cells and podosomes near instantaneously due to its high penetration velocity of 5.6 µm/min (Hopwood, 1967). The thin cell edge, where the majority of podosomes are located, is therefore fixed within seconds. If the channels alternate between an open and closed state, only a fraction of podosomes would display concavities at a given time. Podosome maturation and the dynamics of podosome turnover could affect the presence of cavities. The average podosome life time is on the order of minutes (Linder, 2007), consistent with rapid assembly and disassembly. As only

mature, functional podosomes may contain an open channel for enzyme secretion, while assembling or disassembling podosomes may be closed.

4.5 Conclusions

After cell inversion structures at the basal cell side can be investigated by high-resolution scanning microscopy techniques. In this chapter, this technique was applied to study the structure of the basal podosome surface. In agreement with the hypothesis that the F-actin core of podosomes contains a central tubular membrane structure involved in enzyme secretion for matrix degradation, a central depression in the podosome basal membrane could be frequently detected by AFM and SEM. While these results do not conclusively prove the existence of a central channel spanning the podosome core, they still provide important additional support for this idea.

5 Studying fibronectin fibrillogenesis in living cells by atomic force microscopy

5.1 Abstract

Fibronectin (FN) is an abundant glycoprotein of the extracellular matrix (ECM). In tissues, cells remodel globular FN molecules into complex fibrillar matrices. However, the dynamics of cellular remodeling and the transition through intermediate fibrillar stages are still incompletely understood on the nanoscale. In this chapter, initial and later stages of FN fibrillogenesis were visualized by combining high resolution microscopy techniques, atomic force microscopy (AFM) and fluorescence microscopy imaging, directly in living fibroblasts. FN nanofibrils originate in the vicinity of cellular adhesion complexes during membrane retraction. The very first fibrils are created below the cell staying hidden to AFM, so that the earliest detectable FN nanofibrils contain already about 8 molecules. With progressing cell spreading, these fibrillar precursors are elongated and reinforced to include several hundred FN molecules. Ultimate fibril dimensions crucially depend on integrin-receptor-driven mechanisms. For example, in presence of Mn^{2+}, a known activator of integrin receptor binding to FN, both the final fibril size and the fibril extension speed are increased. Spatial aspects of FN remodeling also strongly depend on cell density. While FN fibrillogenesis by individual fibroblasts occurs primarily beneath cells, fibroblasts in denser layers collectively remodel FN into lateral structures preferentially at regions of cell-cell contacts, emphasizing the role of FN in regulating cell-cell interactions. High-resolution AFM under physiological conditions in combination with fluorescence microscopy thus provides unique insight into structural and temporal aspects of cell-driven FN fibrillogenesis.

5.2 Introduction

FN is a large (∼460 - 500 kDa), homodimeric glycoprotein of the ECM (Hynes, 1985; McDonald, 1988). It mediates cell attachment (Yamada and Olden, 1978) and matrix cross-linking (Dallas et al., 2005; Pereira et al., 2002; Sottile and Hocking, 2002; Velling et al., 2002) and plays an indispensable role during development, wound healing (To and Midwood, 2011) and matrix repair (Singh et al., 2010). FN consists of two nearly identical monomers linked by disulfide bridges near the C-terminus (Hynes, 1985). The FN monomers are composed of types I (FNI), II (FNII) and III (FNIII) repeating units (Fig. 1.2) (Hynes, 1985). The repeating units are organized into different functional domains that provide interactions with other ECM molecules or with cellular receptors.

The reorganization of FN monomers into large fibrils is a hallmark of FN function (McDonald, 1988; Singh et al., 2010). FN fibrillogenesis is a complex multistep process which has been studied extensively on the molecular level (McDonald, 1988; Singh et al., 2010). Initially, dimeric globular FN proteins are secreted in a compact conformation. Afterwards, these globular FN molecules are converted into an extended, active conformation through cellular contraction forces mediated via actin cytoskeleton and transmitted by integrin receptors. During this process FN-FN binding sites are progressively exposed, allowing FN molecules to align and to form larger fibrils. The divalent cation Mn^{2+} increases the binding affinity of different integrins, such as $\alpha_5\beta_1$, to FN (Gailit and Ruoslahti, 1988; Mould et al., 1995b) and accelerates the FN fibrillogenesis process (Sechler et al., 1997). Accumulated FN fibrils are then stabilized inside fibrillar networks and undergo strong, non-covalent, protein–protein interactions (Ohashi et al., 1999; Schwarzbauer and DeSimone, 2011). The fibril insolubility is depend on formation of interactions between partially unfolded FNIII modules, for example $FNIII_9$ (Litvinovich et al., 1998) and $FNIII_{13-14}$, $FNIII_{5-6}$, $FNIII_{8-9}$ (Smith et al., 2007). Therefore, for the insoluble FN matrix formation the FN unfolded dimers first associate with each other and then undergo conformational changes for irreversibly incorporation in to fibrils (Schwarzbauer and DeSimone, 2011).

FN fibrillogenesis has been mostly investigated using fluorescently labeled FN and fluorescence energy transfer (FRET) spectroscopy (Baneyx et al., 2001; Karuri et al., 2009; Wolff and Lai, 1989). FRET experiments have provided evidence for conformational changes occurring within single FNIII modules, as well as the entire FN molecule. This processes occur during different stages of fibril formation (Baneyx et al., 2001). Cell-mediated extension of FN molecules has been shown to involve FNIII domain unfolding (Smith et al., 2007). However, complete unfolding of FN modules or FN proteins *in vitro* may result in severe conformational changes inconsistent with natural processes occurring in tissues (Ulmer et al., 2008). Therefore, cell-induced remodeling of homogenous FN sub-

strates into fibrillar matrices has also been studied directly by fluorescence microscopy. These experiments have shown that cells stretch individual FN fibrils by up to four times of their initial length during matrix formation (Ohashi et al., 1999). However, with conventional optical microscopy techniques small fibrillar FN intermediates ($< 200\,\text{nm}$) cannot be resolved due to the optical limitation. Therefore, many open questions, regarding the deep understanding of the organization of FN molecule organization into fibrils and fibril maturation require high resolution microscopy methods able to resolve individual FN building blocks.

Important information about the structure of single FN dimers has been obtained by electron microscopy imaging (Erickson et al., 1981; Erickson and Carrell, 1983; Koteliansky et al., 1980; Price et al., 1982; Tooney et al., 1983). For instance, by transmission electron microscopy (TEM) the length and width of a single folded plasma FN molecule were measured to be 15.5 and 8.8 nm, respectively (Koteliansky et al., 1980). The scanning transmission electron microscopy images of freeze-dryed FN molecules on carbon surface reveal the average dimensions of 16 nm x 24 nm (width x length) (Tooney et al., 1983), while the electron micrographs of rotary-shadowed FN show folded dimers with dimensions of 32 nm x 51 nm (Erickson and Carrell, 1983; Price et al., 1982). The length and height of the unfolded FN molecule were estimated to be 120 - 160 nm and 2 – 3 nm, respectively (Engel et al., 1981; Erickson et al., 1981; Erickson and Carrell, 1983). Scanning electron microcopy (SEM) revealed a mean counter length of 130 nm of extended FN dimers adsorbed to mica (Tooney et al., 1983). However, preparation of EM samples typically include drying and staining or sputtering steps, which can not only affect the molecular structure of FN but also make this technique incompatible for observing the fibrillogenesis process *in vivo*. In general, most studies investigating cell-induced fibrillogenesis were performed on fixed and stained samples, providing only a snapshot state of FN fibrillogenesis rather than visualizing the entire process from initial precursors to fully-formed fibrils.

Another powerful technique for both, obtaining high resolution images under physiological conditions and for characterizing the unfolding mechanism of molecules is AFM. Both, conformational changes of entire FN molecules and the unfolding of individual FNIII modules have been analyzed by single-molecule AFM force spectroscopy (Oberhauser et al., 2002) giving deeper insight into unfolding events involved in matrix assembly with more accuracy. AFM tapping mode revealed a length of the extended FN dimers of 120 - 160 nm and a height of $\sim 1\,\text{nm}$ in air (Lin et al., 2000) and liquid (Chen et al., 2007). Furthermore, AFM images of FN molecules adsorbed to different surfaces have revealed morphological changes depending on surface hydrophobicity (unfolded or compact conformation), including different FN dimer configurations, ring-shaped and beaded-filament or FN ag-

gregates. Some of these structures were proposed to represent early and intermediate states of FN fibrillogenesis (Chen et al., 2007).

In this chapter, results of live-cell time lapse AFM imaging in combination with fluorescence microscopy are presented, visualizing for the first time the initial steps of FN fibril formation by living fibroblasts. Also the number of FN molecules incorporated into FN fibrils at different stages of fibrillogenesis was estimated from AFM scans. Adding Mn^{2+} to the cells accelerates the FN fibrillogenesis dynamics. Moreover, the cell density seems to strongly influence the FN remodeling. Altogether, these results provide a novel insight into the dynamics of FN fibrillogenesis.

5.3 Results

5.3.1 Investigating FN fibrillogenesis by TIRF microscopy

Fibroblasts have a well-characterized role in FN remodeling in different tissues (Grinnell, 1984; Singer et al., 1984). Fibroblasts, such as the REF52 (rat embryonic fibroblast) cell line, also provide useful model systems to study cell-induced FN fibrillogenesis in tissue culture experiments. To assess the general dynamics of FN fibrillogenesis in REF52 cells, different stages of fibrillogenesis were visualized using conventional fluorescence microscopy imaging. Cells were seeded on homogeneous coatings of FN labeled with Alexa Fluor 488® (FN-AF488) and incubated for 10, 30, 60 or 240 min. After fixation and immunostaining for vinculin, a marker protein for focal adhesion (FA) cell-matrix contact sites, the FN layer and FAs were imaged by TIRF microscope (Fig. 5.1A). To improve the clarity of newly formed FN fibrils against the diffuse background of the unremodeled FN layer, the background from the FN-AF488 fluorescence images was subtracted by using a "rolling ball" algorithm (Fig. 5.1A). After 10 min of incubation, cells had begun to spread and to recruit vinculin to FAs (Fig. 5.1A, 10 min). In this stage, only few and small fibrillar FN structures were visible. The bulk of FN showed an almost fully homogeneous distribution, indicating that FA formation precedes FN remodeling. After 30 min, cells formed more and larger FAs, especially at the cell periphery (Fig. 5.1A, 30 min). FN fibrils were still difficult to discern on raw but became apparent on the background-subtracted images. In accordance, a fluorescence intensity profile line showed increased roughening (Fig. 5.1B). After 60 min, full size FA contacts had formed and the FN layer was markedly remodeled in the vicinity of these contacts (Fig. 5.1A, 60 min). In agreement with FA-induced fibrillogenesis, the FN-AF488 and vinculin fluorescence intensity profiles showed partial correlation (Fig. 5.1B, 60 min). After 240 min, cells had fully spread, formed a mature array of FA sites and extensively remodeled FN below the cell body (Fig. 5.1A, 240 min). The intensity profile of vinculin fluorescence remained at a similar level as before, but the FN-AF488 profile peaks had increased in height and number compared to previous time points (Fig. 5.1B, 240 min). Furthermore, the spatial correlation between FA and FN structures is maximal at 240 min.

To visualize the spatial overlap of FA and FN fibrils in more detail, cells were fixed after 240 min and stained for paxillin as an alternative FA marker (Fig. 5.2). An extensive co-localization of paxillin and fibrillar FN at FAs could be observed, although paxillin was usually oriented more towards the center of the cell body, while FN fibrils were concentrated on the outer part of focal adhesions (Fig.5.2). Together, these results provided a picture of the dynamics of FN fibril formation over the first 4 hours of cell spreading and verified the active role of focal adhesions in this process.

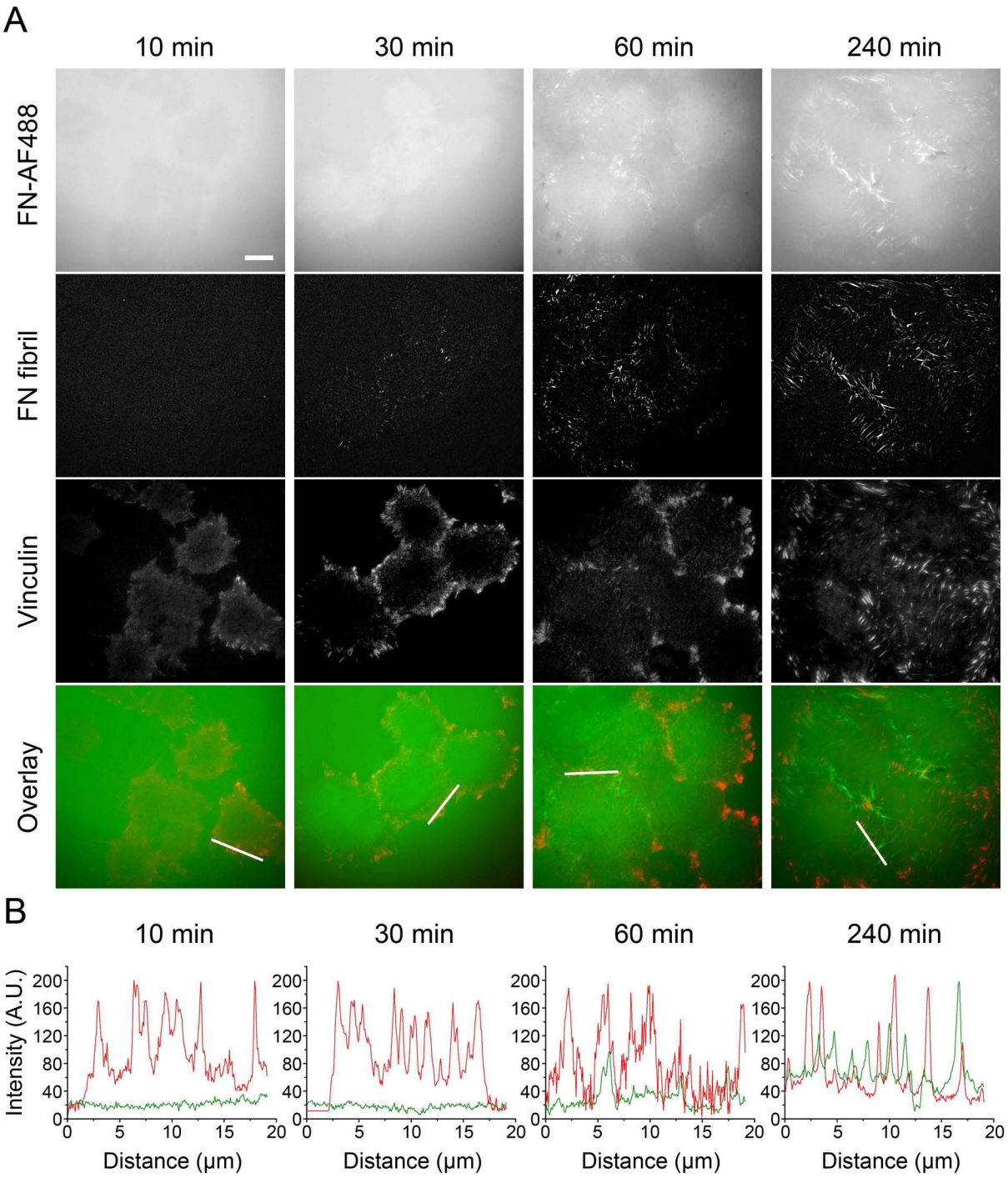

Figure 5.1: Dynamics of cell-induced FN fibrillogenesis. (A) REF52 cells were incubated on a homogenous coating of FN-AF488 for 10, 30, 60 or 240 min. TIRF microscopy images of FN demonstrate the progressive formation of FN fibrils (top row). Background subtraction (see Section 2.2.12.4) increases the visibility of newly formed FN fibrils (second row). Immunostaining for vinculin visualizes emerging FAs (third row). Overlay of unprocessed FN (green) and vinculin (red) images (bottom row). Scale bar: 10 µm. B. Fluorescence intensity profiles of FN (green lines) and vinculin (red lines) generated along cross sections (white lines) in A at corresponding time points.

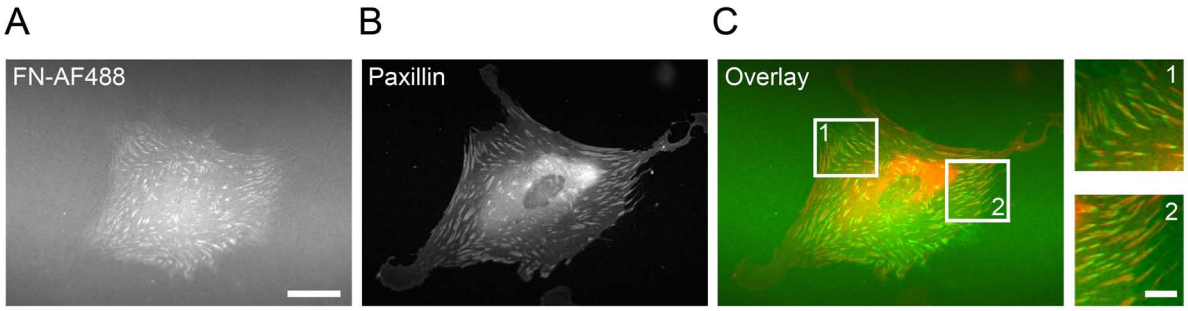

Figure 5.2: Visualizing partial colocalization of paxillin and FN-AF488 fibrils with fluorescence microscope. REF52 cells were incubated on FN-AF488 (A) for 4 h and paxillin (B) was stained to visualize FAs. Cropped regions from the overlay image (C) demonstrate the association of FN fibrils and focal adhesions at the basal side of the cell. Scale bars: 20 µm (A) and 2.5 µm (C2).

The fluorescence images also provided a means for quantitating longitudinal and latitudinal FN fibril growth. Plotting fibril length (Fig. 5.3A) and width (Fig. 5.3C) at different time points in histogram form allows visualizing considerable structural heterogeneity of fibrils, which cannot be represented by averaged results. The smallest detectable precursors were typically ~ 0.3 µm in length and $\sim$ 0.2 - 0.3 µm in width, approaching the resolution limit of the optical microscope. Fibrils then grew up to ~ 2 µm in length and $\sim 0.3 - 1$ µm in width, with some rare fibrils reaching a length of up to 6 µm. Determining the aspect ratio of individual fibrils (width divided by length) (Fig. 5.3B) confirmed that fibrils progressively transformed from a near-circular shape after 10 min to a strongly elongated shape after 240 min. The averaged longitudinal and lateral fibril growth was plotted to determine the dynamics of fibril extension (Fig. 5.3B). Between 10 and 240 min, the mean fibril length increased by a factor of ~ 6.33 from 0.3 ± 0.1 µm (10 min) to 1.9 ± 0.6 µm (240 min). Over the same time, the mean fibril thickness increased from 0.2 ± 0.1 µm (10 min) to 0.5 ± 0.1 µm (240 min), or by a factor of 2.5. Interestingly, plotting fibril width versus length for all time points revealed a highly-linear correlation (coefficient of determination $R^2 = 0.989$, Fig. 5.3B) and longitudinal and latitudinal fibril growth remained constant at a ratio of ~ 4.3:1 over the entire time course, indicating a uniform extension mechanism of the fibrils. Dividing mean final fibril length (~ 1.9 µm) by time (240 min) yielded a comparatively slow averaged fibril elongation rate of ~ 8 nm/min. However, fibrils might grow not at a constant speed but in bursts characterized by higher speed over short time intervals, in which case averaging over time would underestimate the effective fibrillar extension speed.

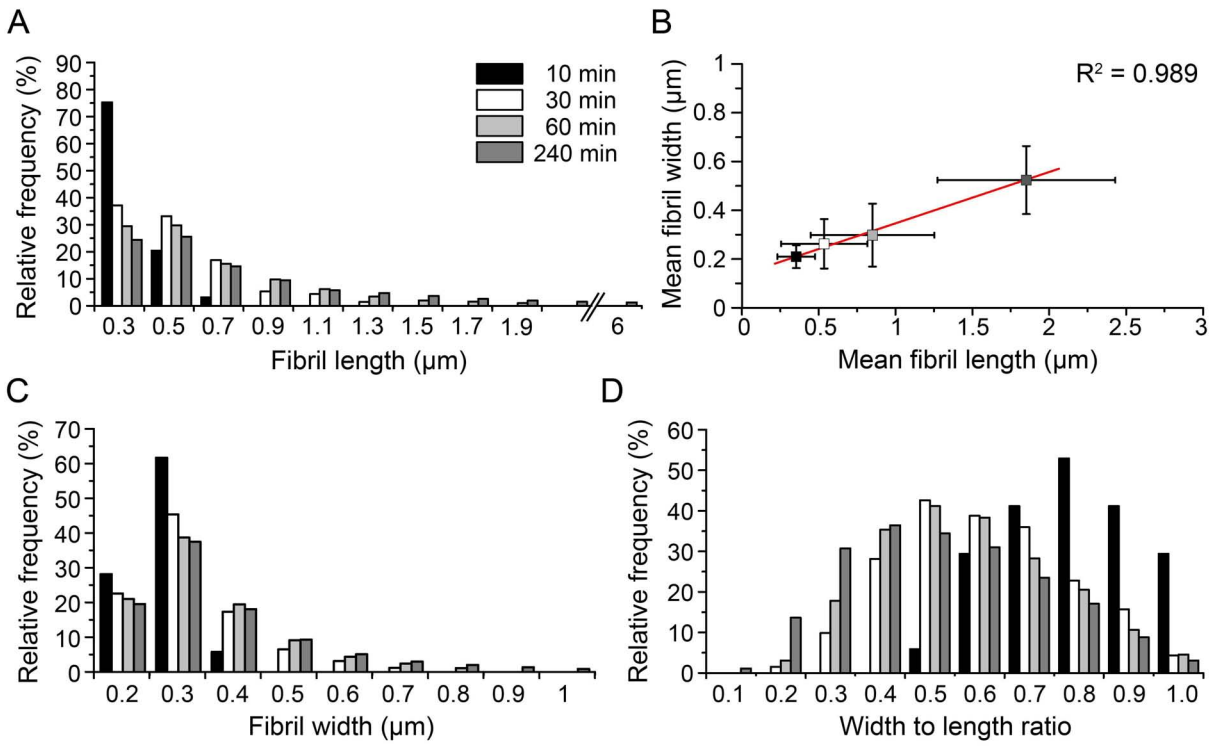

Figure 5.3: Quantification of FN fibril dimensions at time points 10, 30, 60 and 240 min. The data are taken from fluorescence images of more than 50 cells at each time point from two independent experiments. The histograms of the FN fibril width (A) and length (C) show that the FN width as well as FN length increases with time with a maximal value of 1 µm and 6 µm, respectively, after 240 min. (B) Plotting the mean fibril width versus mean fibril length reveals a nearly linear correlation between both parameters (coefficient of determination $R^2 = 0.989$). The ratio between longitudinal and latitudinal growth remained constant at $\sim$4.3:1 over the entire time course. (D) Relative frequency of the width to length ratio at different time points.

5.3.2 Investigating FN fibrillogenesis by AFM in combination with fluorescence microscopy

Analyzing early FN fibrils from fluorescence microscopy images provides a reliable measure of fibril dimensions at later stages of extension. However, at early stages of fibrillogenesis, fibril dimensions approach the resolution limits of conventional optical microscopy ($\sim$200 nm), preventing accurate quantification from fluorescence images. Moreover, FN fibrils are 3D structures and fluorescence images do not provide any information regarding the fibril height. Therefore, for obtaining additional insight into the FN fibril ultrastructure, AFM was used to image the cell-remodeled FN layer after incubation for 4 h and chemical fixation. Using FN-AF488 allowed for complementary fluorescence microscopy during AFM imaging. While cells were spreading on planar cell culture substrates, FN was remodeled into fibrils primarily at the basal cell side (Gudzenko and Franz, 2013). There-

fore, preliminary fibrils were not directly accessible to the AFM tip. Nevertheless, FN fibrils could be visualized by AFM at the rear end of strongly polarized cells (Fig. 5.4A), where fibrils apparently became gradually exposed during cell migration. AFM height and deflection images revealed a complex entanglement of cellular retraction fibers and fibrillar FN structures at the cell rear. The FN fibrils were usually oriented in the same direction as the cellular retraction structures, suggesting that the FN fibrils were created during cell retraction. An overlay of AFM and fluorescence images collected from the same area identified the majority of these structures as FN fibrils (Fig. 5.4A). Nevertheless, since the fibrillar structures appeared to be tightly associated with cellular structures (Fig. 5.4A, overlay image), unambiguous identification and height quantification of FN fibrils was impossible from these AFM images. When extending the cell incubation time on FN to 16 h, cells had frequently vacated whole areas of remodeled FN, and these cell-free areas could then be easily scanned by AFM (Fig. 5.4B). Higher-resolution AFM images of these areas revealed a complex array of mainly parallel fibrils, which often appeared frayed at one end (Fig. 5.4C). Again, overlay with the corresponding fluorescence image demonstrated excellent overall structural agreement between the AFM and light microscopy images. However, the light microscopy images failed to resolve the FN fibril ultrastructure visible in AFM images. In particular, only AFM images revealed the gradual transition of frayed nanofibrils into thicker structures progressive fibril bundling.

To further investigate the correlation between fluorescence and AFM images, height (blue lines) and fluorescence intensity profiles (red lines) were extracted along lines traversing the fibril arrays at different positions and plotted together in single diagrams (Fig. 5.4D and E). As expected, the fluorescence signal was generally of lower spatial resolution, while the height profiles from the AFM image contained more structural detail and easily resolved fibrils thinner than 200 nm. The AFM cross sections yielded additional information about height variations along the FN fibrils. Fibril were typically ~ 10 nm high at the frayed front end (Fig. 5.4D, blue trace) and maximally 30 nm at the fibril center and rear end (Fig. 5.4E, blue trace), indicating gradually increasing fibril height along the cellular pulling direction. At the fibril front (cell distal orientation), height and fluorescence intensity signals correlated weakly at best (Fig. 5.4D), indicating that light microscopy images are particularly unsuitable for investigating FN fibril structure at this location. In contrast, in the central region, where fibrils reached their greatest width, fluorescence and AFM height signals correlated well (Fig. 5.4E).

5.3.3 Imaging FN fibrillogenesis in living cells by time-lapse AFM

AFM scanning generates high resolution images, among others also under physiological conditions, and is therefore a unique tool to investigate cell-induced matrix rearrangement

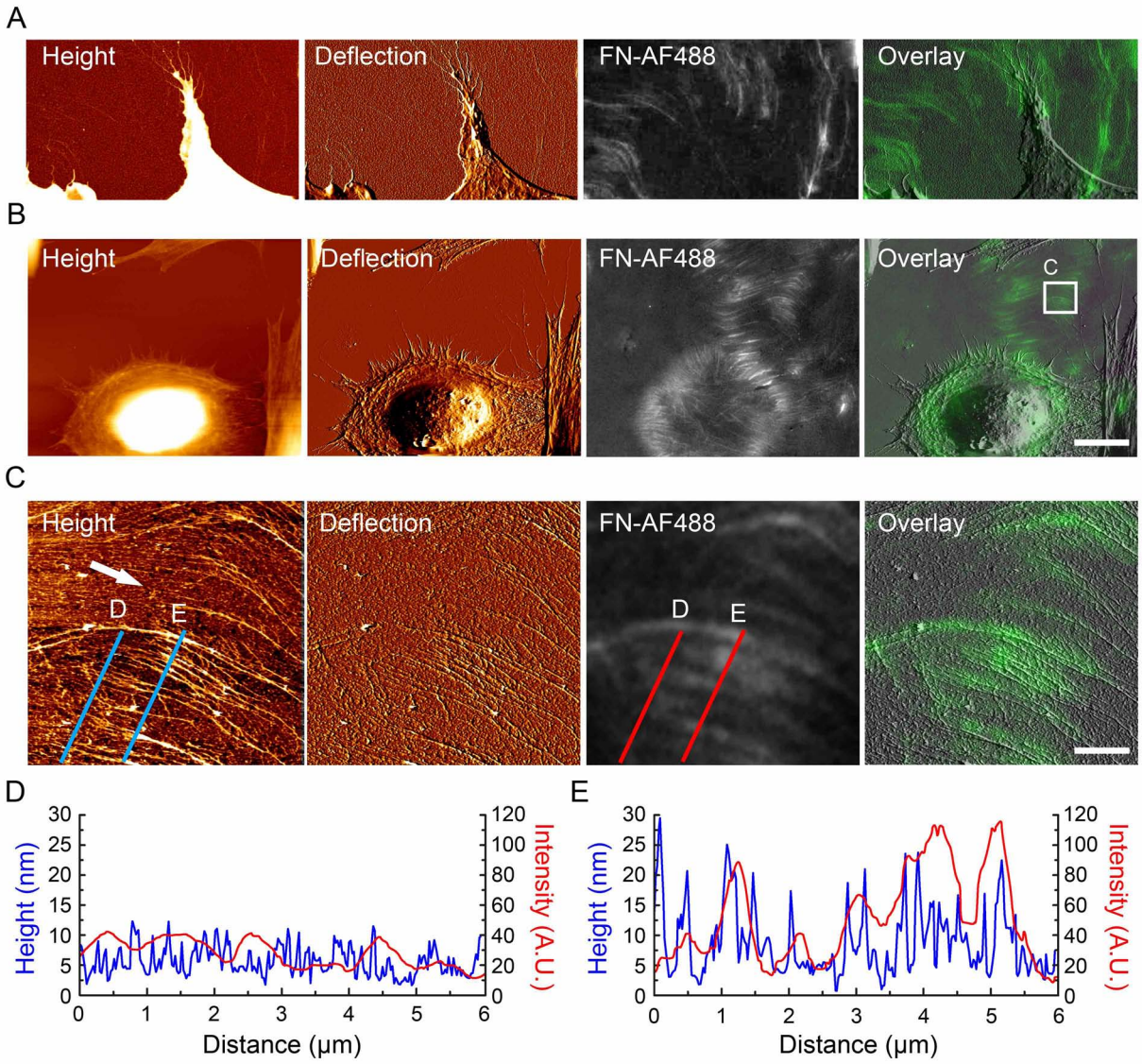

Figure 5.4: Investigating FN fibril structure by combined AFM and fluorescence microscopy. (A) REF52 cells were incubated on fluorescently-labeled FN and fixed after 4 h. AFM height and deflection images visualize cellular protrusions and associated FN fibrils along the cell edge. Overlay of the AFM deflection image with the fluorescence image demonstrates the complex entanglement of cellular protrusions and FN fibrils. (B) After 16 h, the FN layer frequently displays fibrillar structures also in cell-free areas apparently previously vacated by migrating cells. (C) The cell-free region indicated by the white rectangle in (B) scanned by AFM at higher resolution visualizing FN fibril ultrastructure. (D) Superimposition of height and fluorescence intensity profiles generated along the blue and the corresponding red line "D" in panel (C) across a thinner, distal section of an array of FN fibrils. (E) Superimposition of height and fluorescence intensity profiles generated along the blue and red line "E" across a proximal, thicker section of an array of FN fibrils. The AFM profile lines (in blue) provide a significantly higher spatial resolution than the corresponding fluorescence intensity profiles (in red). Scale bars: 5 µm (A), 20 µm (B), 2 µm (C).

with near molecular resolution in living cells (Friedrichs et al., 2007). To monitor the initial steps and dynamics of FN fibril formation directly, AFM time-lapse scanning of unfixed cells was performed. To minimize a potentially destructive influence of the AFM tip on cell and FN morphology, scans were performed in contact mode using a low scan force (< 1 nN) and moderate scan speeds. To maximize the frame rate while maintaining adequate image resolution, scan regions were limited to $10 \times 10\,\mu m^2$ at 512×512 pixels. Using these conditions and a line scan frequency of 2 Hz, image series were recorded with approximately one image every 4 min. To increase the vertical resolution of the AFM images, ultraflat cleaved mica disks were used as supports, instead of rough glass coverslips (Wittenburg et al., 2013).

Before starting live cell imaging, cells were incubated on FN for 5 min to ensure initial cell attachment and initiation of spreading. According to images obtained on fixed cells (Fig. 5.4A and B), FN fibrillogenesis occurs primarily near the cell edge. To increase the probability of observing active fibrillogenesis events within a limited scan frame ($10 \times 10\,\mu m^2$), regions at the cell periphery were therefore chosen for live cell imaging. In agreement, AFM time lapse recordings showed that FN fibrils frequently emerged during membrane retraction (Fig. 5.5A and Movie 5.1). Fibrils were usually aligned in the direction of the retracting membrane, suggesting that fibrils formed as the result of traction forces applied by the retracting cell membrane (Fig. 5.5A, 47 min). Occasionally, cells went through several cycles of membrane retraction and extension, apparently re-contacting the newly formed fibrils (Fig. 5.5A, 31 - 69 min). Overall, fibrillar arrays imaged in time series experiments showed similar dimensions as fixed samples. However, during live cell scanning the AFM image quality of FN fibrils sometimes appeared degraded due to poor sample tracing (Fig. 5.5A, 47 min). Nevertheless, once cells had completely moved out of the scan area, tip-sample tracing usually stabilized, revealing a structurally intact array of FN nanofibrils (Fig. 5.5A, 85 min). The mechanically instable regions apparently did not correspond to flexible FN fibrils moved back and forth by the scanning tip. Instead, soft cellular structures, such as membranous extensions, appeared to be transiently connected to the FN fibrils during cell retraction and could not be stably imaged.

The time-lapse series provided the first direct view of the initial stages of cell-induced FN fibrillogenesis. Fibrils extended at a mean rate of 22 - 65 nm/min and widened at a rate of 7 – 10 nm/min. While the ratio of longitudinal and latitudinal fibril growth was in a similar range ($\sim$ 1.9:1 – 6:1) as the data obtained by fluorescence microcopy ($\sim$ 4.3:1), AFM revealed a substantially higher rate of FN fibrillogenesis compared to the fluorescence analysis. This analysis, however, required interpolating fibril dimensions over longer time periods (240 min), potentially averaging out burst-like fibril growth events with higher extension speeds. Judging by AFM time lapse imaging, initial fibrillar extension appeared to be completed within 30 – 60 min, and thus at considerably shorter time frames as pre-

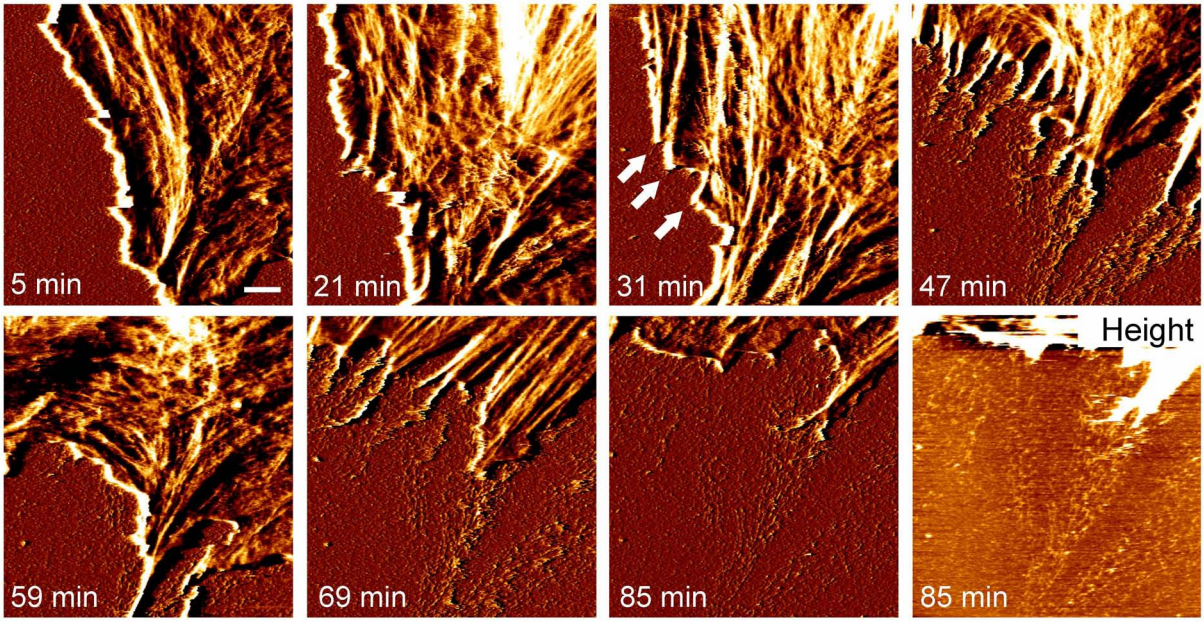

Figure 5.5: Investigating FN fibrillogenesis by time-lapse AFM of living REF52 cells. Cells were placed on with FN coated mica and a region of $10 \times 10\,\mu m^2$ was scanned by AFM in contact mode. The deflection time-lapse images show cell edge on homogeneous FN after initial cell spreading (5 min). The cell first protrudes (21 min), after 31 min it retracts and FN fibrils appear at the cell protrusions indicated by white arrows. After 85 min, the region which was initially hidden by the cell is covered with small FN fibrils (height image). Scale bar 1.5 µm.

viously assumed based on the light microscopy images. The AFM time-lapse series also revealed a fibril height increase with time. The earliest detectable fibrillar precursors had a height of 1.6 to 4 nm (Fig. 5.5A, 31 min). As the membrane continued to retract, these small fibrils appeared to merge into larger fibrils reaching a height of 6 - 9 nm and a maximal length of 1 µm (Fig. 5.5A, 85 min). The height values on native FN fibrils were lower than those obtained on fixed fibrils (see Fig. 5.4E), suggesting a subtle influence of the glutaraldehyde fixation protocol on fibril height.

Several previous structural studies have been carried out on cellular FN reorganization using PFA- or glutaraldehyde-treatment to stabilize FN structures for AFM scanning (Tooney et al., 1983). However, it was unclear if chemical cross linking affects the fibril structure, for instance, by bundling thin neighboring fibrils into larger fibrillar structures. The AFM images of chemically-fixed FN fibrils showed a comparable nanoarchitecture as FN imaged in unfixed, living cells, confirming that fixation is not harmful to the structure of early FN fibrils. However, a subtle effect of fixation on fibril height was observed. Importantly, however, chemical fixation is not required for high-resolution imaging with

AFM. On the contrary, working with living cells allows observing the FN fibrillogenesis process in real time.

5.3.4 Mn^{2+} promotes early FN fibrillogenesis

Extracellular Mn^{2+} activates integrin receptors and enhances cell attachment, spreading and migration on FN and other substrates (Afshari et al., 2010a; Afshari et al., 2010b; Byzova et al., 2000). Traction force experiments have shown that integrin activation with Mn^{2+} increases cytoskeletal tension transmitted onto FN (Lin et al., 2013), stimulating the assembly of a mature, deoxycholate-insoluble FN matrix after several hours of incubation (Brenner et al., 2000; Sechler et al., 1997). However, less is known whether Mn^{2+} also affects the formation dynamics and structure of early FN fibrils. In a previous study using fluorescence microscopy analysis, Sechler et. al detected no significant differences in FN matrix assembly in Mn^{2+}- treated or untreated cells after 30 min of incubation (Sechler et al., 1997), but a significant effect of Mn^{2+} on FN fibril morphology starting after 4 h of incubation. However, due to the limited resolution of conventional fluorescence microscopy, subtle nanoscale structural differences may not be detectable at the earliest stages of fibrillogenesis when fibrils are still small.

To assess the impact of Mn^{2+} on the morphology of early FN fibrils, live cell scanning was performed by AFM in the presence of 1 mM Mn^{2+}. In this case, cells began to form fibrils almost immediately (6 min) after cell seeding (Fig. 5.6A). After 30 min, FN fibrils had reached an average length of ~ 2 µm and a height of up to 30 nm, in contrast to ~ 1 µm and ~ 6 nm, respectively, in the absence of Mn^{2+} (Fig. 5.6C and D). Cells also formed FN fibrils at higher speed in the presence of Mn^{2+} (157 ± 107 nm/min) than in its absence (42 ± 28 nm/min). Unexpectedly, the rate of membrane retraction was also enhanced in Mn^{2+}-containing medium, which may provide an additional mechanism for the enhanced velocity of fibrillogenesis. Mn^{2+} addition therefore has a profound impact on early FN fibril formation, leading to accelerated initiation of fibril formation, increased growth rates and larger final fibrillar dimensions. Here, the resolution advantage of AFM can reveal new important structural insight into FN fibrillogenesis depending on the integrin activation state.

5.3.5 FN fibrils form during membrane retraction

As fibrillar FN structures became visible at the same rate as the membrane retracted, this raised the possibility that preformed FN fibrils at the basal cell side only became progressively uncovered by the retracting cell membrane sheet during AFM scanning, instead of being created during membrane retraction. However, given the short time interval

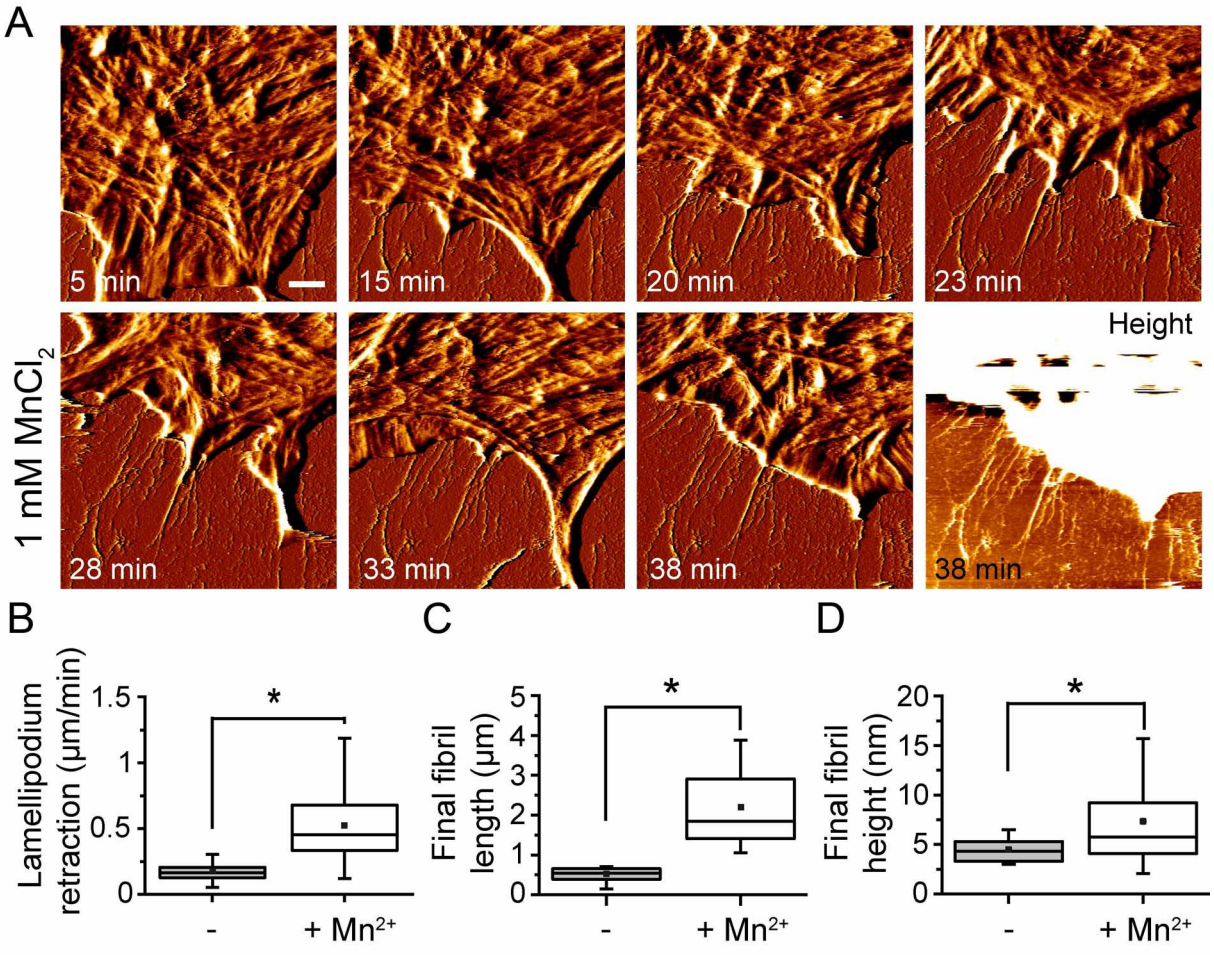

Figure 5.6: Investigating FN fibrillogenesis by time-lapse AFM in living REF52 cells in presence of Mn^{2+}. Cells were placed on FN coated mica and a region of $10\,x\,10\,\mu m^2$ was scanned by AFM in contact mode. (A) In presence of 1mM Mn2+, FN fibrils are visible already on the first AFM image (5 min, white arrows). After 38 min, long FN fibrils are created after membrane retraction (height image). Scale bar: 1.5 µm. To illustrate the influence of Mn^{2+} on FN fibril creation, the figures (B – D) show Box-and-Whisker plots of analyzed parameters from at least 9 independent experiments per condition. (B) The velocity of lamellipodium retraction in presence of Mn^{2+} is significantly higher than without it. The FN fibril length (C) and height (D) in presence of Mn^{2+} is increased compared to absence of Mn^{2+}. The statistically significant differences between the two conditions ($p < 0.01$) are denoted by one asterisk.

between cell seeding and starting AFM imaging (5 min), extensive fibril preformation at the basal cell side is unlikely. Instead, fibrils appeared to form de novo as a result of contractile forces exerted on the FN matrix during membrane retraction. In agreement, continuously imaging the same FN area before (Fig. 5.7A) and after (Fig. 5.7D) cells had extended and retracted a membrane sheet (Fig. 5.7C) indicated that FN reorganization occurred primarily at the moment of membrane retraction, but not during the brief (5 to 15 min) period the area was fully covered by the membrane extension. Determining the height profile of the unmodified FN layer before cell contact (Fig. 5.7B) and of the reorganized FN matrix after cell contact at the same position (Fig. 5.7E) again confirmed that the maximal height of the FN layer had increased from 0.5 - 3 nm to 4 - 10 nm after cell contact, consistent with FN fibril formation.

Pre-deposited plasma FN can serve as an anchor point for additional FN deposition by cells (Master Thesis Marcus Schäfer, 2013). Despite the fairly short interaction time between the extended membrane sheet and the FN layer, fibroblasts may likewise not only remodel the pre-coated plasma FN layer, but also deposit additional endogenously-synthesized FN on top. However, using a height threshold to estimate the total volume of the FN layer before and after fibrillar rearrangement yielded almost identical volume values (Fig. 5.8A and B). Therefore, remodeling appeared to occur exclusively from the pre-deposited plasma FN, not by deposition of additional cellular FN.

5.3.6 Beads on a string ultrastructure of FN fibrils

Cell-induced FN fibrils in AFM scans often appeared structurally inhomogeneous along their length (Fig. 5.4, 85 min and Fig. 5.7D). Higher resolution scans ($5 \times 5\,\mu m^2$ scan area at 512×512 pixels) of cell-induced FN fibrils revealed a complex height profile along the fibrils. Bead-like domains appeared to be interspersed by more elongated stretches (Fig. 5.9A). The height of the inter-bead structure was in the range of 1 - 2 nm, which corresponds to the diameter of a fully extended FN molecule (~ 2 nm) as demonstrated by EM and rotary shadowing (Erickson et al., 1981). In contrast, the height of the bead-like structures was typically 3 - 6 nm, close to the diameter of folded FN domains. In some regions, three or more neighboring globular domains appeared to be evenly spaced (Fig. 7B-G). This was most apparent in thinner fibrils, while bigger fibrils usually displayed no obvious periodicity. Similar periodic bead-on-a-string structures with a periodicity of $\sim$ 60 nm have been previously observed by Nelea *et al.* using high-resolution AFM scanning of FN adsorbed onto negatively-charged mica in a cell-free system (Nelea and Kaartinen, 2010). In this study, the regular bead spacing was proposed to originate from the staggered array of extended FN dimers, leading to the antiparallel juxtaposition of bulky $FNIII_{1-7}$ domain regions every 60 nm. Compared to the cell-free system used by

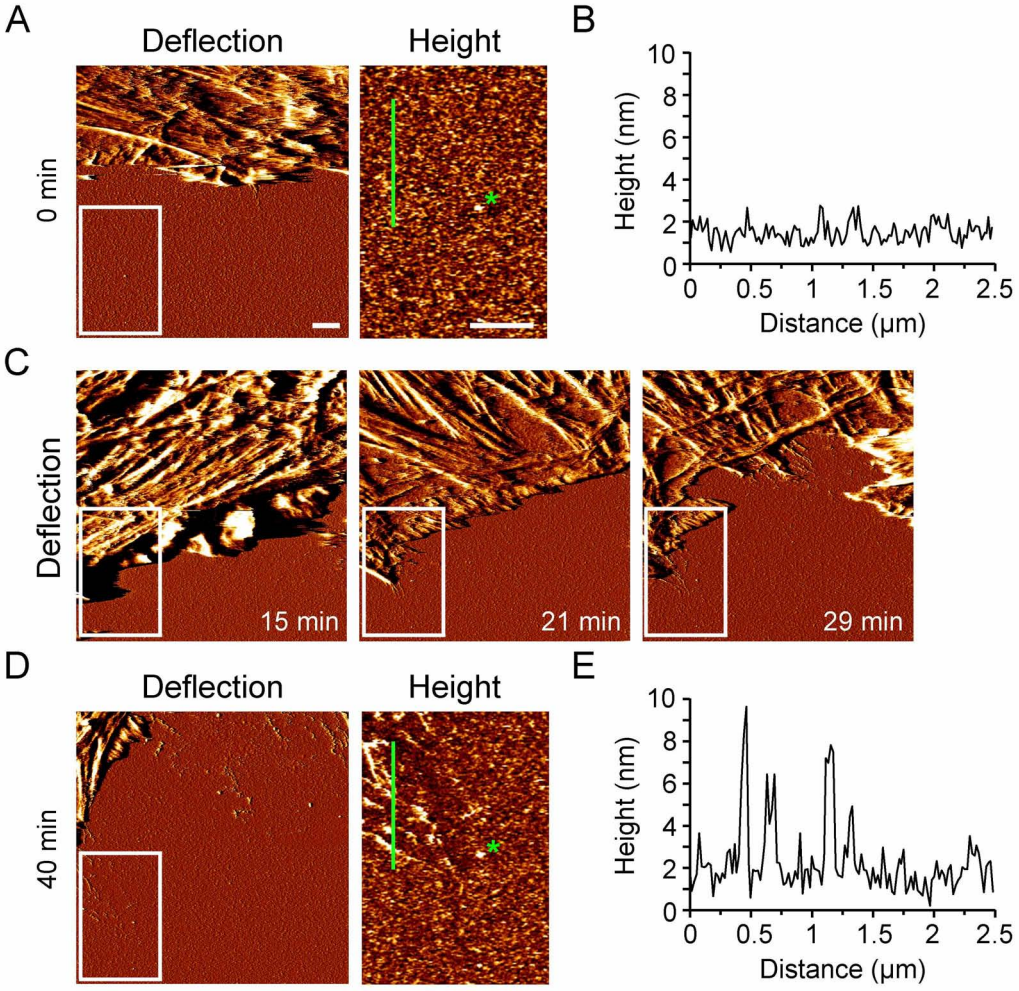

Figure 5.7: Analyzing the FN substrate before and after rearrangement by living cells in presence of 1 mM Mn^{2+}. A cell edge (a region of 10 x 10 µm^2) was observed by AFM in contact mode for 40 min. (A) AFM deflection image (left) shows a part of a lamellipodium on FN before rearrangement (time point zero). A magnification of the marked region in (A, left) shows homogeneously distributed FN (right). (B) The height profile along the light green line in (height) demonstrates quite small variations of the FN heights of max. 3 nm. (C) During the next 21 mins, the cell protruded and covered a part of the imaged area, before it started to retract back (29 min). (D) AFM deflection and height images of the same regions as in (A) after lamellipodium retraction (40 min) show FN fibrils. (E) From the AFM height image (D, right) the FN fibril height profile (D, light green line) can be extracted showing FN fibrils with heights up to 10 nm proving that the FN fibrillogenesis took place. Green asterisks indicate the representative, unchanged structure in (A, height) and (D, height). Scale bars: 1 µm. The whole time lapse can be seen in Movie 5.3.

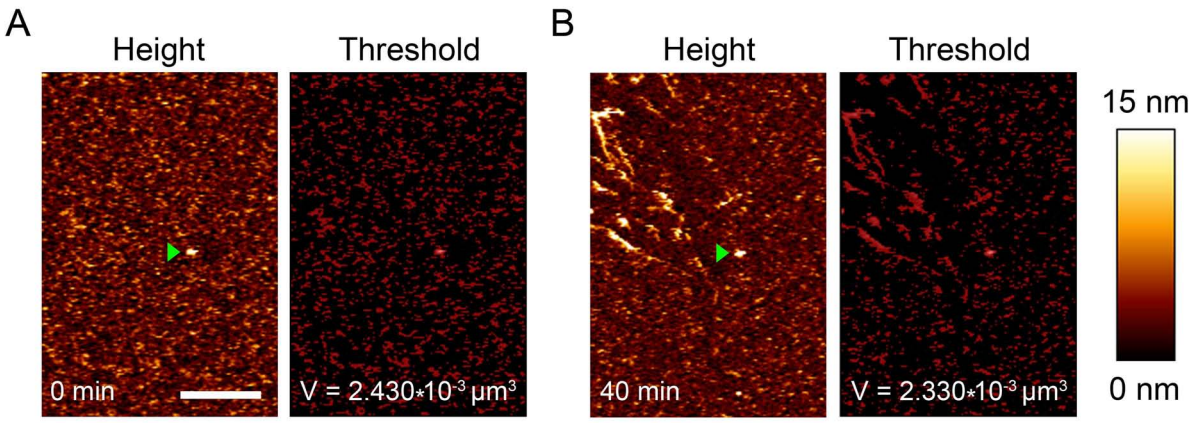

Figure 5.8: Total volume of the FN molecules before and after rearrangement by living cell. The AFM height images of the FN region at the time point 0 (A, left) and 40 min (B, left) were analyzed with Gwyddion 2.20 software. The white spot on the height images marked with the green triangle represent the reference height (22 nm). For volume analysis, the FN molecules and fibrils with heights exceeding 0.81 nm were marked via threshold algorithm. The total volume of the marked structures was calculated from the threshold images (A and B, right) via Grain Statistics algorithm. The resulting values of 2.430×10^{-3} µm^3 and 2.330×10^{-3} µm^3 for 0 and 40 min, respectively, are similar confirming, that the FN fibrils are build from on the substrate present globular FN. Scale bar 1 µm.

Nelea *et al.*, in cell-induced FN fibrils the inter-bead distance varied more widely and the array of globular domains was less regular. Nevertheless, the presence of regular globular features suggested a regular stagger of FN dimers in cell-induced FN fibrils. To quantitate the inter-bead distance, height profiles generated along seven nanofibrils were Fourier-transformed to generate a power spectrum which highlights the most frequent inter-domain distances. Due to the limited number of nanofibrils analyzed and the limited resolution of the AFM images, the power spectra were of comparatively low density and therefore provided only approximate spacing values. Nevertheless, typical interdomain spacing values of $\sim$ 77, 97, 118 and 150 nm could be determined, while the increase in spacing appeared to occur at values between $\sim 20-30$ nm.

5.3.7 Investigation of FN fibrils at the basal cell side with AFM

In the previous experiments, the structure of initial FN nanofibrils formed within the first hours after cell seeding was analyzed. Sometimes, these nanofibrillar arrays were also present in cell-free areas. Apparently, random cell migration occasionally leads to vacation of these initial fibrillar arrays. After long incubation times (16 h), however, cells had occasionally created much larger FN superfibrils (length 10 µm) located either directly beside or below the cell body, indicating additional mechanisms of fibril restructuring and

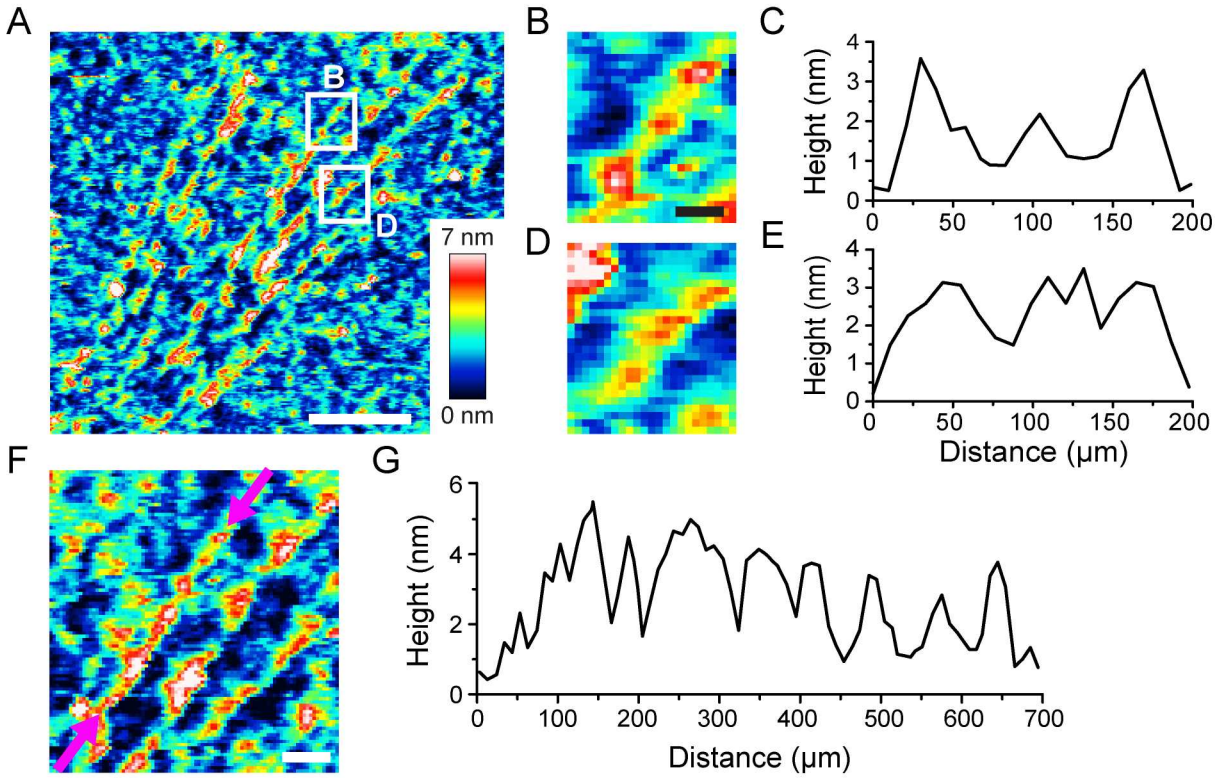

Figure 5.9: Ultrastructural analysis of cell-produced FN fibrils. (A) AFM height image of FN fibrils created by living cells. (B) and (D) AFM height images of single short FN fibrils show periodic, beaded structure. The height profiles along the fibrils of (B) and (D) is plotted in (C) and (E). (F) AFM height image of 700 nm long FN fibril with corresponding height profile (G) shows a ∼70 nm periodic, beaded structure. Scale bars: 500 nm (A), 50 nm (B) and 100 nm (F).

maturation. Superfibrils next to the cell body were usually straight, while cell-associated fibrils were often bent. Ordered fibrils next to cells and unorganized FN fibrils below cells have been previously described and explained with the large difference between forces below the cell body and at the cell periphery (Jong et al., 2006; Ladoux and Nicolas, 2012). Traditionally, the structure of FN fibrils associated with the basal cell side are investigated by fluorescence microscopy, without resolving details of the fibril structure, as they are inaccessible for direct observation by surface scanning techniques, such as SEM or AFM. To investigate whether FN superfibrils below the cell body or in cell free areas differed structurally, a recently developed method for inverting adherent cells together with the underlying matrix was used (Gudzenko and Franz, 2013), so that the basal cell side can be investigated by AFM or SEM. In this procedure, cells are incubated on PDMS coated with FN-AF488 for 16 h and afterwards fixed. Then, both, fluorescence and AFM images of the cells and FN are first taken from the apical side (Fig. 5.10A). After embedding in

a transparent UV-curable adhesive, cells are inverted and fluorescence and AFM images are collected from the basal side of the same regions (Fig. 5.10A). AFM height images of inverted cells demonstrate well-established FN fibrils at the basal cell membrane, overall corresponding well to the fluorescence signal. The AFM images revealed additional structural details not resolved by fluorescence microscopy. For instance, the curved basal FN fibrils were often structurally less homogeneous (Fig. 5.10B) and appeared in loose bundles (Fig. 5.10B), possibly as a result of decreased cellular tension below the cell body. The individual superfibrils below or next to cells, however, had similar diameters ($\sim$100 - 150 nm, Fig. 5.10D-G), indicating that cells did not further remodel or enlarge fibrils at the basal cell side.

5.3.8 Impact of cell density on FN organization

In the previous experiments, cells were seeded at comparatively low densities (10 - 100 cells/mm^2) to observe how single cells or small groups of adjacent cells reorganize FN molecules into fibrils (Fig. 5.11A). In this case, cells remodeled FN primarily at the basal side. However, working with denser cell cultures (500 cells/mm^2) showed strong FN accumulation in particular between cells (Fig. 5.11B). Furthermore, in dense cultures FN was often completely removed from the substrate, indicated by black areas on the TIRF microscopy images (Fig. 5.11D). A 3D reconstruction of confocal image stack revealed that FN in dense cell cultures was partially organized into large structures extending into z-direction. Combining fluorescence images with AFM images demonstrated that these lateral FN agglomerates localized preferentially between cells at areas of cell-cell contact (Fig. 5.11F and G, black arrows). In low density cultures, there was no correlation between FN intensity and height signal at cell borders (Fig. 5.11D and E, black arrows). This indicates that at higher densities cells remodel FN collectively into 3D structures extending several µm perpendicularly from the cell substrate at sites of cell-cell contact, whereas at lower density individual cells remodeled FN horizontally directly on the substrate. Thus, when investigating cellular FN remodeling, the influence of cell density must be considered.

FN accumulation at areas of cell-cell contact has an important function during development. For instance, FN fibrils accumulation in narrow epithelial clefts is essential for the initiation of epithelial branching (Daley and Yamada, 2013; Sakai et al., 2003). Healing wounds and fibrotic tissues display a higher fibroblast density than healthy organs as a result of higher cell proliferation rates (Muller and Rodemann, 1991; Rodemann and Muller, 1991) and these fibroblasts secrete higher levels of ECM components, including FN. FN accumulation between cells has also been suggested to facilitate a switch from cell-cell to cell-matrix adhesion (Sakai et al., 2003).

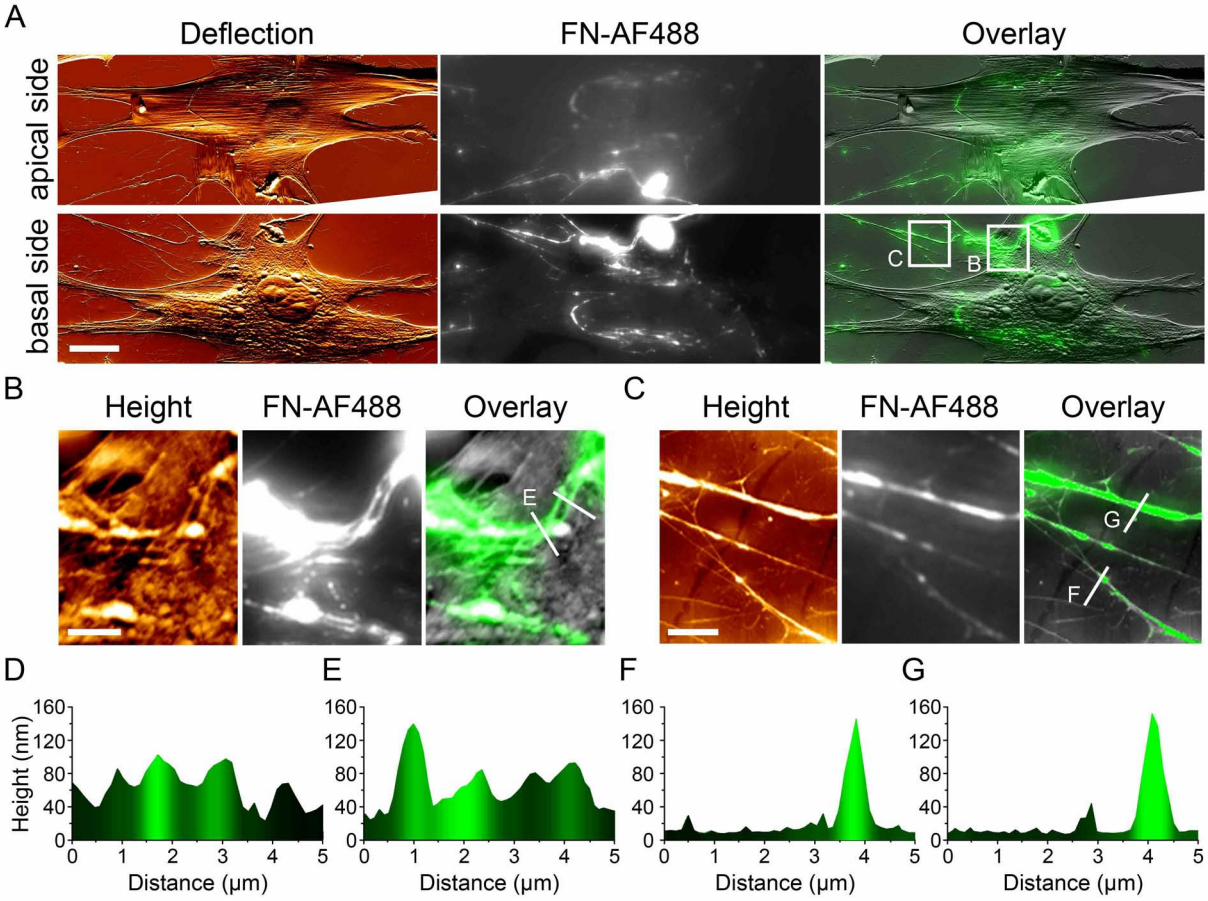

Figure 5.10: Verification of FN fibrils by AFM at the basal cell side. (A) AFM deflection images of REF52 cell (left), fluorescence images of FN-AF488 (middle panels) and AFM/fluorescence overlay (right) images showing the apical (top panels) and the basal (bottom panels) side of a cell and FN fibrils. The region from the basal cell side with attached FN fibrils (B) and the region near the cell with FN fibrils (C) are represented by corresponding height, fluorescence and overlay images. The height profiles of FN fibrils underneath (D and E) and near the cell (F and G) show both thin (~ 20 nm) and thick (up to 100 nm) fibrils. The height profiles are overlaid with the corresponding fluorescence images for a better representation of the FN fibrils. Scale bars: 20 µm (A), 5 µm (B and C).

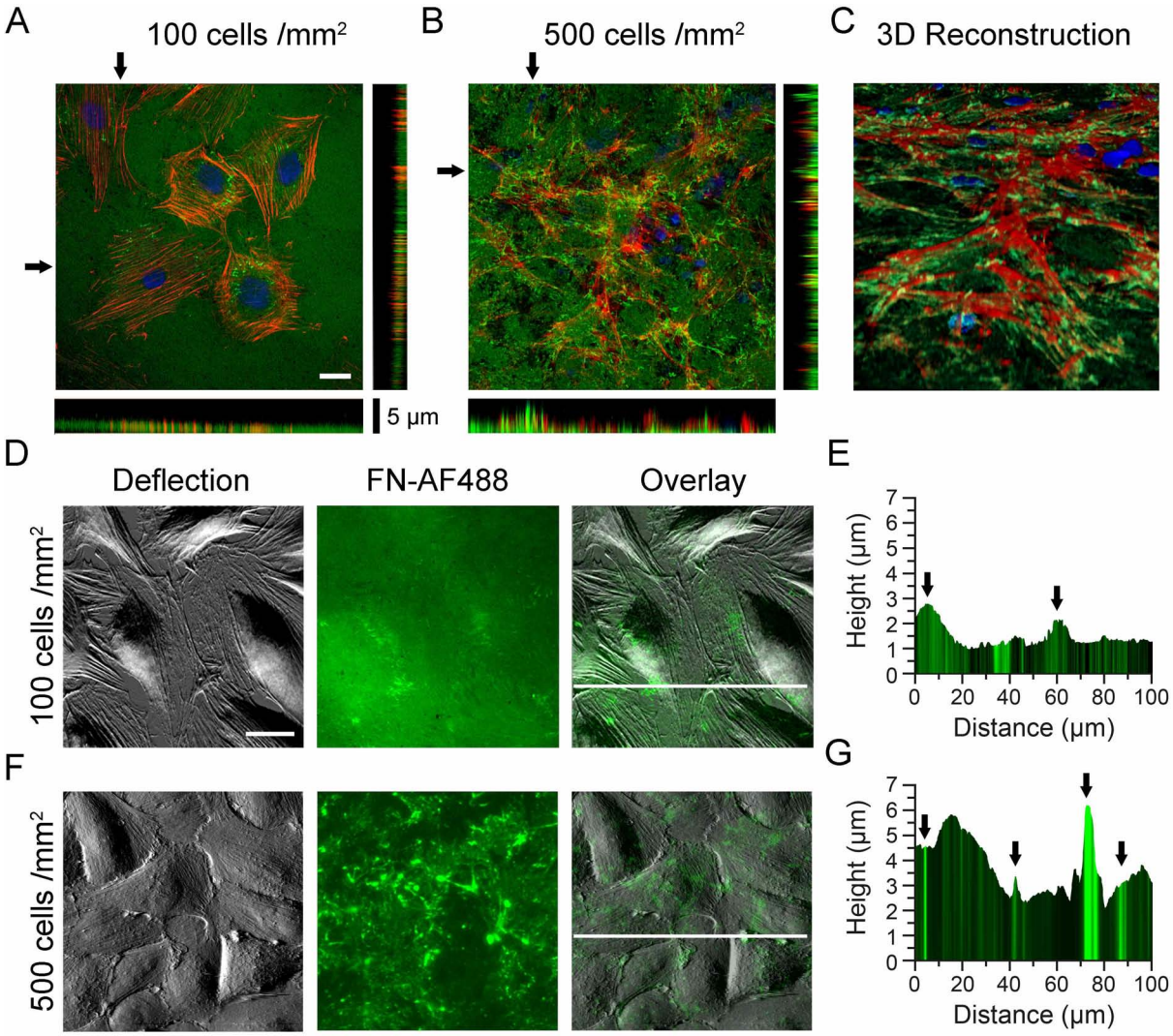

Figure 5.11: Influence of REF52 cell density on FN fibril creation. Cells at a density of 100 (A) and 500 (B) cells per mm^2 were incubated on FN-AF488 for 4 h, fixed and immunostained with phalloidin-TRITC for actin and DAPI for nucleus visualization. The fluorescence images were taken with a confocal microscope allowing getting also 3D information about FN fibril position. The overlays of the whole z-stack for cell density of 100 and 500 cells/mm^2 are shown in (A) and (B), respectively. The yz- and xz-projections (black arrows in A and B) are extracted for each condition. While at lower cell density the cells are flat and FN is homogeneously distributed between and below cells (A), at a density of 500 cells per mm^2 FN is partially removed from the surface and can be even detected above the cell (B). Scale bar: 20 µm (white bar) and 5 µm (black bar). (C) The 3D reconstruction image of a z-stack (B), visualizes this FN distribution clearer. Moreover, a 100 x 100 $µm^2$ large region of cell layers at a density of 100 (D) and 500 cells/mm^2 (F) was scanned with AFM. The height profiles overlaid with the corresponding FN fluorescence signal along the white line in (D) and (F) confirm that at higher cell density the FN peaks between cells (black arrows) may be higher than the cell edge. Scale bar: 20 µm.

5.4 Discussion

5.4.1 Timeline of cell-mediated FN fibrillogenesis

In this study, initial steps of cell-induced FN fibrillogenesis were investigated by using AFM and fluorescence microscopy. By continuous AFM life-cell imaging under physiological conditions, the dynamic formation of initial FN fibrils from their molecular precursors can be visualized at nanometer resolution for the first time. Under optimized AFM scanning conditions, cell-driven fibrillogenesis processes could be visualized over several hours without affecting cell or FN morphology. The AFM images revealed the formation of thin fibrillar FN networks that cannot be resolved with conventional fluorescence microscopy. The high resolution AFM images also showed a progressive formation of thick and long fibrils from thinner precursors and fibril bundling. A detailed analysis of AFM and fluorescence images provided additional quantitative information on fibril creation and growth.

According to AFM images and results from previous studies (Pankov et al., 2000), early FN fibrillogenesis on cell culture substrates can be divided into three phases (Fig. 5.12). Firstly, FN nanofibrils are formed at the cell periphery near focal adhesion sites after ~ 10 min of spreading. These initial fibrils are less than 300 nm long and have a diameter of less than 10 nm (Fig. 4A). These values are in agreement with earlier observations using EM that fibrils have a diameter of ~ 5 nm at this stage (Chen et al., 1978). During subsequent cell-substrate interaction (< 1 h), cells reorganize these initial fibrillar precursors into larger fibrils predominantly at the cell periphery but to some degree also more centrally beneath the cell body. At this time, fibrils are oriented mainly perpendicular to the cell edge and reach a length of 1 µm, a maximal width of 300 nm and a height of 30 nm. Cells may re-contact these early fibrils several times through cycles of membrane extension and retraction. Cells then either vacate these structures or continue to remodel FN into superfibrils, which may reach a length of up to 6 µm.

5.4.2 Estimation of the FN molecules number inside the FN fibril

The AFM images provide a means to roughly estimate the FN fibril volume and the number of FN molecules at different stages of fibrillogenesis. Knowing the number of FN dimer building blocks constituting individual fibrils formed would be of great help for better understanding the FN fibril function. Such information could, for instance, generate new insight into how cellular traction forces are shared by individual FN molecules in fibrils. AFM scanning generates topographic images from which the volume of sample features can be approximated (Barkay et al., 2005). However, while AFM images yield precise (< 0.1 nm) information about the sample height, lateral sample dimensions cannot

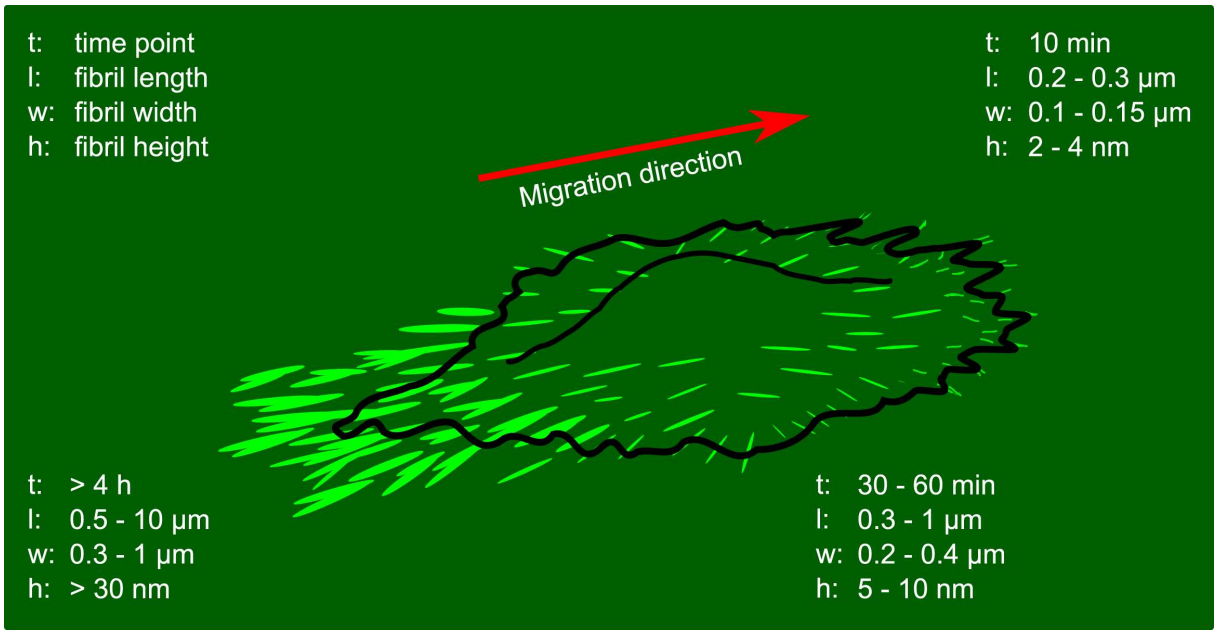

Figure 5.12: Chronological sequence of cell mediated FN fibrillogenesis. After initial spreading, the cell forms protrusions and starts to extend FN molecules, which are initially in globular compact conformation. After 10 min, the cell creates smaller fibrils with a length (l) of 0.2 – 0.3 µm, a width (w) of 0.1 – 0.15 µm and a height (h) of 2 – 4 nm. The cell protrusion and retraction events during the next 60 min lead to increased fibril lengths of up to 1 µm, widths of up to 0.4 µm and heights between 5 and 10 nm. After 4 h, the cell reorganizes FN molecules further and migrates away leaving fibrils with up to 10 µm length, 0.3 – 1 µm width and higher than 30 nm behind.

be extracted directly: Due to the finite width of the cantilever tip, measured sample profiles are a convolution of the sharp image with the shape of the tip (Fig. 1.16) (Baro and Reifenberger, 2012). However, lateral sample dimensions can be approximated if the reduction of lateral resolution due to tip convolution effects is accounted for. The precise tip geometry of commercial AFM cantilevers varies, but the nominal tip radius usually provides a workable solution for estimating the tip convolution lateral sample dimensions (Fig. 5.13 and (Barkay et al., 2005)). Thus, the number of single FN dimers incorporated into FN fibrils at different stages of fibrillogenesis can be estimated.

From EM studies it is known that the diameter d of a single extended FN dimer is approximately 2 - 3 nm (Engel et al., 1981; Erickson et al., 1981). Unfortunately, the precise lateral and longitudinal arrangement of FN dimers in the fibers is still unknown. Likewise, the molecular density of FN molecules in fibrils has not been conclusively established. Recently, Bradshaw *et. al.* determined the FN monomer concentration in micrometer-sized unstressed fibrils formed *in vitro* using quantitative deep UV transmission microscopy as 177 mg/ml (Bradshaw et al., 2012). Based on these data, approximately three-quarters of the unstressed FN fiber is composed of solute (Bradshaw et al., 2012), suggesting a rather loose lateral spacing of FN molecules and an effective cross section area occupied

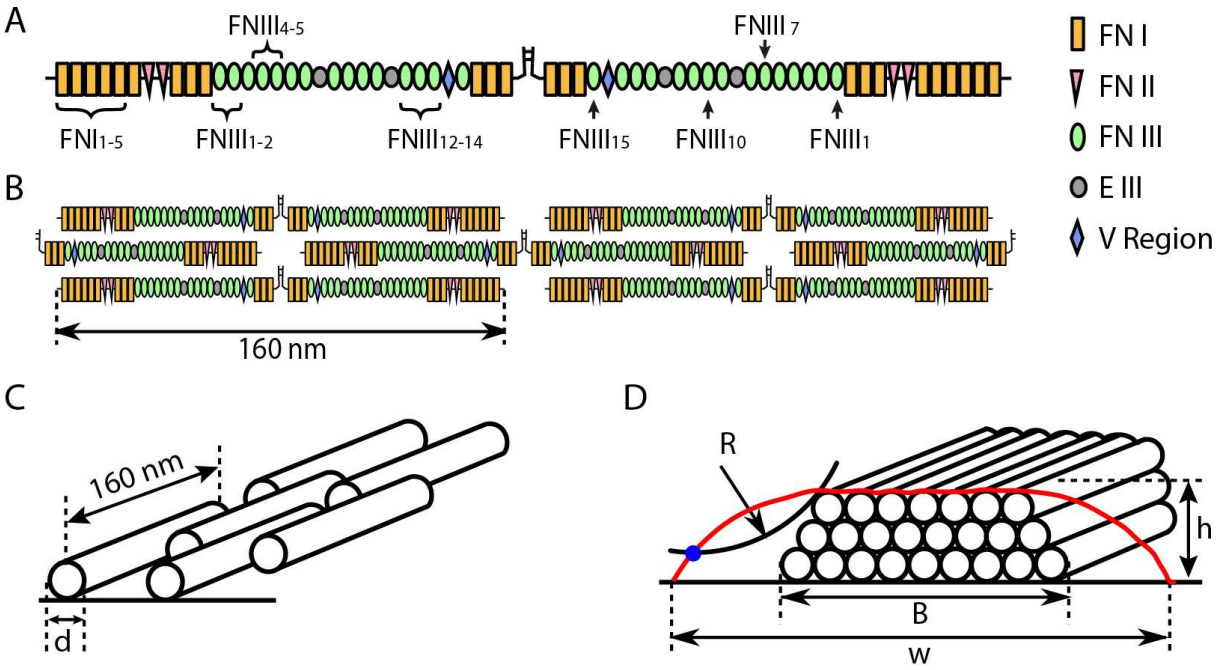

Figure 5.13: Estimation of the FN molecule number inside the FN fibril. (A) The dimeric FN molecule is schematically shown. The FN-FN interacting sites and cryptic sites are indicated with curly brackets and arrows, respectively. (B) Possible interaction of fully extended FN molecules with each other over FN-FN binding sites in the domain I_{1-5}, III_{1-2}, III_{4-5} and III_{12-14} inside the fibril. (C and D) Assuming that the FN subunits interact with other FN subunits over the whole length, the simplified model for FN fibril organization can be used to estimate the FN molecules number inside the FN fibril. d, B and h denote the molecule diameter and fibril width and height, respectively. Due to the finite tip radius R and the resulting convolution, the fibril appears on AFM scans larger having the width w.

by an individual FN dimer of 43 nm^2 (Bradshaw et al., 2012). Under external stress, FN dimers may further extend and FNIII domains may partially unfold, leading to a reduction in molecular diameter and hence a denser possible packing arrangement. Nevertheless, the final diameter and packing density of fully stretched FN dimers in physiological fibrils is still unknown, although TEM images suggest dense packing of FN molecules in cell-stretched FN fibrils (Dzamba and Peters, 1991; Singer et al., 1984).

To estimate the number of FN dimers populating a transversal fibrillar cross section, the fibrillar cross section is assumed to have an elliptical shape with a dense (hexagonal) fibril packing. As the fibril width the tip-deconvoluted value from AFM height images is used (Fig. 1.16). The earliest detectable fibrils forming within the first 30 min of matrix contact had a mean cross section area of $64 \pm 24\,nm^2$. The diameter of a single FN molecule is 3 nm yielding a cross section area of $\sim 7\,nm^2$, so that the area is taken up by ~ 8 hexagonally stacked FN molecules. Cross-sections of late fibrils (1 h, mean fibril diameter 357 ± 215 nm) could incorporate ~ 46 FN molecules. Using the same model, early fibrils formed in presence of Mn^{2+} contain approximately 44 FN molecules per cross

section (mean diameter 345 ± 63 nm), and up to 167 ± 105 molecules at later stages (mean fibril diameter 1298 ± 817 nm). Thus, the cross section profile of early FN nanofibrils may contain only few FN molecules. In agreement, EM studies have shown that FN nanofibrils can contain as few as 2 or 3 molecules (Peters et al., 1990; Peters et al., 1998). Integrin activation by Mn^{2+} apparently causes a strong increase in the number of FN molecules incorporated into early and later nanofibrils.

Estimating the total number of FN molecules in an entire FN fibril requires taking into account the FN dimer length and the lateral stagger of these dimers. An extended FN molecule is ~ 130 - 160 nm long (Erickson and Carrell, 1983). Based on EM studies using immunogold labeling, staggers of 48 nm in early and 82 nm in mature fibrils have been suggested (Dzamba and Peters, 1991; Erickson and Carrell, 1983). In this study also prominent periodic features on the order of 70 - 80 nm was detected with AFM (Fig. 5.9). Previously, extended FN dimers have been suggested to interact in an antiparallel manner in FN nanofibrils (Dzamba and Peters, 1991; To and Midwood, 2011) so that FNI_{1-5} domains from one dimer would interact with $FNIII_{12-14}$ domains from an adjacent dimer (To and Midwood, 2011). Such an antiparallel arrangement of fully extended FN dimers (160 nm) would create an extensive overlap zones of 60 nm and short gap zones of 20 nm (Fig. 5.9), Thus, each FN dimer would lead to a net-extension of the fibril by ~ 100 nm (half the extended dimer length plus gap zone). Combining this stagger with the cross section data, mature FN fibrils (diameter 64 ± 24 nm, length 0.51 ± 0.18 nm) would contain ~ 30 molecules, while more mature fibrils with maximal length of 6 µm may contain up to ~ 300 molecules. Mature fibrils with length of 10 µm formed in presence of Mn^{2+} may even contain up to ~ 500 molecules.

5.5 Conclusions

Although the FN fibrillogenesis was extensively studied in the past, there are still many open questions regarding fibril formation, structure and composition. AFM combined with fluorescence microscopy allows for detailed imaging of FN fibrils at high resolution at different stages of fibrillogenesis. Furthermore, with the cell inversion technique, in particular the initial fibrils formed at the cell basal side can be visualized. In contrast to studying fixed samples, live-cell time lapse AFM imaging shows the fibril creation, accompanied with cell migration, in real time. Thus, novel insight is provided into FN fibril creation, extension and arrangement. Moreover, the highly resolved AFM images from time-lapse show bead-string structure of FN fibrils allowing estimating the FN molecule stagger inside fibrils and so providing data about fibril structure. Furthermore, the number of FN molecules inside a fibril was approximated from AFM images. It was shown, that the fibril growth is accelerated after integrin activation with Mn^{2+}, resulting in higher amount of FN molecules inside a fibril. FN fibrillogenesis strongly depends on the cell density. In denser cell cultures, the FN fibrils are accumulated at areas of cell-cell contact, showing different mechanisms in matrix creation. These data might help to better understand the FN function during biological processes.

6 Inhibiting fibronectin fibrillogenesis using visible light

6.1 Abstract

Tissue fibronectin (FN) is usually assembled into a branched fibrillar matrix. FN fibrillogenesis is a highly regulated, cell mediated multistep process, which has been extensively studied using different techniques, among others, fluorescence microscopy. Although FN fibrillogenesis is a highly dynamic process, the initial fibril creation has not been observed in real time with fluorescence microscopy until now. Instead, fixed samples at different stages of fibril creation were analyzed, possibly missing early or intermediate stages. Observing FN fibrillogenesis in real time may therefore be helpful to understand also the early steps of fibril creation. However, initial attempts at time-lapse imaging of cell-induced FN fibrillogenesis by fluorescence microscopy failed. Surprisingly, FN fibrillogenesis appeared to be prevented in the focal area, but progressed normally in regions outside the illuminated focus circle. Apparently, light induces changes to the FN molecule which efficiently blocks the formation of fibrils. Light-induced changes on cells, such as photo toxicity, could be ruled out because illuminating the FN layer before cell seeding also blocked fibril formation. To test the influence of different irradiation parameters on the ability of FN to be reorganized into fibrils, the illumination wavelength was adjusted in the range between 400 and 640 nm using a monochromator, while the light intensity was controlled via gradient photo masks printed on transparent film. These experiments demonstrated that the photoactive effect on FN increased with decreasing wavelengths. The photo effect occurred on unlabeled FN, but was further enhanced by covalent labeling of FN with different fluorophores. Together, these experiments suggested that photo damage induced by light with short wavelength prevents FN fibrillogenesis, for instance via the production of oxygen radicals or singlet oxygen. In agreement, when the concentration of these harmful reagents in the cell culture medium was lowered by adding the radical scavenger enzyme Oxyrase® and when FN was labeled with a dye requiring long excitation wavelength (Alexa Fluor® 633), FN fibrillogenesis could be successfully imaged

for the first time using TIRF microscopy, providing additional insight into the dynamics of this process.

6.2 Introduction

FN is a dimeric extracellular matrix glycoprotein. The dimer structure is mediated by disulfide bonds at the C-terminus. The FN monomer has a multi-domain structure composed of an array of repeated modular units (FN type I, II and III repeats) (Hynes, 1985). The FN multimodular structure provides flexibility of the FN molecule, which is crucial for the FN function (Erickson et al., 1981; Rocco et al., 1987). Secreted FN has a compact conformation (Hynes, 1985), which can then be remodelled into a branched fibrillar matrix in tissues (Chen et al., 1978; Singer, 1979). The formation of such a fibrillar matrix, or fibrillogenesis, is a highly regulated multistep process (McDonald, 1988; Singh et al., 2010). Cells bind FN via integrins mostly at the RGD sequence of $FNIII_{10}$ repeat and unfold the FN molecule into an extended conformation by applying mechanical tension via the actomyosin system (Mosher, 1993; Sechler et al., 2000; Wu et al., 1995; Halliday and Tomasek, 1995). During this process FN-FN binding sites are exposed and FN molecules can interact with each other to be assembled into fibrils (Hocking et al., 2000; Singh et al., 2010). Much of the insight into FN fibrillogenesis was obtained by fluorescence microscopy. For instance, labeling FN with a fluorescent dye and imaging samples fixed at different stages of fibrillogenesis provided a first look at this complex process (Pankov and Momchilova, 2009). In other fluorescence microscopy studies, real-time observations were made of FN fibrillogenesis at later stages, where FN fibrils were already created (Jong et al., 2006; Ohashi et al., 2002). These experiments provided valuable information about the rate of fibril extension and fibril orientation at the basal cell side (De Jong et al., 2006; Ohashi et al., 2002). In this way, it was shown that cellular adhesions stretch FN molecules against the substrate by translocating $\alpha_5\beta_1$ integrin receptors from the cell periphery towards the cell center (Ohashi et al., 2002; Pankov et al., 2000). Many of these studies were performed in different cell lines, but FN fibrillogenesis was also studied in a physiological situation in the blastocoel roof of the Xenopus embryo (Winklbauer and Stoltz, 1995). The assembly of FN into fibrils is a rather rapid process in embryos. The rate of fibril extension in embryos was measured to be 4.7 µm/min (Winklbauer and Stoltz, 1995), which differs from fibril extension by cells (0.1 - 0.2 µm/min) (Ohashi et al., 2002).

Suprisingly, so far only FN fibril rearrangement, but not the formation of initial fibrils have been observed in real time by fluorescence microscopy. Apparently, collecting time-lapse images of FN by fluorescence microscopy remains a challenge, probably be-

cause exposure with UV and/or visible light affects its structure or function (DeRosa and Crutchley, 2002; Pattison et al., 2012).

Light is an electromagnetic wave characterized by its wavelength and intensity. To the human's eye, visible light has a wavelength ranging from 390 to 750 nm (Starr et al., 2007). Light with shorter wavelengths (give range) is called ultraviolet (UV) and it is subdivided into three groups: UVA (315 - 400 nm), UVB (260 - 315 nm), and UVC (100 - 260 nm). On the other side of the visible light spectrum lies the infrared (IR) region.

As Einstein showed electromagnetic radiation is carried by single wave packets, the photons (Einstein, 1905). The photon energy E is proportional to the wave frequency f and inversely proportional to the wavelength λ,

$$E = hf = \frac{hc}{\lambda} \tag{6.1}$$

where h is the Planck's constant and c is the speed of light. Thus, the shorter the wavelength, the higher the energy of a photon. On the one hand, highly energetic UV photons can interact with the atomic structure and split atomic bonds, causing damage to proteins. On the other hand, lower energy infrared photons are the main compound of thermal radiation (Einstein, 1905; Tong and Kohane, 2012). Therefore, light toxicity is classified into two main groups: photothermal and photochemical damage (Pattison et al., 2012; Tong and Kohane, 2012).

First attempts to image cell-induced FN fibril creation by fluorescence microscopy were unsuccessful, pointing to a harmful influence of exposure to light on FN functionality. Therefore, the influence of visible light on fibrillogenesis was investigated in detail and the results summarized in this Chapter. The inability of cells to create fibrils after exposure to light could be attributed to the effect of oxygen radicals during exposure. However, after optimizing the experimental conditions (labeling dye and therefore the required excitation wavelength, light intensity, the imaging (or illumination) rate and the concentration of Oxyrase® to remove oxygen radicals), FN fibrillogenesis could be imaged for the first time.

6.3 Results

6.3.1 FN rearrangement by fibroblasts

FN fibril rearrangement by living cells has been successfully visualized by fluorescence microscopy (Jong et al., 2006; Ohashi et al., 2002). Furthermore, the fibril creation by human voreskin fibroblasts (HFF) (Pankov et al., 2000) as well as REF52 cells (Section 5.3.1) was visualized with fluorescent microscopy at different time points. However, aspects concerning dynamics of fibrillogenesis cannot be awered by such snapshot imaging. In particular, time-lapse imaging is required to visualize the coordinated process involving integrin receptor binding and clustering and actin cytoskeleton polymerization during FN fibril formation. To image the early steps of FN fibrillogenesis, MEF (mouse embryonic fibroblasts) cells were used. By transiently transfecting the cells via electroporation (see section 2.2.6.1) with a plasmid DNA containing the vinculin-EGFP construct, and seeding the cells on FN labeled with AlexaFluor® 568 dye (FN-AF568), both, the FA and FN dynamics can be observed by TIRF imaging. The frame rate was set to one frame per minute (Movie 6.1), because AFM time-lapse imaging (section 5.3.3) demonstrates that the fibrillogenesis takes place on a scale of minutes. However, imaging an individual cell on the FN-AF568 layer showed that the cell had not reorganized the FN at all, even after 60 min of incubation (Fig. 6.1). Thus, the time-lapse experiments yielded a different result compared to the previous experiments with AFM time-lapse imaging, where the REF52 cells have created an extensive fibrillar network after 60 min. Nevertheless, the MEF cells spread normally during time-lapse and displayed normal vinculin clustering at FA at the cell periphery. Moreover, vinculin displayed dynamic assembly and disassembly during imaging (Movie 6.1), indicating that functional cell adhesion contacts had formed.

It is known that 1 mM Mn^{2+} increases the affinity of integrins to FN and enhances the formation of new cell adhesions (Dransfield et al., 1992; Edwards et al., 1988; Fernandez et al., 1998; Kirchhofer et al., 1990; Mould et al., 1995b). As a consequence, the fibrillogenesis process also becomes strongly enhanced (Sechler et al., 1997). The stimulatory effect of Mn^{2+} was also confirmed by AFM time lapse imaging of cells on FN (see Chapter 5, Movie 5.2). However, attempts to observe active fibrillogenesis by fluorescence microscopy in presence of Mn^{2+} were also unsuccessful.

To verify the ability of MEF cells for fibril formation, they were incubated on FN for five different time points (10, 30, 60 min, 4 and 16 h). For that, a Fluorodish was coated with FN-AF488 at a high concentration (2.5 µg/cm^2) to ensure homogeneous FN distribution (similar to the experiment described in Section 5.3.1). The fluorescence images (Fig. 6.2, top row) taken after cell fixation demonstrate different stages of FN reorganization. However, due to the high concentration of FN-AF488 on the substrate,

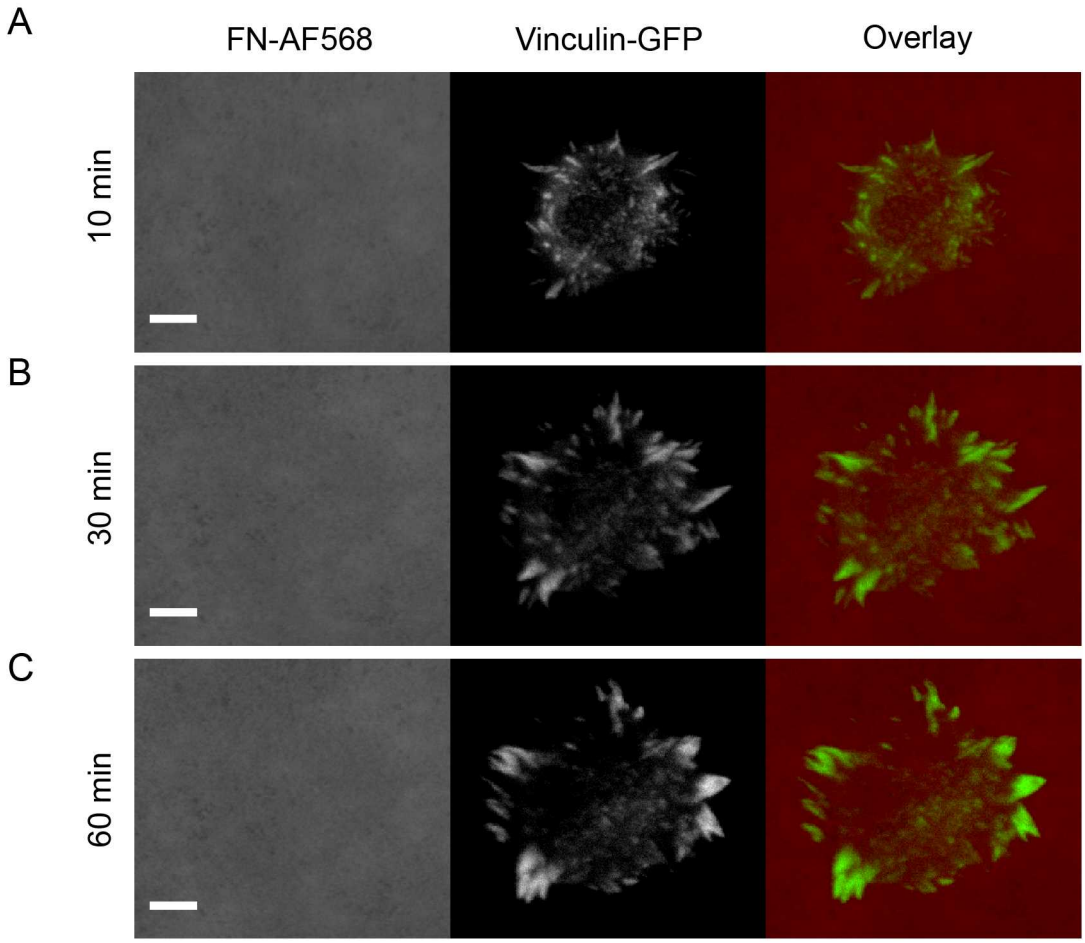

Figure 6.1: Imaging MEF cells expressing vinculin-EGFP on FN-AF568 with TIRFM. Representative fluorescence images of FN-AF568 (left), vinculin-EGFP (middle) and overlay (right) 10, 30 and 60 min after cell seeding. (A) After attachment and initial cell spreading (10 min), the cell starts to form FAs, but FN is homogeneously distributed under and near the cell. (B) After 30 min, FAs are distributed at the cell periphery. However, the FN distribution does not show any changes. (C) Even after 60 min no FN fibrils can be observed, although the cell spreads normally and forms large FA clusters. Scale bar 5 µm.

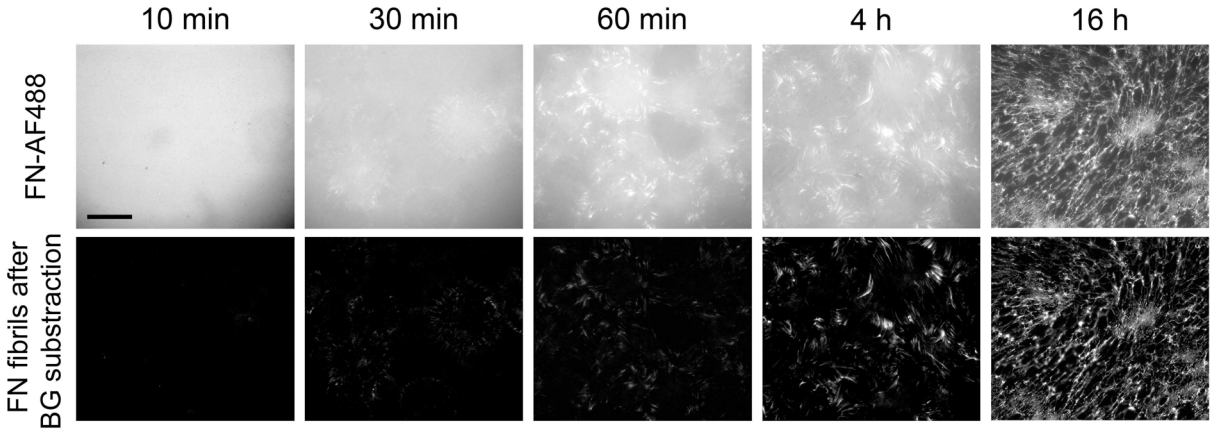

Figure 6.2: Observing FN fibril creation by fluorescence microscopy. MEF cells were incubated on FN-AF488 for different times (10, 30, 60 min, 4 and 16 h), fixed and imaged with a fluorescence microscope (upper row).The background of the fluorescence images was subtracted (lower row) for better fibril clarity at different stages of fibril creation. The first fibrils can be identified already after 10 min of incubation, while after 16 h the entire FN substrate is reorganized into fibrils. Scale bar 50 µm.

small fibrils cannot be identified on the images. To enhance the clarity of the images in the fluorescence micrographs, the background was subtracted from the original FN-AF488 fluorescence images using a "rolling ball" algorithm in ImageJ (Fig. 6.2, bottom row). On the filtered images the first FN fibrils appearing as white dots could be identified already after 10 min of incubation. With increasing incubation time, the number of FN fibrils increased and darker regions resulting from removed FN by cells from the substrate started to appear. Finally, after 16 h, a dense matrix containing branched fibrils appeared, indicating almost complete reorganization of FN-AF488.

To summarize, the fluorescence images of FN demonstrate that MEF cells are able to reorganize FN into fibrils, however, not during fluorescence time-lapse imaging. So, the influence of illumination of FN on fibrillogenesis is discussed in the following.

6.3.2 Inhibition of FN fibrillogenesis as a function of exposure time

Time lapse fluorescence microscopy imaging of labeled FN revealed that cells had not created any fibrils within the imaging field even after longer incubation times (Movie 6.1). The fibril-free area, however, was restricted to the region initially illuminated during fluorescence imaging. In contrast, neighboring areas, which were not illuminated during time lapse, always contained a multitude of fibrils. The border between the illuminated and non-illuminated areas reveals a rather abrupt transition from a fibril-free to a fibril-rich area (Fig. 6.3B). This suggests that FN fibrillogenesis may have been inhibited by light focused onto the sample during imaging. To clarify whether FN fibrillogenesis or cell

behavior are affected by expose to light could be answered by the following experiment: FN was illuminated first and cells were seeded afterwards. This procedure prevented FN fibrillogenesis similar to the results obtained during time-lapse imaging, indicating that the fibrillogenic properties of FN change within the focal area during exposure, and that the absence of fibrillogenesis in this area did not result from cell damage. Nevertheless, to exclude any potential cell damage due to extended illumination, all experiments described in the following were performed by first illuminating the FN substrate, and incubating the cells on these substrates afterwards in the dark, followed by chemical fixation and fluorescence imaging.

In a first set of experiments, the negative influence of visible light on FN fibrillogenesis was investigated as a function of exposure time. For this, different regions with an area of $0.02\,\mathrm{mm}^2$ each on an FN-AF488 substrate were exposed at a power of $0.1\,\mathrm{mW/mm}^2$ and a wavelength of $480 \pm 20\,\mathrm{nm}$ for 1, 3, 5, 7, 10 and 30 sec using a 63x LD Plan-Neofluar objective (numerical aperture of 0.75). After culturing MEF cells on the exposed substrates and chemical fixation, overview fluorescence images were collected using a 20x objective (Fig. 6.3A). With increasing exposure time, circular areas on the sample corresponding to homogeneous, unmodified FN regions become visible (from left to right). Size and intensity of the unremodeled regions on the FN substrate increased with exposure time, indicating a dose-dependent illumination effect. Apparently, longer exposure time fully inhibited FN reorganization, making the homogenous FN area appears brighter (see Fig. 6.1 after 10 min of incubation). The corresponding phase contrast image (Fig. 6.3A) demonstrates a homogeneous cell distribution on the whole sample, verifying that cells were present everywhere on the substrate. However, cells were unable to rearrange pre-illuminated FN-AF488 molecules. An explanation might be that the excitation of the labeling dye leads to radical formation affecting FN properties.

To test whether the labeling dye is responsible for light-induced prevention of FN fibrillogenesis, experiments were repeated using unlabeled FN. To visualize the FN coating, FN was stained with a polyclonal anti-FN antibody after cell incubation in these experiments (Fig. 6.3C). Fibrillogenesis was inhibited on exposed areas of unlabeled FN similar to fluorescently-labeled FN, indicating that the fluorescent label itself did not prevent fibril formation. However, the inhibitory effect could not be observed for exposure times of less than 10 sec, in contrast to 3 sec with labeled FN. This indicates that the labeling dye enhances the sensitivity of FN molecules to irradiation, but is not required for the photo-induced effect. The contrast between the exposed and non-exposed regions of non-labeled FN is also much lower compared to FN-AF488 samples even after longer exposure times (Fig. 6.3A and B), further indicting that the fluorescent dye enhances the inhibitory effect of light. However, in these experiments fibroblasts were incubated for 16 h, by which time they had secreted substantial cellular FN, which was detected by

antibody staining in addition to the substrate FN. In contrast to the exposed substrate FN, cells had reorganized the secreted FN into fibrils in all area of the substrate, causing a reduction in image contrast.

6.3.3 Investigating mechanical properties of FN by AFM

The previous experiments showed that cells are unable to reorganize exposed FN into fibrils. Fibrillogenesis is primarily a mechanical process, and mechanical properties of FN before and after exposure should therefore be compared. AFM is well-suited to investigate the mechanical stability of surface coatings. For instance, Friedrichs *et al.* (Friedrichs et al., 2007), studied the mechanical properties of different collagen matrices by scanning the substrate with increasing force exerted by the AFM tip. In case of FN, this procedure may result in partial unfolding of the FN molecules and fibril creation. Of interest in these experiments is the minimal scan force inducing the structural rearrangement of FN. To be able to determine this force, AFM cantilevers were force-calibrated before scanning. For a quantitative comparison of the created fibrils, the roughness parameters R_a (average value of absolute height amplitudes), R_p (standard deviation of the height amplitudes) and R_q (peak-to-peak distance) of the scanned area were extracted from the obtained AFM data (Section 2.2.11.1.2). To obtain reliable roughness results from these AFM scans, it is important to use an atomically flat surface, such as freshly cleaved mica, for FN coating.

After coating mica with non-exposed FN, the substrate was rinsed with PBS to remove unbound FN and scanned with AFM in contact mode in PBS. First, an overview scan of a $15\,\mathrm{x}\,15\,\mu m^2$ region of native FN was performed with a minimal scanning force of 0.1 nN to verify the homogeneous distribution of the FN. Afterwards, five smaller ($3\,\mathrm{x}\,3\,\mu m^2$) areas inside the overview region were scanned with different forces ranging from 0.1 to 3 nN. Finally, a second overview scan of the same region was performed with the minimal force of 0.1 nN to visualize potential FN rearrangement. Area scanned with forces between 0.1 and 0.5 nN do not show fibril formation (Fig. 6.4A). In contrast, forces of 1 nN or above were sufficient to reorganize FN into fibrils. An AFM scan force of 3 nN yields maximal rearrangement and maximal roughness parameters (Table 6.1).

The same rearrangement experiment was repeated with exposed FN. To prepare exposed FN, FN was irradiated on the AxioObserver inverted light microscope at $9\,mW/cm^2$ for 10 min and rinsed with PBS before scanning. The AFM images of $3\,\mathrm{x}\,3\,\mu m^2$ large scan areas of exposed FN with forces ranging from 0.1 to 2 nN do not show observable changes in the FN distribution (Fig. 6.4B). FN rearrangement into fibrils starts from applying an AFM scan force of 3 nN. In contrast to non-exposed FN, where maximal rearrangement occurs at a force of 3 nN, a force of 6 nN is needed for a comparable rearrangement of

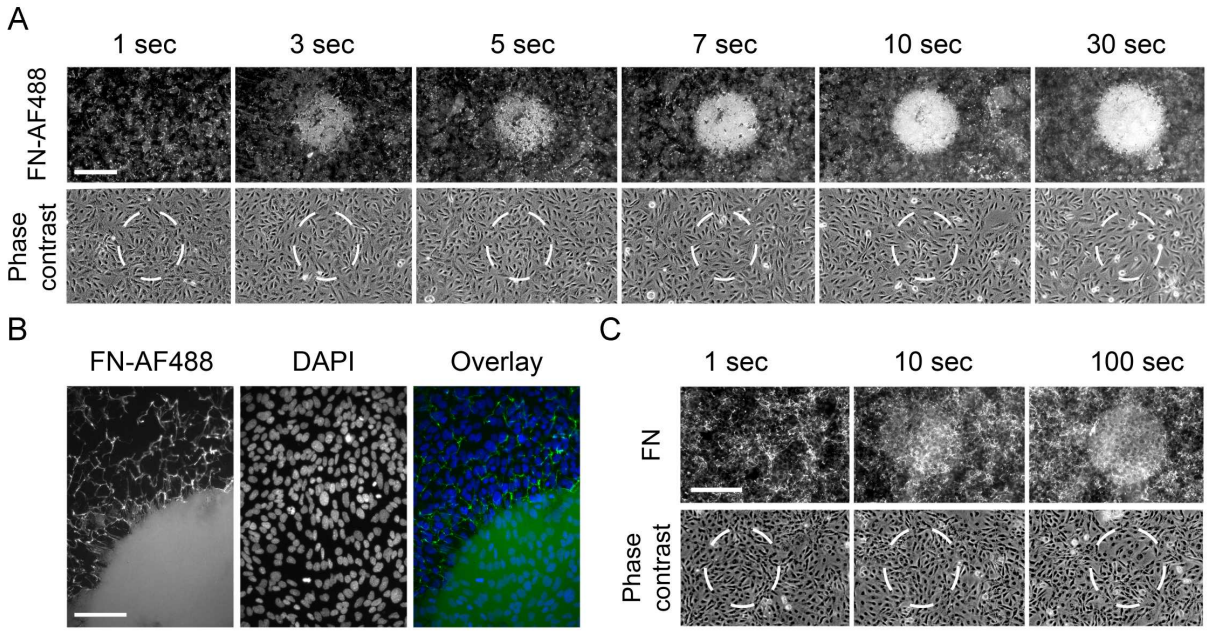

Figure 6.3: The degree of FN fibrillogenesis as a function of exposure time. Areas of 0.02 mm^2 on a FN substrate were exposed at a wavelength of 480 nm and a power of 0.1 mW/mm^2 for 1, 3, 5, 7, 10 and 30 sec. After culturing cells on the substrates for 16 h and subsequent fixing, images of the sample were taken. (A) Fluorescence images of FN (upper row) show circular regions containing non-reorganized FN, which appear brighter in comparison to the darker areas containing reorganized fibrils. Phase contrast images of MEF cells (lower row) demonstrate a homogeneous cell distribution over the whole sample including the exposed areas (marked by dashed white circles). (B) A higher magnification of the border of an illuminated area reveals a sharp transition from a homogenous distribution on exposed FN to a fibrillar distribution on non-exposed FN (left). Cell nuclei staining with DAPI (middle) and the overlay image (right) demonstrate the homogeneous cell distribution on the FN substrate. (C) Areas of 0.02 mm^2 of non-labeled FN were exposed for 1, 10 and 100 sec. After culturing and fixing MEF cells, FN was visualized by antibody staining. The bright round regions (upper row) demonstrate that exposed FN was not reorganized into fibrils. Some FN fibrils on the exposed areas can be attributed to staining of secreted cellular FN. Scale bars 50 µm (A and C), 15 µm (B).

exposed FN (Table 6.1). This suggests that exposed FN is stiffer than non-exposed FN, which may also explain the inability of cells to reorganize exposed FN. However, although larger forces are required for rearranging of exposed FN molecules, this is still possible if external forces are large enough.

These AFM rearrangement experiments demonstrate that higher forces are required for reorganizing exposed FN. One could think of two explanations for the inhibitory effect of light on FN fibrillogenesis. First, exposure of FN may induce additional intra- or inter-molecular cross-links molecules similar to chemically fixed proteins. Cross-linking of FN in its globular, folded conformation may prevent its unfolding and subsequent fibril formation. To verify this idea, unexposed FN was fixed with 1% glutaraldehyde for 30 min. Glutaraldehyde is a fixative that cross-links the proteins via amines (Kiernan, 2000). After rinsing the fixed substrates with PBS and incubation with 0.1% BH_4 to deactivate free aldehyde groups on the FN surface, the surfaces were scanned with AFM as before. The resulting AFM image demonstrates that it is impossible to reorganize glutaraldehyde-fixed FN into fibrils even using forces up to 6 nN (Fig. 6.4C). These results are supported by the roughness parameters, which do not increase throughout the whole force range between 0.1 and 6 nN. Thus, glutaraldehyde fixation prevents FN fibrillogenesis completely. However, this is not the case with exposed FN, where some residual FN rearrangement is still possible at elevated forces. Thus, light-exposed FN behaves differently from chemically-fixed FN. Irradiation of FN may also result in fewer molecular crosslinks than chemical fixation.

A second explanation for the increased stiffness of FN after exposure to light may be thermal denaturation. Generally, thermal denaturation of proteins leads to loss of function as a result of changes in protein folding (Tanford, 1968). FN is a thermally stable protein between 4 and 60°C. To prepare thermally denatured FN, it should therefore be incubated at 60°C for at least 30 min (Ingham et al., 1984). The effect of force application on fibrillogenesis of thermally denatured FN was again investigated by force-modulated AFM scanning. Even at the maximal force applied by the AFM tip of 6 nN, no fibrillar structures could be induced in thermally-denatured FN (Fig. 6.4D). The roughness parameter values of thermally denatured FN also do not increase with higher scanning force, similar to chemically fixed FN. However, R_a, R_q and R_p at 0.1 nN are larger than those of FN, exposed FN and fixed FN. This might be a result of aggregation of FN molecules due to denaturation. A closer look at the scratched areas shows that some FN molecules are apparently shifted back and forth during scanning, an effect never observed with exposed FN, indicating an overall weakening of the molecular structure of thermally-denatured FN. In conclusion, thermal denaturing as a result of exposure to a high-powered light source did not appear to be responsible for altered fibrillogenic properties.

		scanning force							
		0.1 nN	**0.5 nN**	**1 nN**	**2 nN**	**3 nN**	**4 nN**	**5 nN**	**6 nN**
FN	$\mathbf{R_a}$ **(nm)**	0.41	0.53	0.62	0.87	1.75			
	$\mathbf{R_q}$ **(nm)**	0.54	0.67	0.78	1.14	2.36			
	$\mathbf{R_p}$ **(nm)**	2.95	3.26	4.06	13.68	23.11			
FN*	$\mathbf{R_a}$ **(nm)**	0.54	0.44	0.41	0.44	0.56	0.69	0.73	1.54
	$\mathbf{R_q}$ **(nm)**	0.71	0.57	0.53	0.56	0.70	0.87	0.92	1.97
	$\mathbf{R_p}$ **(nm)**	6.41	5.88	5.84	5.15	5.40	7.34	7.66	19.84
FN-GA	$\mathbf{R_a}$ **(nm)**	0.57	0.48	0.40	0.38	0.37	0.37	0.37	0.41
	$\mathbf{R_q}$ **(nm)**	0.75	0.61	0.51	0.48	0.48	0.47	0.47	0.51
	$\mathbf{R_p}$ **(nm)**	7.56	5.66	4.01	4.54	4.27	6.03	5.64	5.23
FN-TD	$\mathbf{R_a}$ **(nm)**	1.22	1.13	1.16	1.15	1.10	1.02	0.99	1.01
	$\mathbf{R_q}$ **(nm)**	1.42	1.47	1.55	1.48	1.41	1.29	1.26	1.28
	$\mathbf{R_p}$ **(nm)**	17.8	18.11	24.05	19.03	15.84	13.91	13.66	13.05

Table 6.1: Roughness parameters R_a (average value of absolute height amplitudes), R_q (standard deviation of the height amplitudes) and R_p (peak-to-peak distance) estimated after FN reorganization with an AFM tip. FN (untreated), FN* (exposed), FN-GA (glutaraldehyde-fixed), FN-TD (thermally-denatured at 60°C for 30 min).

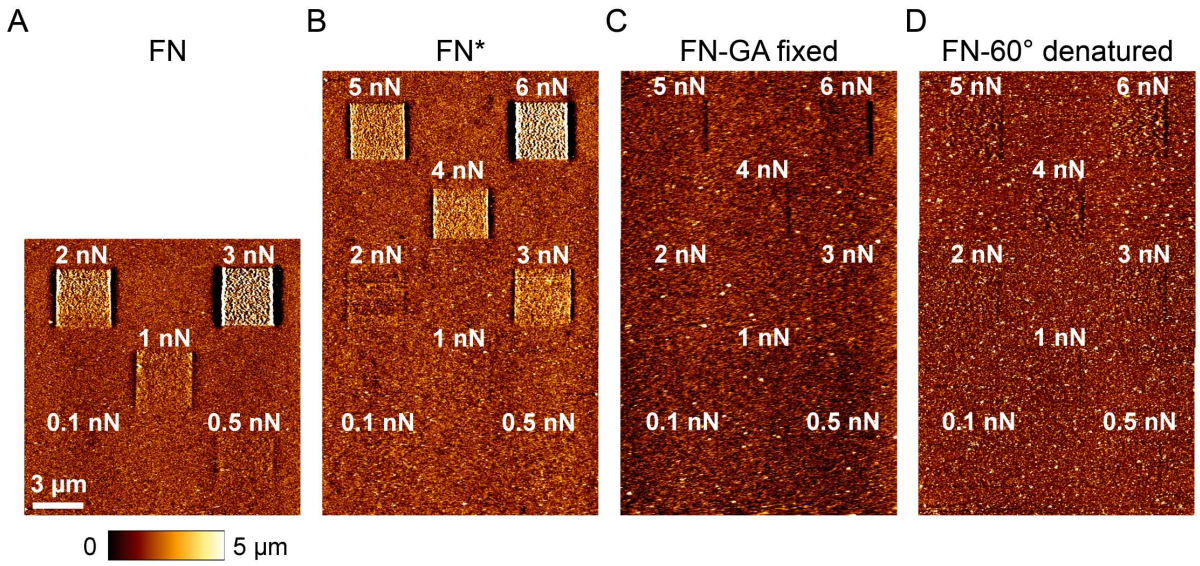

Figure 6.4: FN rearrangement by AFM. Untreated FN (A), light-exposed (B), glutaraldehyde-fixed (C) and thermally-denatured FN (D). Areas of $3 \times 3\,\mu m^2$ were scanned on each sample with different scan forces ranging from 0.1 to 6 nN. Afterwards an overview scan at a minimal force of 0.1 nN was performed to visualizes scratched areas. Scale bar 3 µm.

6.3.4 Investigating wavelength-dependent effects on FN fibrillogenesis

The previous experiments verify that the FN fibrillogenesis prevention depends on the exposure duration. However, it is well known that the impact of light on biological samples strongly varies with the light wavelength (Pattison et al., 2012). To investigate the influence of wavelength on fibrillogenesis, a monochromator (Polychrome 5000) was used to generate light of distinct wavelength. Reactions between light and FN takes place on the molecular level and the quantum nature of light has to be taken into account when comparing to results obtained at different wavelengths. Therefore, the power of the incident light on the sample as a function of the wavelength has to be measured and the total number of photons hitting the sample has to be matched by adjusting the exposure time.

To systematically test the influence of the light wavelength, distinct areas on the sample ($0.02\,mm^2$) were exposed as before with wavelengths ranging from 400 to 640 nm in 40 nm steps. Afterwards, MEF cells were cultured on FN for 16 h, fixed and non-labeled FN was stained with polyclonal anti-FN antibody and imaged. The fluorescence images demonstrate that fibroblasts were unable to efficiently reorganize exposed unlabeled FN into fibrils up to a wavelength of 560 nm (Fig. 6.5A). The same experiment was also per-

formed with labeled FN-AF488 and FN-AF568. The different labeling dyes affected how FN responds to light at longer wavelengths. While FN-AF488 cannot be rearranged after illumination at 600 nm, FN-AF568 is completely reorganized by cells after illumination with the same wavelength. Even at 640 nm, fibrillogenesis of FN-AF488 is appreciably affected (Fig. 6.5A, B, C), demonstrating a severe impact of the labeling dye on the photo-induced suppression of FN fibrillogenesis. These experiments were repeated at least three times for each condition and the mean intensity profiles of the corresponding images were plotted to compare the intensity distributions of the exposed areas (Fig. 6.5D, E, F). The photo-affected area of FN-AF568 at a wavelength of 560 nm is slightly larger in comparison to the other wavelengths. Interestingly, the AF568 dye has an absorption maximum at 577 nm, which is in the vicinity of 560 nm, indicating that at this particular wavelength the interaction between light and the labeling dye is strongest. Similarly, FN-AF488 features a larger affected area at 480 nm (Fig. 6.5E), which is also in good agreement with the dye excitation maximum of 494 nm. However, another explanation for the slightly varying photo-affected areas might be a slight defocusing during sample displacement.

6.3.5 Using a photo mask to control cell-induced FN fibrillogenesis

The previous experiments demonstrated that cell-induced FN fibrillogenesis could be spatially controlled by selectively exposing certain regions on the FN substrate. A structured photomask allows for an even greater control over the illumination pattern. Suitable photomasks, such as a gradient photomask, were produced by laser printing grayscale patterns on a transparent film (Fig. 6.6, Mask). The mask was attached with adhesive tape to the bottom of a Fluorodish from the outer side. The Fluorodish was then coated on the inside with FN-AF488 and exposed through this mask at a power of 0.1 mW/cm^2 for 5 min. Afterwards, MEF cells were seeded on the prepared substrate and incubated for 16 h. After cell fixation and nuclei staining with DAPI, the FN-AF488 substrate was imaged by fluorescence microscopy. The fluorescence images reveal a smooth transition from homogeneously distributed to remodeled, fibrillar FN (Fig. 6.6, FN-AF488). The obtained FN pattern correlates very well with the photomask (Fig. 6.6, Mask). Fibrillogenesis was blocked only in the transparent regions of the mask, while the opaque regions had protected FN from exposure, permitting subsequent cell-induced FN rearrangement. Even individual round areas, reflecting the pixel limit of the laser printer, are reproduced truthfully in the FN fibrillogenesis pattern. DAPI staining of nuclei serves to demonstrate a homogenous cell distribution in exposed and non-exposed areas (Fig. 6.6, DAPI), indicating that exposure to light only affects the ability of FN to create fibrils, but not the ability of cells to adhere and spread. Furthermore, different gray-scale intensity

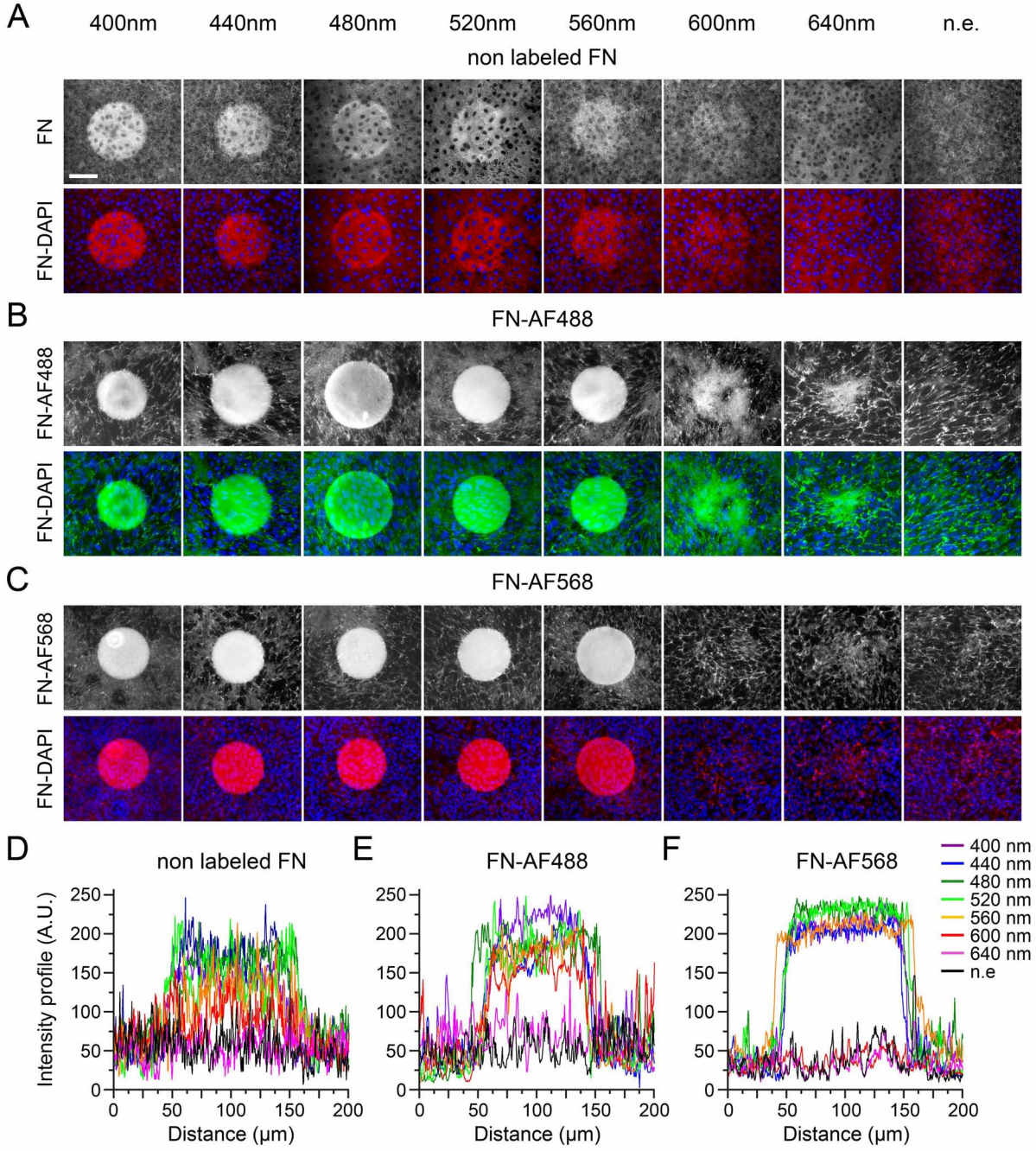

Figure 6.5: Supression of fibrillogenesis as a function of wavelength. Equal circular areas (0.02 mm^2) on unlabeled FN (A), FN-AF488 (B) and FN-AF568 (C) were illuminated through a 63x lens (numerical aperture of 0.75) with different wavelengths ranging from 400 to 640 nm in 40 nm steps. After culturing and fixing MEF cells, unlabeled FN was stained with a polyclonal anti-FN antibody. Fluorescence images of exposed areas surrounded by non-exposed areas (A-C). Intensity profiles extracted from the corresponding fluorescence images (mean values from three independent experiments at each condition) (D, E, F). The plateaus on the intensity profiles correspond to a lower degree of FN reorganization. Scale bar 50 µm (A).

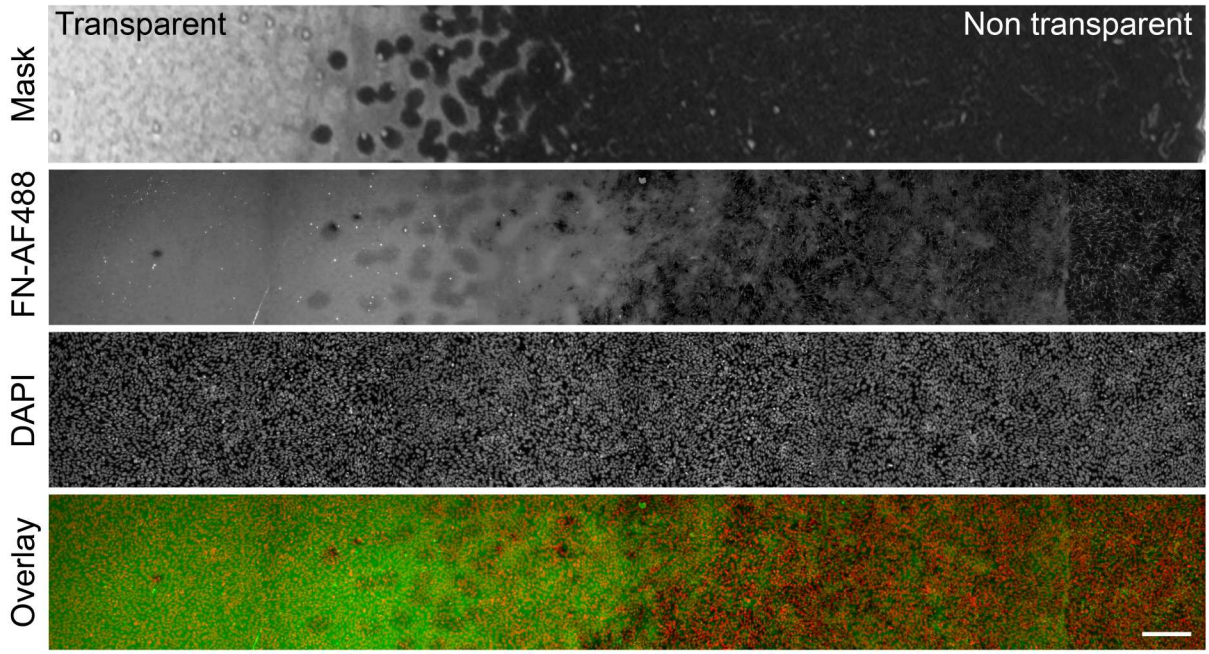

Figure 6.6: Guiding FN fibrillogenesis using a graded photomask. FN-AF488 was exposed through a gradient mask (upper image) printed on transparent film. FN was imaged after cell culturing, fixation and nuclei staining with DAPI. The fluorescence image of FN-AF488 (row second from top) demonstrates that the fibrillogenesis process was blocked in a dose-dependent manner below the transparent or semi-transparent regions. DAPI staining verifies a homogeneous cell distribution throughout the imaged region. Scale bar 200 µm.

on the remodeled FN substrate indicated a dose-dependent effect of illumination on FN fibrillogenesis.

Different photomask patterns can be chosen to produce, for example, stripe or dot patterns. It is even possible to produce complex patterns with this method. For demonstration purposes, two photomasks were printed showing the KIT Logo or the molecular model of an FN type III domain. After cell incubation, approximately 50 overlapping areas on the substrate were imaged using a 10x objective and the collected fluorescence images were aligned using Photoshop. The resulting overview image (Fig. 6.7A and C) again demonstrates the excellent match between the original photomask and the pattern of reorganized FN.

6.3.6 Reducing the impact of light on the FN properties by removing reactive oxygen species (ROS)

The previous experiments demonstrated that the degree of inhibition of FN fibrillogenesis by exposure with light depends on light intensity, exposure time, wavelength, but also the used labeling dye. In these experiments FN was maintained in PBS buffer during

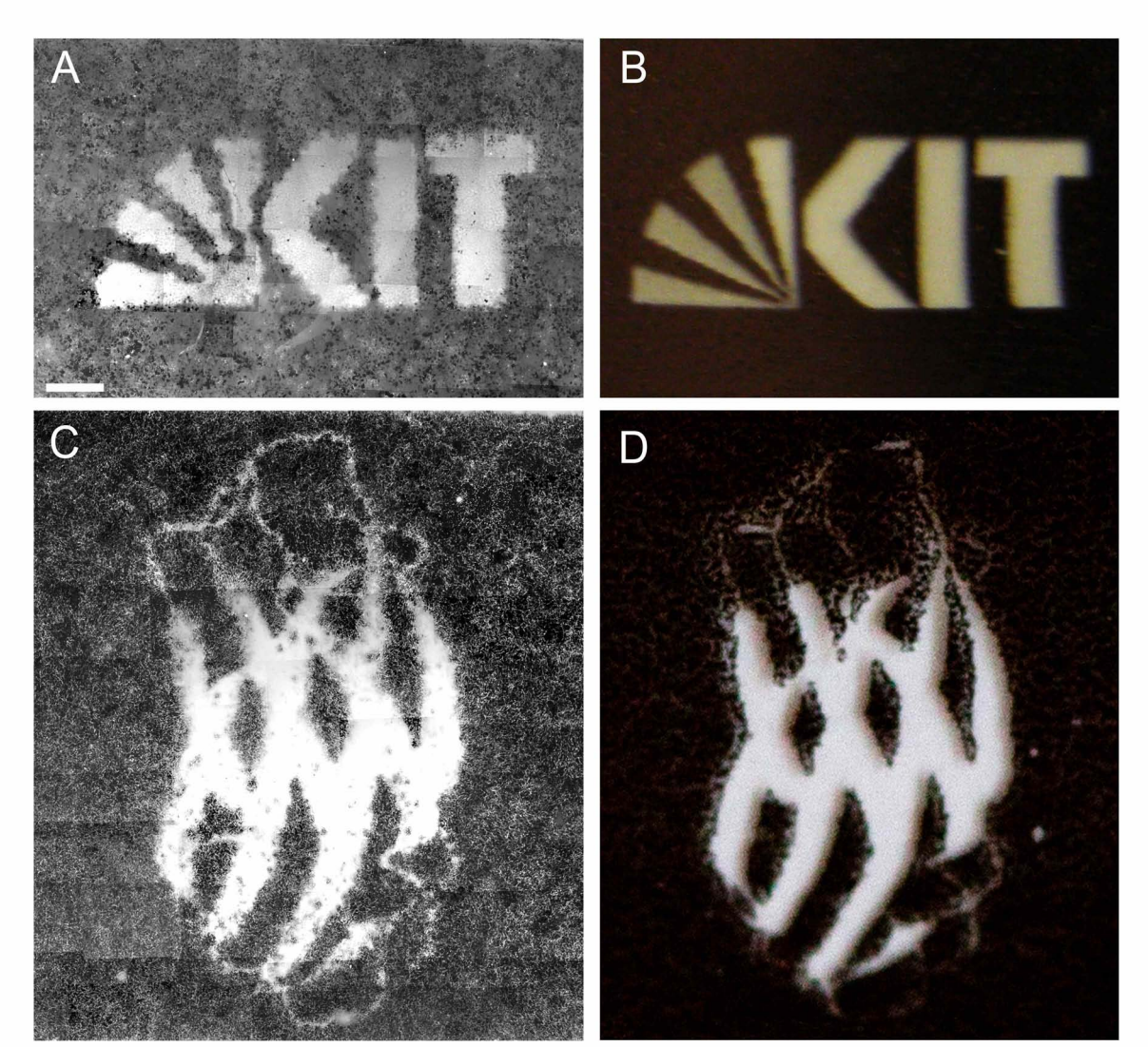

Figure 6.7: Exposing FN-AF488 through the mask of the KIT logo (B) or of a model of the FN type III domain (D) at 0.1 mW for 5 min. Corresponding fluorescence images of FN-AF488 reorganized by MEF cells for 16 h (A) and (C) demonstrate an excellent agreement to the masks. The bright regions represent transparent (B, D) and therefore exposed FN areas with prevented fibrillogenesis (A, C), while FN is reorganized below the opaque regions on the photomasks. Scale bar 200 µm.

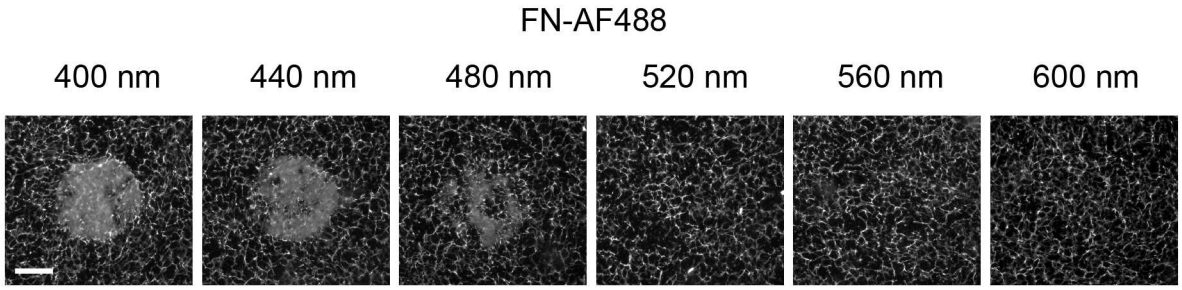

Figure 6.8: Reducing the photo damage to FN by removing ROS from the medium. FN was exposed with wavelengths ranging from 400 to 600 nm. The medium was supplemented with 0.5 U/ml Oxyrase® and 10 mM DL-lactate as a substrate for Oxyrase®N fibrillogenesis occurs at wavelengths $\geqslant$ 520 nm. However, exposing FN with 400 and 440 nm still prevents the fibrillogenesis process (bright circles). Scale bar 50 µm.

exposure, and the aqueous solution may provide the molecular mechanisms for the changed properties of exposed FN. Exposure of aqueous solutions to light with high-energy, such as the UVB (260 - 320 nm) or UVA (320 - 400 nm) bands, causes production of reactive oxygen species (ROS) including singlet oxygen ($^1O_2$), superoxide ($O_2^{\bullet-}$), its protonated form (hydroperoxyl radical; $HOO^{\bullet-}$), hydrogen peroxide (H_2O_2) and the hydroxyl radical ($HO^{\bullet}$) (Burns et al., 2012). The creation rate of $^1O_2$ is enhanced in presence of so called photosensitizers, molecules absorbing UV and visible light, such as organic dyes (DeRosa and Crutchley, 2002) or other chromophores (Pattison et al., 2012). However, the ROS level can be kept low by adding biocatalytic oxygen-reducing agents. Oxyrase® from Escherichia coli, for example, is such an enzyme (Adler et al., 1983).

To verify whether ROS in the medium contributes to the inhibition of fibrillogenesis, 0.5 U/ml Oxyrase® was added to the PBS solution and FN-AF488 was exposed with wavelengths ranging from 400 to 600 nm using a 63x objective. Afterwards, the PBS was replaced by DMEM medium and MEF cells were seeded on FN and incubated for 16 h. After cell fixation, overview images of exposed areas were taken with a 20x objective (Fig. 6.8). The fluorescence images of FN-AF488 demonstrate the inhibition of fibrillogenesis by FN exposure at wavelengths shorter than 480 nm, similar to the corresponding experiments without Oxyrase® (Fig. 6.4B). However, at 480 nm the affected area is much smaller and has a smooth transition from the remodeled to unremodeled FN, while above 520 nm no inhibition of fibrillogenesis was observed. Since inhibition of fibrillogenesis is quite strong in absence of Oxyrase® the ROS likely play a main part in changing the properties of FN during illumination.

6.3.7 Optimized conditions for visualizing FN fibrillogenesis by fluorescence microscopy

Due to the strong photo-induced inhibition of FN fibrillogenesis, this process cannot be observed by conventional fluorescence time-lapse imaging. However, the presented results provide some possibilities to minimize photo-damage of FN during time-lapse imaging. Since fibrillogenesis is strongly suppressed at wavelengths below 400 to 560 nm (Section 6.3.3), it would be beneficial to label FN with a dye that is excited at longer wavelength. For instance, AlexaFluor®633 is excited at a wavelength of 632 nm, potentially minimizing the negative effect of the excitation light on the FN. As described in the previous section, removing ROS from the medium by adding Oxyrase® substantially reduces the impact of light on FN. To further minimize photo damage, images are collected at low frequency (one image every 30 min). Furthermore, the integrin affinity to FN can be enhanced by adding 1 mM Mn^{2+} to the imaging medium resulting in the acceleration of the FN fibrillogenesis (Edwards et al., 1988; Fernandez et al., 1998; Mould et al., 1995b). Using a combination of these strategies to minimize photo damage, FN fibrillogenesis induced by HFF cells can be observed by fluorescence time-lapse microscopy for the first time, albeit with comparatively low time resolution (Movie 6.2 and Fig. 6.9). In

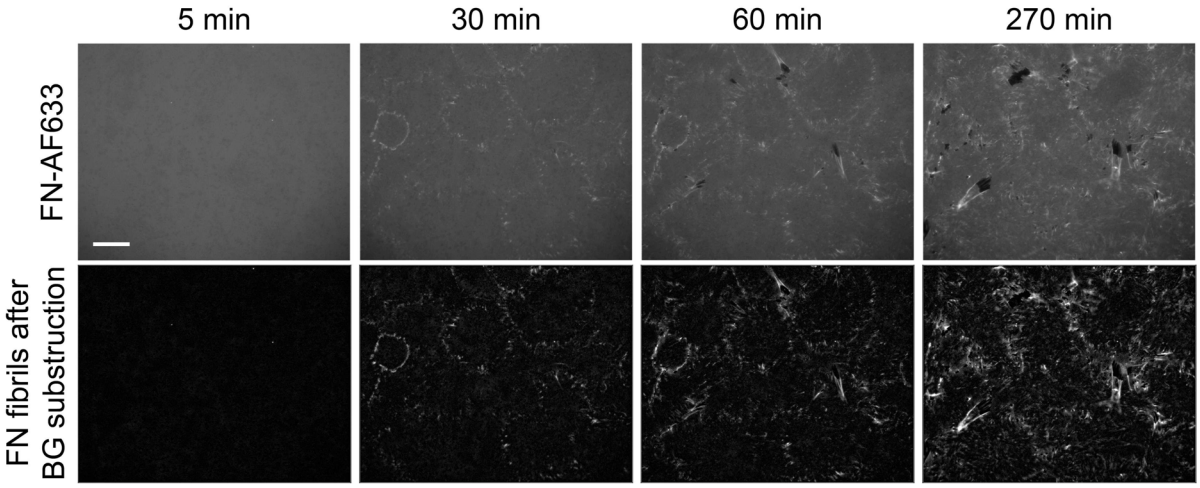

Figure 6.9: Imaging FN fibrillogenesis by fluorescence microscopy. FN-AF633 reorganized by HFF cells in DMEM medium containing 1% FCS, 1 mM $MnCl^2$, 0.5 U/ml Oxyrase® and 10 mM DL-lactate. Fluorescence images of FN-AF633 taken after 5, 30, 60, and 270 min show an increasing number of fibrils (top row). Background fluorescence was subtracted in images on the lower row to increase image contrast and to improve fibril visibility. Scale bar 20 µm.

these movies imaging started immediately after cell seeding and was performed for a total duration of 270 min. To improve the visibility of FN fibrils, image contrast was increased

by background subtracting (Fig. 6.9, lower row). As early as 30 min, small fibrils are distributed over the entire imaged region. At this time, the mean fibril length is 0.6 ± 0.2 µm and the mean velocity of fibril formation is 37 ± 9 nm/min. This value is lower than the velocity obtained by AFM time-lapse imaging (157 ± 107 nm/min, see Section 5.3.4). A reason might be the different temporal and spatial resolutions between the fluorescence and AFM time-lapse. AFM images were taken at a much higher rate (every 3 min) and with nm resolution, so that the fibril dynamics can be analyzed more precisely. Furthermore, according to the fluorescence images taken 60 and 90 min after cell seeding, the fibril growth rate decreases to 13 ± 5 nm/min at later time points. Starting after 60 min, and becoming more clearly after 270 min, cells start to remove FN fibrils from the surface, leaving dark, FN-free areas behind (Fig. 6.9).

6.4 Discussion

Fluorescence microscopy is one of the most frequently used microscopy techniques in biology and permits observing labeled proteins in real time. Fluorescence microscopy would therefore suggest itself also as a useful technique to observe the dynamic rearrangement of FN. Although FN fibrillogenesis can be visualized by life-cell AFM scanning (Section 5.3.3, Movie 5.1 and Movie 5.2), the creation of initial FN fibrils is hidden from surface scanning techniques because it takes place primarily underneath adherent cells. Therefore one would profit substantially from visualizing the FN fibrillogenesis with a fluorescence microscope. Furthermore, specific labeling would also allow for investigating the contribution of different types of proteins in this process. A number of previous studies investigating FN fibrillogenesis by fluorescence microscopy have been either performed using chemically-fixed samples or visualizing fibril extension of already created fibrils (Ohashi et al., 2002; Pankov et al., 2000). However, the initial steps of fibril creation have so far not been observed in real time. Initial attempts to visualize FN fibril creation by fluorescence time-lapse imaging failed. Surprisingly, while the imaged area remained free from fibrils, fibrils were created – unobserved – everywhere else on the sample. Obviously, illumination of the sample during time-lapse imaging prevented fibrillogenesis completely. To distinguish whether illumination negatively affected the FN molecules or the cells remodeling it into fibrils, small areas of the FN substrate were exposed to light first and cells were seeded afterwards and incubated in the dark. Again, no fibrils were created in the previously exposed areas, reproducing the results from the time lapse experiments. Thus, FN properties related to the fibrillogenesis process are changed irreversibly by exposure to visible light.

6.4.1 Photo damage to proteins

In general, photo damage depends on several parameters, including irradiation power density, irradiation time and wavelength (Tong and Kohane, 2012). In the case of FN, the degree of fibrillogenesis decreases with increasing exposure time and intensity (sections 6.3.2 and 6.3.4). Therefore, these parameters should be chosen to be as low as possible to minimize the damage to FN. However, an essential parameter is also wavelength, because it influences the character of the photo damage. Irradiation by UV and visible light causes photochemical injury, resulting in protein oxidation. There are two major pathways for photo-induced damage of proteins (Bensasson, 1983; Pattison et al., 2012). The first pathway is mediated by UVB irradiation (280 – 315 nm), where the irradiation energy is directly absorbed by amino acid residues (e.g. tryptophan, tyrosine, phenylalanine, histidine, methionine, cysteine and cysteine disulfide bonds). This energy absorption

results in the formation of electronically-excited states but also in photo-ionization reactions. However, this pathway is unlikely to occur in FN experiments presented in this thesis, because the energy of the used light (400 - 640 nm) was lower than that of UVB irradiation. A second pathway involves the absorption of energetically lower UVA and visible light (315 – 390 nm and 390 – 700 nm) by photosensitizing components (Pattison et al., 2012), such as porphyrins (Afonso et al., 1999), vitamins (Clausen et al., 2010) and polyaromatic compounds (Phillips, 2010). One further group of sensitizers is formed by labeling dye molecules. The irradiation experiments of labeled and non-labeled FN (Section 6.3.2) verified that labeled FN is more sensitive to photo damage. The sensitizers are excited into a short singlet state and then either decay to the ground state while emitting light (fluorescence) or to the more stable triplet state, allowing reactions with surrounding molecules (Phillips, 2010). The sensitizers can transfer their energy to proteins or water molecules from the medium resulting in formation of radicals, e.g. $ROO^{\bullet}$, $RO^{\bullet}$, $O_2^{\bullet -}$ or $OH^{\bullet}$ (Balasubramanian et al., 1990), which, in turn, can affect other molecules. This process is referred to as a type I mechanism. The type II mechanism involves energy transfer from a sensitizer in triplet state to molecular oxygen, resulting in the creation of singlet oxygen ($^1O_2$) (Davies, 2003). This highly reactive molecule oxidizes other molecules in the immediate vicinity of the initially excited sensitizer. Thus, both type I and type II mechanisms involve short-range electron transfers, which could explain the sudden drop in FN damage at the transition zone from exposed to non-exposed FN (Fig. 6.3B).

Irradiation with light at longer wavelengths than those of visible light (> 700 nm, infrared light) induces photo thermal damages and denaturation of proteins. Studies on FN fragments (Litvinovich and Ingham, 1995; Odermatt et al., 1982; Vuento et al., 1980) as well as whole FN molecules (Ingham et al., 1984; Pauthe et al., 2002) have demonstrated that FN is thermally stable between 4 and 60°C and fully recovers its specific conformational state at 20°C (Nelea et al., 2008). Above 60°C, thermal denaturation starts and is completed by incubating the solution for 30 min (Ingham et al., 1984). Thermally denatured FN showed different mechanical properties compared to exposed FN. The FN rearrangement experiment (Section 6.3.3) demonstrates that thermally denatured FN cannot create fibrils by reorganizing it with the AFM tip. However, the rearrangement of exposed FN results in fibril formation, albeit at an applied force stronger than that for non-exposed FN. The difference in the underlying mechanical properties is also confirmed by the large difference in roughness parameters (Table 6.1).

Due to the illumination induced effect on FN, exposure time should be kept as short and intensity as low as possible when imaging fibrillogenesis. Furthermore, a labeling dye with an excitation wavelength as long as possible should be chosen. For example, using AlexaFluor® 633 dye with an excitation wavelength of 632 nm for FN labeling allows for observing fibrillogenesis for several hours at low frame rates. The results can be further

improved by adding enzymes such as Oxyrase® to remove ROS from the medium and to suppress radical and $^1O_2$ formation.

6.4.2 Possible targets for photo-induced damages in FN

The different plasma FN splice variants contain in average 52 tyrosine, 46 phenylalanine, 38 histidine, 26 methionine and 44 cysteine residues. Furthermore, FN consists of at least 31 intra-chain disulfide bonds (-S-S-), two inter-chain disulfide bonds (Petersen et al., 1983) and two sulfhydryl (SH) groups per monomer (Smith et al., 1982). Disulfide bridges in FN are necessary for its biological activity (Ali and Hynes, 1978). Tyrosine residues in peptides are oxidized by $^1O_2$ to form dienone alcohol, which can react with neighboring nucleophiles such as thiols and amines, leading to protein cross-linking (Davies, 2003). Phenylalanine oxidation occurs only by irradiation at short wavelengths. On the one hand, the phenylalanine oxidation leads to the formation of hydroxylated benzyl ring products, and on the other hand by deprotonation of the phenylalanine molecule to the creation of benzyl radicals (Davies et al., 1991). Direct absorption of UV or visible light by histidine is not a major mechanism for causing damages. Damages at histidines occur predominantly by energy transfer from sensitizers via type II reactions (Pattison et al., 2012). The oxidation of histidine by $^1O_2$ leads to the formation of histidine-histidine and histidine-lysine cross-linked products (Pattison et al., 2012). Methionine residues can be oxidized by many species including $HO^\bullet$, H_2O_2 and $^1O_2$ (Schöneich, 2005). The oxidation by $^1O_2$ leads to the formation of a zwitterionic species (R_2S^+-OO^-) which can oxidize other methionines or eliminate H_2O_2 to form a single molecule of MetSO (Sysak et al., 1977). Cysteine photo-oxidation via $^1O_2$ results in the formation of cysteic acids (RSO_3H) (Pattison et al., 2012). Photo-oxidation of disulfide bonds via electron transfer from sensitizers yields disulfide radical anions ($RSSR^{\bullet-}$), which can rapidly dissociate into thiyl anion (RS^-) and thiyl radical ($RS^\bullet$) or transfer electrons to O_2, creating $O_2^{\bullet-}$ (Creed, 1984). The irradiation influence of FN is not well understood due to the complexity of the molecule and requires further studies.

6.4.3 Protein aggregation and fragmentation as a consequence of protein photo oxidation

Photo oxidation of proteins results in their fragmentation or in irreversible cross-linking by the formation of intermolecular covalent bonds (Bedwell et al., 1989; Dean et al., 1984; Wolff and Dean, 1986). The introduction of intermolecular crosslink's can lead to the formation of insoluble aggregates (Wang, 2005b). Non-covalent aggregates are formed solely via weak interaction forces, such as van der Waals, hydrophobic or electrostatic

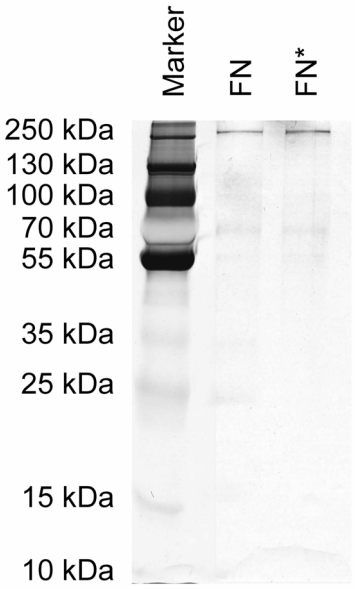

Figure 6.10: Analysis of FN on a 7.5% PAA gel. FN and irradiated FN (FN*) were loaded on the PAA gel (1 ng each), separated under non-reducing conditions and visualized by silver staining. The main band in both samples runs at approximately 250 kDa.

interactions, whereas covalent aggregates are formed via disulfide bond linkages through free thiol groups or via non-disulfide cross-linking pathways such as dityrosines (Mahler et al., 2009). Protein aggregation occurs also during chemical fixation. Therefore, the mechanical properties of chemically fixed FN were compared to those of exposed FN. The AFM rearrangement experiment (Section 6.3.3) demonstrates that fixed FN is a stiff substrate, at least for maximal applied forces up to 6 nN. However, roughness parameters extracted from AFM scans of glutaraldehyde-fixed FN (Table 6.1) were comparable to those of exposed FN if the scans were performed at a minimal force of 0.1 nN, suggesting a common molecular arrangement of the FN in both cases. However, artificial fibrillar structures could be created at larger scanning forces on exposed FN, while on fixed FN this was impossible. The results of the rearrangement experiment do not clearly prove that the changed properties of exposed FN are attributed to protein aggregation.

Some proteins can be cleft by photo-inducible fragmentation in the presence of sensitizers (Davies, 2003; Michaeli and Feitelson, 1994; Pattison et al., 2012; Sharma and Rokita, 2012). For instance, it was shown that lysozymes undergo photolysis in presence of O_2 by tryptophan oxidation and radical formation (Hawkins and Davies, 2001). In case of exposed FN, it should be verified whether the photo-inducible fragmentation occurs. To compare the molecular mass of exposed and non-exposed FN, they were separated by protein electrophoresis on a 7.5% PAA gel under non-reducing conditions followed by its visualizing via silver staining (Fig. 6.10). The results show that irradiated FN (FN*) runs at the same height as native FN, indicating that exposure does not cause FN fragmentation. FN aggregation, however, should be analyzed on a low concentration PAA gel (4%) or with other techniques, such as mass spectroscopy.

6.5 Conclusions

Time-lapse fluorescence microscopy imaging can provide important insights into dynamic biological processes. In the case of FN fibrillogenesis, however, a standard imaging approach does not work due to severe photo sensitivity of the FN molecule. In this chapter, the inhibitory influence of visible light on FN fibrillogenesis is discussed. Based on the presented results, a modified approach for successfully observation of fibrillogenesis is developed and consists of (1) minimizing exposure time and intensity, (2) using a labeling dye with an excitation maximum at longer wavelengths and (3) enzymatically decreasing the concentration of ROS in the imaging medium.

7 Concluding remarks and future directions

7.1 Cell inversion as a tool for exposing basal surface structures

Interactions between cells and the surrounding ECM regulate many cellular processes, such as differentiation, proliferation and migration (Berrier and Yamada, 2007; Gumbiner, 1996). The interplay between cells and the ECM is complex and involves many aspects, in particular, the chemical and mechanical properties of the ECM (Fig. 7.1). To investigate these interactions, two kinds of microscopy techniques are most widely used. On the one hand, optical microscopes can provide images of the entire cell, including inner cellular structures, but with limited resolution. On the other hand, scanning microscopes, such as AFM and SEM provide high-resolution images but only of the sample surface. These restrictions makes it usually impossible to collect detailed images of the basal side of adherent cells. However, exactly at the basal side the majority of cell-matrix interactions take place. There are many open questions regarding the nanoscale arrangement of cell-matrix contacts which would benefit from high-resolution imaging.

In this thesis, a new protocol for exposing the cell basal side was developed (Chapter 3), so that it can be directly investigated with scanning microscopy techniques. Moreover, this cell inversion technique provides further important advantages. The preparation protocol is fast, easy and very efficient. Thus, it is possible to study one and the same cell from both its apical and basal side. Furthermore, the optical properties of the sample do not suffer from the preparation, so that fluorescence microscopy still can be used for locating labeled cellular structures. In future, the presented inversion technique could be used to provide additional insight into the ultrastructure of cell adhesions. For example, it was shown that the spacing of integrins plays a key role for cell adhesion (Ruoslahti, 1996). In fact, if the distance between ligands the integrins bind to exceeds $\sim 70\,\mathrm{nm}$, FAs cannot form and the cells cannot adhere to the substrate (Arnold et al., 2004). These experiments indicate that regular integrin clustering is essential for effective integrin-mediated signaling. However, the molecular mechanism behind integrin clustering is not yet understood completely.

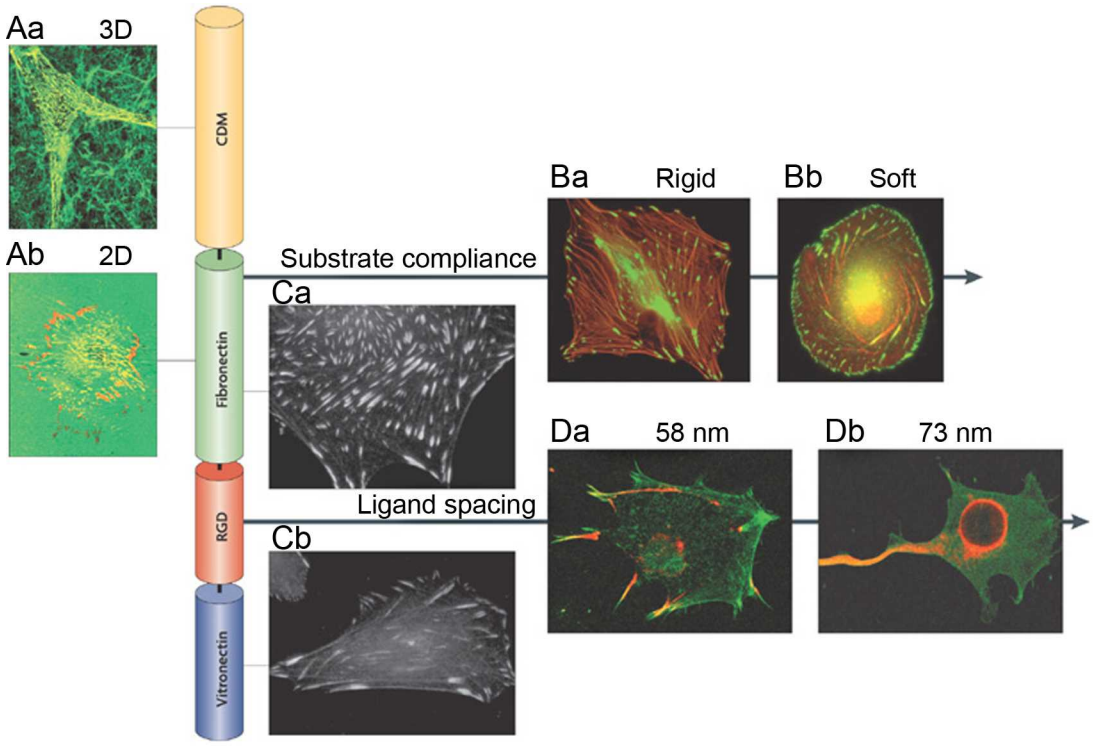

Figure 7.1: Complexity of cell-ECM interactions. The vertical "axis" containing colored cylindrical segments represents the biochemical diversity of the ECM, consisting of, for example, vitronectin, RGD sequence, fibronectin (FN), and cell-derived natural composite matrix (CDM). The ECM can vary in rigidity, ligand spacing and dimensionality. Fluorescence images demonstrate several possible cellular responses. (A) Cell morphology depending on substrate dimensionality. Cells inside 3D matrices have an elongated morphology (Aa), whereas cells on 2D spread radially (Ab). Integrin α_5 (red) localizes to FAs in cells on 2D substrates that are coated with FN (green), whereas it is organized into thin, elongated adhesions in a 3D matrix. (B) Cell shape, as well as the organization of GFP-paxillin-labelled FAs (green) and phalloidin-labelled F-actin (red) strongly differ in cells that are plated onto rigid from that on soft FN-coated substrates. (C) The organization of FAs differs in cells on rigid 2D matrices depending of the biochemical nature of ECM molecule. Cells on FN (Ca) have different FA distributions and size than cells on vitronectin (Cb). (D) Cells show differences in spreading on nanopatterned surfaces consisting of adhesive nanodots spaced at varying distances. Successful spreading and formation of FAs was observed on surfaces with a 58 nm dot spacing (Da) but failure on surface with a 73 nm dot spacing (Db) (adapted from (Geiger et al., 2009)).

Knowing the organization of integrins inside the adhesion sites (FAs, focal complexes and fibrillar adhesions), in particular, the exact integrin spacing would provide new insights into assembly and function of cell adhesions (Wehrle-Haller, 2012).

7.2 Investigating podosome organization with the cell inversion technique

Podosomes are dot-like and highly dynamic adhesive structures found in osteoclasts, macrophages and endothelial cells (Linder, 2007). During osteoclast maturation, single podosomes cluster together and form rings, which mature in several steps into a dense podosome ring called the "sealing zone" (Lakkakorpi et al., 1989; Destaing et al., 2003) (Fig. 7.2A-D). This zone provides tight attachment to the substrate and forms an isolated compartment in which bone tissue is extensively resorbed through the action of secreted proteases and protons (Vaananen et al., 2000; Gimona et al., 2008). The exact molecular mechanism of the podosome ring formation is, however, not fully understood. Moreover, matrix degradation was also observed below single podosomes without any sealing zone (Linder, 2007), so that the role of a single podosome in matrix degradation is still under debate (Nitsch et al., 1989; Ochoa et al., 2000).

The developed cell inversion method in this work was used to study the basal surface of single podosomes of osteoclasts (Chapter 4). Furthermore, the cell inversion method can be used to investigate also the podosome ring formation. Preliminary results are presented in Fig. 7.2A´-D´, showing the basal side of osteoclasts at different stages of podosome ring formation. Single, spatially separated podosomes (Fig. 7.2A´) aggregate and form several small rings (Fig. 7.2B´), which, in turn, congregate to establish a large podosome ring along the entire cell periphery (Fig. 7.2C´). Finally, individual podosomes fuse to form the sealing zone (Fig. 7.2D´). In further studies, the precise basal structure of the podosome rings with still distinguishable podosomes and the transition from such rings to the dense podosome structure forming the sealing zone border could be analyzed with AFM and SEM.

Another promising method to investigate the structure of individual podosomes and of podosome rings is focused ion beam (FIB) milling in combination with SEM imaging in a dual beam apparatus (Fig. 7.3A). Nanometer-thick layers can be milled away from the sample in a defined region by FIB, exposing a cross-section for imaging with SEM. FIB/SEM imaging has already been used to study different biological samples (Drobne et al., 2005). For example, cell-substrate interfaces of cells grown on micro- and nanopatterned substrates were studied using FIB/SEM (Fig. 7.3B-D), providing information about cell-ECM anchor points (Martinez et al., 2008). Thus, the FIB/SEM technique

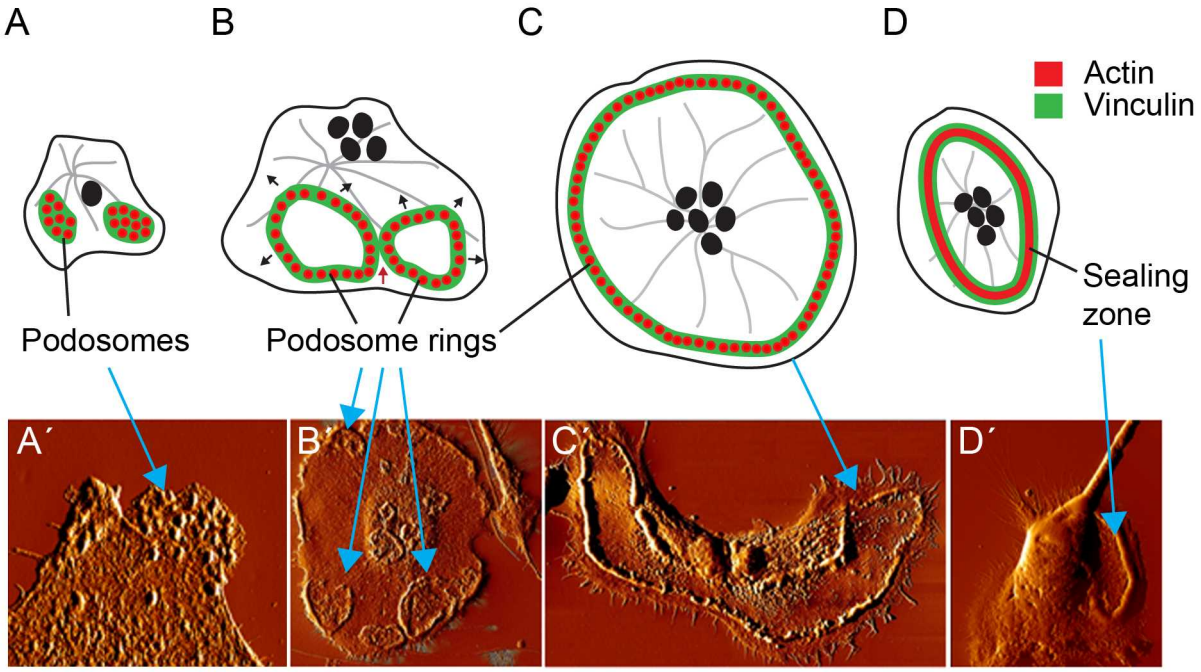

Figure 7.2: Different stages of podosome ring formation in osteoclasts. (A) Osteoclast precursor cells contain individual podosomes which are clearly separated from each other. (B) Podosome rings composed of a dense actin core (red circles) surrounded by integrin associated proteins (green). (C) Podosome ring around the cell periphery. (D) A mature osteoclast with a dense podosome ring called the sealing zone. In the sealing zone, single podosomes cannot be distinguished with conventional fluorescence microscopy any more. Instead, a dense actin ring (red) is surrounded by outer and inner rings of integrin-associated proteins (green) (adapted from (Destaing et al., 2003)). (A´-D´) AFM deflection images of the basal side of osteoclasts after inversion at different stages of podosome development corresponding to the organization of podosomes in (A-D).

is suitable for investigating cell-substrate adhesions and, therefore, also podosome structure. Moreover, this technique allows not only for obtaining a single cross-section, but sequential milling and imaging steps can produce 3D maps of samples. Such 3D maps of podosomes would help to elucidate the podosome structure in greater detail.

7.3 Studying FN fibrillogenesis in living cells by AFM

FN is an ubiquitous, multifunctional, high-molecular weight dimeric glycoprotein that is implicated in a wide array of fundamental biological processes regulating cell behavior and modification of the extracellular environment (Hynes, 1990). Fibroblasts secrete FN and incorporate it into matrices in form of fibrils. This so called FN fibrillogenesis has been studied extensively in the past, but there are still debates regarding, for example, the exact organization of FN molecules inside the fibrils.

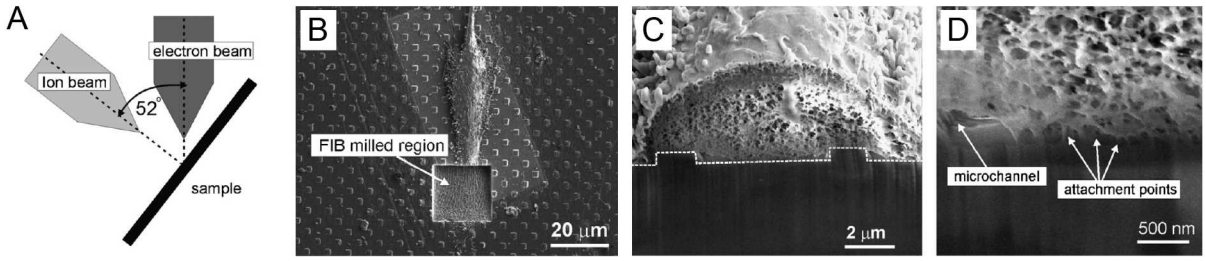

Figure 7.3: Investigating cell-substrate interactions using the FIB/SEM technique. (A) Schematic diagram of the FIB/SEM dual beam apparatus. The sample is tilted by 52° with respect to the electron beam. The ion beam has also an inclination of 52°, so that ion milling occurs at 90° to the sample, while electron imaging takes place at 52°. In this way, the cross-section perpendicular to the substrate can be imaged. (B) SEM image of a cell on a micropatterned substrate. A region of the cell was milled with FIB. (C) SEM image of a cross-section of a cell on a micropatterned substrate. The dashed line indicates the profile of the pattern on the substrate. (D) Magnified view of the cell-substrate interface showing microcavities around the substrate pillars and cell attachments pointing to the surface (adapted from (Martinez et al., 2008)).

In this work, the FN fibrillogenesis by living cells was imaged with the high resolution AFM time-lapse. Unfortunately, the AFM tip has no access to the basal side of living cells, where the initial steps of fibril creation take place. However, as soon as the cell membrane retracts, e.g. during cell migration, thin fibrils become visible at the cell edge. If a cell protrudes and retracts its membrane several times over the same area, the progression of fibril growth can be observed, ultimately resulting in the formation of large superfibrils. Usually, this process takes several hours. By activating integrins with Mn^{2+}, fibrillogenesis is significantly accelerated, facilitating the imaging and analysis of fibril extension dynamics and arrangement. Interestingly, in dense cell cultures FN fibrils accumulate between cell-cell contacts, revealing different mechanisms in matrix creation and remodeling compared to single cells.

Furthermore, AFM images of unfixed samples show a bead-on-a-string structure of FN fibrils, from which conclusions about the stagger of FN molecules inside fibrils can be drawn. Also, the number of FN molecules inside a fibril can be approximated based on the measured diameter of FN fibrils, the known diameter of a single FN molecule and by assuming a dense cylindrical packing of FN molecules in fibrils. Altogether, these data could help one to understand better the function of FN and the mechanisms of fibril formation in different biological contexts.

A recently developed AFM technique, so called force-distance (F-D) curve-based AFM imaging, allows for obtaining high resolution scanning images and simultaneous recording of an F-D curve at each pixel (Dufrene et al., 2013). Furthermore, by functionalizing the AFM tip with relevant biomolecules, this technique allows for obtaining information

about the physical and/or biological interactions between the tip and sample (Muller and Dufrene, 2008) with spatial resolution in the nanometer range and exquisite force control (Dufrene et al., 2013). Thus, e.g., maps of indentation, elasticity, adhesion, energy dissipation, electrostatic repulsion and surface charge distribution can be created (Heinz and Hoh, 1999). Furthermore, the architecture of fragile biological samples, such as living cells, cellular membranes, protein complexes, viruses and nucleic acids, can be imaged at low scanning force. In particular, the formation of fragile FN fibrils and soft cellular structures, such as membranous extensions, could be imaged with minimized affection, while maintaining spatial and temporal resolution.

7.4 Light-induced changes of FN preventing fibrillogenesis

AFM can produce highly resolved time-lapse images of biological samples. However, the size of the scanned area is rather limited and it is impossible to observe the processes taking place at the basal side of a living cell. For visualizing the dynamic relocation of specific membrane proteins in the context of a living cell, such as integrin translocation during fibril formation, it is necessary to use fluorescence microscopy. However, cell-induced FN fibrillogenesis is strongly inhibited by exposure to light. In Chapter 6 of this thesis, critical points for imaging FN fibrillogenesis by fluorescence microscopy were identified.

However, the question regarding possible conformational changes in the FN molecule or the introduction of additional intra- or intermolecular bonds caused by UV and visible light is still open. Exposing FN may also lead to denaturation, aggregation or fragmentation. Therefore, the molecular structure of exposed FN should be analyzed and compared to non-exposed FN. As a first step, protein mass spectrometry coupled with whole protein ionization by electrospray ionization (ESI) (Fenn et al., 1989) or matrix-assisted laser desorption/ionization (MALDI) (Jensen et al., 1996) could be used to compare exposed and non-exposed FN molecules. Furthermore, FN protein analysis could also be facilitated by mass analysis of peptide fragments produced by either chemical or enzymatic treatment (Trauger et al., 2002).

Another approach to investigate the differences between exposed and native FN is to compare intramolecular interactions. An FN monomer is composed of FNI, FNII and FNIII repeating units, which are organized into functional domains (Fig. 1.2). Interactions between FN domains can be quantified using AFM-based single-molecule force spectroscopy (SMFS) (Meadows and Walker, 2005; Oberhauser et al., 2002) by pulling single FN molecules away from the substrate with the AFM tip (Fig. 7.4). The FN repeats inside the molecule are stabilized by intra- and/or intermolecular interactions and

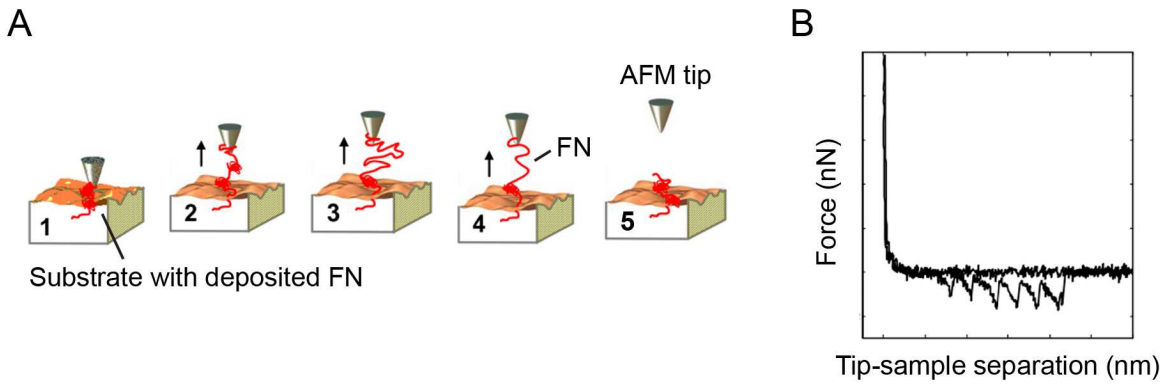

Figure 7.4: Investigating FN mechanics by AFM-SMFS. (A) Principle of AFM-SMFS. The AFM tip is approached to surface coated with FN. (1) During contact, non-specific interactions occur between the AFM tip and FN molecules. (2-4) The AFM tip is elevated from the surface with one end of the FN molecule attached. (B) Sequential FN unfolding occurs during tip elevation, resulting in several peaks in the F-D curve. (A5) After elongation of the molecule and complete unfolding, the FN molecule detaches from the tip or the surface (adapted from (Meadows and Walker, 2005)).

therefore can withstand mechanical tension applied during pulling up to several hundred pN (Craig et al., 2004; Craig et al., 2001; Gao et al., 2002; Oberhauser et al., 2002). When the externally applied force overcomes the stability of an FN repeat, the repeat unfolds spontaneously, yielding a distinct unfolding peak in the force-distance (F-D) curve (Fig. 7.4B). Other FN repeats then unfold subsequently, resulting in multiple peaks along F-D curve (Meadows and Walker, 2005). In contrast, more stable repeat will remain folded. Recording and comparing F-D curves of native and exposed FN could help to identify the structural differences.

Bibliography

Adler, H. I., W. D. Crow, C. T. Hadden, J. Hall, and R. Machanoff. 1983. "New Techniques for Growing Anaerobic-Bacteria - Experiments with Clostridium-Butyricum and Clostridium-Acetobutylicum". In: *Biotechnology and Bioengineering*, pp. 153–161.

Afonso, S. G., R. Enriquez de Salamanca, and A. M. Batlle. 1999. "The photodynamic and non-photodynamic actions of porphyrins". In: *Braz J Med Biol Res* 32, pp. 255–66.

Afshari, F. T., J. C. Kwok, M. R. Andrews, B. Blits, K. R. Martin, A. Faissner, C. Ffrench-Constant, and J. W. Fawcett. 2010b. "Integrin activation or alpha 9 expression allows retinal pigmented epithelial cell adhesion on Bruch's membrane in wet age-related macular degeneration". In: *Brain* 133, pp. 448–64.

Afshari, F. T., J. C. Kwok, L. White, and J. W. Fawcett. 2010a. "Schwann cell migration is integrin-dependent and inhibited by astrocyte-produced aggrecan". In: *Glia* 58, pp. 857–69.

Aguirre, K. M., R. J. McCormick, and J. E. Schwarzbauer. 1994. "Fibronectin self-association is mediated by complementary sites within the amino-terminal one-third of the molecule". In: *J Biol Chem* 269, pp. 27863–8.

Ali, I. U. and R. O. Hynes. 1978. "Role of disulfide bonds in the attachment and function of large, external, transformation-sensitive glycoprotein at the cell surface". In: *Biochimica Et Biophysica Acta* 510, pp. 140–50.

Andersson, Ann-Sofie, Petra Olsson, Ulf Lidberg, and Duncan Sutherland. 2003. "The effects of continuous and discontinuous groove edges on cell shape and alignment". In: *Experimental Cell Research* 288, pp. 177–188.

Aota, S., M. Nomizu, and K. M. Yamada. 1994. "The short amino acid sequence Pro-His-Ser-Arg-Asn in human fibronectin enhances cell-adhesive function". In: *J Biol Chem* 269, pp. 24756–61.

Arnold, J. R. and P. J. Boor. 1986. "Improved transmission electron microscopy (TEM) of cultured cells through a "floating sheet" method". In: *J Ultrastruct Mol Struct Res* 94, pp. 30–6.

Arnold, M., E. A. Cavalcanti-Adam, R. Glass, J. Blummel, W. Eck, M. Kantlehner, H. Kessler, and J. P. Spatz. 2004. "Activation of integrin function by nanopatterned adhesive interfaces". In: *Chemphyschem* 5, pp. 383–8.

Arroyo, A. G., J. T. Yang, H. Rayburn, and R. O. Hynes. 1996. "Differential requirements for alpha4 integrins during fetal and adult hematopoiesis". In: *Cell* 85, pp. 997–1008.

Axelrod, D. 2001. "Total internal reflection fluorescence microscopy in cell biology". In: *Traffic* 2, pp. 764–74.

Axelrod, D., T. P. Burghardt, and N. L. Thompson. 1984. "Total internal reflection fluorescence". In: *Annu Rev Biophys Bioeng* 13, pp. 247–68.

Bader, B. L., H. Rayburn, D. Crowley, and R. O. Hynes. 1998. "Extensive vasculogenesis, angiogenesis, and organogenesis precede lethality in mice lacking all alpha v integrins". In: *Cell* 95, pp. 507–19.

Balasubramanian, D., X. Du, and Jr. Zigler J. S. 1990. "The reaction of singlet oxygen with proteins, with special reference to crystallins". In: *Photochemistry and Photobiology* 52, pp. 761–8.

Baneyx, G., L. Baugh, and V. Vogel. 2001. "Coexisting conformations of fibronectin in cell culture imaged using fluorescence resonance energy transfer". In: *Proceedings of the National Academy of Sciences of the United States of America* 98, pp. 14464–14468.

Baneyx, G., L. Baugh, and V. Vogel. 2002. "Fibronectin extension and unfolding within cell matrix fibrils controlled by cytoskeletal tension". In: *Proc Natl Acad Sci U S A* 99, pp. 5139–43.

Barkay, Z., A. Teller, E. Ganor, Z. Levin, and Y. Shapira. 2005. "Atomic force and scanning electron microscopy of atmospheric particles". In: *Microsc Res Tech* 68, pp. 107–14.

Baro, A.M. and R.G. Reifenberger. 2012. *Atomic Force Microscopy in Liquid: Biological Applications*. Wiley.

Bedwell, S., R. T. Dean, and W. Jessup. 1989. "The action of defined oxygen-centred free radicals on human low-density lipoprotein". In: *Biochem J* 262, pp. 707–12.

Bèguin, L., A. Vernier, R. Chicireanu, T. Lahaye, and A. Browaeys. 2013. "Direct Measurement of the van der Waals Interaction between Two Rydberg Atoms". In: *Physical Review Letters* 110, p. 263201.

Bélanger, M. C. and Y. Marois. 2001. "Hemocompatibility, biocompatibility, inflammatory and in vivo studies of primary reference materials low-density polyethylene and polydimethylsiloxane: A review". In: *Journal of Biomedical Materials Research* 58, pp. 467–477.

Benoit, M., D. Gabriel, G. Gerisch, and H. E. Gaub. 2000. "Discrete interactions in cell adhesion measured by single-molecule force spectroscopy". In: *Nat Cell Biol* 2, pp. 313–7.

Benoit, M. and H. E. Gaub. 2002. "Measuring cell adhesion forces with the atomic force microscope at the molecular level". In: *Cells Tissues Organs* 172, pp. 174–89.

Bensasson, R. V. 1983. "Flash-Photolysis, Pulse-Radiolysis - Contribution to the Chemistry of Free-Radicals in Biological-Systems". In: *Bulletin Des Societes Chimiques Belges* 92, pp. 615–616.

Bergkvist, Magnus, Jan Carlsson, and Sven Oscarsson. 2003. "Surface-dependent conformations of human plasma fibronectin adsorbed to silica, mica, and hydrophobic surfaces, studied with use of Atomic Force Microscopy". In: *Journal of Biomedical Materials Research Part A* 64A, pp. 349–356.

Berrier, A. L. and K. M. Yamada. 2007. "Cell-matrix adhesion". In: *J Cell Physiol* 213, pp. 565–73.

Best, R. B., D. J. Brockwell, J. L. Toca-Herrera, A. W. Blake, D. A. Smith, S. E. Radford, and J. Clarke. 2003. "Force mode atomic force microscopy as a tool for protein folding studies". In: *Analytica Chimica Acta* 479, pp. 87–105.

Biela, S. A., Y. Su, J. P. Spatz, and R. Kemkemer. 2009. "Different sensitivity of human endothelial cells, smooth muscle cells and fibroblasts to topography in the nano-micro range". In: *Acta Biomaterialia* 5, pp. 2460–6.

Binnig, G., C. F. Quate, and Ch Gerber. 1986. "Atomic Force Microscope". In: *Physical Review Letters* 56, pp. 930–933.

Binnig, G. and H. Rohrer. 1999. "In touch with atoms". In: *Reviews of Modern Physics* 71, S324–S330.

Block, M. R., C. Badowski, A. Millon-Fremillon, D. Bouvard, A. P. Bouin, E. Faurobert, D. Gerber-Scokaert, E. Planus, and C. Albiges-Rizo. 2008. "Podosome-type adhesions and focal adhesions, so alike yet so different". In: *Eur J Cell Biol* 87, pp. 491–506.

Boettner, D. R., R. J. Chi, and S. K. Lemmon. 2012. "Lessons from yeast for clathrin-mediated endocytosis". In: *Nat Cell Biol* 14, pp. 2–10.

Bossy, B., E. Bossy-Wetzel, and L. F. Reichardt. 1991. "Characterization of the integrin alpha 8 subunit: a new integrin beta 1-associated subunit, which is prominently expressed on axons and on cells in contact with basal laminae in chick embryos". In: *EMBO J* 10, pp. 2375–85.

Boucaut, J. C., K. E. Johnson, T. Darribere, D. L. Shi, J. F. Riou, H. B. Bache, and M. Delarue. 1990. "Fibronectin-rich fibrillar extracellular matrix controls cell migration during amphibian gastrulation". In: *Int J Dev Biol* 34, pp. 139–47.

Boudreau, N. and M. J. Bissell. 1998. "Extracellular matrix signaling: integration of form and function in normal and malignant cells". In: *Curr Opin Cell Biol* 10, pp. 640–6.

Bowden, E. T., M. Barth, D. Thomas, R. I. Glazer, and S. C. Mueller. 1999. "An invasion-related complex of cortactin, paxillin and PKCmu associates with invadopodia at sites of extracellular matrix degradation". In: *Oncogene* 18, pp. 4440–9.

Bradshaw, M. J., M. C. Cheung, D. J. Ehrlich, and M. L. Smith. 2012. "Using molecular mechanics to predict bulk material properties of fibronectin fibers". In: *PLoS Comput Biol* 8, e1002845.

Braga, P.C. and D. Ricci. 2004. *Atomic Force Microscopy: Biomedical Methods and Applications*. Humana Press.

Brenner, K. A., S. A. Corbett, and J. E. Schwarzbauer. 2000. "Regulation of fibronectin matrix assembly by activated Ras in transformed cells". In: *Oncogene* 19, pp. 3156–63.

Brodsky, B. and A. V. Persikov. 2005. "Molecular structure of the collagen triple helix". In: *Adv Protein Chem* 70, pp. 301–39.

Buccione, R., J. D. Orth, and M. A. McNiven. 2004. "Foot and mouth: podosomes, invadopodia and circular dorsal ruffles". In: *Nat Rev Mol Cell Biol* 5, pp. 647–57.

Burghardt, T. P. and D. Axelrod. 1981. "Total internal reflectionfluorescence photobleaching recovery study of serum albumin adsorption dynamics". In: *Biophys J* 33, pp. 455–67.

Burns, J. M., W. J. Cooper, J. L. Ferry, D. W. King, B. P. DiMento, K. McNeill, C. J. Miller, W. L. Miller, B. M. Peake, S. A. Rusak, A. L. Rose, and T. D. Waite. 2012. "Methods for reactive oxygen species (ROS) detection in aqueous environments". In: *Aquatic Sciences* 74, pp. 683–734.

Burns, S., A. J. Thrasher, M. P. Blundell, L. Machesky, and G. E. Jones. 2001. "Configuration of human dendritic cell cytoskeleton by Rho GTPases, the WAS protein, and differentiation". In: *Blood* 98, pp. 1142–9.

Burridge, K. and M. Chrzanowska-Wodnicka. 1996. "Focal adhesions, contractility, and signaling". In: *Annu Rev Cell Dev Biol* 12, pp. 463–518.

Byzova, Tatiana V., Wes Kim, Ronald J. Midura, and Edward F. Plow. 2000. "Activation of Integrin $\alpha_V\beta_3$ Regulates Cell Adhesion and Migration to Bone Sialoprotein". In: *Experimental Cell Research* 254, pp. 299–308.

Calderwood, D. A. 2004. "Integrin activation". In: *J Cell Sci* 117, pp. 657–66.

Calle, Y., G. E. Jones, C. Jagger, K. Fuller, M. P. Blundell, J. Chow, T. Chambers, and A. J. Thrasher. 2004. "WASp deficiency in mice results in failure to form osteoclast sealing zones and defects in bone resorption". In: *Blood* 103, pp. 3552–61.

Campbell, I. D. and M. J. Humphries. 2011. "Integrin structure, activation, and interactions". In: *Cold Spring Harb Perspect Biol* 3, a004994.

Canty, E. G. and K. E. Kadler. 2005. "Procollagen trafficking, processing and fibrillogenesis". In: *J Cell Sci* 118, pp. 1341–53.

Chellaiah, M., N. Kizer, M. Silva, U. Alvarez, D. Kwiatkowski, and K. A. Hruska. 2000. "Gelsolin deficiency blocks podosome assembly and produces increased bone mass and strength". In: *J Cell Biol* 148, pp. 665–78.

Chen, H., L. Yuan, W. Song, Z. K. Wu, and D. Li. 2008. "Biocompatible polymer materials: Role of protein-surface interactions". In: *Progress in Polymer Science* 33, pp. 1059–1087.

Chen, L. B., A. Murray, R. A. Segal, A. Bushnell, and M. L. Walsh. 1978. "Studies on intercellular LETS glycoprotein matrices". In: *Cell* 14, pp. 377–91.

Chen, Y., Y. Wu, and J. Cai. 2007. "Atomic force microscopic investigation on the potential early intermediate stages of fibrillogenesis of fibronectin within fibrils". In: *Biochem Biophys Res Commun* 361, pp. 391–7.

Chiang, H. Y., V. A. Korshunov, A. Serour, F. Shi, and J. Sottile. 2009. "Fibronectin is an important regulator of flow-induced vascular remodeling". In: *Arterioscler Thromb Vasc Biol* 29, pp. 1074–9.

Chiusaroli, R., H. Knobler, C. Luxenburg, A. Sanjay, S. Granot-Attas, Z. Tiran, T. Miyazaki, A. Harmelin, R. Baron, and A. Elson. 2004. "Tyrosine phosphatase epsilon is a positive regulator of osteoclast function in vitro and in vivo". In: *Mol Biol Cell* 15, pp. 234–44.

Cho, J., J. L. Degen, B. S. Coller, and D. F. Mosher. 2005. "Fibrin but not adsorbed fibrinogen supports fibronectin assembly by spread platelets. Effects of the interaction of alphaIIb beta3 with the C terminus of the fibrinogen gamma-chain". In: *J Biol Chem* 280, pp. 35490–8.

Cho, J. and D. F. Mosher. 2006. "Enhancement of thrombogenesis by plasma fibronectin cross-linked to fibrin and assembled in platelet thrombi". In: *Blood* 107, pp. 3555–63.

Chung, C. Y., L. Zardi, and H. P. Erickson. 1995. "Binding of tenascin-C to soluble fibronectin and matrix fibrils". In: *J Biol Chem* 270, pp. 29012–7.

Cisneros, D. A., C. Hung, C. M. Franz, and D. J. Muller. 2006. "Observing growth steps of collagen self-assembly by time-lapse high-resolution atomic force microscopy". In: *J Struct Biol* 154, pp. 232–45.

Clausen, M. R., K. Huvaere, L. H. Skibsted, and J. Stagsted. 2010. "Characterization of peroxides formed by riboflavin and light exposure of milk. Detection of urate hydroperoxide as a novel oxidation product". In: *J Agric Food Chem* 58, pp. 481–7.

Colige, A., F. Ruggiero, I. Vandenberghe, J. Dubail, F. Kesteloot, J. Van Beeumen, A. Beschin, L. Brys, C. M. Lapiere, and B. Nusgens. 2005. "Domains and maturation processes that regulate the activity of ADAMTS-2, a metalloproteinase cleaving the aminopropeptide of fibrillar procollagens types I-III and V". In: *J Biol Chem* 280, pp. 34397–408.

Corbett, S. A., L. Lee, C. L. Wilson, and J. E. Schwarzbauer. 1997. "Covalent cross-linking of fibronectin to fibrin is required for maximal cell adhesion to a fibronectin-fibrin matrix". In: *J Biol Chem* 272, pp. 24999–5005.

Cox, S., E. Rosten, J. Monypenny, T. Jovanovic-Talisman, D. T. Burnette, J. Lippincott-Schwartz, G. E. Jones, and R. Heintzmann. 2012. "Bayesian localization microscopy reveals nanoscale podosome dynamics". In: *Nature Methods* 9, pp. 195–200.

Craig, D., M. Gao, K. Schulten, and V. Vogel. 2004. "Tuning the mechanical stability of fibronectin type III modules through sequence variations". In: *Structure* 12, pp. 21–30.

Craig, D., A. Krammer, K. Schulten, and V. Vogel. 2001. "Comparison of the early stages of forced unfolding for fibronectin type III modules". In: *Proc Natl Acad Sci U S A* 98, pp. 5590–5.

Creed, D. 1984. "The Photophysics and Photochemistry of the near-Uv Absorbing Amino-Acids .3. Cystine and Its Simple Derivatives". In: *Photochemistry and Photobiology* 39, pp. 577–583.

Curtis, Adam S. G. and Chris D. W. Wilkinson. 1998. "Reactions of cells to topography". In: *Journal of Biomaterials Science, Polymer Edition* 9, pp. 1313–1329.

Daley, W. P. and K. M. Yamada. 2013. "ECM-modulated cellular dynamics as a driving force for tissue morphogenesis". In: *Curr Opin Genet Dev* 23, pp. 408–14.

Dallas, S. L., Q. Chen, and P. Sivakumar. 2006. "Dynamics of assembly and reorganization of extracellular matrix proteins". In: *Curr Top Dev Biol* 75, pp. 1–24.

Dallas, S. L., P. Sivakumar, C. J. Jones, Q. Chen, D. M. Peters, D. F. Mosher, M. J. Humphries, and C. M. Kielty. 2005. "Fibronectin regulates latent transforming growth factor-beta (TGF beta) by controlling matrix assembly of latent TGF beta-binding protein-1". In: *J Biol Chem* 280, pp. 18871–80.

Dao, Lu. 2012. "Characterizing the Integrin-mediated Adhesion Profile of Single Cells by AFM-based Force Spectroscopy". PhD thesis. Karlsruhe Institute for Technology.

Davidson, L. A., B. D. Dzamba, R. Keller, and D. W. Desimone. 2008. "Live imaging of cell protrusive activity, and extracellular matrix assembly and remodeling during morphogenesis in the frog, Xenopus laevis". In: *Dev Dyn* 237, pp. 2684–92.

Davies, M. J. 2003. "Singlet oxygen-mediated damage to proteins and its consequences". In: *Biochem Biophys Res Commun* 305, pp. 761–70.

Davies, M. J., B. C. Gilbert, and R. M. Haywood. 1991. "Radical-Induced Damage to Proteins - Esr Spin-Trapping Studies". In: *Free Radical Research Communications* 15, pp. 111–127.

De Arcangelis, Adele and Elisabeth Georges-Labouesse. 2000. "Integrin and ECM functions: roles in vertebrate development". In: *Trends in Genetics* 16, pp. 389–395.

De Jong, K. L., H. C. MacLeod, P. R. Norton, and N. O. Petersen. 2006. "Fibronectin organization under and near cells". In: *European Biophysics Journal with Biophysics Letters* 35, pp. 695–708.

Dean, R. T., C. R. Roberts, and L. G. Forni. 1984. "Oxygen-centred free radicals can efficiently degrade the polypeptide of proteoglycans in whole cartilage". In: *Biosci Rep* 4, pp. 1017–26.

DeRosa, Maria C. and Robert J. Crutchley. 2002. "Photosensitized singlet oxygen and its applications". In: *Coordination Chemistry Reviews* 233-234, pp. 351–371.

Destaing, O., F. Saltel, J. C. Geminard, P. Jurdic, and F. Bard. 2003. "Podosomes display actin turnover and dynamic self-organization in osteoclasts expressing actin-green fluorescent protein". In: *Mol Biol Cell* 14, pp. 407–16.

Diaspro, A. 2010. *Optical Fluorescence Microscopy: From the Spectral to the Nano Dimension*. Springer-Verlag Berlin Heidelberg.

Dickson, R. M., D. J. Norris, and W. E. Moerner. 1998. "Simultaneous imaging of individual molecules aligned both parallel and perpendicular to the optic axis". In: *Physical Review Letters* 81, pp. 5322–5325.

Dransfield, I., C. Cabanas, A. Craig, and N. Hogg. 1992. "Divalent cation regulation of the function of the leukocyte integrin LFA-1". In: *J Cell Biol* 116, pp. 219–26.

Drobne, D., M. Milani, A. Zrimec, V. Leser, and M. Berden Zrimec. 2005. "Electron and ion imaging of gland cells using the FIB/SEM system". In: *J Microsc* 219, pp. 29–35.

Duband, J. L., S. Rocher, K. M. Yamada, and J. P. Thiery. 1986. "Interactions of migrating neural crest cells with fibronectin". In: *Prog Clin Biol Res* 226, pp. 127–39.

Dufour, S., J. L. Duband, and J. P. Thiery. 1986. "Role of a major cell-substratum adhesion system in cell behavior and morphogenesis". In: *Biol Cell* 58, pp. 1–13.

Dufrene, Y. F., D. Martinez-Martin, I. Medalsy, D. Alsteens, and D. J. Muller. 2013. "Multiparametric imaging of biological systems by force-distance curve-based AFM". In: *Nat Methods* 10, pp. 847–54.

Dzamba, B. J. and D. M. Peters. 1991. "Arrangement of cellular fibronectin in noncollagenous fibrils in human fibroblast cultures". In: *J Cell Sci* 100 (Pt 3), pp. 605–12.

Dzamba, B. J., H. Wu, R. Jaenisch, and D. M. Peters. 1993. "Fibronectin binding site in type I collagen regulates fibronectin fibril formation". In: *J Cell Biol* 121, pp. 1165–72.

Edwards, J. G., H. Hameed, and G. Campbell. 1988. "Induction of fibroblast spreading by Mn2+: a possible role for unusual binding sites for divalent cations in receptors for proteins containing Arg-Gly-Asp". In: *J Cell Sci* 89 (Pt 4), pp. 507–13.

Einstein, A. 1905. "Generation and conversion of light with regard to a heuristic point of view". In: *Ann Phys Berlin* 17, pp. 132–148.

Engel, J., E. Odermatt, A. Engel, J. A. Madri, H. Furthmayr, H. Rohde, and R. Timpl. 1981. "Shapes, domain organizations and flexibility of laminin and fibronectin, two multifunctional proteins of the extracellular matrix". In: *Journal of Molecular Biology* 150, pp. 97–120.

Engel, Jürgen. 1994. "[22] Electron microscopy of extracellular matrix components". In: *Methods in Enzymology*. Ed. by Eva Engvall Erkki Ruoslahti. Vol. Volume 245. Academic Press, pp. 469–488.

Erickson, H. P. and N. A. Carrell. 1983. "Fibronectin in extended and compact conformations. Electron microscopy and sedimentation analysis". In: *J Biol Chem* 258, pp. 14539–44.

Erickson, H. P., N. Carrell, and J. McDonagh. 1981. "Fibronectin molecule visualized in electron microscopy: a long, thin, flexible strand". In: *J Cell Biol* 91, pp. 673–78.

Fassler, R., E. Georges-Labouesse, and E. Hirsch. 1996. "Genetic analyses of integrin function in mice". In: *Curr Opin Cell Biol* 8, pp. 641–6.

Fassler, R. and M. Meyer. 1995. "Consequences of lack of beta 1 integrin gene expression in mice". In: *Genes Dev* 9, pp. 1896–908.

Fenn, J. B., M. Mann, C. K. Meng, S. F. Wong, and C. M. Whitehouse. 1989. "Electrospray ionization for mass spectrometry of large biomolecules". In: *Science* 246, pp. 64–71.

Fernandez, C., K. Clark, L. Burrows, N. R. Schofield, and M. J. Humphries. 1998. "Regulation of the extracellular ligand binding activity of integrins". In: *Front Biosci* 3, pp. d684–700.

ffrench-Constant, C. 1995. "Alternative splicing of fibronectin–many different proteins but few different functions". In: *Exp Cell Res* 221, pp. 261–71.

Fleischmajer, R. and R. Timpl. 1984. "Ultrastructural localization of fibronectin to different anatomic structures of human skin". In: *J Histochem Cytochem* 32, pp. 315–21.

Fogerty, F. J. and D. F. Mosher. 1990. "Mechanisms for organization of fibronectin matrix". In: *Cell Differ Dev* 32, pp. 439–50.

Fotiadis, Dimitrios, Lorenz Hasler, Daniel J. Muller, Henning Stahlberg, Jorg Kistler, and Andreas Engel. 2000. "Surface Tongue-and-groove Contours on Lens MIP Facilitate Cell-to-cell Adherence". In: *Journal of Molecular Biology* 300, pp. 779–789.

Fraley, S. I., Y. Feng, R. Krishnamurthy, D. H. Kim, A. Celedon, G. D. Longmore, and D. Wirtz. 2010. "A distinctive role for focal adhesion proteins in three-dimensional cell motility". In: *Nat Cell Biol* 12, pp. 598–604.

Frantz, C., K. M. Stewart, and V. M. Weaver. 2010. "The extracellular matrix at a glance". In: *J Cell Sci* 123, pp. 4195–200.

Franz, C. M. and D. J. Muller. 2005. "Analyzing focal adhesion structure by atomic force microscopy". In: *Journal of Cell Science* 118, pp. 5315–5323.

Franz, C. M., A. Taubenberger, P. H. Puech, and D. J. Muller. 2007. "Studying integrin-mediated cell adhesion at the single-molecule level using AFM force spectroscopy". In: *Sci STKE* 2007, pl5.

Freundlich, M. M. 1963. "Origin of the Electron Microscope". In: *Science* 142, pp. 185–8.

Friedland, J. C., M. H. Lee, and D. Boettiger. 2009. "Mechanically activated integrin switch controls alpha5beta1 function". In: *Science* 323, pp. 642–4.

Friedrichs, J., A. Taubenberger, C. M. Franz, and D. J. Muller. 2007. "Cellular remodelling of individual collagen fibrils visualized by time-lapse AFM". In: *Journal of Molecular Biology* 372, pp. 594–607.

Friedrichs, Jens, Jonne Helenius, and Daniel J. Muller. 2010. "Quantifying cellular adhesion to extracellular matrix components by single-cell force spectroscopy". In: *Nat. Protocols* 5, pp. 1353–1361.

Fritz, M., M. Radmacher, and H. E. Gaub. 1994. "Granula motion and membrane spreading during activation of human platelets imaged by atomic force microscopy". In: *Biophysical Journal* 66, pp. 1328–1334.

Gaidano, G., L. Bergui, M. Schena, M. Gaboli, O. Cremona, P. C. Marchisio, and F. Caligaris-Cappio. 1990. "Integrin distribution and cytoskeleton organization in normal and malignant monocytes". In: *Leukemia* 4, pp. 682–7.

Gailit, J. and E. Ruoslahti. 1988. "Regulation of the fibronectin receptor affinity by divalent cations". In: *J Biol Chem* 263, pp. 12927–32.

Gao, M., D. Craig, O. Lequin, I. D. Campbell, V. Vogel, and K. Schulten. 2003. "Structure and functional significance of mechanically unfolded fibronectin type III1 intermediates". In: *Proc Natl Acad Sci U S A* 100, pp. 14784–9.

Gao, M., D. Craig, V. Vogel, and K. Schulten. 2002. "Identifying unfolding intermediates of FN-III(10) by steered molecular dynamics". In: *J Mol Biol* 323, pp. 939–50.

García, A. J., M. D. Vega, and D. Boettiger. 1999. "Modulation of Cell Proliferation and Differentiation through Substrate-dependent Changes in Fibronectin Conformation". In: *Molecular Biology of the Cell* 10, pp. 785–798.

Gartner, L.P. and J.L. Hiatt. 2010. *Concise Histology*. Elsevier Health Sciences.

Gawden-Bone, C., Z. Zhou, E. King, A. Prescott, C. Watts, and J. Lucocq. 2010. "Dendritic cell podosomes are protrusive and invade the extracellular matrix using metalloproteinase MMP-14". In: *J Cell Sci* 123, pp. 1427–37.

Geiger, B. and A. Bershadsky. 2002. "Exploring the neighborhood: adhesion-coupled cell mechanosensors". In: *Cell* 110, pp. 139–42.

Geiger, B., A. Bershadsky, R. Pankov, and K. M. Yamada. 2001. "Transmembrane crosstalk between the extracellular matrix-cytoskeleton crosstalk". In: *Nat Rev Mol Cell Biol* 2, pp. 793–805.

Geiger, B., J. P. Spatz, and A. D. Bershadsky. 2009. "Environmental sensing through focal adhesions". In: *Nature Reviews Molecular Cell Biology* 10, pp. 21–33.

George, E. L., E. N. Georges-Labouesse, R. S. Patel-King, H. Rayburn, and R. O. Hynes. 1993. "Defects in mesoderm, neural tube and vascular development in mouse embryos lacking fibronectin". In: *Development* 119, pp. 1079–91.

Gerhart, J. and M. Kirschner. 1997. *Cells, Embryos and Evolution*. Wiley.

Giancotti, F. G. and E. Ruoslahti. 1999. "Integrin signaling". In: *Science* 285, pp. 1028–32.

Gimona, M., R. Buccione, S. A. Courtneidge, and S. Linder. 2008. "Assembly and biological role of podosomes and invadopodia". In: *Curr Opin Cell Biol* 20, pp. 235–41.

Gimona, M., C. Grashoff, and P. Kopp. 2005. "Oktoberfest for adhesion structures". In: *EMBO Rep* 6, pp. 922–6.

Gingell, D., O. S. Heavens, and J. S. Mellor. 1987. "General electromagnetic theory of total internal reflection fluorescence: the quantitative basis for mapping cell-substratum topography". In: *J Cell Sci* 87 (Pt 5), pp. 677–93.

Godyna, S., D. M. Mann, and W. S. Argraves. 1995. "A quantitative analysis of the incorporation of fibulin-1 into extracellular matrix indicates that fibronectin assembly is required". In: *Matrix Biol* 14, pp. 467–77.

Goh, K. L., J. T. Yang, and R. O. Hynes. 1997. "Mesodermal defects and cranial neural crest apoptosis in alpha5 integrin-null embryos". In: *Development* 124, pp. 4309–19.

Goodman, S.R. 2007. *Medical Cell Biology*. Elsevier Science.

Goto, Tetsuya, Kung S. Wong, and Donald M. Brunette. 1999. "Observation of Fibronectin Distribution on the Cell Undersurface Using Immunogold Scanning Electron Microscopy". In: *Journal of Histochemistry & Cytochemistry* 47, pp. 1487–1493.

Grant, R. P., C. Spitzfaden, H. Altroff, I. D. Campbell, and H. J. Mardon. 1997. "Structural requirements for biological activity of the ninth and tenth FIII domains of human fibronectin". In: *J Biol Chem* 272, pp. 6159–66.

Grinnell, F. 1984. "Fibronectin and wound healing". In: *J Cell Biochem* 26, pp. 107–16.

Grinnell, Frederick and Marian K. Feld. 1981. "Adsorption characteristics of plasma fibronectin in relationship to biological activity". In: *Journal of Biomedical Materials Research* 15, pp. 363–381.

Gudzenko, T. and C. M. Franz. 2013. “Inverting adherent cells for visualizing ECM interactions at the basal cell side”. In: *Ultramicroscopy* 128C, pp. 1–9.

Gumbiner, B. M. 1996. “Cell adhesion: the molecular basis of tissue architecture and morphogenesis”. In: *Cell* 84, pp. 345–57.

Halliday, N. L. and J. J. Tomasek. 1995. “Mechanical properties of the extracellular matrix influence fibronectin fibril assembly in vitro”. In: *Exp Cell Res* 217, pp. 109–17.

Harburger, D. S. and D. A. Calderwood. 2009. “Integrin signalling at a glance”. In: *J Cell Sci* 122, pp. 159–63.

Hawkins, C. L. and M. J. Davies. 2001. “Generation and propagation of radical reactions on proteins”. In: *Biochimica Et Biophysica Acta* 1504, pp. 196–219.

Hayat, M. A. 2000. *Principles and techniques of electron microscopy : biological applications*. 4th. Cambridge University Press, xix, 543 p.

Heinz, W. F. and J. H. Hoh. 1999. “Spatially resolved force spectroscopy of biological surfaces using the atomic force microscope”. In: *Trends Biotechnol* 17, pp. 143–50.

Hellen, E. H. and D. Axelrod. 1991. “Kinetics of epidermal growth factorreceptor binding on cells measured by total internal reflectionfluorescence recovery after photobleaching”. In: *J Fluoresc* 1, pp. 113–28.

Henderson, E., P. G. Haydon, and D. S. Sakaguchi. 1992. “Actin filament dynamics in living glial cells imaged by atomic force microscopy”. In: *Science* 257, pp. 1944–6.

Hershberger, R. P. and L. A. Culp. 1990. “Cell-type-specific expression of alternatively spliced human fibronectin IIICS mRNAs”. In: *Mol Cell Biol* 10, pp. 662–71.

Hinshaw, J. E. 2000. “Dynamin and its role in membrane fission”. In: *Annu Rev Cell Dev Biol* 16, pp. 483–519.

Hiura, K., S. S. Lim, S. P. Little, S. Lin, and M. Sato. 1995. “Differentiation dependent expression of tensin and cortactin in chicken osteoclasts”. In: *Cell Motil Cytoskeleton* 30, pp. 272–84.

Hocking, D. C., R. K. Smith, and P. J. McKeown-Longo. 1996. “A novel role for the integrin-binding III-10 module in fibronectin matrix assembly”. In: *J Cell Biol* 133, pp. 431–44.

Hocking, D. C., J. Sottile, and K. J. Langenbach. 2000. “Stimulation of integrin-mediated cell contractility by fibronectin polymerization”. In: *J Biol Chem* 275, pp. 10673–82.

Hocking, D. C., J. Sottile, and P. J. McKeown-Longo. 1994. “Fibronectin’s III-1 module contains a conformation-dependent binding site for the amino-terminal region of fibronectin”. In: *J Biol Chem* 269, pp. 19183–7.

Hoffmann, C., J. Leroy-Dudal, S. Patel, O. Gallet, and E. Pauthe. 2008. “Fluorescein isothiocyanate-labeled human plasma fibronectin in extracellular matrix remodeling”. In: *Anal Biochem* 372, pp. 62–71.

Hogan, B. L. 1999. “Morphogenesis”. In: *Cell* 96, pp. 225–33.

Hopwood, D. 1967. “Some aspects of fixation with glutaraldehyde. A biochemical and histochemical comparison of the effects of formaldehyde and glutaraldehyde fixation on various enzymes and glycogen, with a note on penetration of glutaraldehyde into liver”. In: *J Anat* 101, pp. 83–92.

Howe, A., A. E. Aplin, S. K. Alahari, and R. L. Juliano. 1998. “Integrin signaling and cell growth control”. In: *Curr Opin Cell Biol* 10, pp. 220–31.

Huang, B. 2010. “Super-resolution optical microscopy: multiple choices”. In: *Curr Opin Chem Biol* 14, pp. 10–4.

Huang, B., M. Bates, and X. Zhuang. 2009. "Super-resolution fluorescence microscopy". In: *Annu Rev Biochem* 78, pp. 993–1016.

Humphries, J. D., A. Byron, and M. J. Humphries. 2006. "Integrin ligands at a glance". In: *J Cell Sci* 119, pp. 3901–3.

Hurst, I. R., J. Zuo, J. Jiang, and L. S. Holliday. 2004. "Actin-related protein 23 complex is required for actin ring formation". In: *J Bone Miner Res* 19, pp. 499–506.

Hynes, R. 1985. "Molecular biology of fibronectin". In: *Annual Review of Cell Biology* 1, pp. 67–90.

Hynes, R. O. 2002a. "Integrins: bidirectional, allosteric signaling machines". In: *Cell* 110, pp. 673–87.

Hynes, R. O., J. C. Lively, J. H. McCarty, D. Taverna, S. E. Francis, K. Hodivala-Dilke, and Q. Xiao. 2002b. "The diverse roles of integrins and their ligands in angiogenesis". In: *Cold Spring Harb Symp Quant Biol* 67, pp. 143–53.

Hynes, Richard O. 1990. *Fibronectins*. Springer Series in Molecular Biology. Springer New York.

Ingham, K. C., S. A. Brew, T. J. Broekelmann, and J. A. McDonald. 1984. "Thermal stability of human plasma fibronectin and its constituent domains". In: *J Biol Chem* 259, pp. 11901–7.

Ingham, K. C., S. A. Brew, S. Huff, and S. V. Litvinovich. 1997. "Cryptic self-association sites in type III modules of fibronectin". In: *J Biol Chem* 272, pp. 1718–24.

Jensen, O. N., S. Kulkarni, J. V. Aldrich, and D. F. Barofsky. 1996. "Characterization of peptide-oligonucleotide heteroconjugates by mass spectrometry". In: *Nucleic Acids Res* 24, pp. 3866–72.

Jiang, S. T., W. J. Chuang, and M. J. Tang. 2000. "Role of fibronectin deposition in branching morphogenesis of Madin-Darby canine kidney cells". In: *Kidney Int* 57, pp. 1860–7.

Johansson, S., G. Svineng, K. Wennerberg, A. Armulik, and L. Lohikangas. 1997. "Fibronectin-integrin interactions". In: *Front Biosci* 2, pp. d126–46.

Johnson, K. J., H. Sage, G. Briscoe, and H. P. Erickson. 1999. "The compact conformation of fibronectin is determined by intramolecular ionic interactions". In: *J Biol Chem* 274, pp. 15473–9.

Jones, J. E. 1924. "On the Determination of Molecular Fields. II. From the Equation of State of a Gas". In: *Proceedings of the Royal Society of London. Series A* 106, pp. 463–477.

Jong, KathyL, HeatherC MacLeod, PeterR Norton, and NilsO Petersen. 2006. "Fibronectin organization under and near cells". In: *European Biophysics Journal* 35, pp. 695–708.

Kadler, K. E., A. Hill, and E. G. Canty-Laird. 2008. "Collagen fibrillogenesis: fibronectin, integrins, and minor collagens as organizers and nucleators". In: *Curr Opin Cell Biol* 20, pp. 495–501.

Kadler, K. E., Y. Hojima, and D. J. Prockop. 1987. "Assembly of collagen fibrils de novo by cleavage of the type I pC-collagen with procollagen C-proteinase. Assay of critical concentration demonstrates that collagen self-assembly is a classical example of an entropy-driven process". In: *J Biol Chem* 262, pp. 15696–701.

Kadler, K. E., D. F. Holmes, J. A. Trotter, and J. A. Chapman. 1996. "Collagen fibril formation". In: *Biochem J* 316 (Pt 1), pp. 1–11.

Kalb, E., J. Engel, and L. K. Tamm. 1990. "Binding of proteins to specific target sites in membranes measured by total internal reflection fluorescence microscopy". In: *Biochemistry* 29, pp. 1607–13.

Kanchanawong, P., G. Shtengel, A. M. Pasapera, E. B. Ramko, M. W. Davidson, H. F. Hess, and C. M. Waterman. 2010. "Nanoscale architecture of integrin-based cell adhesions". In: *Nature* 468, pp. 580–4.

Karuri, N. W., Z. Lin, H. S. Rye, and J. E. Schwarzbauer. 2009. "Probing the conformation of the fibronectin III1-2 domain by fluorescence resonance energy transfer". In: *J Biol Chem* 284, pp. 3445–52.

Kauf, A. C., S. M. Hough, and R. D. Bowditch. 2001. "Recognition of fibronectin by the platelet integrin alpha IIb beta 3 involves an extended interface with multiple electrostatic interactions". In: *Biochemistry* 40, pp. 9159–66.

Kausche, G. A., E. Pfankuch, and H. Ruska. 1939. "Die Sichtbarmachung von pflanzlichem Virus im Ubermikroskop". In: *Naturwissenschaften* 27, pp. 292–299.

Khan, Shahid, Daniel Pierce, and Ronald D. Vale. 2000. "Interactions of the chemotaxis signal protein CheY with bacterial flagellar motors visualized by evanescent wave microscopy". In: *Current Biology* 10, pp. 927–930.

Kiernan, John. 2000. "Formaldehyde, formalin, paraformaldehyde and glutaraldehyde: What they are and what they do". In: *Microscopy Today* 00-1 pp. 8-12 (2000).

Kiosses, W. B., S. J. Shattil, N. Pampori, and M. A. Schwartz. 2001. "Rac recruits high-affinity integrin alphavbeta3 to lamellipodia in endothelial cell migration". In: *Nat Cell Biol* 3, pp. 316–20.

Kirchhofer, D., J. Gailit, E. Ruoslahti, J. Grzesiak, and M. D. Pierschbacher. 1990. "Cation-dependent changes in the binding specificity of the platelet receptor GPIIb/-IIIa". In: *J Biol Chem* 265, pp. 18525–30.

Klotzsch, E., M. L. Smith, K. E. Kubow, S. Muntwyler, W. C. Little, F. Beyeler, D. Gourdon, B. J. Nelson, and V. Vogel. 2009. "Fibronectin forms the most extensible biological fibers displaying switchable force-exposed cryptic binding sites". In: *Proc Natl Acad Sci U S A* 106, pp. 18267–72.

Knox, P., S. Crooks, and C. S. Rimmer. 1986. "Role of fibronectin in the migration of fibroblasts into plasma clots". In: *J Cell Biol* 102, pp. 2318–23.

Koteliansky, V. E., M. V. Bejanian, and V. N. Smirnov. 1980. "Electron microscopy study of fibronectin structure". In: *FEBS Letters* 120, pp. 283–286.

Kottke-Marchant, K., A. A. Veenstra, and R. E. Marchant. 1996. "Human endothelial cell growth and coagulant function varies with respect to interfacial properties of polymeric substrates". In: *J Biomed Mater Res* 30, pp. 209–20.

Kubitscheck, U. 2013. *Fluorescence Microscopy: From Principles to Biological Applications*. Wiley.

Kuznetsov, Y. G., A. J. Malkin, and A. McPherson. 1997. "Atomic force microscopy studies of living cells: visualization of motility, division, aggregation, transformation, and apoptosis". In: *J Struct Biol* 120, pp. 180–91.

Lacey, D. L., E. Timms, H. L. Tan, M. J. Kelley, C. R. Dunstan, T. Burgess, R. Elliott, A. Colombero, G. Elliott, S. Scully, H. Hsu, J. Sullivan, N. Hawkins, E. Davy, C. Capparelli, A. Eli, Y. X. Qian, S. Kaufman, I. Sarosi, V. Shalhoub, G. Senaldi, J. Guo, J. Delaney, and W. J. Boyle. 1998. "Osteoprotegerin ligand is a cytokine that regulates osteoclast differentiation and activation". In: *Cell* 93, pp. 165–76.

Ladoux, Benoit and Alice Nicolas. 2012. "Physically based principles of cell adhesion mechanosensitivity in tissues". In: *Reports on Progress in Physics* 75, p. 116601.

Lakkakorpi, P. T., M. H. Helfrich, M. A. Horton, and H. K. Vaananen. 1993. "Spatial organization of microfilaments and vitronectin receptor, alpha v beta 3, in osteoclasts. A study using confocal laser scanning microscopy". In: *J Cell Sci* 104 (Pt 3), pp. 663–70.

Lakkakorpi, P., J. Tuukkanen, T. Hentunen, K. Jarvelin, and K. Vaananen. 1989. "Organization of osteoclast microfilaments during the attachment to bone surface in vitro". In: *J Bone Miner Res* 4, pp. 817–25.

Lal, R. and S. A. John. 1994. "Biological applications of atomic force microscopy". In: *American Journal of Physiology - Cell Physiology* 266, pp. C1–C21.

Lang, T., I. Wacker, J. Steyer, C. Kaether, I. Wunderlich, T. Soldati, H. H. Gerdes, and W. Almers. 1997. "Ca2+-triggered peptide secretion in single cells imaged with green fluorescent protein and evanescent-wave microscopy". In: *Neuron* 18, pp. 857–63.

Larsen, M., C. Wei, and K. M. Yamada. 2006. "Cell and fibronectin dynamics during branching morphogenesis". In: *J Cell Sci* 119, pp. 3376–84.

Lauterborn, W. and T. Kurz. 2003. *Coherent Optics: Fundamentals and Applications*. Springer.

Leahy, D. J., I. Aukhil, and H. P. Erickson. 1996. "2.0 A crystal structure of a four-domain segment of human fibronectin encompassing the RGD loop and synergy region". In: *Cell* 84, pp. 155–64.

Lee, J. N., X. Jiang, D. Ryan, and G. M. Whitesides. 2004. "Compatibility of mammalian cells on surfaces of poly(dimethylsiloxane)". In: *Langmuir* 20, pp. 11684–91.

Lehto, V. P., T. Hovi, T. Vartio, R. A. Badley, and I. Virtanen. 1982. "Reorganization of cytoskeletal and contractile elements during transition of human monocytes into adherent macrophages". In: *Lab Invest* 47, pp. 391–9.

Leite, F. L. and P. S. P. Herrmann. 2005. "Application of atomic force spectroscopy (AFS) to studies of adhesion phenomena: a review". In: *Journal of Adhesion Science and Technology* 19, pp. 365–405.

Lener, T., G. Burgstaller, L. Crimaldi, S. Lach, and M. Gimona. 2006. "Matrix-degrading podosomes in smooth muscle cells". In: *Eur J Cell Biol* 85, pp. 183–9.

Li, L., H. H. Huang, C. L. Badilla, and J. M. Fernandez. 2005. "Mechanical unfolding intermediates observed by single-molecule force spectroscopy in a fibronectin type III module". In: *J Mol Biol* 345, pp. 817–26.

Liao, Y. F., P. J. Gotwals, V. E. Koteliansky, D. Sheppard, and L. Van De Water. 2002. "The EIIIA segment of fibronectin is a ligand for integrins alpha 9beta 1 and alpha 4beta 1 providing a novel mechanism for regulating cell adhesion by alternative splicing". In: *J Biol Chem* 277, pp. 14467–74.

Lin, G. L., D. M. Cohen, R. A. Desai, M. T. Breckenridge, L. Gao, M. J. Humphries, and C. S. Chen. 2013. "Activation of beta 1 but not beta 3 integrin increases cell traction forces". In: *FEBS Lett* 587, pp. 763–9.

Lin, H., R. Lal, and D. O. Clegg. 2000. "Imaging and mapping heparin-binding sites on single fibronectin molecules with atomic force microscopy". In: *Biochemistry* 39, pp. 3192–6.

Linder, S. 2007. "The matrix corroded: podosomes and invadopodia in extracellular matrix degradation". In: *Trends Cell Biol* 17, pp. 107–17.

Linder, S. and M. Aepfelbacher. 2003. "Podosomes: adhesion hot-spots of invasive cells". In: *Trends Cell Biol* 13, pp. 376–85.

Linder, S. and P. Kopp. 2005. "Podosomes at a glance". In: *J Cell Sci* 118, pp. 2079–82.

Litvinovich, S. V., S. A. Brew, S. Aota, S. K. Akiyama, C. Haudenschild, and K. C. Ingham. 1998. "Formation of amyloid-like fibrils by self-association of a partially unfolded fibronectin type III module". In: *Journal of Molecular Biology* 280, pp. 245–58.

Litvinovich, S. V. and K. C. Ingham. 1995. "Interactions between type III domains in the 110 kDa cell-binding fragment of fibronectin". In: *J Mol Biol* 248, pp. 611–26.

Luxenburg, C., D. Geblinger, E. Klein, K. Anderson, D. Hanein, B. Geiger, and L. Addadi. 2007. "The architecture of the adhesive apparatus of cultured osteoclasts: from podosome formation to sealing zone assembly". In: *PLoS One* 2, e179.

Magnusson, M. K. and D. F. Mosher. 1998. "Fibronectin: structure, assembly, and cardiovascular implications". In: *Arterioscler Thromb Vasc Biol* 18, pp. 1363–70.

Mahler, H. C., W. Friess, U. Grauschopf, and S. Kiese. 2009. "Protein Aggregation: Pathways, Induction Factors and Analysis". In: *Journal of Pharmaceutical Sciences* 98, pp. 2909–2934.

Maki, J. M., R. Sormunen, S. Lippo, R. Kaarteenaho-Wiik, R. Soininen, and J. Myllyharju. 2005. "Lysyl oxidase is essential for normal development and function of the respiratory system and for the integrity of elastic and collagen fibers in various tissues". In: *Am J Pathol* 167, pp. 927–36.

Manabe, R., N. Ohe, T. Maeda, T. Fukuda, and K. Sekiguchi. 1997. "Modulation of cell-adhesive activity of fibronectin by the alternatively spliced EDA segment". In: *J Cell Biol* 139, pp. 295–307.

Mao, Y. and J. E. Schwarzbauer. 2005a. "Fibronectin fibrillogenesis, a cell-mediated matrix assembly process". In: *Matrix Biol* 24, pp. 389–99.

Mao, Y. and J. E. Schwarzbauer. 2005b. "Stimulatory effects of a three-dimensional microenvironment on cell-mediated fibronectin fibrillogenesis". In: *J Cell Sci* 118, pp. 4427–36.

Marchisio, P. C., D. Cirillo, L. Naldini, M. V. Primavera, A. Teti, and A. Zambonin-Zallone. 1984. "Cell-substratum interaction of cultured avian osteoclasts is mediated by specific adhesion structures". In: *J Cell Biol* 99, pp. 1696–705.

Martinez, E., E. Engel, C. Lopez-Iglesias, C. A. Mills, J. A. Planell, and J. Samitier. 2008. "Focused ion beam/scanning electron microscopy characterization of cell behavior on polymer micro-/nanopatterned substrates: A study of cell-substrate interactions". In: *Micron* 39, pp. 111–116.

Mathur, A. B., G. A. Truskey, and W. M. Reichert. 2000. "Atomic force and total internal reflection fluorescence microscopy for the study of force transmission in endothelial cells". In: *Biophys J* 78, pp. 1725–35.

McDonald, J. A. 1988. "Extracellular matrix assembly". In: *Annual Review of Cell Biology* 4, pp. 183–207.

McKeown-Longo, P. J. and D. F. Mosher. 1983. "Binding of plasma fibronectin to cell layers of human skin fibroblasts". In: *J Cell Biol* 97, pp. 466–72.

Meadows, P. Y. and G. C. Walker. 2005. "Force microscopy studies of fibronectin adsorption and subsequent cellular adhesion to substrates with well-defined surface chemistries". In: *Langmuir* 21, pp. 4096–107.

Meshel, Adam S., Qize Wei, Robert S. Adelstein, and Michael P. Sheetz. 2005. "Basic mechanism of three-dimensional collagen fibre transport by fibroblasts". In: *Nat Cell Biol* 7, pp. 157–164.

Michaeli, A. and J. Feitelson. 1994. "Reactivity of Singlet Oxygen toward Amino-Acids and Peptides". In: *Photochemistry and Photobiology* 59, pp. 284–289.

Moller, C., M. Allen, V. Elings, A. Engel, and D. J. Muller. 1999. "Tapping-mode atomic force microscopy produces faithful high-resolution images of protein surfaces". In: *Biophys J* 77, pp. 1150–8.

Moreno-Herrero, Fernando and Julio Gomez-Herrero. 2012. "AFM: Basic Concepts". In: *Atomic Force Microscopy in Liquid*. Wiley-VCH Verlag GmbH Co. KGaA, pp. 1–34.

Morris, V.J., A.R. Kirby, and A.P. Gunning. 1999. *Atomic Force Microscopy for Biologists*. Imperial College Press.

Mosher, D. F. 1993. "Assembly of Fibronectin into Extracellular-Matrix". In: *Current Opinion in Structural Biology* 3, pp. 214–222.

Mosher, D. F. and R. B. Johnson. 1983. "Specificity of fibronectin–fibrin cross-linking". In: *Ann N Y Acad Sci* 408, pp. 583–94.

Mould, A. P., S. K. Akiyama, and M. J. Humphries. 1995b. "Regulation of integrin alpha 5 beta 1-fibronectin interactions by divalent cations. Evidence for distinct classes of binding sites for Mn2+, Mg2+, and Ca2+". In: *J Biol Chem* 270, pp. 26270–7.

Mould, A. P., A. N. Garratt, J. A. Askari, S. K. Akiyama, and M. J. Humphries. 1995a. "Regulation of integrin alpha 5 beta 1 function by anti-integrin antibodies and divalent cations". In: *Biochem Soc Trans* 23, 395S.

Mulholland, J., D. Preuss, A. Moon, A. Wong, D. Drubin, and D. Botstein. 1994. "Ultrastructure of the yeast actin cytoskeleton and its association with the plasma membrane". In: *J Cell Biol* 125, pp. 381–91.

Muller, D. J. and Y. F. Dufrene. 2008. "Atomic force microscopy as a multifunctional molecular toolbox in nanobiotechnology". In: *Nat Nanotechnol* 3, pp. 261–9.

Muller, D. J. and A. Engel. 2002. "Conformations, flexibility, and interactions observed on individual membrane proteins by atomic force microscopy". In: *Methods Cell Biol* 68, pp. 257–99.

Muller, D. J., D. Fotiadis, S. Scheuring, S. A. Muller, and A. Engel. 1999. "Electrostatically balanced subnanometer imaging of biological specimens by atomic force microscope". In: *Biophys J* 76, pp. 1101–11.

Muller, D. J., F. A. Schabert, G. Buldt, and A. Engel. 1995. "Imaging purple membranes in aqueous solutions at sub-nanometer resolution by atomic force microscopy". In: *Biophys J* 68, pp. 1681–6.

Muller, G. A. and H. P. Rodemann. 1991. "Characterization of human renal fibroblasts in health and disease: I. Immunophenotyping of cultured tubular epithelial cells and fibroblasts derived from kidneys with histologically proven interstitial fibrosis". In: *Am J Kidney Dis* 17, pp. 680–3.

Murphy, D. A. and S. A. Courtneidge. 2011. "The 'ins' and 'outs' of podosomes and invadopodia: characteristics, formation and function". In: *Nat Rev Mol Cell Biol* 12, pp. 413–26.

Myllyharju, J. and K. I. Kivirikko. 2004. "Collagens, modifying enzymes and their mutations in humans, flies and worms". In: *Trends Genet* 20, pp. 33–43.

Nelea, V. and M. T. Kaartinen. 2010. "Periodic beaded-filament assembly of fibronectin on negatively charged surface". In: *J Struct Biol* 170, pp. 50–9.

Nelea, V., Y. Nakano, and M. T. Kaartinen. 2008. "Size distribution and molecular associations of plasma fibronectin and fibronectin crosslinked by transglutaminase 2". In: *Protein J* 27, pp. 223–33.

Nermut, M. V. 1989. "Strategy and Tactics in Electron-Microscopy of Cell-Surfaces". In: *Electron Microscopy Reviews* 2, pp. 171–196.

Ni, H., P. S. Yuen, J. M. Papalia, J. E. Trevithick, T. Sakai, R. Fassler, R. O. Hynes, and D. D. Wagner. 2003. "Plasma fibronectin promotes thrombus growth and stability in injured arterioles". In: *Proc Natl Acad Sci U S A* 100, pp. 2415–9.

Nijweide, P. J., E. H. Burger, and J. H. M. Feyen. 1986. "Cells of Bone - Proliferation, Differentiation, and Hormonal-Regulation". In: *Physiological Reviews* 66, pp. 855–886.

Nitsch, L., E. Gionti, R. Cancedda, and P. C. Marchisio. 1989. "The podosomes of Rous sarcoma virus transformed chondrocytes show a peculiar ultrastructural organization". In: *Cell Biol Int Rep* 13, pp. 919–26.

Noy, A. 2007. *Handbook of Molecular Force Spectroscopy*. Springer.

Oberhauser, A. F., C. Badilla-Fernandez, M. Carrion-Vazquez, and J. M. Fernandez. 2002. "The mechanical hierarchies of fibronectin observed with single-molecule AFM". In: *Journal of Molecular Biology* 319, pp. 433–447.

Oberleithner, H., G. Giebisch, and J. Geibel. 1993. "Imaging the lamellipodium of migrating epithelial cells in vivo by atomic force microscopy". In: *Pflugers Arch* 425, pp. 506–10.

Ochoa, G. C., V. I. Slepnev, L. Neff, N. Ringstad, K. Takei, L. Daniell, W. Kim, H. Cao, M. McNiven, R. Baron, and P. De Camilli. 2000. "A functional link between dynamin and the actin cytoskeleton at podosomes". In: *J Cell Biol* 150, pp. 377–89.

Odermatt, E., J. Engle, H. Richter, and H. Hormann. 1982. "Shape, conformation and stability of fibronectin fragments determined by electron microscopy, circular dichroism and ultracentrifugation". In: *J Mol Biol* 159, pp. 109–23.

Ohashi, T., D. P. Kiehart, and H. P. Erickson. 1999. "Dynamics and elasticity of the fibronectin matrix in living cell culture visualized by fibronectin-green fluorescent protein". In: *Proceedings of the National Academy of Sciences of the United States of America* 96, pp. 2153–2158.

Ohashi, T., D. P. Kiehart, and H. P. Erickson. 2002. "Dual labeling of the fibronectin matrix and actin cytoskeleton with green fluorescent protein variants". In: *J Cell Sci* 115, pp. 1221–9.

Pankov, R., E. Cukierman, B. Z. Katz, K. Matsumoto, D. C. Lin, S. Lin, C. Hahn, and K. M. Yamada. 2000. "Integrin dynamics and matrix assembly: tensin-dependent translocation of alpha(5)beta(1) integrins promotes early fibronectin fibrillogenesis". In: *J Cell Biol* 148, pp. 1075–90.

Pankov, R. and A. Momchilova. 2009. "Fluorescent labeling techniques for investigation of fibronectin fibrillogenesis (labeling fibronectin fibrillogenesis)". In: *Methods Mol Biol* 522, pp. 261–74.

Pankov, R. and K. M. Yamada. 2002. "Fibronectin at a glance". In: *J Cell Sci* 115, pp. 3861–3.

Paranko, J., L. J. Pelliniemi, A. Vaheri, J. M. Foidart, and T. Lakkala-Paranko. 1983. "Morphogenesis and fibronectin in sexual differentiation of rat embryonic gonads". In: *Differentiation* 23 Suppl, S72–81.

Pattison, D. I., A. S. Rahmanto, and M. J. Davies. 2012. "Photo-oxidation of proteins". In: *Photochem Photobiol Sci* 11, pp. 38–53.

Pauthe, E., J. Pelta, S. Patel, D. Lairez, and F. Goubard. 2002. "Temperature-induced beta-aggregation of fibronectin in aqueous solution". In: *Biochimica Et Biophysica Acta* 1597, pp. 12–21.

Pereira, M., B. J. Rybarczyk, T. M. Odrljin, D. C. Hocking, J. Sottile, and P. J. Simpson-Haidaris. 2002. "The incorporation of fibrinogen into extracellular matrix is dependent on active assembly of a fibronectin matrix". In: *J Cell Sci* 115, pp. 609–17.

Peters, D. M. P., Y. Chen, L. Zardi, and S. Brummel. 1998. "Conformation of Fibronectin Fibrils Varies: Discrete Globular Domains of Type III Repeats Detected". In: *Microsc Microanal* 4, pp. 385–396.

Peters, D. M., L. M. Portz, J. Fullenwider, and D. F. Mosher. 1990. "Co-assembly of plasma and cellular fibronectins into fibrils in human fibroblast cultures". In: *J Cell Biol* 111, pp. 249–56.

Petersen, T. E., H. C. Thogersen, K. Skorstengaard, K. Vibe-Pedersen, P. Sahl, L. Sottrup-Jensen, and S. Magnusson. 1983. "Partial primary structure of bovine plasma fibronectin: three types of internal homology". In: *Proc Natl Acad Sci U S A* 80, pp. 137–41.

Petit, V. and J. P. Thiery. 2000. "Focal adhesions: structure and dynamics". In: *Biol Cell* 92, pp. 477–94.

Pfaff, M. and P. Jurdic. 2001. "Podosomes in osteoclast-like cells: structural analysis and cooperative roles of paxillin, proline-rich tyrosine kinase 2 (Pyk2) and integrin alphaVbeta3". In: *J Cell Sci* 114, pp. 2775–86.

Phillips, D. 2010. "Light relief: photochemistry and medicine". In: *Photochem Photobiol Sci* 9, pp. 1589–96.

Pickford, A. R. and I. D. Campbell. 2004. "NMR studies of modular protein structures and their interactions". In: *Chem Rev* 104, pp. 3557–66.

Pitt, W. G., S. H. Spiegelberg, and S. L. Cooper. 1987. "Adsorption of Fibronectin to Polyurethane Surfaces: Fourier Transform Infrared Spectroscopic Studies". In: *Proteins at Interfaces*. Vol. 343. ACS Symposium Series. American Chemical Society. Chap. 21, pp. 324–338.

Poole, Kate, Khaled Khairy, Jens Friedrichs, Clemens Franz, David A. Cisneros, Jonathon Howard, and Daniel Mueller. 2005. "Molecular-scale Topographic Cues Induce the Orientation and Directional Movement of Fibroblasts on Two-dimensional Collagen Surfaces". In: *Journal of Molecular Biology* 349, pp. 380–386.

Porter, K. R., A. Claude, and E. F. Fullam. 1945. "A Study of Tissue Culture Cells by Electron Microscopy : Methods and Preliminary Observations". In: *J Exp Med* 81, pp. 233–46.

Potts, J. R. and I. D. Campbell. 1994. "Fibronectin structure and assembly". In: *Curr Opin Cell Biol* 6, pp. 648–55.

Price, T. M., M. L. Rudee, M. Pierschbacher, and E. Ruoslahti. 1982. "Structure of fibronectin and its fragments in electron microscopy". In: *Eur J Biochem* 129, pp. 359–63.

Pytela, R., M. D. Pierschbacher, and E. Ruoslahti. 1985. "Identification and isolation of a 140 kd cell surface glycoprotein with properties expected of a fibronectin receptor". In: *Cell* 40, pp. 191–8.

Rest, M. van der and R. Garrone. 1991. "Collagen family of proteins". In: *Federation Proceedings* 5, pp. 2814–23.

Revel, J.P. and K. Wolken. 1973. "Electronmicroscope investigations of the underside of cells in culture". In: *Experimental Cell Research* 78, pp. 1–14.

Richards, R. G., P. C. Lloyd, B. A. Rahn, and I. A. Gwynn. 1993. "A new method for investigating the undersurface of cell monolayers by scanning electron microscopy". In: *J Microsc* 171, pp. 205–13.

Ridley, Anne J., Martin A. Schwartz, Keith Burridge, Richard A. Firtel, Mark H. Ginsberg, Gary Borisy, J. Thomas Parsons, and Alan Rick Horwitz. 2003. "Cell Migration: Integrating Signals from Front to Back". In: *Science* 302, pp. 1704–1709.

Rief, M., M. Gautel, F. Oesterhelt, J. M. Fernandez, and H. E. Gaub. 1997. "Reversible unfolding of individual titin immunoglobulin domains by AFM". In: *Science* 276, pp. 1109–1112.

Rocco, M., M. Carson, R. Hantgan, J. McDonagh, and J. Hermans. 1983. "Dependence of the shape of the plasma fibronectin molecule on solvent composition. Ionic strength and glycerol content". In: *J Biol Chem* 258, pp. 14545–9.

Rocco, M., E. Infusini, M. G. Daga, L. Gogioso, and C. Cuniberti. 1987. "Models of fibronectin". In: *EMBO J* 6, pp. 2343–9.

Rodemann, H. P. and G. A. Muller. 1991. "Characterization of human renal fibroblasts in health and disease: II. In vitro growth, differentiation, and collagen synthesis of fibroblasts from kidneys with interstitial fibrosis". In: *Am J Kidney Dis* 17, pp. 684–6.

Rotsch, C., K. Jacobson, and M. Radmacher. 1999. "Dimensional and mechanical dynamics of active and stable edges in motile fibroblasts investigated by using atomic force microscopy". In: *Proc Natl Acad Sci U S A* 96, pp. 921–6.

Roure, O. du, A. Buguin, H. Feracci, and P. Silberzan. 2006. "Homophilic interactions between cadherin fragments at the single molecule level: an AFM study". In: *Langmuir* 22, pp. 4680–4.

Rozario, T. and D. W. DeSimone. 2010. "The extracellular matrix in development and morphogenesis: a dynamic view". In: *Dev Biol* 341, pp. 126–40.

Ruoslahti, E. 1991. "Integrins". In: *J Clin Invest* 87, pp. 1–5.

Ruoslahti, E. 1996. "RGD and other recognition sequences for integrins". In: *Annu Rev Cell Dev Biol* 12, pp. 697–715.

Ruoslahti, E. 1999. "Fibronectin and its integrin receptors in cancer". In: *Adv Cancer Res* 76, pp. 1–20.

Ruska, E. and M. Knoll. 1931. *Die magnetische Sammelspule fur schnelle Elektronenstrahlen*. Vol. 12, 389–400, and 448.

Sabatier, L., D. Chen, C. Fagotto-Kaufmann, D. Hubmacher, M. D. McKee, D. S. Annis, D. F. Mosher, and D. P. Reinhardt. 2009. "Fibrillin assembly requires fibronectin". In: *Mol Biol Cell* 20, pp. 846–58.

Sakai, T., M. Larsen, and K. M. Yamada. 2003. "Fibronectin requirement in branching morphogenesis". In: *Nature* 423, pp. 876–81.

Salo, J., P. Lehenkari, M. Mulari, K. Metsikko, and H. K. Vaananen. 1997. "Removal of osteoclast bone resorption products by transcytosis". In: *Science* 276, pp. 270–3.

Schermelleh, Lothar, Rainer Heintzmann, and Heinrich Leonhardt. 2010. "A guide to super-resolution fluorescence microscopy". In: *The Journal of Cell Biology* 190, pp. 165–175.

Schnapp, L. M., J. M. Breuss, D. M. Ramos, D. Sheppard, and R. Pytela. 1995a. "Sequence and tissue distribution of the human integrin alpha 8 subunit: a beta 1-associated alpha subunit expressed in smooth muscle cells". In: *J Cell Sci* 108 (Pt 2), pp. 537–44.

Schnapp, L. M., N. Hatch, D. M. Ramos, I. V. Klimanskaya, D. Sheppard, and R. Pytela. 1995b. "The human integrin alpha 8 beta 1 functions as a receptor for tenascin, fibronectin, and vitronectin". In: *J Biol Chem* 270, pp. 23196–202.

Schneider, S. W., K. C. Sritharan, J. P. Geibel, H. Oberleithner, and B. P. Jena. 1997. "Surface dynamics in living acinar cells imaged by atomic force microscopy: identification of plasma membrane structures involved in exocytosis". In: *Proc Natl Acad Sci U S A* 94, pp. 316–21.

Schoenenberger, C. A. and J. H. Hoh. 1994. "Slow cellular dynamics in MDCK and R5 cells monitored by time-lapse atomic force microscopy". In: *Biophys J* 67, pp. 929–36.

Schöneich, Christian. 2005. "Methionine oxidation by reactive oxygen species: reaction mechanisms and relevance to Alzheimer's disease". In: *Biochimica et Biophysica Acta (BBA) - Proteins and Proteomics* 1703, pp. 111–119.

Schwarzbauer, J. E. and D. W. DeSimone. 2011. "Fibronectins, their fibrillogenesis, and in vivo functions". In: *Cold Spring Harb Perspect Biol* 3.

Schwarzbauer, J. E. and J. L. Sechler. 1999. "Fibronectin fibrillogenesis: a paradigm for extracellular matrix assembly". In: *Curr Opin Cell Biol* 11, pp. 622–7.

Sechler, J. L., S. A. Corbett, and J. E. Schwarzbauer. 1997. "Modulatory roles for integrin activation and the synergy site of fibronectin during matrix assembly". In: *Mol Biol Cell* 8, pp. 2563–73.

Sechler, J. L., A. M. Cumiskey, D. M. Gazzola, and J. E. Schwarzbauer. 2000. "A novel RGD-independent fibronectin assembly pathway initiated by alpha4beta1 integrin binding to the alternatively spliced V region". In: *J Cell Sci* 113 (Pt 8), pp. 1491–8.

Sechler, J. L. and J. E. Schwarzbauer. 1998. "Control of cell cycle progression by fibronectin matrix architecture". In: *J Biol Chem* 273, pp. 25533–6.

Shahin, V., Y. Ludwig, C. Schafer, D. Nikova, and H. Oberleithner. 2005. "Glucocorticoids remodel nuclear envelope structure and permeability". In: *J Cell Sci* 118, pp. 2881–9.

Sharma, V.K. and S.E. Rokita. 2012. *Oxidation of Amino Acids, Peptides, and Proteins: Kinetics and Mechanism*. Wiley.

Shattil, S. J., C. Kim, and M. H. Ginsberg. 2010. "The final steps of integrin activation: the end game". In: *Nat Rev Mol Cell Biol* 11, pp. 288–300.

Shoulders, M. D. and R. T. Raines. 2009. "Collagen structure and stability". In: *Annu Rev Biochem* 78, pp. 929–58.

Singer, II. 1979. "The fibronexus: a transmembrane association of fibronectin-containing fibers and bundles of 5 nm microfilaments in hamster and human fibroblasts". In: *Cell* 16, pp. 675–85.

Singer, II, D. W. Kawka, D. M. Kazazis, and R. A. Clark. 1984. "In vivo co-distribution of fibronectin and actin fibers in granulation tissue: immunofluorescence and electron microscope studies of the fibronexus at the myofibroblast surface". In: *J Cell Biol* 98, pp. 2091–106.

Singer, II, D. M. Kazazis, and S. Scott. 1989. "Scanning electron microscopy of focal contacts on the substratum attachment surface of fibroblasts adherent to fibronectin". In: *J Cell Sci* 93 (Pt 1), pp. 147–54.

Singh, P., C. Carraher, and J. E. Schwarzbauer. 2010. "Assembly of fibronectin extracellular matrix". In: *Annu Rev Cell Dev Biol* 26, pp. 397–419.

Sivakumar, P., A. Czirok, B. J. Rongish, V. P. Divakara, Y. P. Wang, and S. L. Dallas. 2006. "New insights into extracellular matrix assembly and reorganization from dynamic imaging of extracellular matrix proteins in living osteoblasts". In: *J Cell Sci* 119, pp. 1350–60.

Smith, D. E., D. F. Mosher, R. B. Johnson, and L. T. Furcht. 1982. "Immunological identification of two sulfhydryl-containing fragments of human plasma fibronectin". In: *J Biol Chem* 257, pp. 5831–8.

Smith, J W, R S Piotrowicz, and D Mathis. 1994. "A mechanism for divalent cation regulation of beta 3-integrins". In: *Journal of Biological Chemistry* 269, pp. 960–7.

Smith, Michael L., Delphine Gourdon, William C. Little, Kristopher E. Kubow, R. Andresen Eguiluz, Sheila Luna-Morris, and Viola Vogel. 2007. "Force-Induced Unfolding of Fibronectin in the Extracellular Matrix of Living Cells". In: *PLoS Biol* 5, e268.

Sottile, J. and D. C. Hocking. 2002. "Fibronectin polymerization regulates the composition and stability of extracellular matrix fibrils and cell-matrix adhesions". In: *Mol Biol Cell* 13, pp. 3546–59.

Stamov, D. R., A. Mullner, Y. Wegrowski, S. Brezillon, and C. M. Franz. 2013. "Quantitative analysis of type I collagen fibril regulation by lumican and decorin using AFM". In: *Journal of Structural Biology* 183, pp. 394–403.

Starr, C., C. A. Evers, and L. Starr. 2007. *Biology: Concepts and Applications*. Vol. 7th ed. Brooks Cole.

Stephens, L. E., A. E. Sutherland, I. V. Klimanskaya, A. Andrieux, J. Meneses, R. A. Pedersen, and C. H. Damsky. 1995. "Deletion of beta 1 integrins in mice results in inner cell mass failure and peri-implantation lethality". In: *Genes Dev* 9, pp. 1883–95.

Steyer, J. A. and W. Almers. 1999. "Tracking single secretory granules in live chromaffin cells by evanescent-field fluorescence microscopy". In: *Biophys J* 76, pp. 2262–71.

Steyer, J. A. and W. Almers. 2001. "A real-time view of life within 100 nm of the plasma membrane". In: *Nat Rev Mol Cell Biol* 2, pp. 268–75.

Sysak, P. K., C. S. Foote, and T. Y. Ching. 1977. "Chemistry of Singlet Oxygen .25. Photooxygenation of Methionine". In: *Photochemistry and Photobiology* 26, pp. 19–27.

Takada, Y., X. Ye, and S. Simon. 2007. "The integrins". In: *Genome Biol* 8, p. 215.

Takagi, J. 2004. "Structural basis for ligand recognition by RGD (Arg-Gly-Asp)-dependent integrins". In: *Biochem Soc Trans* 32, pp. 403–6.

Takagi, J., B. M. Petre, T. Walz, and T. A. Springer. 2002. "Global conformational rearrangements in integrin extracellular domains in outside-in and inside-out signaling". In: *Cell* 110, pp. 599–11.

Takagi, J., K. Strokovich, T. A. Springer, and T. Walz. 2003. "Structure of integrin alpha5beta1 in complex with fibronectin". In: *EMBO J* 22, pp. 4607–15.

Takei, K., V. I. Slepnev, V. Haucke, and P. De Camilli. 1999. "Functional partnership between amphiphysin and dynamin in clathrin-mediated endocytosis". In: *Nat Cell Biol* 1, pp. 33–9.

Tanford, C. 1968. “Protein denaturation”. In: *Adv Protein Chem* 23, pp. 121–282.

Taubenberger, A., D. A. Cisneros, J. Friedrichs, P. H. Puech, D. J. Muller, and C. M. Franz. 2007. “Revealing early steps of alpha2beta1 integrin-mediated adhesion to collagen type I by using single-cell force spectroscopy”. In: *Mol Biol Cell* 18, pp. 1634–44.

Teixeira, Ana I., George A. Abrams, Paul J. Bertics, Christopher J. Murphy, and Paul F. Nealey. 2003. “Epithelial contact guidance on well-defined micro- and nanostructured substrates”. In: *Journal of Cell Science* 116, pp. 1881–1892.

Thompson, N. L. and D. Axelrod. 1983. “Immunoglobulin surface-binding kinetics studied by total internal reflection with fluorescence correlation spectroscopy”. In: *Biophys J* 43, pp. 103–14.

Thompson, N. L., T. P. Burghardt, and D. Axelrod. 1981. “Measuring surface dynamics of biomolecules by total internal reflection fluorescence with photobleaching recovery or correlation spectroscopy”. In: *Biophys J* 33, pp. 435–54.

Tiwari, S., J. A. Askari, M. J. Humphries, and N. J. Bulleid. 2011. “Divalent cations regulate the folding and activation status of integrins during their intracellular trafficking”. In: *J Cell Sci* 124, pp. 1672–80.

To, W. S. and K. S. Midwood. 2011. “Plasma and cellular fibronectin: distinct and independent functions during tissue repair”. In: *Fibrogenesis Tissue Repair* 4, p. 21.

Todd, I., J. S. Mellor, and D. Gingell. 1988. “Mapping cell-glass contacts of Dictyostelium amoebae by total internal reflection aqueous fluorescence overcomes a basic ambiguity of interference reflection microscopy”. In: *J Cell Sci* 89 (Pt 1), pp. 107–14.

Tong, R. and D. S. Kohane. 2012. “Shedding light on nanomedicine”. In: *Wiley Interdiscip Rev Nanomed Nanobiotechnol* 4, pp. 638–62.

Toomre, Derek, Jurgen A. Steyer, Patrick Keller, Wolfhard Almers, and Kai Simons. 2000. “Fusion of Constitutive Membrane Traffic with the Cell Surface Observed by Evanescent Wave Microscopy”. In: *The Journal of Cell Biology* 149, pp. 33–40.

Tooney, N. M., M. W. Mosesson, D. L. Amrani, J. F. Hainfeld, and J. S. Wall. 1983. “Solution and surface effects on plasma fibronectin structure”. In: *J Cell Biol* 97, pp. 1686–92.

Trauger, S. A., W. Webb, and G. Siuzdak. 2002. “Peptide and protein analysis with mass spectrometry”. In: *Spectroscopy-an International Journal* 16, pp. 15–28.

Tressel, T., J. B. McCarthy, J. Calaycay, T. D. Lee, K. Legesse, J. E. Shively, and H. Pande. 1991. “Human plasma fibronectin. Demonstration of structural differences between the A- and B-chains in the III CS region”. In: *Biochem J* 274 (Pt 3), pp. 731–8.

Turner, C E, J R Glenney, and K Burridge. 1990. “Paxillin: a new vinculin-binding protein present in focal adhesions”. In: *The Journal of Cell Biology* 111, pp. 1059–1068.

Ulmer, J., B. Geiger, and J. P. Spatz. 2008. “Force-induced fibronectin fibrillogenesis in vitro”. In: *Soft Matter* 4, pp. 1998–2007.

Vaananen, H. K., H. Zhao, M. Mulari, and J. M. Halleen. 2000. “The cell biology of osteoclast function”. In: *J Cell Sci* 113 (Pt 3), pp. 377–81.

Vale, R. D., T. Funatsu, D. W. Pierce, L. Romberg, Y. Harada, and T. Yanagida. 1996. “Direct observation of single kinesin molecules moving along microtubules”. In: *Nature* 380, pp. 451–3.

Van Vliet, A., H. J. Baelde, L. J. Vleming, E. de Heer, and J. A. Bruijn. 2001. "Distribution of fibronectin isoforms in human renal disease". In: *J Pathol* 193, pp. 256–62.

Velling, T., J. Risteli, K. Wennerberg, D. F. Mosher, and S. Johansson. 2002. "Polymerization of type I and III collagens is dependent on fibronectin and enhanced by integrins alpha 11beta 1 and alpha 2beta 1". In: *J Biol Chem* 277, pp. 37377–81.

Vuento, M., E. Salonen, K. Salminen, M. Pasanen, and U. K. Stenman. 1980. "Immunochemical characterization of human plasma fibronectin". In: *Biochem J* 191, pp. 719–27.

Wang, R., R. A. Clark, D. F. Mosher, and X. D. Ren. 2005a. "Fibronectin's central cell-binding domain supports focal adhesion formation and Rho signal transduction". In: *J Biol Chem* 280, pp. 28803–10.

Wang, W. 2005b. "Protein aggregation and its inhibition in biopharmaceutics". In: *Int J Pharm* 289, pp. 1–30.

Webb, D. J., J. T. Parsons, and A. F. Horwitz. 2002. "Adhesion assembly, disassembly and turnover in migrating cells – over and over and over again". In: *Nat Cell Biol* 4, E97–100.

Wehrle-Haller, Bernhard. 2012. "Structure and function of focal adhesions". In: *Current Opinion in Cell Biology* 24, pp. 116–124.

Weis, R. M., K. Balakrishnan, B. A. Smith, and H. M. McConnell. 1982. "Stimulation of fluorescence in a small contact region between rat basophil leukemia cells and planar lipid membrane targets by coherent evanescent radiation". In: *J Biol Chem* 257, pp. 6440–5.

Wennerberg, K., L. Lohikangas, D. Gullberg, M. Pfaff, S. Johansson, and R. Fassler. 1996. "Beta 1 integrin-dependent and -independent polymerization of fibronectin". In: *J Cell Biol* 132, pp. 227–38.

Wierzbicka-Patynowski, I. and J. E. Schwarzbauer. 2003. "The ins and outs of fibronectin matrix assembly". In: *J Cell Sci* 116, pp. 3269–76.

Wilson, C. L. and J. E. Schwarzbauer. 1992. "The alternatively spliced V region contributes to the differential incorporation of plasma and cellular fibronectins into fibrin clots". In: *J Cell Biol* 119, pp. 923–33.

Winklbauer, R. and C. Stoltz. 1995. "Fibronectin fibril growth in the extracellular matrix of the Xenopus embryo". In: *J Cell Sci* 108 (Pt 4), pp. 1575–86.

Wipff, P. J., H. Majd, C. Acharya, L. Buscemi, J. J. Meister, and B. Hinz. 2009. "The covalent attachment of adhesion molecules to silicone membranes for cell stretching applications". In: *Biomaterials* 30, pp. 1781–9.

Wittenburg, G., G. Lauer, S. Oswald, D. Labudde, and C. M. Franz. 2013. "Nanoscale topographic changes on sterilized glass surfaces affect cell adhesion and spreading". In: *J Biomed Mater Res A*.

Wolf, Katarina and Peter Friedl. 2009. "Mapping proteolytic cancer cell-extracellular matrix interfaces". In: *Clinical and Experimental Metastasis* 26, pp. 289–298.

Wolff, Carl and Ching-San Lai. 1989. "Fluorescence energy transfer detects changes in fibronectin structure upon surface binding". In: *Archives of Biochemistry and Biophysics* 268, pp. 536–545.

Wolff, S. P. and R. T. Dean. 1986. "Fragmentation of proteins by free radicals and its effect on their susceptibility to enzymic hydrolysis". In: *Biochem J* 234, pp. 399–403.

Wozniak, Michele A., Katarzyna Modzelewska, Lina Kwong, and Patricia J. Keely. 2004. "Focal adhesion regulation of cell behavior". In: *Biochimica et Biophysica Acta (BBA) - Molecular Cell Research* 1692, pp. 103–119.

Wu, C., J. S. Bauer, R. L. Juliano, and J. A. McDonald. 1993. "The alpha 5 beta 1 integrin fibronectin receptor, but not the alpha 5 cytoplasmic domain, functions in an early and essential step in fibronectin matrix assembly". In: *J Biol Chem* 268, pp. 21883–8.

Wu, C., V. M. Keivens, T. E. O'Toole, J. A. McDonald, and M. H. Ginsberg. 1995. "Integrin activation and cytoskeletal interaction are essential for the assembly of a fibronectin matrix". In: *Cell* 83, pp. 715–24.

Yadavalli, V. K., D. V. Svintradze, and R. M. Pidaparti. 2010. "Nanoscale measurements of the assembly of collagen to fibrils". In: *Int J Biol Macromol* 46, pp. 458–64.

Yamada, K. M. and K. Olden. 1978. "Fibronectins–adhesive glycoproteins of cell surface and blood". In: *Nature* 275, pp. 179–84.

Yamaguchi, H., F. Pixley, and J. Condeelis. 2006. "Invadopodia and podosomes in tumor invasion". In: *Eur J Cell Biol* 85, pp. 213–8.

Zaidel-Bar, R. and B. Geiger. 2010. "The switchable integrin adhesome". In: *Journal of Cell Science* 123, pp. 1385–1388.

Zamir, E., M. Katz, Y. Posen, N. Erez, K. M. Yamada, B. Z. Katz, S. Lin, D. C. Lin, A. Bershadsky, Z. Kam, and B. Geiger. 2000. "Dynamics and segregation of cell-matrix adhesions in cultured fibroblasts". In: *Nat Cell Biol* 2, pp. 191–6.

Zardi, L., C. Cecconi, O. Barbieri, B. Carnemolla, M. Picca, and L. Santi. 1979. "Concentration of fibronectin in plasma of tumor-bearing mice and synthesis by Ehrlich ascites tumor cells". In: *Cancer Res* 39, pp. 3774–9.

Zhong, C., M. Chrzanowska-Wodnicka, J. Brown, A. Shaub, A. M. Belkin, and K. Burridge. 1998. "Rho-mediated contractility exposes a cryptic site in fibronectin and induces fibronectin matrix assembly". In: *J Cell Biol* 141, pp. 539–51.

Zhou, Xiongtu, Jian Shi, Fan Zhang, Jie Hu, Xin Li, Li Wang, Xueming Ma, and Yong Chen. 2010. "Reversed cell imprinting, AFM imaging and adhesion analyses of cells on patterned surfaces". In: *Lab Chip* 10, pp. 1182–1188.

Ziegler, U., A. Vinckier, P. Kernen, D. Zeisel, J. Biber, G. Semenza, H. Murer, and P. Groscurth. 1998. "Preparation of basal cell membranes for scanning probe microscopy". In: *FEBS Lett* 436, pp. 179–84.

Appendix

Movies (included in CD)

Movie 5.1 Investigating FN fibrillogenesis by time-lapse AFM in living REF52 cells. Cells were placed on FN coated mica and a region of $10\,\mathrm{x}\,10\,\mu\mathrm{m}^2$ was scanned by AFM in contact mode after initial spreading of 5 min. Images were collected every ~ 3 min. The deflection time-lapse images show retraction of cell edge on FN creating fibrils. Scale bar 1.5 µm.

Movie 5.2 Investigating FN fibrillogenesis by time-lapse AFM in living REF52 cells in presence of 1 mM Mn^{2+}. Cells were placed on FN coated mica and incubated on it in presence of 1 mM Mn^{2+} for 5 min to ensure initial spreading. A region of $10\,\mathrm{x}\,10\,\mu\mathrm{m}^2$ was scanned by AFM in contact mode. Images were collected every 3 min. The deflection time-lapse images show retraction of cell edge on FN creating fibrils. Scale bar 1.5 µm.

Movie 5.3 FN rearrangement by cells in presence of 1 mM Mn^{2+}. A region of $10\,\mathrm{x}\,10\,\mu\mathrm{m}^2$ was scanned by AFM in contact mode for 40 min. AFM images were taken approximatly every 4 min. In the beginning, a part of a lamellipodium is shown. The major part of the imaged region demonstrates that FN had a homogeneous distribution before rearrangement. During the next 21 min, the cell protruded and covered a part of the imaged area, before it started to retract back (29 min) leaving fibrils back on the substrate. After 40 min, many large FN fibrils are present on the substrate. Scale bars: 1 µm.

Movie 6.1 Imaging of vinculin-EGFP expressing MEF cells on FN-AF568 with TIRFM. MEF cells, transiently expressing the vinculin-EGFP construct for visualizing FAs were seeded on FN-AF568. The area around one representative FN-AF568 cell was imaged every minute to monitor FN rearrangement into fibrils. However, the time-lapse imaging does not show any changes of the FN distribution, although the cell spreads

normally and creates FAs at its periphery. Moreover, FAs demonstrate dynamic behavior during imaging. Scale bar 5 µm.

Movie 6.2 Visualizing FN fibrillogenesis in HFF cells by time-lapse fluorescence microscopy. HFF cells were seeded on FN-AF633, to exposure the sample at 625 nm wavelength. Images were collected every 30 min to minimize the irradiation time. Furthermore, Oxyrase® was added to the imaging medium to remove oxygen preventing creation of reactive oxygen. To improve integrin binding to FN, imaging medium was supplemented with 1 mM Mn^{2+}. The time-lapse demonstrates fibril creation by cells during imaging. Scale bar 20 µm.

Curriculum Vitae

Not included in the electronic version.

List of publications

Articles

- **Gudzenko, T. and C. M. Franz**. (2013). Inverting adherent cells for visualizing ECM interactions at the basal cell side. *Ultramicroscopy* 128:1-9.
- **Rahul P. Langhe, Tetyana Gudzenko, Michaell Bachmann, Clemens M. Franz and Jubin Kashef**. Cadherin-11 localizes to focal adhesions and promotes cell-substrate adhesion. In revision.

Posters

- **Tetyana Gudzenko and Clemens M. Franz**. Combining AFM and TIRF Microscopy to Investigate Cell-mediated Fibronectin Fibrillogenesis. JPK's XX. Annual International Symposium on SPM & Optical Tweezers for Life Sciences. Berlin (Germany). October, 2011.
- **Tetyana Gudzenko and Clemens M. Franz**. Investigating fibronectin fibrillogenesis by combining TIRFM and AFM. CFN summer school on nano-biology. Bad Herrenalb (Germany). September, 2011.
- **Tetyana Gudzenko and Clemens M. Franz**. Investigation of podosomes by high-resolution AFM. Gordon-Kenan research seminar and Gordon research conference on science of adhesion. Bates college (USA). July, 2011.
- **Tetyana Gudzenko and Clemens M. Franz**. Observing cell-induced fibronectin fibrillogenesis by combined atomic force and total internal reflection microscopy. Gordon-Kenan research seminar and Gordon research conference on fibronectin, integrins and related molecules. Lucca (Italy). April-May, 2011.

Talk

- **Tetyana Gudzenko and Clemens M. Franz**. Investigating cell-induced fibronectin fibrillogenesis by combining TIRFM and AFM. The XIV. Annual Linz Winter Workshop and Hands-on Winter School. Linz (Austria). January-February, 2012.

Acknowledgements

I would like to express my very great appreciation to Dr. Clemens Franz for offering me the opportunity to make research in his group. Thank you very much, for your academic and personal support, valuable and constructive suggestions during the planning and development of this interesting and challenging work.

I would like to express my deep gratitude to Prof. Dr. Martin Bastmeyer for providing me with access to facilities in his lab, especially for using all available microscopes.

My sincere thanks go to my friends and colleagues as well as students for the great time, helpful discussions, advices and continuous support. Carina Gonnermann was my single colleague for the last two years. Carina, thank you for the nice atmosphere in the office and in the cellar during AFM scans. I like to express greatest thanks to Ramona Ring for the excellent technical support in the lab and encouragement. Ramona, vielen Dank für deine technische und persönliche Unterstützung, die meine Arbeit immer vorangetrieben haben. Furthermore, I thank my former colleagues: Dr. Anna Müller for introducing me to the secrets of scanning electron microscopy and helping me with the daily routine, Dr. Lu Dao for nice travelling time to all conferences we attended, Dr. Anna Burcza and Dr. Dimitar Stamov for valuable discussions, ideas and nice time.

I thank all my current and former colleagues from Zoology Institute I for your collaboration, discussions and ideas. Especially, Dr. Jana Ustinova (for introducing me to my Chef), Dr. Tatjana Authenried (for being a very helpful contact person in all questions and problems), Michaell Bachman (for imaging my samples with SIM and PALM), Benjamin Richter (for creating me 3D substrates), Hao Chen (for introducing me to Collibri microscope) and Marcus Weschenfelder (for introducing and supporting me with the Apotome).

I would also like to extend my thanks to the colleagues and technicians of the CFN and physical department of KIT for their help in offering me the access to the electron microscope and resources: Dr. Joachim Fischer for helping me to build up an optical setup for my experiments, Stephan Kühn for supporting me with SEM, Patrice Brenner for preparing experiments with SEM/FIB, Andreas Elkeries for solving all technical questions concerning software and hardware, Mrs. Bender and Mrs. Mösle (our secretaries) for taking care of bureaucratic staff.

Many thanks go to all my friends in Karlsruhe, Nürnberg and Charkiw for the nice time on weekends.

Last but by no means least, I would like to thank my family and close relatives for your love, support and the opportunity to start and pursue a career in science. I am particularly indebted to my parents, my sister Olga and brother Aleksander for their never-ending encouragement. Very special thanks go to my husband Grigorij. “Hasi”,

thank you very much for your believing in me and your help in all aspects of this work. You supported me not only from the technical side (MatLab, LaTeX, Inskape and so on) but also with your interest in my research and critical discussions about my work. Many thanks go also to our sweet daughter Veronika for your patience, "Kuschelstunden" and all painted pictures. I promise to have more time for you in future. I send also special thanks to my mother-in-law. Liebe Schwiegermutter, ich bedanke mich bei dir für Deine Hilfe, insbesondere für die Ganztagsbetreuung von Veronika während der letzten vier Monate. Ohne Dich hätte meine Arbeit kein Abschluß gefunden. Vielen Dank an meine Schwägerin Swetlana und meinen Schwager Alexander Sachnov und deren Kinder Anton und Georg für die gemeinsamen Reisen und gegenseitige Besuche, die mich aufgebaut und motiviert haben.